

# **Photonic Technologies for Broadband Microwave Wireless Systems, Instrumentation and Sensing**

Von der Fakultät für Ingenieurwissenschaften der  
Universität Duisburg-Essen  
zur Erlangung der Lehrbefähigung im  
Lehrgebiet Optoelektronik

genehmigte Habilitationsschrift

von

Dr.-Ing. Andreas Stöhr

aus

Duisburg



## Acknowledgement

This work originates from my scientific research activities at the department of Optoelektronik at University Duisburg-Essen in Duisburg, Germany, and during my two Center-of-Excellence research fellowships at the National Institute of Information and Communications Technology in Tokyo, Japan, and my research fellowship at France Telecom – Orange Laboratories in Lannion, France.

I would foremost like to thank my former advisor and former head of the Optoelektronik department at University Duisburg-Essen, Prof. Dieter Jäger. He encouraged me to embark on a journey towards photonics and microwaves and he offered me unrestricted opportunities that have allowed me to carry out my scientific research work. His valuable suggestions, his fairness and endorsement have inspired me on countless occasions.

I am furthermore thankful to Madame Prof. Beatrice Cabon, not only for reviewing my habilitation thesis but also for the fruitful and long-lasting scientific cooperation during a number of European projects. Her way of managing international and interdisciplinary research teams has always acted as a model to me.

Deep gratitude also goes to Prof. Ken-ichi Kitayama for his inspiration and support during my two unforgettable stays at the National Institute of Information and Communications Technology in Tokyo. For inspiration and support, I am also gratefully thankful to Prof. Alwyn Seeds from University College London. The fruitful discussions with both and their stimulating ideas are greatly appreciated. Both have contributed a long way towards my decision to continue research in this direction.

Further gratitude goes to Dr. Benoît Charbonnier for his great support and valuable cooperation during my stay at France Telecom – Orange Laboratories in Lannion.

I also thank all Professors and habilitated members of the department for Elektrotechnik und Informationstechnik for their favorable cooperation. Special thanks go to Prof. Franz-Josef Tegude and my colleague and friend Dr. Rüdiger Buß for countless discussions and for their merely endless stimulating encouragements.

Many thanks also go to the members of the Optoelektronik department at University Duisburg-Essen and the scientists, graduate, and undergraduate students that have supported me during the course of my habilitation. Especially, I would like to thank Dr.-Ing. Thomas Alder, Dipl.-Ing. Robert Heinzelmann, Dipl.-Ing. Sascha Fedderwitz, and Dr.-Ing. Mario Weiß.

I thank Britta Buß for carefully reviewing my habilitation thesis.

My parents and my family have always supported my scientific endeavors for which I am gratefully thankful. Without them, I wouldn't be where I am.

Finally, my most heartfelt thanks go to my wife Monika for her amazing patience, her continuous care and simply for being there whenever needed. Her cheerful character and the breeziness nature of my two beloved sons, Tom and Alexander have always built the solid ground that allowed me to continue my journey.

## Table of Contents

<b>Acknowledgement .....</b>	<b>3</b>
<b>Table of Contents .....</b>	<b>5</b>
<b>1 Introduction .....</b>	<b>7</b>
1.1 The roots of microwave photonics .....	7
1.2 History and definition of microwave photonics .....	10
1.3 Scope of this work .....	11
<b>2 Photonic Millimeter-wave and THz Signal Generation.....</b>	<b>14</b>
2.1 Optical heterodyning .....	15
2.1.1 Dual-wavelength and dual-mode lasers for optical heterodyning .....	21
2.1.2 Mode-locked laser diodes .....	27
2.1.3 Optical comb line selection.....	30
2.1.4 Optical injection locking.....	32
2.1.5 Optical phase lock loops .....	34
2.1.6 Optical injection phase lock loops .....	36
2.2 Optical intensity modulation and direct detection.....	38
2.3 Opto-electronic oscillator .....	43
2.4 Nonlinear optical frequency generation techniques .....	45
2.4.1 All-optical frequency up-conversion using MZM .....	45
2.4.2 Four wave mixing in SOA and in highly nonlinear fibers .....	46
2.4.3 Cross phase modulation in highly nonlinear optical fibers.....	50
2.4.4 Cross absorption modulation in EAM & cross gain modulation in SOA..	52
<b>3 Fiber-Optic Millimeter-Wave and THz Transport.....</b>	<b>55</b>
3.1 Attenuation in fiber-optic RF transmission systems .....	55
3.2 Dispersion induced power penalties in fiber-optic RF transmission systems .....	58
3.2.1 Optical double sideband (DSB) signals .....	61
3.2.2 Optical double sideband signals with suppressed carrier (DSB-SC).....	68
3.2.3 Optical combs .....	70
<b>4 Photonic Millimeter-Wave and THz Transmitter and Transceiver.....</b>	<b>73</b>
4.1 Millimeter-Wave and Terahertz Photomixer .....	75
4.1.1 100 GHz broadband travelling-wave photomixer.....	77
4.1.2 300 GHz wideband travelling-wave TW photomixer.....	92
4.1.3 460 GHz antenna integrated travelling-wave TW photomixers .....	97
4.1.4 1000 GHz ultra-wideband antenna and WR integrated photomixer.....	101
4.2 60 GHz Electro-absorption transceiver (EAT).....	104

<b>5</b>	<b>Broadband Photonic Millimeter-Wave Wireless Systems.....</b>	<b>114</b>
5.1	Applications and worldwide markets .....	115
5.2	Worldwide regulations and standardizations .....	121
5.2.1	Unlicensed wireless services in the 60 GHz band .....	122
5.2.2	Licensed wireless services in the 71-76 GHz and 81-86 GHz bands .....	123
5.2.3	Industrial standardization efforts .....	126
5.3	Rationale for using photonics for future broadband wireless systems.....	126
5.4	Link model for broadband photonic mm-wave wireless transmission.....	129
5.4.1	Wireless transmission capacity .....	129
5.4.2	Wireless channel model .....	134
5.4.3	Noise modeling .....	146
5.5	Advanced photonic millimeter-wave wireless system demonstrations.....	153
5.5.1	156 Mbit/s full-duplex 60 GHz photonic wireless system.....	155
5.5.2	10 Gbit/s broadband 60 GHz photonic wireless system .....	161
5.5.3	27 Gbit/s super-broadband 60 GHz photonic wireless system .....	165
5.6	State of the art in broadband photonic wireless demonstrations .....	170
<b>6</b>	<b>Microwave Photonics in Instrumentation and Sensing .....</b>	<b>174</b>
6.1	Applications and worldwide markets .....	174
6.2	Advanced microwave and mm-wave photonic sensors and oscillators .....	182
6.2.1	Microwave (300 MHz - 6 GHz) remote electro-optical EMC sensor.....	182
6.2.2	Millimeter-wave (75-110 GHz) photonic synthesizer .....	192
6.2.3	Phase-noise of the optically generated millimeter-wave signals .....	197
<b>7</b>	<b>Conclusion.....</b>	<b>205</b>
<b>Annexes .....</b>	<b>207</b>	
<b>References .....</b>	<b>225</b>	

# 1 Introduction

The field of research on optoelectronic components and functions and their utilization in microwave systems is termed “microwave photonics” [1-8]. Microwave photonics is an interdisciplinary field of research combining the worlds of radiofrequency engineering and optoelectronics. A recent publication in *Nature Photonics* forecasts a bright future for microwave photonics because it enables functions in microwave systems that are either too complex or cannot at all be achieved directly in the radiofrequency domain. These advantages are expected to be key for the creation of many new opportunities for telecommunication networks as well as for other applications [5]. But before discussing what exactly is meant by the term “microwave photonics”, some mention should be made of the root words first.

## 1.1 The roots of microwave photonics

Although there is no formal definition of the frequency range for “microwaves”, most books and scientific articles define it as the frequency range between 300 MHz and 300 GHz, i.e. as the wavelength range from 1 m down to 1 mm. This covers the ultra-high frequency (UHF) band, the super-high frequency (SHF) band, and the extended high frequency (EHF) bands as defined by the International Telecommunications Union (ITU) (see also Annex V). A bit more specific is the term “millimeter-waves” (mm-waves) that refers to signals in the frequency range from 30 GHz to 300 GHz, i.e. to the wavelength region from 10 mm down to 1 mm. Beyond mm-wave frequencies is the terahertz frequency range that is typically defined from 300 GHz up to 3 THz although in several publications it is also used to cover a broader frequency range from 100 GHz to about 10 THz.

“Photonics” is a term analog to “electronics”. The term “photonics” was coined in 1967 by *Pierre Aigrain*, a French scientist, who gave the following definition: *“Photonics is the science of the harnessing of light. Photonics encompasses the generation of light, the detection of light, the management of light through guidance, manipulation, and amplification, and most importantly, its utilisation for the benefit of mankind.”* [9]. In other words, photonics is the field of research concentrating on the generation, detection, manipulation and transmission of photons (as opposed to electrons). Instead of photonics one could also use the term “optics”, given the fact that the optical part of the spectrum is addressed, but today, optics is seen somewhat more general, i.e. optics covers the field of photonics but also more classical fields such as ray-optics.

In addition to “photonics” and “optics” there exist a number of other terms that are also widely used in the literature. Among them are “electro-optics”, “magneto-optics” or “acousto-optics”. Those expressions are typically used for referring to devices which are optically in nature but in which electrical, magnetic or acoustic effects play an important function. Examples are the Pockels-cell, the Faraday modulator or the acousto-optical Bragg cell, respectively. Another widely used term is “optoelectronics” which refers to devices that are electronics in nature (such as *pn*- or *pin*-diodes) but in which the interaction between electrons and photons plays an essential role. This includes semiconductor laser diodes and photodiodes.

In this work, the terms “photonics” and “optoelectronics” will be largely used - besides the term “microwave photonics”, of course.

Historically, the development of optical systems can be dated back to ancient times. *Aeschylus* writes in his poem Agamemnon that fire signals were used to transport the message about the victory of the Greeks (1184 B.C.) about Troy to the city Argos [10]. Although some modern investigations concluded that it is unlikely that this about 500 km long optical telegraph system was really built as described, it at least shows that the principles of the technique were known to *Aeschylus* who lived about 500 years before Christ (525-456 B.C.). More than 2000 years later, the French technician *Claude Chappe* also constructed an optical telegraph (Sémaphore) [11]. He used different signs allowing the transmission of altogether 192 different words or parts of sentences instead of just one signal (fire on ≡ victory over Troy). But although his telegraph employed code multiplex, it also fundamentally relied on the basic human ability to visualize signals. It was only the invention of the electrical telegraph in the first half of the 19<sup>th</sup> century that has then moved the focus on electrical communication systems [12] for about the next two centuries. Within that period, information was not only transmitted via cables or wires but scientists of the 19<sup>th</sup> century also invented wireless communication systems. Starting off from low carrier frequencies, the need and advantages of higher frequencies was early recognized. In fact more than 100 years ago, in the 1890s, *Chandra Bose* experimentally studied 60 GHz mm-wave wireless systems [13]. But millimeter-waves were not considered for wireless communications only. In the 1960s, a strong increase in data traffic had been forecasted due to the expected enormous utilization of the picturephone, a telephone for voice and picture transmission which was first exhibited at the New York’s world fair in 1964 [14]. To handle this expected increase in data traffic, systems providing more bandwidth were searched and consequently many researchers e.g. at Bell Labs had worked on a low-loss millimeter waveguide system [15]. This experimental pipe was supposed to carry a circularly-polarized millimeter-wave signal capable of transporting the expected data capacity in the future. According to *Robert Lucky* from Bell Labs who had worked on the low-loss millimeter-wave project, the millimeter waveguide carrier system was “*unceremoniously dropped almost the instant the news came in*

1970 that Corning had made an optical glass fiber with the benchmark attenuation of only 20 dB per kilometer” [15]. This invention was based upon the work of Bob Maurer, Peter Schulz and Donald B. Keck on waveguide attenuation and dispersion as well as on the measurement of optical fiber properties. It had not only led to Corning’s move into photonics [16] but it had also directed many researchers and engineers to concentrate on optical communications further on. But although the first “low-loss” indeed was an important milestone, it still was “only” one in a series of previous important inventions that altogether had finally enabled the move to fiber optic communications. Among the most important ones is the theoretical prediction of stimulated emission by Albert Einstein in 1917 [17] (recipient of the Nobel Prize in Physics in 1921 for “*his services to Theoretical Physics, and especially for his discovery of the law of the photoelectric effect*” [18]), the development of the MASER by Charles H. Townes in 1954 (recipient of the Nobel prize for physics for “*fundamental work in the field of quantum electronics, which has led to the construction of oscillators and amplifiers based on the maser-laser principle*” jointly with Nikolai Gennadijewitsch Bassow and Alexander Michailowitsch Prochorow) [19] as well as the later development of the first ruby laser by Theodore H. Maiman in 1960 [20]. This was followed by the development of the first semiconductor laser diode in 1962 [21], the development of double heterostructures by Herbet Krömer and Zhores I. Alferov (recipients of the Nobel Prize in Physics in 2000 for “*developing semiconductor heterostructures used in high-speed- and opto-electronics*”) which had allowed the development of the first continuous-wave (cw) semiconductor lasers [22, 23]. A further important step which had especially stimulated the research at Corning and which in fact is often seen as the birth of fiber-optic communications was the theoretical prediction of the low-loss fundamental mode in glass fibers by Charles K. Kao and Hockham in 1965 (Charles K. Kao received the Nobel Prize in Physics in 2009 for “*groundbreaking achievements concerning the transmission of light in fibers for optical communication*”) [24, 25]. All this inventions and developments finally led to the fact that telecom operators moved to fiber optic communications in 70s and 80s of the last century. Many further inventions followed, among which the development of the Erbium-doped fiber amplifier by David N. Payne should be mentioned [26, 27]. Today, optical fibers have losses on only 0.1-0.2 dB/km and almost the complete worldwide metro and long distance data traffic runs at least once through an optical fiber. But fiber is not only used in metro and long-haul communications, it is now underway to penetrate to the home and even into the home.

In parallel to the enormous success of optical communications, also wireless communications has become an indispensable modern technology, and there is no doubt that especially wireless networks will face a capacity crunch soon. Currently both, not only worldwide internet but also mobile data traffic is doubling about every 1-1½ years (see for example Fig. 5.1). In the wireless domain this is driven by a steady increase of new mobile services fueling the ever increasing demand for higher data rates as well as by mobile operators encouraging their subscribers to

migrate from previous generation mobile standard GSM with a bandwidth of a few hundred kilobits per second over HSPA to future LTE offering a peak bandwidth of up to 150 Mbit/s.

The above discussions imply that future microwave systems (such as broadband wireless) and optical systems (such as fiber-optic communications) will eventually converge. For example, next generation wireless LTE systems are expected to extensively use existing fiber-optic infrastructure for backhauling the mobile traffic and on the other hand current fiber-optic communications make use of wireless last-mile technologies for extending the reach of access and in-house networks. Somehow, it was always clear that microwave and optical technologies are complementary in many aspects, and it is not at all surprising that they converged, forming a new interdisciplinary field of research: “microwave photonics”.

## **1.2 History and definition of microwave photonics**

The field took off under the term “microwave optical interactions” in the late 1970s when first experiments were carried out. It became an internationally recognized field of research in 1991 when the first IEEE LEOS (IEEE Lasers and Electro-Optic Society, renamed into IEEE Photonics Society in 2009) summer topical meeting on “Optical Millimeter Interactions” was held in Newport Beach. This was followed by another topical IEEE LEOS meeting two years later on “Optical Microwave Interactions” in Santa Barbara before it became international in 1994, when the meeting was held in Cernay-la-Ville, Ile de France. The last IEEE LEOS meeting on “Optical Microwave Interactions” was held 1995 in Keystone. After that, the meeting was renamed into “International Topical Meeting on Microwave Photonics (MWP)” and it was further on held as an independent conference in an annually rotating cycle between Asia, Europe and America, taking place in Kyoto in 1996, in Duisburg in 1997, in Princeton in 1998 and so on.

The first appearance of the term “microwave photonics” can be dated back to 1991, when *Dieter Jäger* published a manuscript entitled “Microwave Photonics” dealing with travelling optical and microwave electromagnetic fields in semiconductor waveguide devices [1]. This was followed by a number of publications with the same or similar titles in the early years of this century [2-8, 28] as well as by several books [29-31]. Furthermore, a biannual special issue on microwave photonics is jointly published by the IEEE Photonics and the IEEE MTT-S societies (see e.g. [32]). Today, microwave photonics is generally considered as: “*First, the study of opto-electronic devices and systems processing signals at microwave rates. Second, the use of opto-electronic devices and systems for signal handling in microwave systems*” as defined by *Alwyn Seeds* in 2002 [3].

Since the early days, the field has expanded significantly and is generally considered as a disruptive technology for several radio-frequency applications [33]. By integrating the best out of the photonic and the radiofrequency engineering worlds, Microwave Photonic technologies can enable broadband connectivity with some unique advantages that cannot easily be achieved by other competing technologies such as all-electronic systems. Besides the benefits of a low transmission loss and a low weight due to the use of optical fiber for radio-frequency transport, microwave photonics technologies furthermore potentially enable low phase noise radio-frequency generation and ultra-wide frequency tunability as well as broadband modulation capabilities over the entire microwave band. Today, microwave photonics is addressing a considerable number of commercial applications. Some of these applications have yet already achieved a substantial annual sales market in the order of 100 M€ [34], others are more in the research and development phase (for examples see e.g. [32]). The demand for Microwave Photonic technologies is further fueled by the ever increasing operating frequencies utilized in many applications. According to a recent survey, the interest in Microwave Photonic technologies is especially strong in a growing number of applications utilizing the millimeter-wave frequency range (30-300 GHz) [35].

### 1.3 Scope of this work

The focus of this work is to theoretically study and develop specific photonic-based hybrid or/and monolithic integrated functions operating in the microwave (300 MHz - 300 GHz) frequency band in order to respond to the always growing demand for higher data rate transmission. Next generation fixed wireless technology using radio over fiber technologies for high data rate applications with world record transmission capacities will be demonstrated. For the first time, the presented technologies enable the construction of wireless links operating at transmission speeds previously only known from fiber-optic communications. This capability will be of great value for future mobile backhauling, disaster recovery and temporary high capacity wireless links. At the same time, the proposed photonic-based microwave technologies will be shown, to be also of great value to a number of other generic application fields including sensing, instrumentation, health-care, medical applications and radio-astronomy.

- Chapter two of this work discusses the fundamental theoretical background of four generic photonic techniques for high-frequency millimeter-wave and THz signal generation: optical heterodyning, intensity modulation with subsequent direct detection, the opto-electric oscillator concept and all-optical nonlinear mixing or up-conversion. In addition, several experimental results will be presented including frequency tunable

wideband optical frequency generation from DC up to 110 GHz using novel photodiodes or resonant 60 GHz generation using mode-locked lasers.

- In chapter three, the attenuation and dispersion induced power penalties of fiber-optic systems for millimeter-wave and THz modulated signal transmission systems are theoretically and experimentally studied. This is done for conventional double sideband modulated optical signals but also for more complex optical modulation formats including double sideband with suppressed carrier modulation as well as for optical combs. The dispersion induced maximum single mode fiber transmission length is theoretically and experimentally determined for chirped mm-wave modulated optical double sideband signals. Furthermore, optical approaches including optical pre-chirping are presented that allow extending the maximum fiber length beyond the dispersion-limitation, e.g. for 60 GHz transmission systems.
- The fourth chapter of this work focuses on the technological challenges involved in the development of very high-frequency optical components and functions which are key for fiber-optic transmission systems. Advanced photonic components and functions with exceptional performances will be presented. Among them are 60 GHz transceivers for broadband wireless applications, broadband (DC-110 GHz) and wideband (30-300 GHz) photomixers for frequency-tunable signal generation as well as ultra-fast resonant 460 GHz and wideband (25-1000 GHz) photonic transmitters for applications in radio-astronomy.
- Chapter five puts a focus on today's importance of broadband fixed wireless communications and the role and advantages microwave photonics technologies can bring to this application field. At first, it will be shown that there is a great economical need for broadband wireless systems that could offer much higher data rates as today's wireless systems. Next, new broadband wireless architectures based upon advanced photonic technologies and components which were developed in this work will be presented and discussed. Experimentally, broadband wireless systems with world record performances in terms of maximum wireless data capacity and spectral efficiency will be reported in this chapter.

- In the sixth chapter, it will be demonstrated that microwave photonics can truly be considered as an advanced high-frequency source technology for multiple applications in instrumentation, sensing, security, radar as well as medical applications. Advanced, compact and potentially low-cost photonic-based high-frequency sources and sensors will be presented. This includes a wideband microwave (300 MHz to 6 GHz) photonic-based sensor system for electric field measurements and a millimeter-wave photonic-based synthesizer offering a wide frequency-tuning range from 75 GHz to 115 GHz.
- Chapter 7 will summarize the work and provide a brief outlook of future developments and challenges.

## 2 Photonic Millimeter-wave and THz Signal Generation

Various techniques for the generation of high-frequency millimeter-wave and THz continuous-wave (cw) signals by optical means have been studied in the recent past. Those techniques can be generally categorized into four major groups: Heterodyning of two or more optical cw signals in a photodiode, the direct detection (in a photodiode) of intensity modulated optical signals, the opto-electronic oscillator approach, and optical mixing or up-conversion using highly non-linear optical elements. The following sections of this chapter will cover the fundamental theoretical background for all this four principle approaches and the recent achievements in this field. Also, general advantages and disadvantages of the four principle techniques will be discussed. The focus of chapter 2 will hereby be put on the “generation” of high-frequency signals by optical means; the transport of such optical signals via single-mode glass fibers will be part of the discussions in chapter 3.

A classical approach for optical high-frequency signal generation is based upon heterodyning two (or more) phase-correlated, coherent optical signals in a photodiode. Given that the two (or more) coherent optical signals differ in wavelength, the photodiode’s output will be an RF signal with a frequency defined by the beat frequency between the two (or more) phase-correlated optical input signals. Optical heterodyning inherently requires optical sources having extremely frequency-stable and low-phase noise output signals, which is not at all a trivial requirement. Different lasers for generating such phase-correlated optical modes have been studied in this work and by other research groups; this will be looked at in section 2.1. The advantage of heterodyning two optical modes in a photodetector, which is sometimes also referred to as photomixing, is its insensitivity to the fiber’s chromatic dispersion. Because of that, dual-mode optical heterodyning generally allows the use of rather long fiber-optic transmission lengths which are mainly limited by the fiber’s attenuation even at very high RF frequencies.

On the contrary, fiber-optic transmission of intensity modulated optical signals is strongly dependent on the fiber’s chromatic dispersion. This approach which is also named intensity-modulation direct-detection (IMDD) does not have stringent requirements on the linearity and phase noise of the laser sources. Its major hurdles are the limited modulation bandwidth of lasers and optical modulators and the fact that fiber-spans in IMDD links are severely limited by chromatic dispersion at high RF frequencies. Section 2.2 will review different techniques for high-frequency IMDD links, the dispersion penalties involved in IMDD links will be discussed in chapter 3.

Another approach to generate high-frequency RF signals by optical means is to realize an optoelectric oscillator (OEO) which is described in section 2.3. Generally, an OEO can be considered as an optical medium providing gain with an optical feedback loop. As such, an OEO is an oscillator that converts optical energy, e.g. from a cw laser source, into a pure and stable RF signal. In most cases optical fiber is used as a low-loss energy storage element in an OEO for the generation of very high-spectral-purity and high-stability RF signals. A disadvantage typically associated with conventional OEOs is their limitation in frequency-tuning.

Finally, high-frequency RF signal generation by all-optical up-conversion techniques based upon highly nonlinear optical elements will be looked at in section 2.4. Discussions will include four-wave mixing (FWM), cross phase modulation (XPM) and cross absorption modulation (XAM). Also cross gain modulation in highly nonlinear optical fibers, in active semiconductor optical amplifiers (SOA) and in electro-absorption modulators (EAM) will be discussed. All these nonlinear effects can be exploited to up-convert intermediate frequency (IF) signals to high-frequency RF signals by all-optical means.

## 2.1 Optical heterodyning

As mentioned above, a classical approach for high-frequency signal generation is based upon heterodyning two optical light beams in a high-frequency photodiode. This approach is also referred to as photomixing, i.e. the mixing of two light waves. Often, the utilized o/e converter is thus also referred to as photomixer instead of a photodetector, although from a component point of view there is no fundamental physical difference between a photomixer and a photodetector other than the fact that each component might be optimized in a different way. The concept of

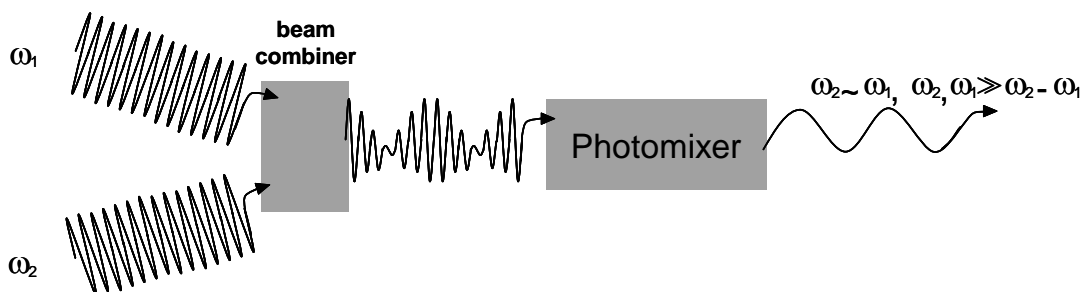


*Fig. 2.1 Principle of optical heterodyne signal generation. Two coherent optical waves with slightly different frequencies  $\omega_1$  and  $\omega_2$  (typically in the infrared region) are superimposed. This results in a "beat" wave whose amplitude envelope varies according to the difference frequency  $\omega_2 - \omega_1$  between the two incident optical waves. Finally, the beat wave is heterodyned in a photomixer.*

optical heterodyning or photomixing is illustrated in Fig. 2.1.

Two optical waves with angular frequencies  $\omega_1$  and  $\omega_2$  are superimposed and injected into a high-frequency photomixer which down-converts the optical input signals to the mm-wave or THz range by generating an electrical signal having the angular frequency  $\omega_2 - \omega_1$ . To explain this in more detail, it is necessary to consider the relation between the generated electrical output signal and the two superimposed optical input waves in a more physical approach. For simplicity, it is assumed that the two optical input waves are linearly polarized monochromatic plane waves which propagate along the  $+z$ -direction. Let

$$\underline{\vec{E}}_1 = \hat{E}_1 \cdot e^{j(\omega_1 t - k_1 z + \phi_1)} \vec{e}_1, \quad (1)$$

and

$$\underline{\vec{E}}_2 = \hat{E}_2 \cdot e^{j(\omega_2 t - k_2 z + \phi_2)} \vec{e}_2, \quad (2)$$

be the complex electrical field vectors of the two optical waves, with field amplitudes  $\hat{E}_1$  and  $\hat{E}_2$ , angular frequencies  $\omega_1$  and  $\omega_2$  and wave numbers  $k_1$  and  $k_2$ . The phase of each optical input wave is considered by  $\phi_1$  and  $\phi_2$ ,  $\vec{e}_1$  and  $\vec{e}_2$  are the unit vectors determining the orientation of the electrical field vector of the linearly polarized optical input waves. Assuming free-space propagation and that  $\mu_r \sim 1$  at optical frequencies, the magnetic fields of the constituent waves can simply be calculated from Faraday's induction principle to be:

$$\begin{aligned} \underline{\vec{H}}_1 &= \sqrt{\frac{\epsilon_0}{\mu_0}} \cdot \underline{\vec{E}}_1 \\ \underline{\vec{H}}_2 &= \sqrt{\frac{\epsilon_0}{\mu_0}} \cdot \underline{\vec{E}}_2. \end{aligned} \quad (3)$$

The intensities of the constituent waves are given by the magnitude of their time averaged Poynting vectors which can be determined from:

$$\langle \vec{S} \rangle = \langle \vec{E} \times \vec{H} \rangle = \frac{1}{T} \int_{t_0}^{t_0+T} \vec{S} \cdot dt = \frac{1}{2 \cdot T} \int_{t_0}^{t_0+T} \underline{\vec{E}} \times \underline{\vec{H}}^* \cdot dt = \frac{1}{2} \operatorname{Re} \left\{ \underline{\vec{E}} \times \underline{\vec{H}}^* \right\}. \quad (4)$$

By including eqs. (2) and (3) into (4), the intensities of the two constituent waves can be derived from the magnitude of the time averaged Poynting vectors:

$$\begin{aligned} I_1 &= \frac{1}{2} \cdot \sqrt{\frac{\epsilon_0}{\mu_0}} \cdot |\underline{\vec{E}}_1|^2 = \frac{1}{2 \cdot z_0} \cdot |\underline{\vec{E}}_1|^2 \\ I_2 &= \frac{1}{2} \cdot \sqrt{\frac{\epsilon_0}{\mu_0}} \cdot |\underline{\vec{E}}_2|^2 = \frac{1}{2 \cdot z_0} \cdot |\underline{\vec{E}}_2|^2 \end{aligned} \quad (5)$$

with  $z_0 \sim 377 \Omega$  representing the free-space impedance. If the two incident optical waves are perfect plane waves and have precisely the same polarization, the resulting electrical field of the optical interference signal is the sum of the two constituent input fields and hence we can write

$$\underline{\vec{E}}_0 = \underline{\vec{E}}_1 + \underline{\vec{E}}_2. \quad (6)$$

Taking the squared absolute value of the optical interference signal we obtain

$$\begin{aligned} |\underline{\vec{E}}_0|^2 &= |\underline{\vec{E}}_1 + \underline{\vec{E}}_2|^2 = |\underline{\vec{E}}_1|^2 + |\underline{\vec{E}}_2|^2 + \underline{\vec{E}}_1 \cdot \underline{\vec{E}}_2^* + \underline{\vec{E}}_1^* \cdot \underline{\vec{E}}_2 \\ &= |\underline{\vec{E}}_1|^2 + |\underline{\vec{E}}_2|^2 + 2 |\underline{\vec{E}}_1| |\underline{\vec{E}}_2| \cos[(\omega_2 - \omega_1)t - (\phi_2 - \phi_1)]. \end{aligned} \quad (7)$$

By introducing eq. (7) into eq. (5), the intensity of the interference signal  $I_0$  is given by:

$$I_0 = I_1 + I_2 + 2 \cdot \sqrt{I_1 \cdot I_2} \cdot \cos[(\omega_2 - \omega_1)t - (\phi_2 - \phi_1)]. \quad (8)$$

Thus, when launching the optical interference signal with the above intensity into a photomixer (or photodetector), a photocurrent  $i_{ph}$  is generated which can be expressed as

$$\begin{aligned} i_{ph} = & \eta_0 \cdot q / h f_1 \cdot P_1 + \eta_0 \cdot q / h f_2 \cdot P_2 \\ & + 2\eta_{fc} \cdot q / h \cdot \sqrt{\frac{P_1 P_2}{f_1 f_2}} \cos[(\omega_2 - \omega_1)t - (\phi_2 - \phi_1)] \end{aligned} \quad (9)$$

where  $q$  is the electron charge and  $P_1$  and  $P_2$  denote the optical power levels of the two constituent optical input waves. The photomixer's DC and high-frequency quantum efficiencies are represented by  $\eta_0$  and  $\eta_{fc}$ . It should be noted that the photomixer's RF quantum efficiency is not independent of the frequency. Several intrinsic and extrinsic effects such as transit time limitations or microwave losses will eventually limit the performance of the photomixer at mm-wave or THz frequencies and consequently the detector's DC responsivity  $\eta_0$  is typically much larger than its high-frequency responsivity  $\eta_{fc}$ . This will be further investigated theoretically and experimentally in section 4.1.

For the case of the two injected optical waves into a photomixer, the photocurrent eq. (9) can be further simplified by considering the fact that the optical frequencies of the two optical input waves are similar ( $f_1 \sim f_2$ ) whereas the difference frequency  $f_c$  in the mm-wave or THz-regime is of course by far smaller (i.e.  $f_c = f_2 - f_1 \ll f_1, f_2$ ). For example: if one employs a photomixer operating in the infrared region, the optical input wavelengths might be  $\lambda_1 = 1.55 \text{ } \mu\text{m}$  ( $f_1 = 193.4 \text{ THz}$ ) and  $\lambda_2 = 1.542 \text{ } \mu\text{m}$  ( $f_2 = 194.4 \text{ THz}$ ). In this case, the difference frequency is exactly  $f_c = 1 \text{ THz}$  and it is about 200 times smaller than the optical frequencies. As a rule of thumb, it can be stated that a small detuning of a laser's wavelength by only 0.8 nm (at 1.55  $\mu\text{m}$ ) results in a remarkable variation of the beat frequency by about 100 GHz.

If we further assume for simplicity that the power levels of the two optical input waves are equal ( $P_2 \sim P_1 \sim P_{opt}$ ), equation (9) becomes

$$i_{ph} = 2 \cdot s_0 \cdot P_{opt} + 2 \cdot s_{fc} \cdot P_{opt} \cdot \cos(2\pi \cdot f_c + \Delta\phi). \quad (10)$$

where

$$f_c = f_2 - f_1, \quad (11)$$

denotes the difference frequency or beat frequency of the two constituent optical input waves and  $\Delta\Phi = \Phi_1 - \Phi_2$ . Here,  $s_0 = \eta_0 \cdot q / (h f_c)$  and  $s_{fc} = \eta_{fc} \cdot q / (h f_c)$  are the photodetector's DC and high-frequency responsivities in (A/W).

Equation (10) is the fundamental equation describing optical heterodyning in a photomixer. The first term in eq. (10) represents the DC photocurrent generated by the constituent optical input waves and the second term is the desired high-frequency signal oscillating at the difference frequency  $f_c$ . From a physical point of view, it is important to note that by optical heterodyning no signal is generated which oscillates at the sum of the two optical frequencies. This is in contrast to nonlinear optical effects (see section 2.4) in a second-order nonlinear medium where not only the difference frequency but also a wave at a higher frequency  $f_1 + f_2$  (up-converter) is generated.

According to the theoretical discussion above, a photonic oscillator generating a continuous-wave sinusoidal local oscillator (LO) signal in the mm-wave or THz frequency range would need to consist of an optical source generating the optical heterodyne signal and a high-frequency photomixer. Schematically, this concept is illustrated in Fig. 2.2.

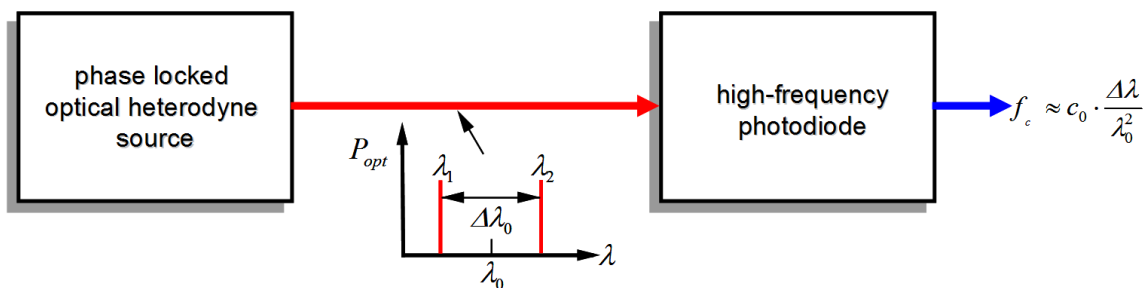


*Fig. 2.2 Principle set-up of a photonic local oscillator consisting of a stabilized optical source generating a phase locked optical heterodyne signal and a high-frequency photodetector generating the electrical beat signal in the THz frequency regime.*

However, the optical heterodyne input signal to the photomixer can also be a multi-wavelength optical input signal as shown in Fig. 2.3. Here, the optical spectrum not only consists of two light waves but of a multi-wavelength signal that features a constant difference frequency  $f_c$  between all neighboring optical modes. Such multi-wavelength optical signals are usually referred to as an optical comb. According to the discussions above, it is obvious that the photomixer here converts the optical multi-wavelength input signal not only into a DC photocurrent and a single RF signal at  $f_c$  but it generates also higher harmonics at  $2f_c$ ,  $3f_c$ , and so on, provided that the photomixer's sensitivity at the higher harmonics is still sufficiently high. It should be mentioned at this point that in contrast to the approach shown in Fig. 2.2, heterodyning of an optical comb strongly depends on the fiber's dispersion, as multiple RF tones at the beat frequency  $f_c$  are superimposed. Since the different optical constituent waves will have travelled with different phase velocities due to the fiber's dispersion, the detector's output strongly depends on the fiber's dispersion. This dispersion effect is further studied theoretically and experimentally in chapter 3.

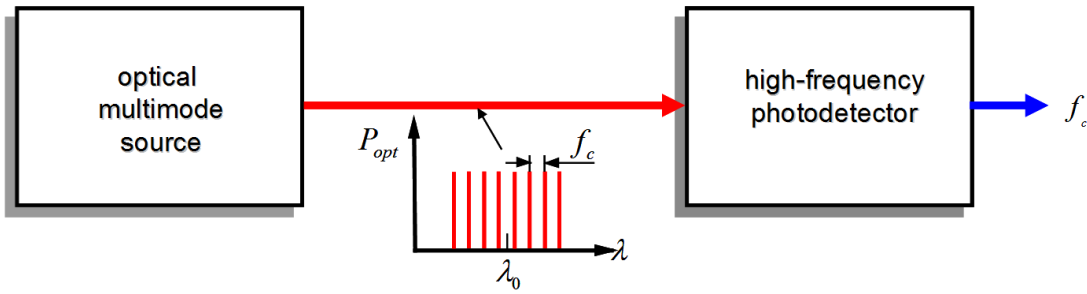


*Fig. 2.3 Principle set-up of a photonic local oscillator consisting of a stabilized optical source for generating an optical comb signal featuring a constant difference frequency  $f_c$  between the adjacent light waves.*

As already mentioned above, a key challenge associated with optical heterodyne systems for low phase noise signal generation is the necessity to develop frequency-stable optical sources with a low optical linewidth and a low relative intensity noise. Recently, different approaches for such frequency stable and low-phase noise optical sources were proposed and investigated within the European IPHOBAC project [35]. This includes dual-wavelength lasers, dual-mode lasers, as well as mode locked lasers [33, 36-39]. The next sections will review some of the developed laser structures for optical heterodyne generation. More details can be found e.g. in [36]. Furthermore, different photonic techniques that can be used to further reduce the phase noise of the generated signals will also be presented. This includes optical injection locking (OIL), optical phase lock loops (OPLL) and optical injection phase lock loops (OIPLL).

Besides the low phase noise and frequency stable lasers, the second key component in an optical heterodyne system is the employed photodetector or photomixer. As can be seen from eq. (10), the output power of the generated oscillator signal is linearly dependent on the detector's responsivity at the oscillation frequency and the optical input power injected into the detector. Thus, for generating high-power oscillator signals in the millimeter-wave and THz frequency range, it is necessary to develop ultra-fast photodetectors exhibiting a high responsivity at the desired oscillation frequencies. Such mm-wave or THz photodetectors must further allow for high optical input power levels, i.e. the detectors must exhibit a large saturation photocurrent level. Those are very stringent requirements that cannot be easily achieved using conventional photodetector structures commonly used in fiber-optic communications. It was rather necessary to develop novel photodetector structures and integration concepts tailored for advanced optical mm-wave and THz signal generation. This work will be reported in chapter 4.

### 2.1.1 Dual-wavelength and dual-mode lasers for optical heterodyning

A straightforward approach for generating an optical heterodyne signal with a difference frequency in the mm-wave or THz regime is to utilize two individual single-mode lasers and to multiplex the optical output waves of the two lasers, e.g. by using an optical coupler. For differentiation, the lasers are usually referred to as dual-wavelength lasers if the two optical waves are generated in two physically independent cavities (or lasers). If the two optical waves, however, represent two longitudinal modes propagating within the same cavity, the lasers are usually referred to as dual-mode lasers.

Optical heterodyning using a dual-wavelength laser is a rather simple way to generate a millimeter-wave signal and the approach further offers a wide frequency-tunability, as the difference frequency can be simply tuned by controlling the wavelength of one of the lasers [41-43]. A key disadvantage of this approach originates from the fact that the optical phases of the two laser modes are not locked; the generated mm-wave or THz signals are thus limited in phase-noise and frequency-stability. Nevertheless, due to its simplicity, optical heterodyning using two independent lasers is an advantageous approach for several applications e.g. for frequency-response characterization of high-frequency photodiodes [40-42] (see also chapter 4).

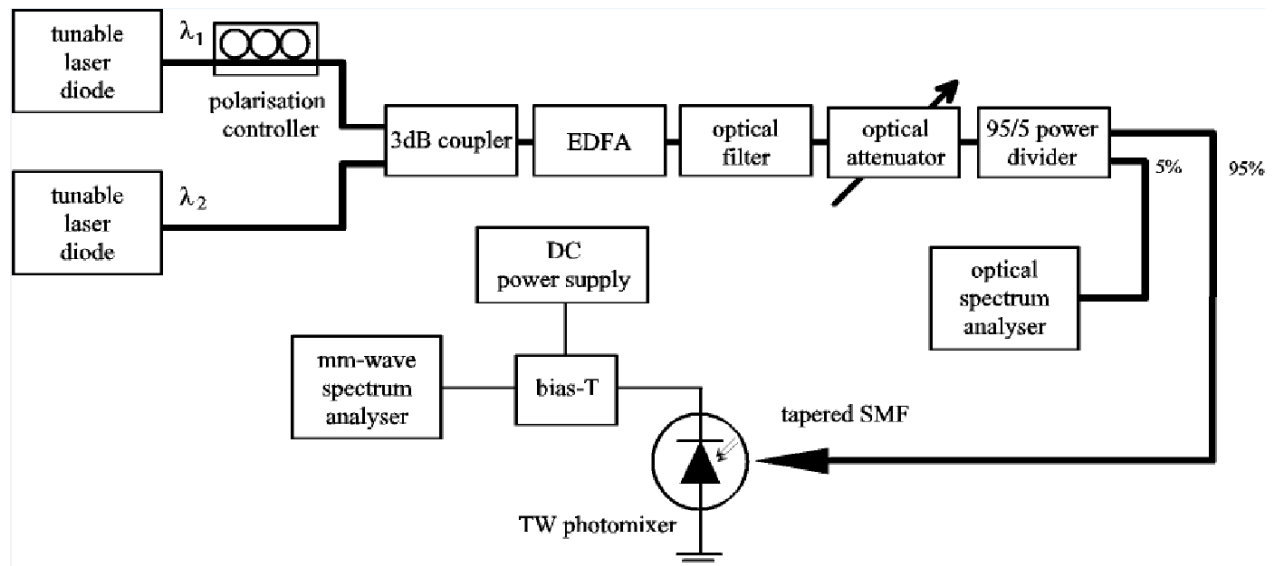


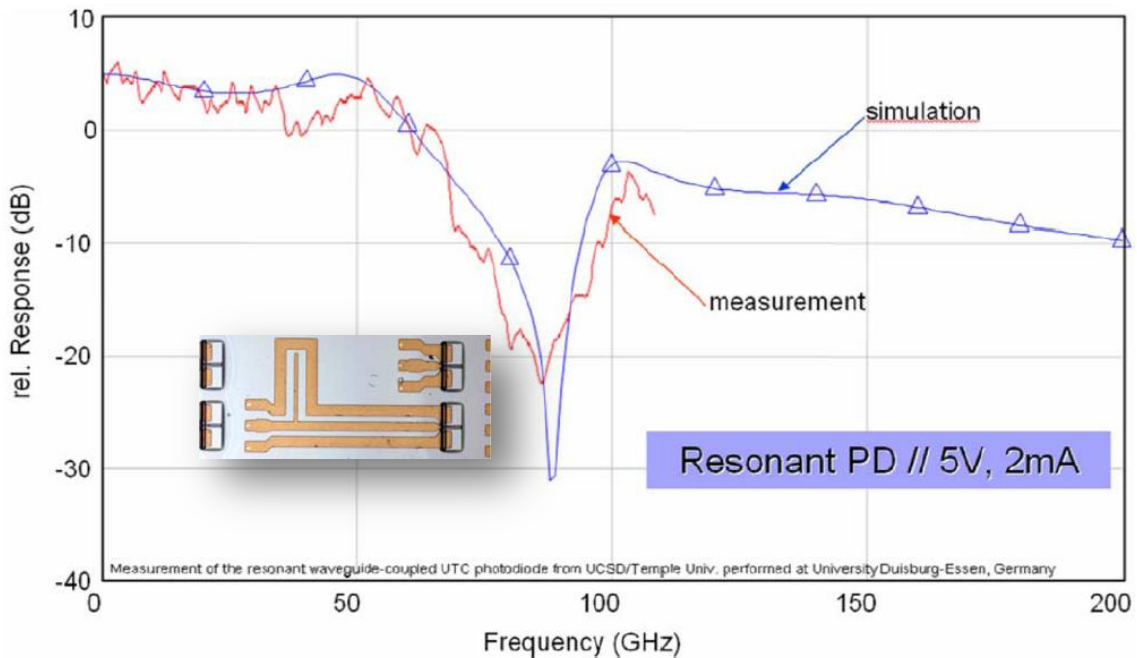
Fig. 2.4 Frequency tunable photonic mm-wave generation using a dual-wavelength laser set-up [40].

Fig. 2.4 shows the basic set-up for testing the frequency response of high-frequency photodiodes [40-42]. For optical mm-wave generation light from a tunable external cavity laser source (TLS) with a frequency  $f_1$  and a further fixed frequency external cavity laser source (LS) with a output frequency  $f_2$  are combined using a standard 3dB-coupler. By adjusting the frequency of the TLS,

both laser modes are separated with a difference frequency of  $\Delta f$ . To ensure an identical polarization state of the two laser sources, a polarization controller (PC) was applied after the TLS. The dual-laser signal is amplified by an erbium-doped fiber amplifier (EDFA) and further filtered by an optical band pass filter (OBPF) to reduce amplified spontaneous emission (ASE) noise of the EDFA. After transmission via a standard single mode fiber (SMF), the photonic mm-wave signal is detected by the high-power pin photodetector.

Although the phase noise is somewhat limited due to the free-running dual-laser approach, the optical heterodyne set-up shown above in Fig. 2.4 allows an experimental scalar network analysis of high-frequency photodiodes up to extremely high frequencies. This would be very difficult if not impossible using external optical modulation. Using specific coplanar-to-waveguide transitions, the developed set-up allows high-frequency measurements up to 330 GHz. Using a coplanar-to-coaxial (W1) transition, high accuracy and broadband frequency-domain characterization can be performed within the frequency range of DC-110 GHz.

For example, Fig. 2.5 shows the relative response of a resonant 100 GHz PD developed and studied in cooperation with Temple University, USA and University College San Diego, USA [44, 45]. The investigated 100 GHz PDs were based upon a uni-travelling carrier (UTC) travelling-wave (TW) waveguide structure resonated by an open stub at 100 GHz with impedance transformation to enhance the output power [44, 45]. As can be seen, the optical heterodyne set-up allows for a very accurate experimental investigation of the PD's responsivity with respect to the envelope modulation frequency up to highest frequency. In fact, up to 40 GHz the accuracy of the optical heterodyne set-up was found to differ by +/- 1 dB from a set-up based upon external intensity modulation [46].



*Fig. 2.5 Measured and simulated normalized frequency response of a resonant 100 GHz photodiode design [44, 45]. Measurements were carried out using an optical heterodyne set-up. The inset shows a photograph of the characterized resonant 100 GHz PD with the UTC-TW PD section on the left hand side and the resonant open stub with impedance transformer on the right hand side.*

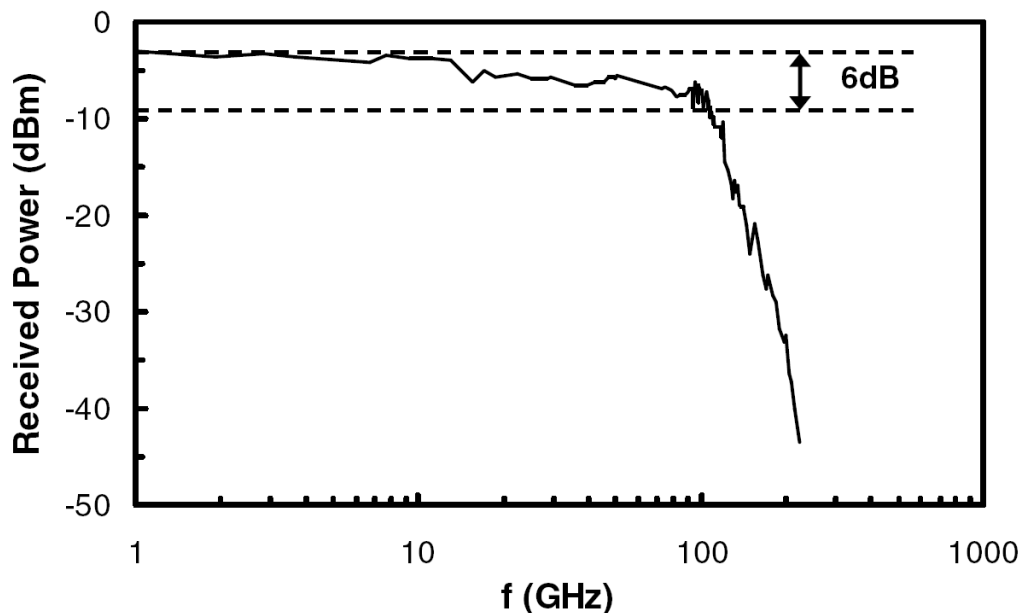


*Fig. 2.6 Output power of a constructed photonic millimeter-wave synthesizer versus millimeter-wave frequency [41].*

Another example of the wideband measurement performance is shown in Fig. 2.6. Here, a developed ultra-broadband photodiode chip has been experimentally characterized within the

frequency range from 1-220 GHz using a heterodyne set-up as shown in Fig. 2.4 [47]. For frequencies up to 110 GHz the photodiode chips were contacted using a coplanar DC-110 GHz probe featuring a coaxial W1 output. For higher frequencies up to 220 GHz coplanar probes featuring a rectangular waveguide output were used. For the electrical power measurements calibrated mixers were used up to 110 GHz. For measurements within the frequency range from 110 GHz to 220 GHz various Schottky detectors were employed. As can be seen from Fig. 2.6, a flat and wideband frequency response has been achieved with a total signal roll-off of only 6 dB within the frequency range from 1 GHz to 100 GHz. For frequencies in excess of 100 GHz, the frequency response of the PD chip drops by 30 dB when the operating frequency is changed from 100 GHz to 200 GHz.

The two above examples clearly demonstrate the usefulness of optical heterodyning for wideband experimental characterization of e.g. photodiodes. As mentioned above, a disadvantage of the free-running laser set-up is the linewidth of the generated signal. For the utilized dual-wavelength 1.55  $\mu$ m laser diode set-up, the linewidth of the generated mm-wave signal was found to be a few MHz [41]. A possibility to improve the frequency stability of the generated mm-wave signal is to integrate two single-mode lasers on a joint substrate [36, 48-52]. Although the two wavelengths from the integrated dual-wavelength laser chip are not really locked in phase, the wavelength stability is much better compared to the approach employing two independent free-running laser sources. This is due to the fact that the two wavelengths are generated using the same chip and therefore, in a first approximation, external influences such as temperature can be considered to have the same impact on each of the two wavelengths and consequently the difference frequency will be more stable.

Within the European IPHOBAC project, different integrated dual-wavelength laser chips were studied for optical millimeter-wave generation using multi-section long-cavity DBR semiconductor lasers with integrated angled facet mode expanders or in-line SOAs (see Fig. 2.7) [36, 50].

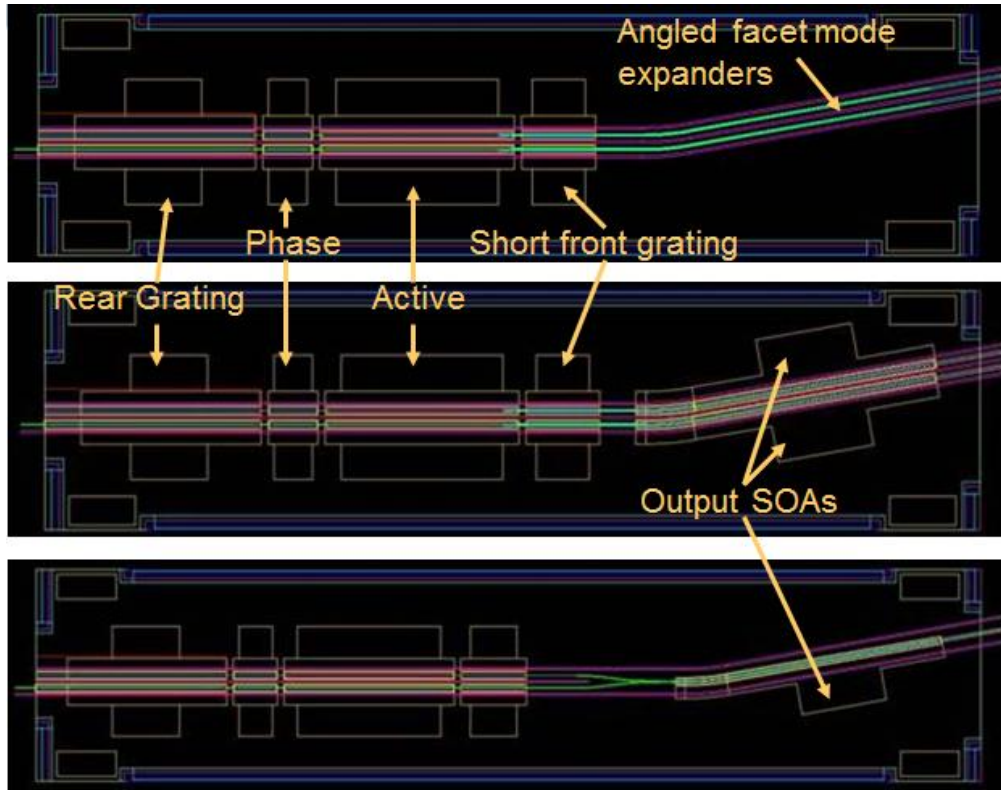


*Fig. 2.7 Mask layouts for dual four-section DBR laser with angled facet mode expanders (top), dual four-section DBR laser with dual-SOA output (middle) and dual four-section DBR laser with single SOA output [36, 50]. The dual-wavelength lasers were fabricated by CIP Technologies Ltd.*

As can be seen, the fabricated waveguide DBR lasers consist of a cavity composed of the rear grating and a short front grating. Besides the electrically isolated active region, the lasers also feature an integrated phase section allowing for external control. Furthermore, to reduce optical return loss (ORL), the lasers feature angled output waveguides either with two passive mode expanders, with two semiconductor optical amplifiers (SOA) or with a 3 dB coupler and a subsequent single SOA. The laser's output wavelength can be tuned by modifying the injection current into the rear or the front DBR section. Further control is possible via the integrated phase section.

As can be seen from Fig. 2.8, the difference frequency between the optical mode of the upper DBR laser and the lower DBR laser can be tuned over a very wide frequency range. By increasing the injection current to the rear grating section of one DBR laser from 0-100 mA, the mode spacing between the optical modes decreases from 8.2 to 0.2 nm corresponding to a frequency tuning range of 24 GHz - 1.012 THz. A 50 degree Centigrade change in temperature causes each of the stripes to tune by about 60 GHz, however the heterodyne frequency changes only by 2.5 GHz. So, according to a first order linear approximation the difference frequency temperature stability is  $\sim 50$  MHz/K. The linewidth was measured to be as low as  $\sim 1$  MHz [36].

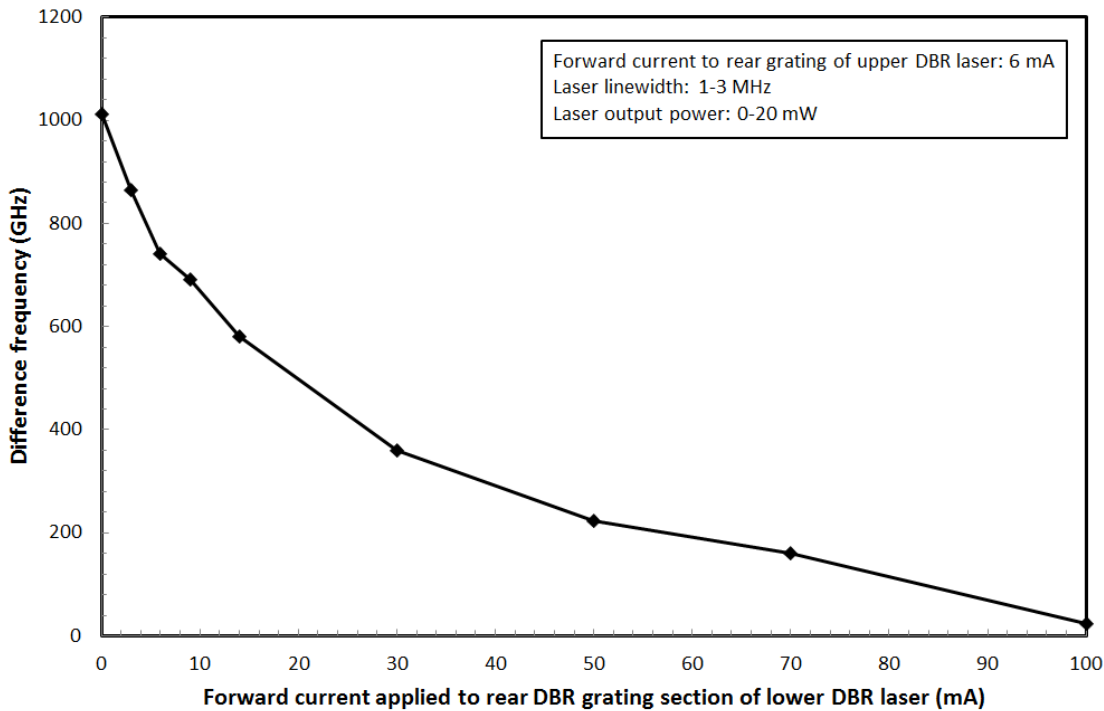


Fig. 2.8 Difference frequency of an integrated dual-wavelength DBR laser depending on the forward current applied to rear grating of the upper DBR laser. The forward current to the rear grating of the lower DBR laser was fixed to 6 mA.

Another interesting approach for realizing a frequency tunable dual-mode laser has recently been demonstrated by Morvan et al. from THALES who successfully achieved frequency tunable dual-mode oscillation in a diode-pumped solid-state laser [53]. The principle is based upon the introduction of an electro-optically tunable birefringent etalon in a classical diode pumped Nd:YAG microlaser. This way, the laser oscillates on two orthogonal polarization states which have a defined frequency difference that can be tuned by varying the driving voltage applied to the etalon. Thanks to the inherent spectral purity and stability of diode-pumped solid-state lasers, high-quality signals with a low phase noise and high frequency stabilization is possible. It is the aim of a collaboration between UDE and THALES within the PHOMIGEN project [54] to transfer this concept to 1.5  $\mu\text{m}$  wavelength by using an Er:Yb:glass laser adapted and a high-frequency InGaAs photoreceiver. This work is actually supported by the European Space Agency (ESA).

### 2.1.2 Mode-locked laser diodes

Mode-locked laser sources are also very attractive solutions for various applications including pulse generation, clock extraction from digital data and optical microwave signal generation and processing [55]. Typically passive MLLDs are fabricated from a standard Fabry-Perot (FP) laser which is modified to include a short saturable absorber (SA) section within the cavity. When the SA section is reversed biased, longitudinal optical modes within the MLLD cavity become phase locked. In conjunction with adjusting the MLLDs cavity length, this results in the pulsed emission of light with a repetition frequency determined by the cavity round trip time. Typically, for InP based MLLDs to operate at mm-wave pulse repetition frequencies, the cavity lengths are in the range of several hundred micrometers.

It is well-known that when a continuous wave RF signal is injected into the MLLD cavity, close to its free running frequency, the MLLD output signal synchronizes itself to the external signal. This condition is known as hybrid mode-locking [56]. The disadvantage of this approach is that it requires the development of multi-section MLLD for incorporating the SA into the laser's cavity as well as external oscillators for phase locking the longitudinal laser modes. A more advantageous approach in terms of complexity has been investigated within the IPHOBAC (Integrated Photonic mm-Wave Functions for Broadband Connectivity) project [35]. In order to generate mm-wave signals with comparably low-phase noise levels and with no need of any additional external locking scheme, we have developed self-pulsating MLLDs for 60 GHz band operation [33, 38, 57]. It has been observed that devices based on quantum dash (QDs) gain medium emitting in the 1.5  $\mu\text{m}$  wavelength range had the property to generate a much narrower beat-note signal linewidth compared with other types of gain media [58]. Thus, the semiconductor laser chips that were used are simple Fabry-Perot cavities with a buried ridge active waveguide. They contain an active layer based on 6 QDs layers grown on InP substrate [58]. Laser cavities of different lengths were cleaved depending on the required mode-locking frequencies: 1715  $\mu\text{m}$  for 24.5 GHz, 1100  $\mu\text{m}$  for 38.5 GHz, 774  $\mu\text{m}$  for 54.8 GHz and 710  $\mu\text{m}$  or 58.8 GHz. The two remarkable features of these devices are the very wide optical spectrum and the very narrow linewidth of the generated beat-note.

As discussed in section 2.1, the o/e-converted power from a mode-locked laser source is obtained due to the beating of the couples of optical modes during the photodetection process. Thus, by using the approach shown in Fig. 2.3, passive mode-locking at a mode-locking frequency of about 60 GHz has been obtained without the use of any specific saturable absorber by using a self-pulsating QD-MLLD [57]. Fig. 2.9 shows the measured output spectra of the MLLD.

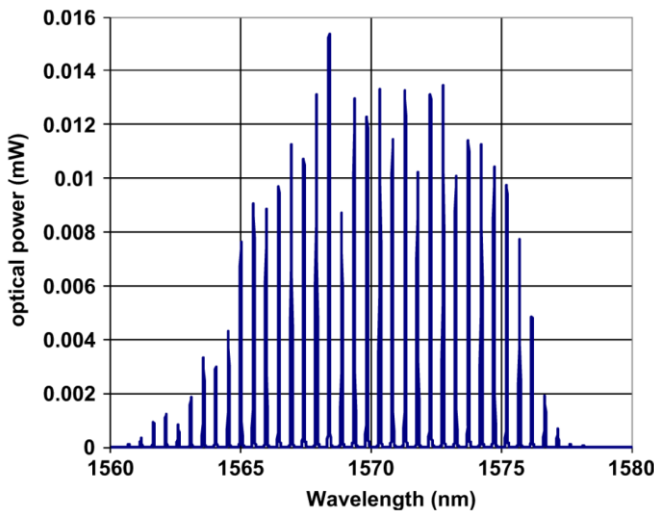


*Fig. 2.9 Optical output spectra of a 710  $\mu\text{m}$  long Fabry-Perot based InP MLLD having a 6 layer active quantum-dash gain material.*

As can be seen from Fig. 2.9, the longitudinal modes of the MLLD spread over a wavelength range of more than 10 nm.

An example of the electrical spectrum of a generated mm-wave heterodyne signal is shown in Fig. 2.10. This result has been achieved using a 774  $\mu\text{m}$  long MLLD with a repetition frequency of 54.8 GHz [59, 60]. The active laser section was forward biased at 370 mA, the resolution bandwidth of the electrical spectrum analyzer was set to 3 kHz. One can observe a beat frequency close to 54.8 GHz. A nearly Lorentzian lineshape is obtained, exhibiting a -3 dB linewidth narrower than 18 kHz.

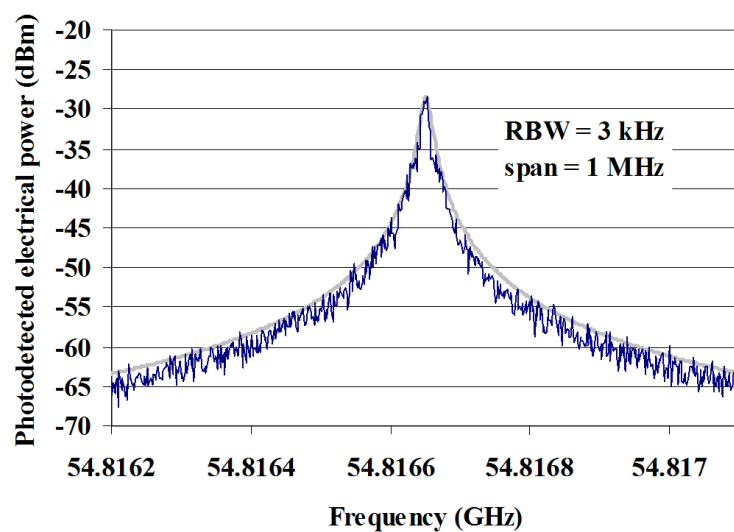


*Fig. 2.10 Self pulsation electrical spectrum of the mode-locked laser diode driven at 370 mA.*

For measuring the phase noise of the generated RF signals, the signals were down-converted to 320 MHz using an Agilent 11970U harmonic mixer associated to a reference source and measured using the phase noise function of a Rohde&Schwarz FSEK30 electrical spectrum analyzer (ESA) [57]. The single sideband (SSB) phase noise of a 58.5 GHz tone generated by a 710  $\mu\text{m}$  long MLLD is presented in Fig. 2.11. At an offset frequency of 10 kHz, the phase noise exhibits a value of -54.4 dBc/Hz. The extremely narrow linewidth for QD lasers is believed to be a consequence of the reduced spontaneous emission rate coupled to the lasing mode, and sufficient four-wave mixing in these QD structures [58].

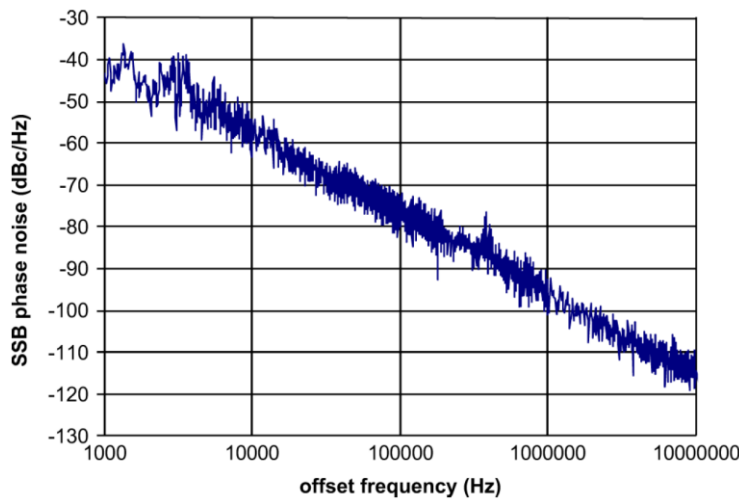


Fig. 2.11 Single side band phase noise of the 58.8 GHz tone generated by a 710  $\mu\text{m}$  long MLLD at a bias current of 211 mA.

Another efficient technique to passively mode lock a laser's longitudinal modes is to incorporate a saturable absorber (SA) into the laser's cavity [61]. Each time, an optical pulse circulating in the laser's cavity hits the SA, it temporarily reduces the overall cavity losses. For steady state operation the laser's gain can be adjusted just below threshold, only when the circulating pulse saturates the absorption in the SA, the overall gain becomes larger than the required threshold gain. This way, only the optical pulse experiences a net gain and the laser starts to pulse, i.e. mode locking is achieved. In addition, various approaches to actively mode lock a laser's longitudinal modes have been reported. In principle, these techniques rely on incorporating a modulator into the laser's cavity [62]. When driving the intra-cavity modulator with a sinusoidal RF signal at frequency  $f_{\text{RF}}$ , it generates upper and lower side bands ( $f_{\text{LM}}-f_{\text{RF}}$ ,  $f_{\text{LM}}+f_{\text{RF}}$ ) to each longitudinal mode  $f_{\text{LM}}$ . If the frequency of the modulation signal  $f_{\text{RF}}$  equals the laser's round trip frequency the longitudinal modes will be locked by the modulating signal. The basic principle can be applied to monolithically integrated multi-section laser diodes [63], but it can of course also be applied to external cavity lasers [64-68]. Spectrally wide optical frequency combs have been generated using optical fiber loops with intra-cavity fiber lasers or optical amplifiers to

provide the necessary gain. In order to achieve active mode locking of the longitudinal fiber loop modes, different types of modulators have been employed including acousto-optical modulators [66, 68], electro-optical phase modulators [65, 67, 69] and electro-absorption modulators [63]. The maximum width of the optical generated combs using active mode locking in fiber loops is well above 1 THz [64]. Also, waveguide type phase modulators incorporated in an external Fabry-Perot cavity have been successfully employed for efficient optical frequency comb generation with spectral width as wide as 2.7 THz [69].

As discussed above, passive or active mode locking is a very suitable technique for generating densely-spaced (beat note frequencies in the microwave and millimeter-wave region) phase-locked optical frequency combs with maximum frequency spans in the THz range. When transmitting such optical frequency combs via fiber before photodetection, it must be considered that each of the longitudinal modes runs at a different speed due to the fiber's dispersion. Consequently, all the different beat notes at the output of a remote located photodetector would exhibit a different phase, resulting in significant power fluctuations with respect to fiber length or beat note frequency. This fiber-dispersion penalty of optical combs is further studied in section 3.2.3. A solution to circumvent any fiber-dispersion penalty is to use tunable filters for suppressing all unwanted longitudinal modes except for the two with the desired beat note frequency. This way, a pure two-tone optical signal is generated which is insensitive to the fiber's chromatic dispersion. Possible techniques for filtering only two longitudinal modes out of an optical frequency comb are briefly discussed in the next section.

### 2.1.3 Optical comb line selection

An optical frequency comb generator (OFCG) provides an array (comb) of spectral lines equally spaced in frequency and with certain phase relationships. An optical heterodyne signal can be obtained by combining two individual lines of the optical comb signal as shown in Fig. 2.12 [70]. The two lines constituting the optical heterodyne signal are not restricted to two neighboring lines; in fact, any two lines out of the optical comb can be heterodyned. Thus, the modulation frequency of the optical heterodyne signal can be a multiple of the free spectral range of the optical comb.

Two major challenges are associated with the approach shown in Fig. 2.12: The challenge to generate the optical comb signal with certain coherence between the modes and a required free spectral range and spectral width on the one hand and the selection of the desired two comb lines on the other hand.

Many approaches aiming at optical frequency comb generation have been presented in the recent past based on the usage of passive semiconductor mode-locked lasers as discussed in the section above, femtosecond solid state mode-locked lasers [71] or erbium-doped fiber lasers [72]. Other optical comb approaches rely on the inclusion of an E/O modulator in an optical fiber loop [64, 70, 73], into the Fabry-Perot cavity of a laser [74] or even into a passive Fabry-Perot waveguide

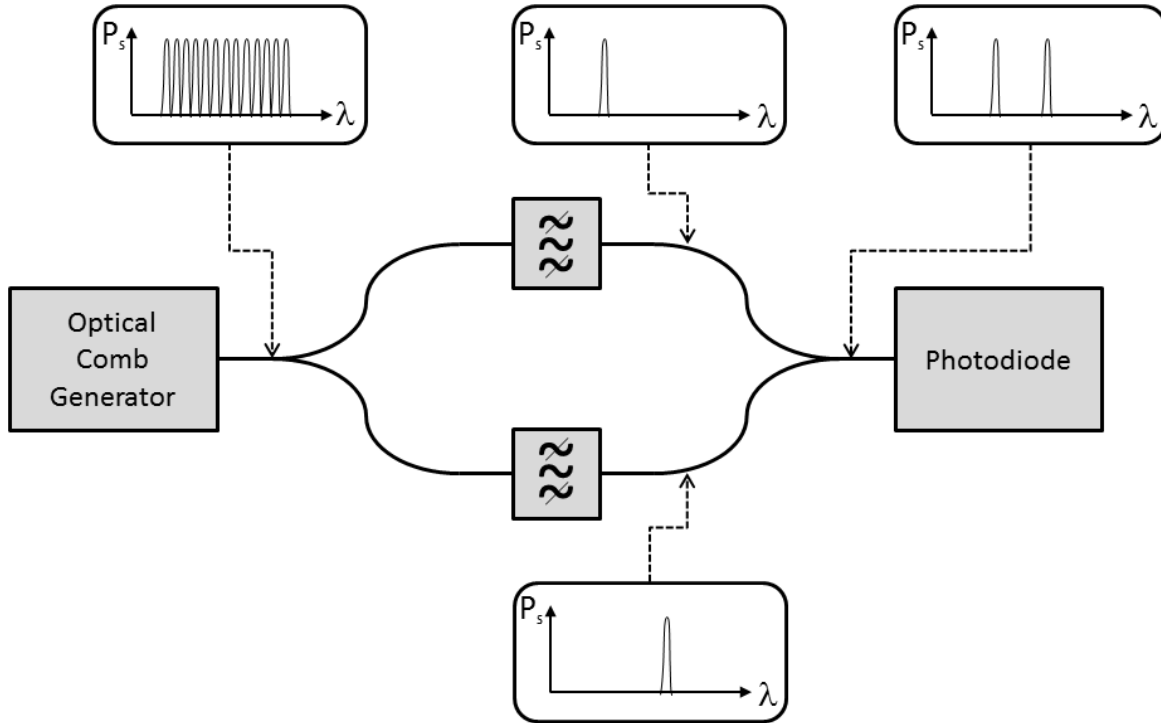


Fig. 2.12 Principle of frequency synthesis scheme [70].

cavity [69]. A simple, compact, all fiber comb generator offering exact referencing to an arbitrary supplied reference frequency and tunable microwave frequency comb-line pacing is presented by Seeds' group in [64]. This optical comb generator is based on phase modulation within an amplified fiber loop, which offers exact referencing to an arbitrary supplied reference frequency and tunable comb-line spacing. At a reference wavelength of 1529 nm up to 103 comb lines within a 40 dB power envelope were generated with free spectral ranges adjustable from 1 to 25 GHz, limited only by the bandwidth of the phase modulator.

After generating the optical comb signal, it is required to select the desired two comb lines. This can be achieved by using tunable optical filters such as Fabry-Perot filters (microsystem, fiber or liquid crystal based), fiber gratings or acousto/electrooptic filters. Such passive filters, however, do not provide sufficient isolation between adjacent channels for optical combs with very small free-spectral ranges in the order of or below 0.5 nm. Here, active filters exploiting the resonant features of e.g. FP, DFB or DRB semiconductor lasers operated below threshold have been shown to exhibit narrow filter bandwidth (0.1nm) [75]. Besides passive or active filtering of the

desired comb line, another possible approach is to optically injection lock the optical comb to two slave lasers. Provided the slave laser's cavity modes corresponds to the desired two comb lines or can be adjusted to them, this approach is advantageously as the selected lines maintain an exact phase lock to the master comb laser and the output power is about that of the free running slave lasers. In the next section, optical injection locking (OIL) will be discussed in more detail.

#### 2.1.4 Optical injection locking

As discussed above, the beating of the optical output waves from two free-running lasers would lead to a signal with high phase noise since the phases of the two individual optical waves are not correlated. This poor phase noise performance will of course be transferred to the generated mm-wave or THz signal. In order to generate a high-spectrally pure signal, the two constituent optical waves must be phase locked. This can be achieved by optical injection locking (OIL). Injection locking is an interesting approach not only to synchronize lasers for microwave signal generation [76, 77], but also to reduce laser linewidth [78] and enhance the laser's modulation bandwidth [79-81]. A conceptual set-up of an injection locked laser system is shown in Fig. 2.13.

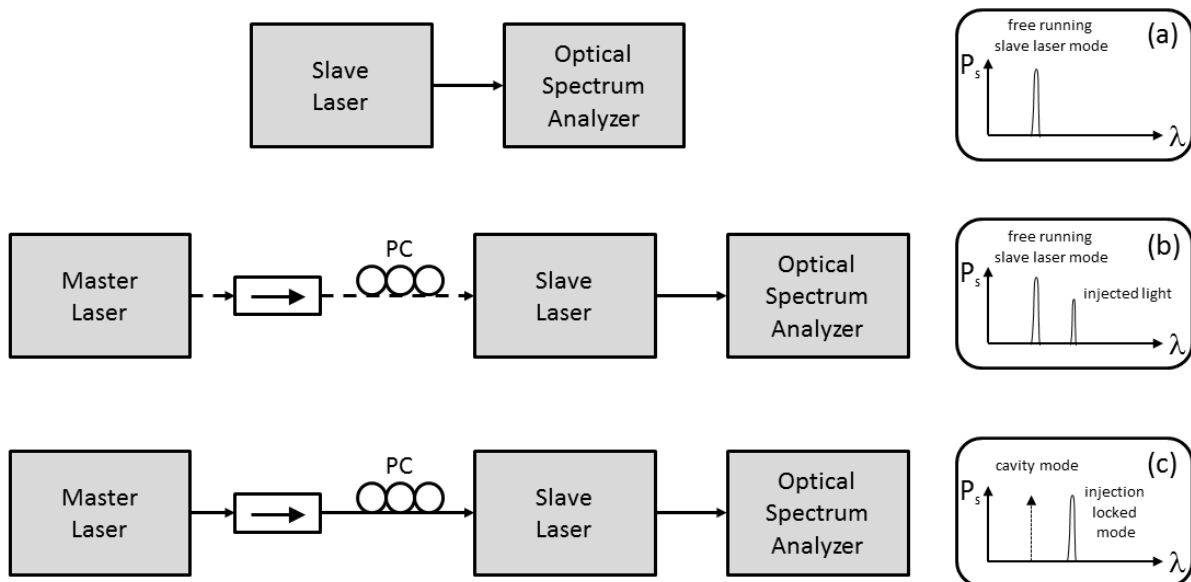


Fig. 2.13 Conceptual diagram of optical injection locking (OIL): free running slave laser (a), free running slave laser with injected light from a master laser (b), and injection locked slave laser (c).

The output light of a slave laser can be injection locked by using light from a master laser. In order to prevent optical reflections back into the master laser, an isolator is placed between the

master and the slave lasers. To achieve optimum performances, it is necessary to either place a polarization controller between the two lasers or to use polarization maintaining fibers and two lasers having the same linear polarization. When running freely, the amplified spontaneous emission (ASE) in the slave laser's cavity captures the gain and dominates the laser emission wavelength (or wavelengths in case of a multi-mode laser), its spectral width and the modulation bandwidth (Fig. 2.13(a)). With external injection from a master laser which must not necessarily have the same wavelength as the slave laser's free running mode, the injected light competes with the spontaneous emission of the slave laser. In case the master laser's wavelength is outside the locking range of the slave laser or the injected power level is not strong enough to dominate, the slave laser will continue lasing at its natural mode, but some residual spectral power density of the injected mode might be observed in the slave laser's output spectra (Fig. 2.13(b)). In case the injected wavelength is within the locking range and its power level is large enough to dominate over the spontaneous emission of the slave laser's natural mode(s), the injection mode will capture the slave laser's gain and the ASE of the other modes is suppressed. At this point, the slave laser locks to the master laser, i.e. its lasing frequency and output phase now equals that of the master laser (Fig. 2.13(c)).

Theoretical properties of injection locked lasers and especially semiconductor lasers [79, 82] were derived from *Adler's* original work on injection locked on vacuum tube microwave oscillators [83]. Experimental studies on injection locking in VCSEL and FP lasers have been the subject of several publications, but also injection locking in DFB lasers or even more complex structures have been investigated [77, 84, 85]. As regards the usage of OIL to synchronize lasers for optical mm-wave and THz generation and transport, early work has been carried out by *Goldberg et al.* in [76, 77]. They have applied a high-power frequency modulated signal to the master laser's DC bias, thus, the master laser emits an optical multimode signal where the mode spacing equals the applied sub-harmonic RF frequency. By injecting locking this signal to a long-cavity FP slave laser with a longitudinal mode spacing equal to a multiple of the sub-harmonic RF reference signal, they succeeded in generating a 35 GHz mm-wave signal with a linewidth of less than 10 Hz [77]. Very recently, OIL has also been applied to a 60 GHz RoF system link (see also chapter 5) [85]. Here an OIL VCSEL was employed to generate an optical 60 GHz RF wireless carrier modulated by a 3 Gb/s ASK data signal which was further transmitted via optical fiber and air. It is worth mentioning that of course OIL could potentially also be used in conjunction with the optical comb approach shown in Fig. 2.12. When replacing the two filters shown in Fig. 2.12 by two wavelength adjustable slave lasers, one could potentially lock the slave lasers to two desired comb lines of an MLLD and thus develop a frequency adjustable and low phase noise optical mm-wave source. Among others, this approach is currently being investigated by the author's group within the PHOMIGEN project in

cooperation with THALES Research and Technology and the European Space Agency (ESA) [54].

### 2.1.5 Optical phase lock loops

The optical injection locking (OIL) technique discussed in the section above is a quite common approach to correlate the phase fluctuations of two lasers for coherent optical heterodyne detection. One of the key challenges associated with using OIL laser systems for low-phase noise mm-wave and THz signal generation is the limited frequency locking range. Even for high optical injection ratios, the locking range is only in the range of a few gigahertz [79]. Thus, assuming OIL of standard DFB lasers with a frequency stability of typically  $\sim 10$  GHz/K, a slight temperature shift of a few Kelvin or even a fraction of a Kelvin can cause an OIL system to become unlocked. An alternative technique for achieving frequency synchronization is to use an optical phase locked loop (OPLL) as sketched in Fig. 2.14.

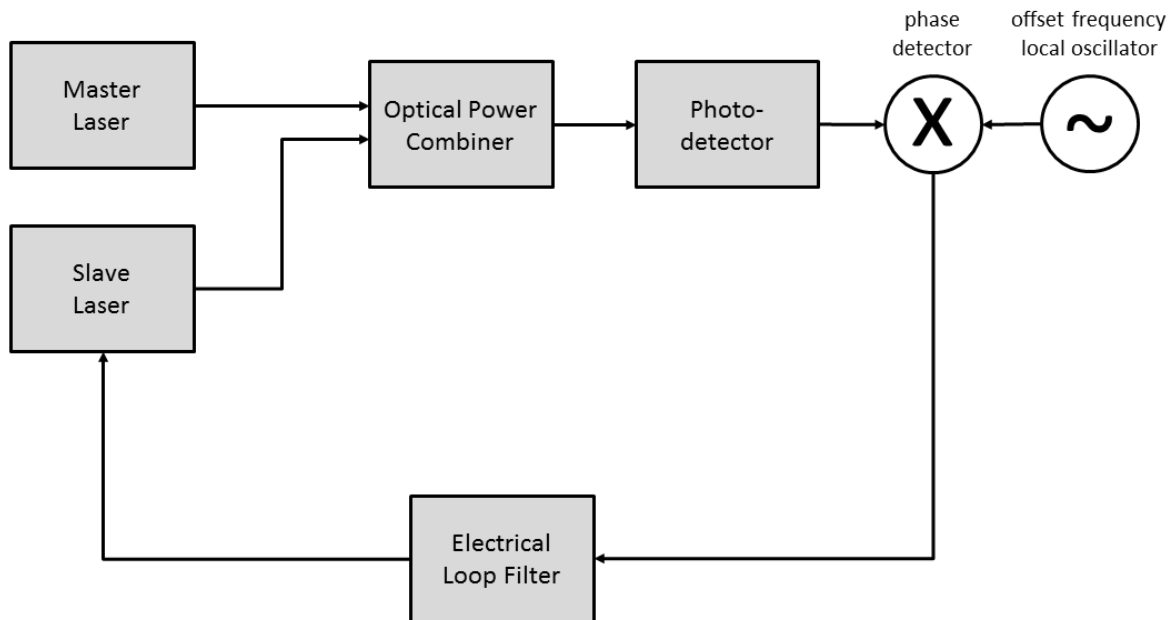


Fig. 2.14 Block diagram of a heterodyne optical phase locked loop (OPLL).

Generally, an OPLL is a negative feedback control loop that forces an optical slave laser to track the frequency and phase of a reference master laser when locked. In case there exists a difference frequency between the lasing frequencies of the slave and the reference master laser, additional control over phase and frequency is provided. Such OPLLs where the slave and master laser frequencies differ are referred to as heterodyne OPLLs [86, 87] whereas OPLLs where slave and master laser have the same emission frequency are termed homodyne OPLLs [88, 89].

Since the first successful demonstrations of an OPLL [90], there has been a remarkable interest in OPLLs, not exclusively but also for microwave photonic applications such as high-frequency signal generation [86, 91]. Synchronization of narrow linewidth solid state lasers can be achieved using an OPLL, but the approach gets more complicated once semiconductor lasers are to be employed due to the large optical linewidth of semiconductor lasers. Of course, the linewidths can be reduced using external cavity lasers (ECL), but this involves mechanical stability issues and ECLs are quite bulky and power consuming. Another option is to increase the OPLL loop bandwidth to compensate for the wider noise spectrum, but this reduces the loop propagation delay time. According to theoretical studies carried out by Ramos et al. in [92], it can be concluded that for a summed optical linewidth (i.e. the sum of the master laser and slave laser linewidth) of only 2 MHz, the loop delay must better be shorter than 1 ns (corresponding to a 300 mm free space path length) and the loop bandwidth must be larger than 100 MHz. For a total optical linewidth of 10 MHz, loop delay and bandwidth must even be shorter than 0.5 ns and greater than 300 MHz, respectively.

Within the IPHOBAC project, one objective was to develop an integrated heterodyne OPLL that would not just allow synchronization of two fixed-frequency semiconductor laser diodes but also allow tuning the frequency between 30-300 GHz. This was to be achieved by using a MLLD instead of a single-mode laser as reference master laser and a second DFB or DBR slave laser. The schematic of the IPHOBAC OPLL set-up is shown in Fig. 2.15 [36].

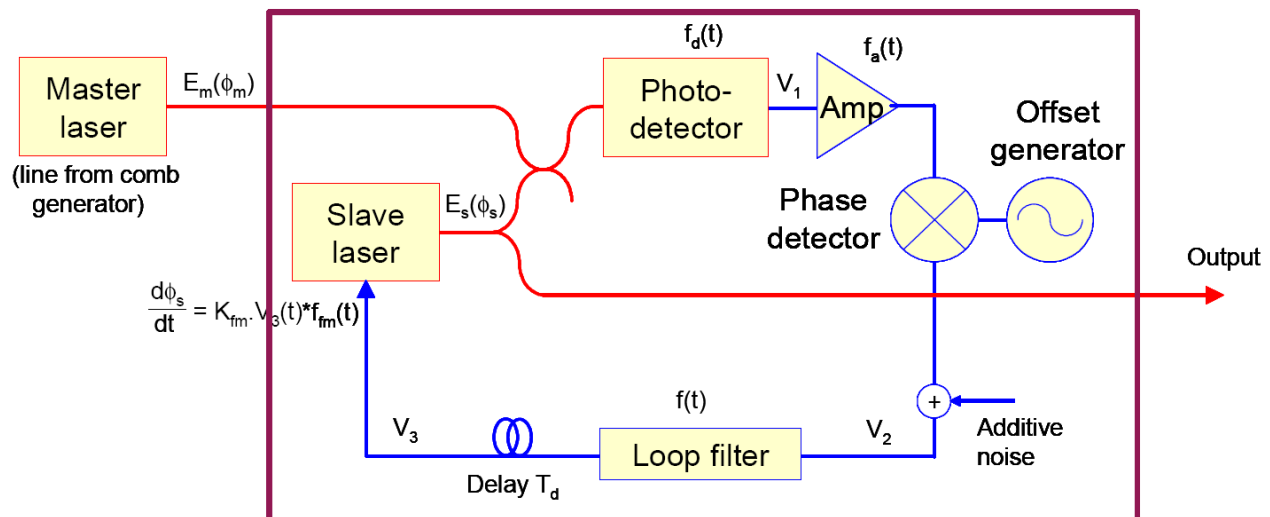


Fig. 2.15 Schematic of the optical phase lock loop developed within IPHOBAC [36].

In the OPLL system shown in Fig. 2.15, the photodetector will detect the heterodyne optical signal formed between one of the comb lines of the reference master laser and the slave laser output. This heterodyne output is compared with an electrical reference in a phase detector. The

phase detector output is processed by a loop filter and is used to tune the laser for achieving phase-lock conditions. By tuning the lasers to select different comb lines (the master source being a comb generator) and setting the electrical reference frequency, an exact frequency synthesis can be carried out. The combined signal of two locked lasers with a beat frequency in the range of 30-300 GHz could then be used to illuminate the THz photodetector with integrated antenna (see chapter 4.1) to complete the ultra-wideband synthesizer. The required high speed short delay loop electronics was provided by the University of Ljubljana. It consists of a fast proportional loop and a slow integral loop built on a 4-layer printed circuit board (PCB) and has a total delay of less than 1ns. This is sufficient to lock lasers with combined linewidth of 2MHz [36].

The OPLL was tested for frequency offsets from 2 GHz to 7 GHz (limited by the loop electronics) and frequency generation of up to 300 GHz. The spectral performance was assessed using fast photodetectors (see also section 4.1.1) for frequencies up to 110 GHz. The measured phase noise is less than -80 dBc/Hz at 100 kHz offset and is better than -75 dBc/Hz at 10 kHz offset. For frequencies between 110 GHz and 300 GHz only the generated power could be measured using an antenna integrated fast photodetector. This way, operation up to 300 GHz has been successfully confirmed [36].

## 2.1.6 Optical injection phase lock loops

For further improving the phase noise of the generated high-frequency signal, *Ramos et al.* have proposed a combined optical injection (see section 2.1.4) and phase locked loop (see section 2.1.5) system (OIPLL) in [93]. As shown in Fig. 2.16, in an OIPLL system the output light from a reference master laser is divided into two paths: one to optically injection lock a slave laser and the second one to be mixed with the slave laser's output light and detected in a photodiode. In case of a homodyne OIPLL, i.e. in the case the output frequencies of the reference master and slave lasers are identical, the DC output of the PD is fed back via an electrical loop filter to control the phase and frequency of the slave laser. In the case of a heterodyne OIPLL, the RF output signal of the PD is first mixed with a reference LO using a phase detector before the electrical output signal of the phase detector is fed back via the loop filter to the slave laser.

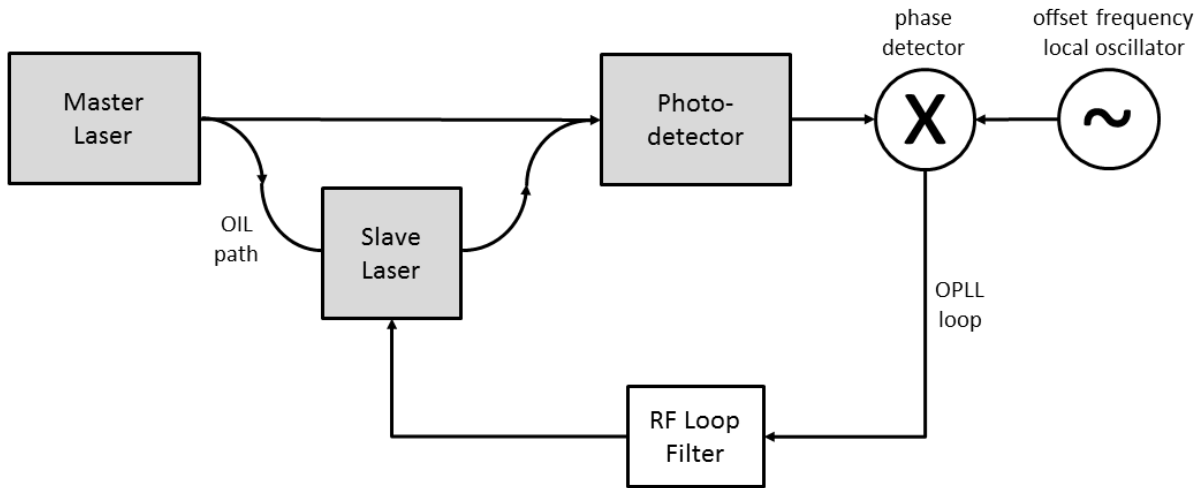


*Fig. 2.16 Block diagram of an OIPLL system [88]. The phase detector and offset frequency LO are necessary in heterodyne OIPLL systems but are not required in homodyne OIPLLs with a DC output signal of the PD.*

Theoretical studies in [93] have shown that the proposed OIPLL system can provide the wide frequency locking range of an OIL system provided the optical injection ration into the slave laser is sufficiently high. Also, an OIPLL system takes advantage of the low phase noise in an OPLL system at low offset frequencies. In other words, at low offset frequencies in the Hz to MHz-range the OIPLL phase error spectrum follows that of an OPLL system which is much better compared to an individual OIL system. At higher offset frequencies in the MHz to GHz range, the phase error of the OIPLL system can follow that of an OIL system which can be significantly better as compared to an individual OPLL. This, however, requires a substantially high optical input power into the slave laser in order to achieve optical injection rates of -30 dB and higher. Finally, in an OIPLL system the locking capabilities are principally improved compared to individual OIL and OPLL systems, as slow long term drifts of the reference master laser's output frequency can be compensated by the electronic loop filter whereas fast phase fluctuations are followed by the optical injection locking path. In summary, an OIPLL can provide better phase noise and locking capabilities in comparison to individual OIL and OPLL systems that provided the optical injection ratio is high and of course the OIPLL set-up is somewhat more complex compared to OIL or OPLL systems.

In [88], individual OIL and OPLL systems were experimentally studied and compared to homodyne and heterodyne OIPLL systems in order to prove the theoretical predictions and requirements. It was found that the OIPLL approach allows the realization of high-performance loops without the necessity of using very narrow-linewidth lasers as well as broadband and short delay loop electronics. Experimentally, a 26 GHz wide frequency locking range was found for a homodyne OIPLL using DFB lasers with a summed linewidth of 36 MHz, a loop bandwidth of

36 MHz, a loop propagation delay of 15 ns and an injection ratio below -30 dB. For heterodyne OPLL using the same lasers with a summed linewidth of 36 MHz and an RF difference frequency larger than 6 GHz, a phase error variance of  $0.003 \text{ rad}^2$  in a 100 MHz bandwidth and a single sideband phase noise level of -94 dBc/Hz at 10 kHz offset were achieved for loop propagation delays of 20 ns and an injection ratio of -30 dB.

## **2.2 Optical intensity modulation and direct detection**

In addition to the above described techniques employing optical injection locking and coherent heterodyne or homodyne detection, high-quality RF signals can also be generated using optical modulation and direct detection. In the case of an analog optical intensity modulation (IM) and direct detection (DD) this approach is also referred to as an IMDD link. Here, direct detection means that the received optical signal impinges directly onto a photodetector. Due to the modulation bandwidth limitation of direct modulated laser diodes which is typically in the microwave region, external intensity modulators are used for external high-frequency RF signal modulation in the mm-wave range.

The most common used modulators for accomplishing intensity modulation are Mach-Zehnder modulators (MZM) and electro-absorption modulators (EAM). In an MZM, the incoming cw light from the laser is typically split equally and fed into two ideally equal length waveguide arms whose outputs recombine to feed the modulators' output waveguide. With zero voltage applied to the modulator electrodes, the light in the two arms experience the same phase shift

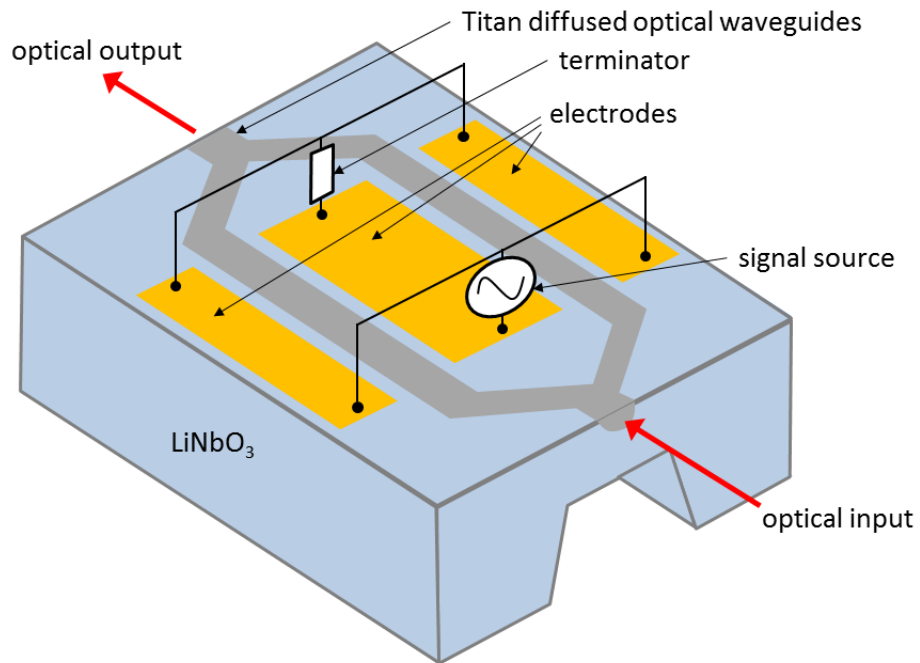


Fig. 2.17 Schematic illustration of a Mach-Zehnder modulator based upon  $\text{LiNbO}_3$ .

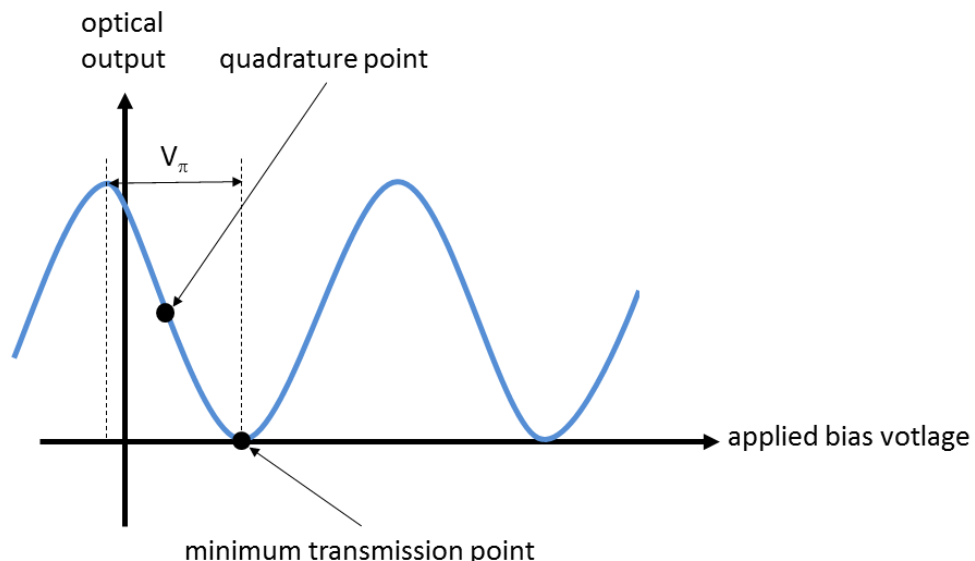


Fig. 2.18 Nonlinear transfer characteristic of an MZM. The maximum transmission point (MATP) might not be achieved exactly at zero Volt applied bias due technological imperfections, e.g. in the case of not equally long waveguides.

while travelling through the arms and thus, they interfere constructively in the modulators' output waveguide, resulting in maximum optical output power. If, however, a voltage is applied to one arm or different voltages to both arms of the modulator, a relative phase shift between the light in the two arms is induced. For a sufficient large voltage the phase of the two arms will be  $180^\circ$  out of phase, and thus, the two optical waves will interfere destructively, resulting in minimum optical output power.

Fig. 2.17 and Fig. 2.18 schematically show the topology of a Lithium Niobate ( $\text{LiNbO}_3$ ) based MZM and the typical non-linear transfer function of an MZM, respectively.

Assuming an ideal MZM with zero optical insertion loss, ideal 3dB couplers, and equally long waveguide arms, the complex electrical field strength of the optical wave in the modulators' output waveguide can be expressed as:

$$\hat{\underline{E}}_{out} = \frac{\hat{\underline{E}}_{in}}{2} e^{(j\beta_1 L)} + \frac{\hat{\underline{E}}_{in}}{2} e^{(j\beta_2 L)} = \hat{\underline{E}}_{in} \cos\left(\frac{\Delta\beta}{2} L\right) e^{j\bar{\beta}L}, \quad (12)$$

where  $\hat{\underline{E}}_0$  is the output field,  $\hat{\underline{E}}_1$  is the input optical field,  $\beta_1$  and  $\beta_2$  are the propagation constants in the two parallel optical arms of the interferometer,  $L$  is the arm's length and

$$\Delta\beta = (\beta_1 - \beta_2) \quad (13)$$

$$\bar{\beta} = (\beta_1 + \beta_2)/2. \quad (14)$$

Using Maxwell's equations and some trigonometric relations (see Annex III), the output intensity related to the input intensity for an ideal MZM can be shown to be:

$$\frac{I_{out}}{I_{in}} = \frac{\left|\hat{\underline{E}}_{out}\right|^2}{\left|\hat{\underline{E}}_{in}\right|^2} = \cos^2\left(\frac{\Delta\beta}{2} L\right) = \cos^2\left(\frac{\pi V}{2V_\pi}\right), \quad (15)$$

where  $V$  is the applied modulating voltage signal and  $V_\pi$  is the voltage required to swing the modulator from its maximum transmission point (MATP) to its minimum transmission point (MITP).

Assuming the modulation signal  $V$  is a sinusoidal voltage with angular frequency  $\omega_m$  and amplitude  $v_m$  superimposed on a DC voltage  $V_{DC}$ , we get:

$$V_m = v_m + V_{DC} \sin(\omega_m t). \quad (16)$$

Using eq. (28) and some trigonometric relations we obtain (Annex III):

$$\frac{I_{out}}{I_{in}} = \frac{1}{2} + \frac{1}{2} \chi \cdot J_0(\pi \frac{V_m}{V_\pi}) + \\ + \chi \cdot \sum_{n=1}^{\infty} J_{2n}(\pi \frac{V_m}{V_\pi}) \cos(2n\omega_m t) - \psi \cdot \sum_{n=1}^{\infty} J_{2n-1}(\pi \frac{V_m}{V_\pi}) \sin((2n-1)\omega_m t) \quad (17)$$

where  $\chi = \cos(\pi V_{DC}/V_\pi)$ , and  $\psi = \sin(\pi V_{DC}/V_\pi)$ . The terms  $J_0$ ,  $J_{2n}$ , and  $J_{2n-1}$  represent Bessel functions of the respective order.

At the particular voltage  $V_{DC} = V_\pi/2$  also known as the “quadrature” point (Fig. 2.18),  $\chi$  becomes zero ( $\chi = 0$ ) and  $\psi$  becomes one ( $\psi = 1$ ). Thus, if the modulator is operated at quadrature, only the modulation frequency  $\omega_m$  and its odd harmonics are present and although the transfer function of the modulator is nonlinear (cosine square), the harmonics’ content at quadrature is low to moderate even at high modulation indices. Thus, in this case the major spectral components of the intensity modulated double sideband (DSB) optical signal comprise the optical carrier, as well as the upper and lower sidebands at the fundamental frequency  $\omega_m$ , apart from the optical carrier frequency.

Another important particular operating voltage is  $V_{DC} = V_\pi$ ; at this voltage the MZM is operated at MITP where  $\chi$  becomes one ( $\chi = 1$ ) and  $\psi$  becomes zero ( $\psi = 0$ ). Note, that in the case of a non-perfect MZMs, the voltage for operating at MITP might slightly deviate from  $V_\pi$  due to technological imperfections. When operating at the MITP, only the even order harmonics are present according to eq. (17). Neglecting higher order modes in a first instance, this results in a double sideband signal with a suppressed carrier (DSB-SC) in the frequency domain. From the theory, the original carrier at  $\omega_m$  should completely disappear but in reality, due to technological imperfections and the finite optical linewidth of the carrier, the fundamental optical frequency gets significantly suppressed but it does not completely disappear. Nevertheless, the two major spectral output components of the output signal are the lower and the upper sidebands at  $2\pi c_0/\lambda_0 - \omega_m$  and  $2\pi c_0/\lambda_0 + \omega_m$ , with  $\lambda_0$  being the input optical wavelength. Thus, when heterodyning the optical output signal of an MZM operated at MITP in a photodiode, the generated RF signal would have twice the modulation frequency  $\omega_m$ , according to eq. (9). This way, all-optical frequency-upconversion (frequency-doubling) is achieved.

Further modulation options exist when using an MZM with two electrodes that can be modulated individually. For example, when operating such a two-arm MZM at quadrature and a phase shift of  $\pi/2$  between the two modulating voltages, a single sideband (SSB) intensity modulated optical signal is generated [94].

In standard single-mode fiber, each optical frequency travels through the fiber at different velocities due to the chromatic dispersion properties of the fiber. Thus, each beating signal between two spectral components has a different phase depending on the fiber length, the dispersion of the fiber, the optical wavelength and the modulating frequency. Because of this fact, DSB-SC and SSB modulation are more advantageous with regard to chromatic dispersion penalties as in these cases only one beating frequency is generated by the photodiode, provided that higher order optical harmonics can be neglected. In contrast, an optical DSB signal generates two beating components at the modulating frequency in the photodetector; the lower sideband beating with the optical carrier and optical carrier beating with upper sideband. In case the phase difference between these two beating signals equals  $\pi$ , they cancel each other out. This will be theoretically and experimentally studied in more detail in section 3.2.

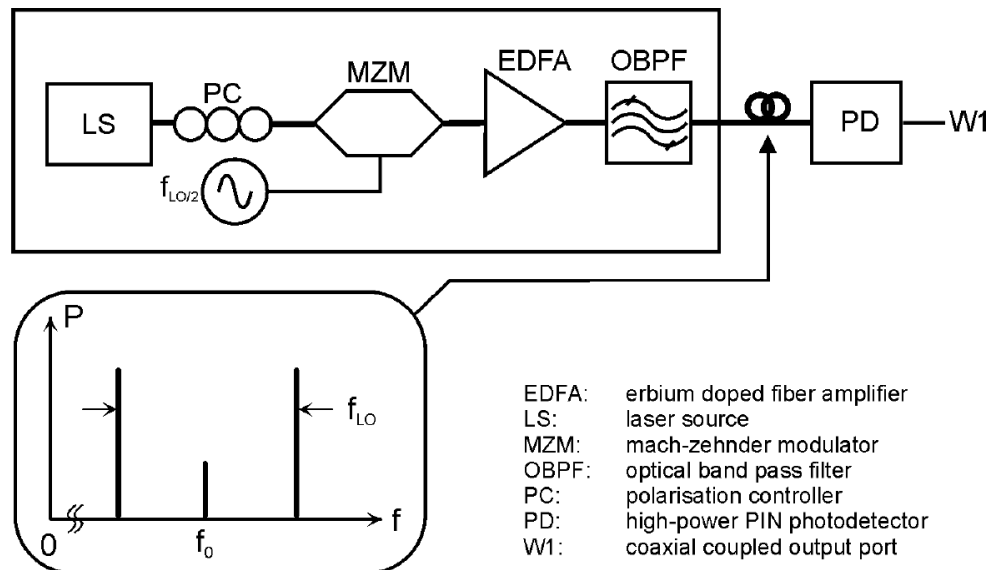


Fig. 2.19 Optical heterodyne set-up for testing photodiodes up to highest frequencies [42].

Similar to the photonic synthesizer concept based upon optical heterodyning shown in section 2.1, the optical generation of a DSB-SC carrier signal using an MZM can also be exploited for constructing photonic synthesizers. In [42], Fedderwitz et al. have demonstrated wideband (W-band) and a broadband (DC-110 GHz) photonic mm-wave synthesizer using advanced photodetectors. For W-band operation, they achieved a 3 dB frequency range of 69-112 GHz, a saturated maximum output power of 0 dBm, a 1 dB compression point of about -4 dBm as well as a dynamic range of 32 dB. For broadband (DC-110 GHz) operation, a photodiode coupled to a W1 coaxial connector was used. Continuous frequency tunability from DC up to 110 GHz was achieved with a power roll-off of less than 6 dB and a maximum output power of about -3 dBm. By constructing a photonic synthesizer employing external modulation using an MZM as shown

in Fig. 2.19, low-phase noise mm-wave generation was demonstrated with a phase noise level of only -70 dBc/Hz at 10 kHz offset from a 100 GHz carrier [42].

### 2.3 Opto-electronic oscillator

A rather new concept for optical microwave signal generation was first reported by *Lewis* in 1992 and later in 1996 experimentally demonstrated by *Yao* and *Maleki* [96]. Although *Yao* and *Maleki* were not the first, they provided a thorough theoretical study about the new approach and named it opto-electric oscillator (OEO) because it is based upon the utilization of an optical fiber loop as a long true time delay (TTD) element. Generally, an OEO is an oscillator that converts optical energy from a cw laser source into a pure and stable microwave signal [95-97]. The general set-up is depicted in Fig. 2.20. As can be seen, an OEO consists of an E/O-converter (optical modulator) and an O/E-converter (photodiode) at both ends of a long optical fiber. Together with the electrical feedback loop, this forms an electrical resonator which makes use of optical fiber as a low-loss transmission element allowing for long propagation times (and thus large energy storage). The long optical fiber thus acts as a delay line for achieving a high quality

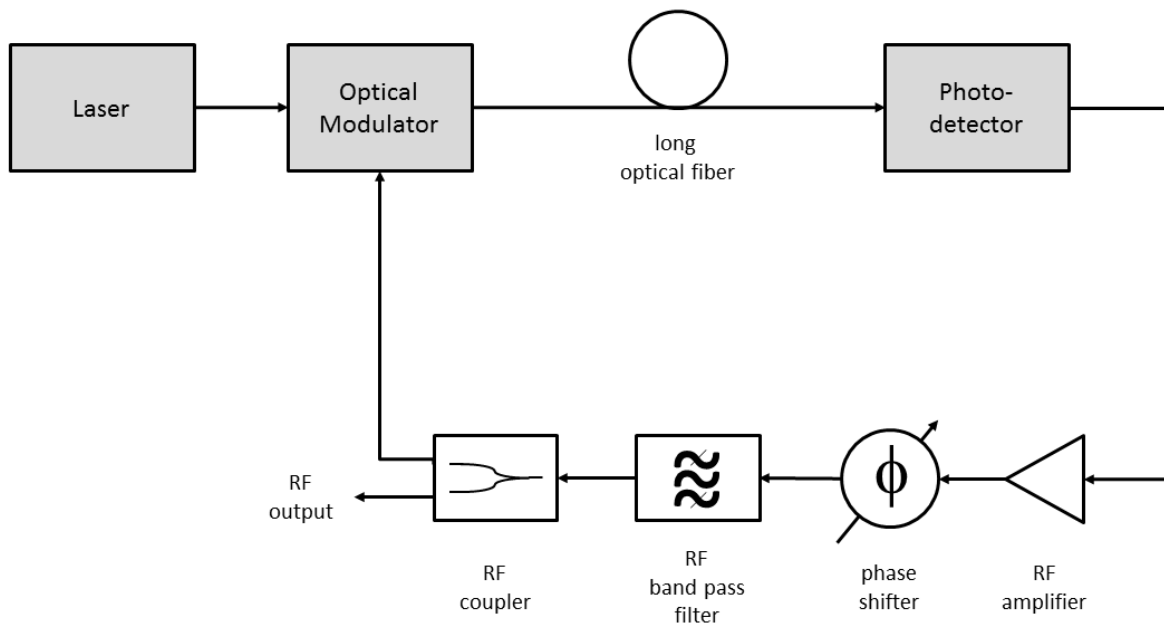


Fig. 2.20 Concept of an opto-electric oscillator (OEO) set-up [95].

factor ( $Q$ ) or low-loss energy storage element and thus, it provides the fundamental requirement for generating a high-spectral-purity and high-stability RF signal. In other words, an OEO can be seen as a long IMDD link (see section 2.2) with an additional electrical feedback loop. It differs from the OPLL approach (discussed in section 2.1.5) in that it relies on incoherent rather than coherent optical detection.

The major challenges coming along with the long optical fiber in an OEO are the stringent requirements on the intra-loop electrical RF filter and the total loop length stability. This is due to the fact that any oscillating RF frequency  $f_{\text{osc}}$  (or longitudinal mode) in an OEO with voltage gain must be a multiple of the reciprocal total delay  $\tau$  of the OEO loop (optical group delay plus electrical phase shift), i.e.  $f_{\text{osc}} = k/\tau$  [96]. For achieving a high  $Q$  factor, the fiber length should be in the range of several 1000s of meters and consequently the total group delay  $\tau$  is long. This, however, yields a very small free spectral range (FSR) or closely spaced modes and thus puts very stringent requirements on the intra-loop frequency discriminating filter, as well as on preserving the total loop length constant in order to prevent from mode-hopping and other instabilities.

Several improvements to the basic OOE have been demonstrated in the recent past [98]. In [97], *Yao and Maleki* presented a dual-loop OEO configuration in which the fiber lengths and thus the total group delays of the individual loops were significantly different. Since any oscillating frequency must be in resonance to both loops, i.e.  $f_{\text{osc}} = m/\tau_1 = k/\tau_2$ , the shorter loop with the larger FSR acts as an RF filter for the longer loop with the higher  $Q$  factor. This way, all parasitic side-modes within the FSR of the shorter loop are suppressed. Additional side-modes outside the FSR of the shorter loop can be suppressed by the electrical RF filter. This approach could potentially be extended to multi-loop OEOs, of course at the expense of providing enough gain and an overall higher expenditure.

Another feature of an OEO subject to optimization is frequency tunability. In a conventional OEO with a very short FSR, the electrical phase shifter is only used for achieving optimum phase locking. Several tuning schemes have been presented, providing either limited continuous tuning [99] or intra-modal switching [100]. However, in all those recent approaches the total frequency tuning range is somewhat limited to a few MHz only, e.g. in 2008, researchers from Technion demonstrated a tunable OEO, but with a limited frequency tuning range and phase noise level of less than 3 MHz and -90 dBc/Hz to -110 dBc/Hz at 100 kHz offset, respectively [98]. In 2010, the authors' group has demonstrated a novel dual-loop OEO approach which was principally based upon using two loops with similar but not equal length, as well as an electrical phase shifter for nearly continuous frequency tuning [101]. This way, we have succeeded in demonstrating a significantly improved frequency resolution and total tuning range of 320 kHz and 1.1 GHz, respectively. Also, the output power variation over the full tuning range is  $< 1$  dB and the linewidth and the phase noise of the generated RF signals, which are  $< 3$  Hz and -105 dBc/Hz at 10 kHz offset, respectively, represent better than state-of-the-art figures. Within the IPHOBAC project, OEOs have furthermore been demonstrated for the generation of higher mm-wave frequencies by using mode-locked semiconductor lasers [39].

## 2.4 Nonlinear optical frequency generation techniques

### 2.4.1 All-optical frequency up-conversion using MZM

Among the different techniques for optical mm-wave signal generation, IMDD using an external modulator is among the most robust techniques. As has been shown in section 2.2, one can even make use of the nonlinear transfer characteristic of an MZM in an IMDD link to achieve all-optically frequency up-conversion. If for example the MZM is operated at  $V_\pi$ , i.e. MITP, the optical carrier gets suppressed and a DSB-SC signal is generated. This way, frequency doubling is achieved when directly detecting the optical DSB-SC signal in the photodiode. This approach was first proposed in [102] in 1992. A 36 GHz signal was successfully generated when the MZM was driven at half the frequency, i.e. 18 GHz. A key advantage of this approach is that very high spectral purity and low phase noise mm-wave signals can be achieved. However, the generation of mm-wave signals in the W-band or at even higher mm-wave frequencies would require modulators with bandwidths in excess of 50 GHz which are extremely expensive and not quite commercially available. In 1994, an approach to generate a frequency quadrupled electrical signal was proposed. By suppressing the optical carrier, as well as the 1<sup>st</sup> and 3<sup>rd</sup> order sidebands by operating the MZM at  $V_\pi$ , only the even order side modes appear in the output spectrum. By using an additional optical filter, e.g. a Fabry-Perot filter, one can furthermore suppress the 2<sup>nd</sup> order side modes and yield frequency quadrupling. This way, a 60 GHz signal was generated in [103] using a 15 GHz LO to drive an MZM.

An approach for all-optical frequency sextupling based upon the use of cascaded modulators was reported in [104]. Here, an electrical drive signal was applied to a first MZM biased at quadrature to completely suppress the even-order optical sidebands and the optical carrier. This way, two coherent carriers are generated which are then modulated by the same microwave signal with a phase deviation of  $\pi/2$  in a second cascaded phase modulator. This way, many optical side modes are generated at the output of the second modulator. By adjusting the drive power level of the second phase modulator, one can furthermore optimize the efficiency for all-optical frequency sextupling.

Within the ESA funded PHOMIGEN project, UDE is currently investigating approaches with cascaded MZM or the use of MZM in a fiber loop for all-optical frequency up-conversion with multiplication levels higher than sextupling. First results will be presented in [105].

### 2.4.2 Four wave mixing in SOA and in highly nonlinear fibers

Recently, novel ultra-long semiconductor optical amplifiers (UL-SOA) have been developed which exhibit strong optical nonlinearities. These nonlinearities in the UL-SOA are mainly due to carrier heating (CH) and spectral hole burning (SHB), however, there is no key “nonlinearity” device parameter describing the nonlinearity of an SOA. Unlike short SOAs, ultra-long-SOAs are saturated after a certain length by the amplified optical signals and by the amplified spontaneous emission (ASE) noise. For this reason, UL-SOAs can be approximately considered to be consisting of two sections: a linear amplifying section and a nonlinear saturated section. Thus, UL-SOAs can be theoretically studied using a lumped element model. At first, the optical field at the SOAs’ input is amplified by the SOAs’ (lumped) gain. The resulting field then enters the SOAs (lumped) nonlinear section. A schematic illustration for the “lumped model” for studying FWM in SOAs is shown in the following figure.

In typically dimensioned bulk SOAs, the transition between these sections takes place after approximately 1 mm of propagation [106, 107]. This is why in most applications SOAs shorter than 1 mm are employed because optical amplification (as well as cross gain modulation (XGM) and cross phase modulation (XPM)) is saturating for longer SOAs. In UL-SOA, the amplifying section can be considered to have the same properties as in a short SOA while the lumped 3<sup>rd</sup> order nonlinear section can be regarded as an additional section exhibiting highly nonlinear properties. In the amplifying section, the carrier density cannot follow a high-frequency modulated optical input signal because of the long carrier lifetime of the inter-band effects. Thus,

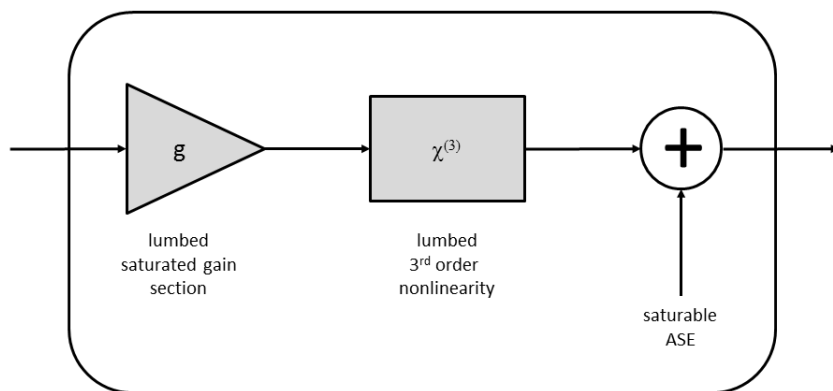


*Fig. 2.21 Lumped element model for an UL-SOA consisting of a linear gain section and a nonlinear section exhibiting a 3<sup>rd</sup> order non-linearity.*

the carrier density experiences only the average optical signal power. In the lumped 3<sup>rd</sup> order nonlinear section, however, the carrier density is clamped to the net transparency level because of the high optical power after the amplifying section. Therefore, fast nonlinear intra-band effects such as spectral hole burning (SHB) and carrier heating (CH) dominate and influence the optical signals. Compared to the slow carrier density pulsation in the linear gain section, the

response time of the fast intra-band effects in the nonlinear section is expected to be about 1000 times shorter [106, 107].

Besides XGM and XPM, an important nonlinear effect observed in the nonlinear section of an UL-SOA is four-wave mixing (FWM) [106-110]. FWM in general is the generation of optical side modes from an optical heterodyne input signal, i.e. from the superposition of two primary optical input waves. Assuming the two constituting optical input waves of the heterodyne signal have a difference frequency of  $\Delta\omega$ , then the intensity of the heterodyne signal contains a beating signal with a frequency of  $\Delta\omega$  (see also section 2.1). This beating signal causes free carrier density pulsations [106] especially in the nonlinear section where carrier density is highest and fast intra-band effects dominate. These carrier density pulsations in turn transform into beating oscillations of the wave number, coupling the different partial waves and thus cause FWM. This way, additional side modes separated by multiples of  $\Delta\omega$  from the two optical input waves are created.

Recently, the capability of UL-SOAs for pulse compression was presented in [108] raising hope that due to their tremendous FWM efficiency, UL-SOAs can generate broad optical combs having an equidistant frequency spacing of  $\Delta\omega$ . Compared to the previously discussed methods of generating short pulses, this scheme should be widely tunable. Initial experimental demonstration of millimeter-wave optical generation using FWM in SOA was reported in [109, 110] up to 60 GHz, but with rather limited phase noise performance and conversion efficiency. FWM has also been exploited in highly nonlinear dispersion shifted fibers (HN-DSF) for optical comb generation, e.g. by *Sefler* and *Kitayama* in [111]. By managing the dispersion in 35 km long DSF, they succeeded in generating an optical comb with a spectral width exceeding 1 THz.

In the PHOMIGEN project funded by ESA, the author's group in cooperation with THALES is investigating novel approaches for optical mm-wave generation in the W-band (75-110 GHz). By exploiting FWM in UL-SOA in conjunction with a cascaded MZM, the aim is to generate very low phase noise mm-wave signals in the W-band for sensor applications. First results are presented below and the applicability of optical signal generation for sensor applications is further discussed in chapter 6.

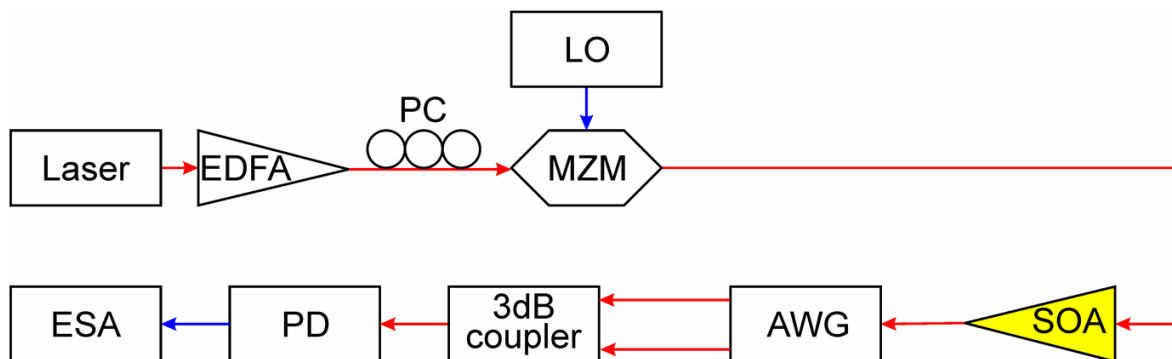
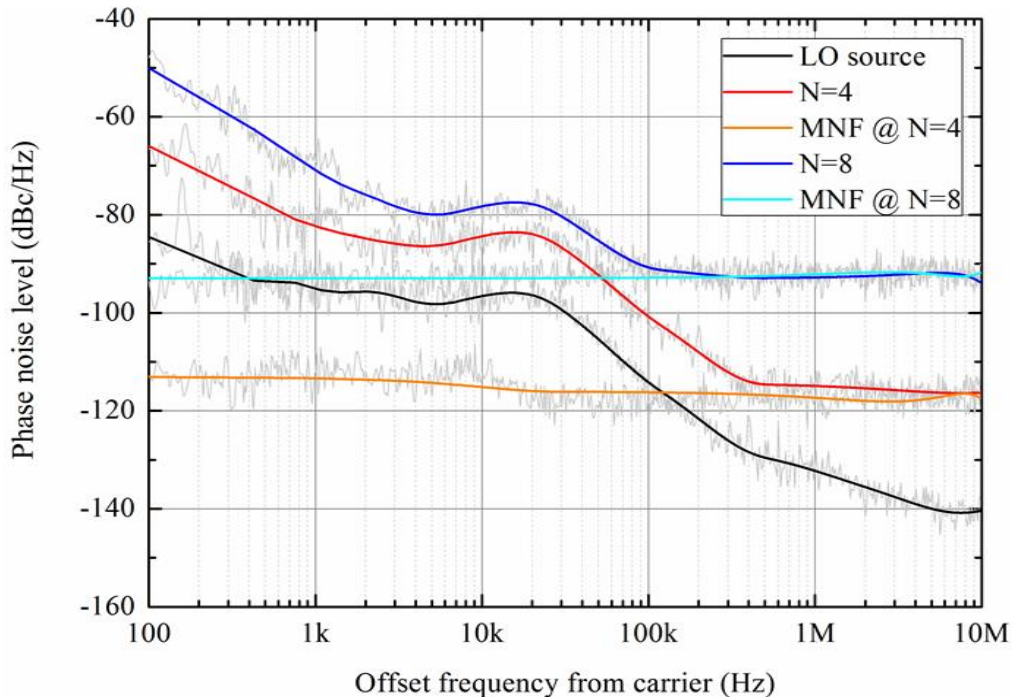


Fig. 2.22 Schematic illustration of the experimental set-up used optical multiplication of a microwave LO frequency by using the carrier-suppression in the Mach-Zehnder modulator as well as nonlinear FWM in the SOA. An arrayed waveguide grating (AWG) is used to filter out the desired optical modes.

Fig. 2.22 shows a schematic diagram of the experimental set-up for photonic millimeter-wave generation based upon an optical multiplication scheme. The MZM is operated at  $V_\pi$  for generating an optical double-sideband signal with a suppressed carrier (DSB-SC), i.e. the difference frequency between the upper and the lower optical side modes equals twice the LO frequency. This optical signal is injected into the SOA for producing higher-order harmonics which will be separately transmitted through single fibers due to the use of an arrayed waveguide grating (AWG). Then two of the fibers from the output of the AWG are combined using a 3-dB coupler which will result in a double-sideband signal with a difference frequency determined by the wavelength spacing of the used fibers. By beating the two wavelengths at a high-frequency PD, an electrical millimeter-wave signal having a frequency determined by the difference frequency of the optical signal is generated. The SOA is driven at high optical input power levels for generating a large number of higher harmonics. The difference frequency of these higher harmonics is determined by the difference frequency of the two output pump modes of the MZM (i.e. twice the LO frequency). An AWG is used to filter out the desired optical modes before heterodyning them in the PD.

At first the phase noise of the optically generated signal has been experimentally investigated to identify any additional noise resulting from the FWM in the SOA. Fig. 2.23 shows the measured phase noise of the LO signal at 4 GHz as well as of the quadrupled signal at 16 GHz and octupled signal at 32 GHz. Also the different noise floor levels of the measurement set-up are indicated. It should be mentioned that an electrical spectrum analyzer had been used for the measurements, i.e. strictly speaking the results represent an all-noise measurement.



*Fig. 2.23 Measured phase noise of the 4 GHz LO signal, as well as of the quadrupled ( $N=4$ ) optically generated signal at 16 GHz and the 8-times optically multiplied signal at 32 GHz. The measurement noise floor (MNF) levels at 16 GHz and 32 GHz are also shown.*

In case no additional noise is added by the nonlinear optical multiplication process, an increase of the phase noise level of the LO signal of 12 dB and 18 dB is expected when quadrupling or octupling the LO frequency. As can be seen from Fig. 2.23, this agrees very well with the measured results (e.g. at 10 kHz offset from the carrier) and is a clear indication that no further significant noise power is added. At higher offset frequencies the measurements are limited by the noise floor which varied with the carrier frequency as can be seen in Fig. 2.23.

Fig. 2.24 shows the experimentally determined conversion RF efficiency versus the LO power applied to the MZM. It should be noted that for safety reasons, the optical input power into the SOA was fixed to +11 dBm and the optical input power into the photodiode was fixed to + 5dBm, corresponding to about 2 mA photocurrent. As can be seen, quadrupling and octupling the LO frequency has been achieved. For the SOA-1117 a maximum RF conversion efficiency for quadrupling and octupling was found to be -38.6 dB and -58 dB, respectively. Of course, when operating at higher optical input power levels resulting in photocurrent of 20 mA, the conversion efficiency would increase by 20 dB.

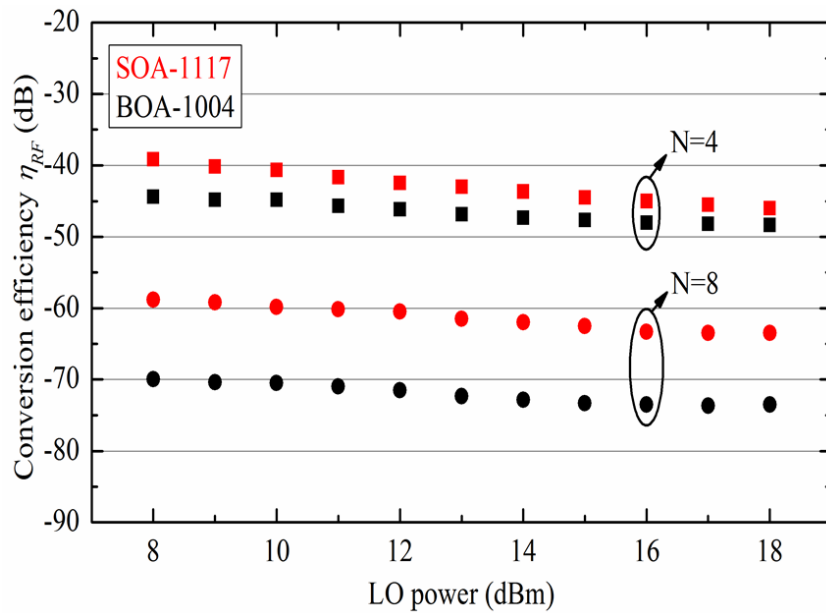


Fig. 2.24 RF conversion efficiency vs. LO drive power for different SOAs.

### 2.4.3 Cross phase modulation in highly nonlinear optical fibers

Like FWM, also cross phase modulation (XPM) results from the third order electric susceptibility  $\chi^{(3)}$  in a nonlinear medium such as optical fibers. Due to the third order nonlinearity in optical fibers, the refractive index  $n(\omega, I)$  not only depends on the angular frequency of the light  $\omega$  but also on the intensity of the propagating optical wave  $I(t)$  (optical Kerr effect).

$$n(\omega, I) = n_0(\omega) + n_{NL} \cdot I(t). \quad (18)$$

Thus, the phase  $\phi_{NL}$  at the output of a nonlinear optical fiber with length  $L$  becomes

$$\phi_{NL} = \frac{2\pi}{\lambda} \cdot n_{NL} \cdot I(t) \cdot L. \quad (19)$$

An optical wave thus modifies its own phase, which is called self-phase modulation (SPM). In case two optical waves with different angular frequencies  $\omega_1$  and  $\omega_2$  propagating along the fiber, the nonlinear refractive index seen by one wave also depends on the intensity of the second wave and vice versa, i.e.

$$\Delta n_{NL,1} = n_{NL} \cdot (I_1 + b \cdot I_2). \quad (20)$$

Here, the cross phase efficiency  $b$  depends on the nonlinear material properties and on the difference frequency  $\omega_1 - \omega_2$ . From eq. (24), one can observe that an optical wave not only influences its own phase but also the phases of other co-propagating optical waves. This effect is called cross-phase modulation (XPM).

Fiber dispersion has two major impacts on the effect of XPM. In the absence of chromatic dispersion, the modulation of the nonlinear refractive index  $\Delta n_{NL}$  would only result in optical phase changes, but the intensity of the optical waves would not be affected. Only in the presence of dispersion, phase fluctuations are continuously converted into intensity fluctuations. On the other hand, due to dispersion the two signals travel at different velocities through the fiber (see also section 3.2). Considering e.g. the case of two co-propagating optical pulses, it is obvious that efficient XPM only occurs as long as the walk-off in time between the two optical pulses is not too large. The latter is also the reason for employing dispersion shifted fiber (DSF) exhibiting zero dispersion in the third optical window whenever telecom 1.55  $\mu\text{m}$  laser diodes are being used.

With respect to optical signal generation, XPM can be exploited for performing all-optical up-conversion of high-frequency RF signals. By using a highly nonlinear dispersion shifted fiber (HNL-DSF) in combination with telecom laser diodes, XPM can be used for all-optical frequency doubling. This concept is schematically shown in Fig. 2.25. Here, an optical double

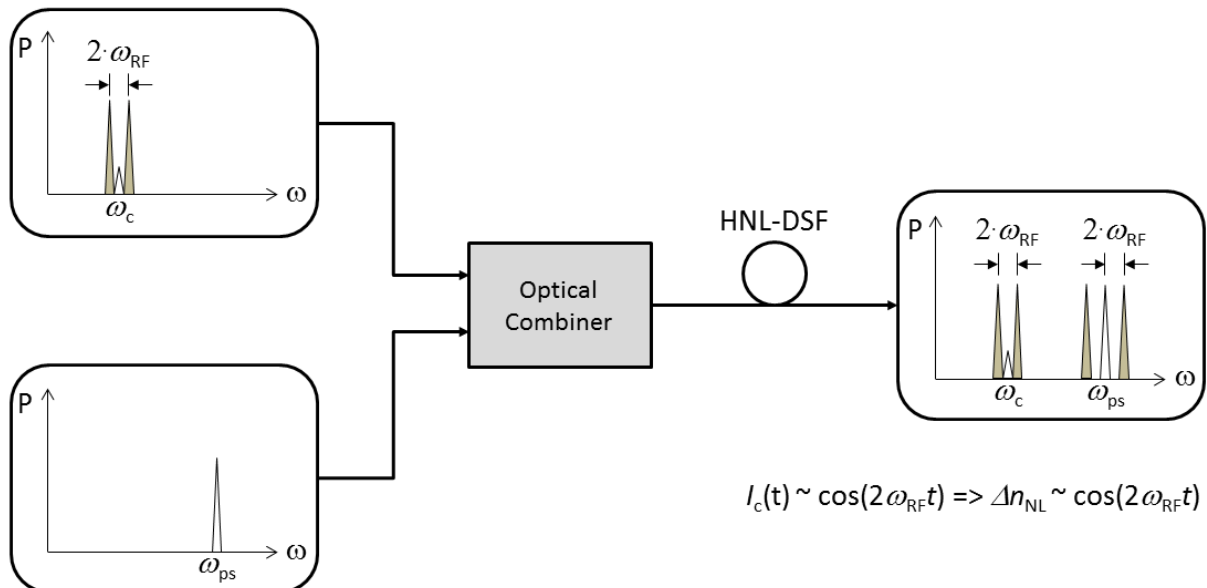


Fig. 2.25 Concept of exploiting XPM in a straight HNL-DSF. The optical input signal into the HNL-DSF is composed of a DSB-SC optical control signal around  $\omega_c$  and an additional cw optic probe signal at  $\omega_{ps}$ .

sideband signal with a suppressed carrier (DSB-SC) (see section 3.2.2 for details on DSB-SC generation) and an additional cw optical probe signal at  $\omega_{ps}$  are injected into an HNL-DSF. According to eq. (10), the intensity of the input control signal varies with  $\cos(2\omega_{RF}t)$ . Provided that the optical intensities are sufficiently high for efficient XPM, the nonlinear refractive index change will thus be modulated at  $2\omega_{RF}$  according to eq. (24) and the RF modulated refractive index will further affect the electric field of the optical probe signal at  $\omega_{ps}$ . Thus, because of XPM as well as phase-to-intensity modulation due to fiber dispersion, two additional waves are generated that can be observed at the output of the HNL-DSF. As can be seen from Fig. 2.25, these newly generated optical waves represent the lower and the upper sideband to the original probe signals at  $\omega_{ps} - 2\omega_{RF}$  and  $\omega_{ps} + 2\omega_{RF}$ . By using a fast photodiode at the output of the HNL-DSF, this optical heterodyne signal around  $\omega_{sp}$  can be converted back into an RF signal at  $2\omega_{RF}$ , i.e. at twice the RF frequency of the input DSB-SC beat signal.

The XPM in the HNL-DSF can even be exploited for all-optical up-converting (frequency doubling) an RF signal simultaneously onto a number of input probe signals. In, altogether 16 optical cw signals with a frequency separation of about 200 GHz were multiplexed using an arrayed waveguide grating (AWG). The 16 optical probe signals were further transmitted via a 10 km long SMF for signal de-correlation before they were injected into a 1 km long HNL-DSF together with an optical DSB-SC signal at 1.563  $\mu$ m and a carrier-to-sideband difference frequency of 20 GHz. With this set-up, all-optical up-conversion onto the 16 optical input carriers was successfully demonstrated.

Cross phase modulation for optical signal generation and up-conversion has also been exploited by making use of the third order nonlinearities of the electric susceptibility in SOAs. However, in this context the term XPM typically refers to a kind of cross-phase modulation which is not based on the Kerr effect where  $\Delta n_{NL} \sim |E|^2$  (eq. (20)), but rather on changes in the refractive index via the carrier density as discussed in section 2.4.2.

#### 2.4.4 Cross absorption modulation in EAM & cross gain modulation in SOA

Cross absorption modulation (XAM) in electro-absorption modulators (EAM) as well as cross gain modulation (XGM) in semiconductor optical amplifiers represent nonlinear effects that can also be exploited for all optical signal processing including optical signal generation and all-optical up-conversion.

Generally, the inter-band or fundamental absorption process in EAM can be controlled via the internal electric field across the active section, i.e. via the externally applied electrical bias voltage. This is due to the Franz-Keldysh effect (FKE) in bulk or the QCSE in multiple quantum well (MQW) EAM [112]. At low optical input power levels, the influence of the carrier density on the FKE or QCSE efficiency is negligible. At higher optical input power levels when the density of the photo-excited carriers is also high, nonlinear effects can significantly affect the dynamics of the fundamental absorption process. There are two sources that contribute to the change in absorption dynamic: band filling and internal field screening. Especially in MQW EAM when carriers are excited into the wells, the fundamental absorption is reduced due to band filling effects. At high carrier densities in the wells, when the occupation density is approaching 100%, photons cannot be absorbed anymore as all available states are already occupied. In addition, the photo-generated carriers in the wells affect the internal electric field and this leads to a significant reduction in the carrier escape time from the wells.

Besides exploiting XAM in EAM, or XPM in HNL-DSF or in SOAs it is also possible to up-convert an optical signal by exploiting cross gain modulation (XGM) in semiconductor optical amplifiers. By injecting an optical heterodyne signal into a nonlinear SOA, the free carrier density in the SOA gets modulated by the optical beating signal provided the beating frequency is below the carrier lifetime determined SOA gain modulation bandwidth. If one now additionally injects an optical cw probe signal, similar to the approach shown in Fig. 2.25, the carrier density modulated at the beat frequency will start affecting the electrical field of the probe signal and thus create a lower and an upper optical sideband at twice the beat frequency. This way, all-optical frequency doubling is achieved. However, due to the long carrier lifetime, efficient XGM is limited up to a few GHz only. Of course, there exist much faster nonlinear effects in saturated SOA such as spectral hole burning (SHB) or carrier-heating (CH) that allow to exploit XGM also at higher frequencies but with rather limited efficiencies.

An approach to up-convert a rather low frequency IF signal to a very high frequency RF signal beyond the SOAs' gain modulation bandwidth is shown in [113]. Here, an optical intensity modulated, i.e. an optical DSB control signal with angular frequencies around  $2\pi c_0/\lambda_{\text{IF}}$  is injected into an SOA together with an optical heterodyne signal with sidebands at  $2\pi c_0/\lambda_{\text{LO}} - \omega_{\text{RF}}/2$  and  $2\pi c_0/\lambda_{\text{LO}} + \omega_{\text{RF}}/2$ . In the experiment, the IF frequency was set to 1 GHz whereas the RF signal was set to 60 GHz, i.e. significantly higher than the gain modulation bandwidth of the SOA which is typically in the order of a few GHz up to 10 GHz. Because of that, the carrier density gets modulated by the IF signal only whereas the effect of the RF signal on the carrier density in the SOA is rather limited due to the long carrier lifetimes. This means that the two optical sidebands of the optical heterodyne signal become modulated by the carrier density modulation due to the XGM effect. This way, a lower and an upper optical sideband are generated next to

each sideband of the optical heterodyne LO signal resulting in altogether four optical waves at the SOAs' output besides the injected optical IF modulated control signal:

$$\begin{aligned} & \frac{2\pi \cdot c_0}{\lambda_{LO}} - \omega_{LO}/2 - \omega_{IF} \\ & \frac{2\pi \cdot c_0}{\lambda_{LO}} - \omega_{LO}/2 + \omega_{IF} \\ & \frac{2\pi \cdot c_0}{\lambda_{LO}} + \omega_{LO}/2 - \omega_{IF} \\ & \frac{2\pi \cdot c_0}{\lambda_{LO}} + \omega_{LO}/2 + \omega_{IF} . \end{aligned} \quad (21)$$

By mixing these four optical signals in a linear photodiode as described in section 2.2, the IF signal gets up-converted to the 60 GHz mm-wave RF frequency.

### 3 Fiber-Optic Millimeter-Wave and THz Transport

#### 3.1 Attenuation in fiber-optic RF transmission systems

Attenuation in an optical fiber is caused by absorption, scattering, and bending losses. Attenuation generally refers to the loss of optical power as light travels through an object.

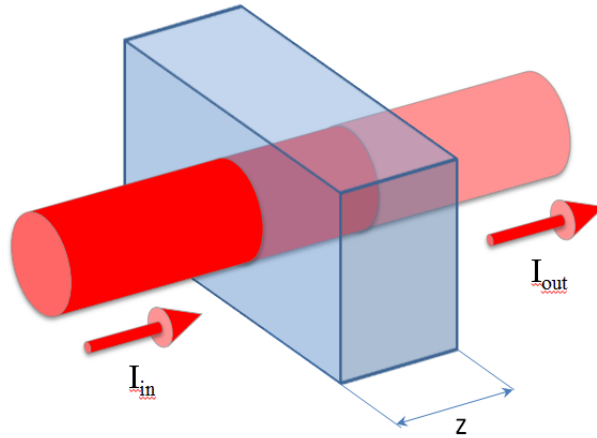


*Fig. 3.1 Schematic of Beer-Lambert absorption of a light beam as it travels through a material.*

For electromagnetic waves at optical frequencies, the attenuation coefficient is related to power or intensity and not to the electrical field as it is done in the microwave domain. Thus, in optics, the intensity change  $dI$  caused by attenuation through an object of infinitely short length  $dz$  is expressed as:

$$dI = -\alpha \cdot I_{in} \cdot dz . \quad (22)$$

This leads to the well-known Beer's law:

$$I(z) = I_{in} \cdot e^{-(\alpha \cdot z)} , \quad (23)$$

with the attenuation coefficient  $\alpha$  given in  $\text{cm}^{-1}$ . Especially for long objects such as optical fibers it is, however, more convenient using the attenuation coefficient given in decibel per length. Thus, eq. (23) is changed into:

$$\frac{I(z)}{I_{in}} = e^{(-\alpha \cdot z)} = 10^{\log(e) \cdot (-\alpha \cdot z)}$$

$$10\log\left(\frac{I(z)}{I_{in}}\right) = 10\log(10^{\log(e) \cdot (-\alpha \cdot z)}) = 10\log(e) \cdot (-\alpha \cdot z) = -\alpha_{dB} \cdot z \quad (24)$$

with  $\alpha_{dB} = 10\log(e) \cdot \alpha \approx 4.343 \cdot \alpha$ .

For optical fibers, where the length  $z$  is usually given in kilometer,  $\alpha_{dB}$  is given in decibels per kilometer (dB/km).

As previously stated, attenuation in an optical fiber is caused by absorption, scattering, and bending losses. Each mechanism of loss is influenced by fiber-material properties and the fiber structure. Absorption is a major cause of signal loss in an optical fiber. It is defined as the portion of attenuation resulting from the conversion of optical power into another energy form, such as heat. Absorption in optical fibers is mainly due to the following:

- Imperfections in the atomic structure of the basic fiber material,
- The intrinsic or basic properties of the fiber-material,
- Presence of impurities from extrinsic materials introduced during fiber fabrication.

Imperfections in the atomic structure induce absorption by the presence of missing molecules or oxygen defects. Absorption is also induced by the diffusion of hydrogen molecules into the glass fiber.

Intrinsic absorption is caused by basic fiber-material properties, it sets the minimum level of absorption. If an optical fiber were absolutely pure, i.e. with no imperfections or impurities, then absorption would be completely intrinsic. In fiber optics, silica (pure glass) fibers are used predominately. Silica fibers are used because of their low intrinsic material absorption within the operation wavelength region which ranges from 700 nm to 1600 nm. For short wavelengths, this region is limited due to Rayleigh scattering and ultraviolet (UV) absorption which becomes significant below 400 nm. For long wavelength, infrared (IR) absorption in the region above 1700 nm sets an upper limit. Fig. 3.3 shows the attenuation levels in silica fiber for the operating wavelength region. The intrinsic absorption in the UV region is caused by electronic absorption bands. Here, high-energy photons interact with electrons, exciting them to a higher energy level. The tail of the ultraviolet absorption band can be seen in Fig. 3.3. Within the operating wavelength region, Rayleigh scattering (named after Lord Rayleigh) is dominating for

wavelength below 1200 nm, as can be seen from Fig. 3.3. Rayleigh scattering is the scattering of light or other electromagnetic radiation by particles much smaller than the wavelength of the light. It occurs when light travels in transparent solids and liquids. Rayleigh scattering is dependent upon the size of the particles and the wavelength of the light; in particular, the scattering coefficient, and hence the intensity of the scattered light, varies for small size parameter inversely with the fourth power of the wavelength ( $\sim\lambda^{-4}$ ). This explains the increasing scattering loss for lower wavelength in Fig. 3.3. For long wavelengths in the IR region, the main cause of absorption is due to vibrational modes of atomic bonds. In silica glass, absorption is caused by the interaction of photons with silicon-oxygen (Si-O) bonds.

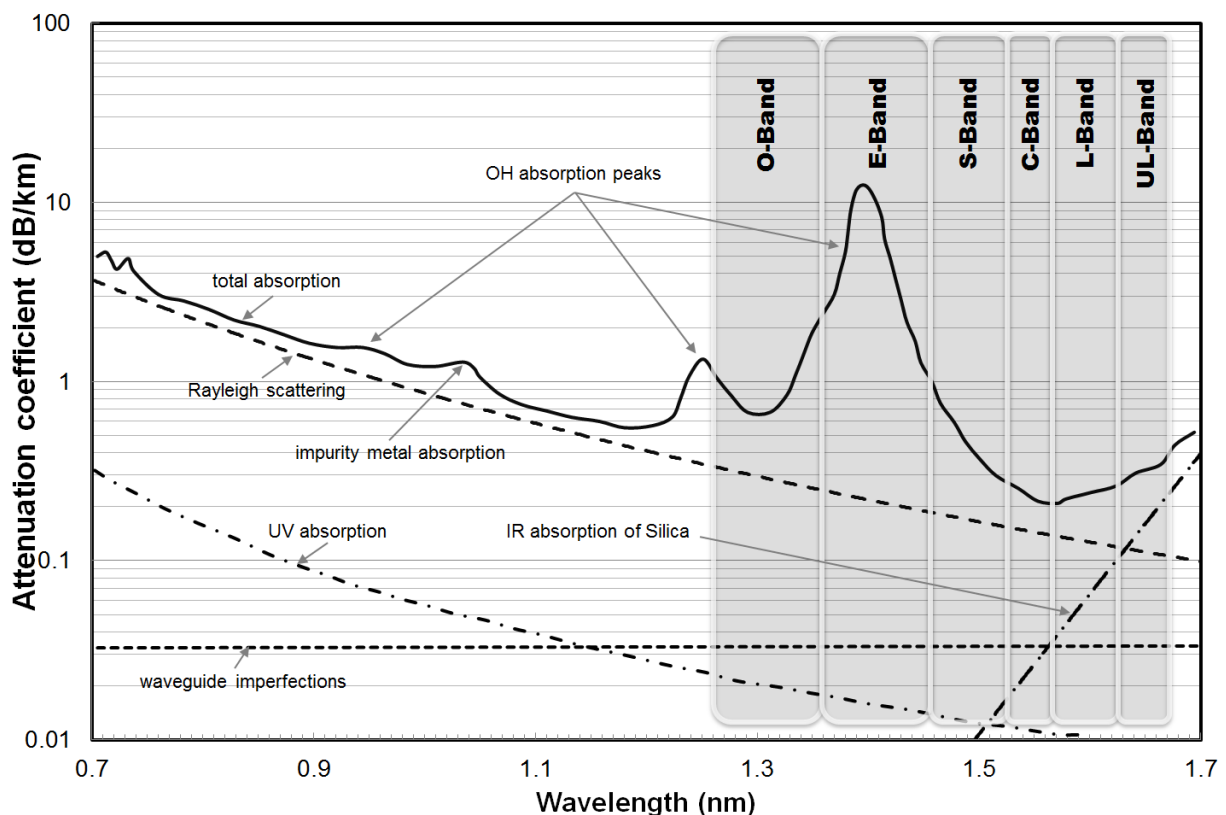


*Fig. 3.2 Attenuation coefficient (solid line) for a standard single mode glass fiber versus optical wavelength. Dashed lines are representing individual loss contributions such as Rayleigh scattering, OH absorption and other effects.*

Extrinsic absorption is caused by impurities originating from external materials introduced into the fiber material during the fabrication process. Metal impurities, such as iron, nickel, and chromium, are introduced into the fiber during fabrication and give rise to absorption. Extrinsic absorption also occurs when hydroxyl ions ( $\text{OH}^-$ ) are introduced into the fiber. Water in silica glass forms a silicon-hydroxyl (Si-OH) bond and this bond has a fundamental absorption line in the Far-IR at 2700 nm. However, harmonics of the fundamental absorption line occur in the

region of operation, increasing extrinsic absorption at 1383 nm, 1250 nm, and 950 nm. Fig. 3.2 shows the presence of the three OH<sup>-</sup> absorption lines.

As can be seen from Fig. 3.2, the total attenuation in silica fiber shows several windows with relatively low attenuation. In the past, these low-absorption regions defined three windows of preferred operation. The first window was centered at 850 nm, which is obviously not due to low-attenuation but to the historical fact that the first laser diodes had been grown on GaAs in the early 60s of the last century and were used around 850 nm. The second window was centered at 1300 nm where the fiber's chromatic dispersion crosses the zero level. The third window was centered at 1550 nm where attenuation in silica fibers is minimum. With the invention of new optical amplifiers also those wavelength regions with comparably high fiber attenuation became accessible for fiber-optic transmissions. Consequently, the wavelength windows were broken down into smaller regions similar to the microwave domain. In Fig. 3.2, the most important optical bands are indicated. The previously named second window is now called O-Band where "O" stands for original, and the third window around 1.55 μm is now named the C-Band ("C" for conventional). The terms E-Band, S-Band, L-Band and UL-Band stand for extended, short, long and ultra-long band, respectively (see 0 for wavelength definitions).

### 3.2 Dispersion induced power penalties in fiber-optic RF transmission systems

Generally, fiber loss is not the major limitation regarding the maximum fiber length in a high-frequency fiber-optic transmission system due to the very low transmission loss (<0.2 dB/km @ 1.55 μm) and the availability of Erbium-doped optical fiber amplifiers. In fact, dispersion  $D$  of optical fibers and the chirp parameter  $\alpha$  of light emitters are the parameters that actually set an upper limit to the product modulation frequency squared times length, i.e.  $f^2 L_{\max}$ , in high-frequency fiber-optic transmission links.

Light chirping is a parasitic property of intensity modulated light. It originates in light emitters that produce a phase shift as the intensity is varied. The electric field of the light wave can be written

$$\left| \vec{E} \right| = \sqrt{I} \cdot e^{j\Phi(I)}, \quad (25)$$

were  $I$  is the light intensity and  $\Phi(I)$  is the phase of the electric field. For electro-absorption, directional coupler type, Mach-Zehnder and reflection modulators, *Koyoma* and *Iga* showed that the chirp parameter  $\alpha$  relates how phase varies with intensity [114]

$$\partial\Phi = \frac{\alpha \cdot \partial I}{2I}. \quad (26)$$

Note that the above definition assumes small-signal conditions and that  $\alpha$  also depends on  $I$  through bias voltage or current.

In the following, an electro-absorption modulator (EAM) will be used to experimentally investigate the maximum achievable product  $f^2 L_{\max}$  in the millimeter-wave region. In case that an EAM is used for optical intensity modulation, the chirp parameter is the derivative of the  $n$  versus  $k$  curve, where  $n$  and  $k$  are the real and imaginary parts of the modal index of the electro-absorption waveguide, respectively [114],

$$\alpha = -\frac{\partial n}{\partial k}. \quad (27)$$

In [115], Devaux et al. have shown that the chirp parameter and the average dispersion of the dispersive media can be found from the resonance frequencies in a high-frequency analogue fiber-optic transmission experiment.

Assuming small signal modulation, the modulated optical intensity can be written as

$$I = I_0 \cdot (1 + m \cdot \cos(2\pi f t)) \text{ with } m \ll 1, \quad (28)$$

with  $m$  being the modulation depth and  $f$  the modulation frequency. The electric field of the corresponding light wave is a periodic function of time and can thus be developed into a Fourier series:

$$|\vec{E}| = e^{j\omega_0 t} \cdot \sum_{-\infty < p < \infty} A_p e^{2j\pi p f t} \quad (29)$$

where  $\omega_0$  is the light pulsation. Equation (25) can be developed into a Fourier series by using equation (26) and (28). Developing  $E$  into an  $m$  power series yields the first three Fourier coefficients when restricted to the first power of  $m$ :

$$\begin{aligned}\underline{A}_{-1} &= \sqrt{I_0} m \frac{(1+j\alpha)}{4} \\ \underline{A}_0 &= \sqrt{I_0} \\ \underline{A}_{+1} &= \sqrt{I_0} m \frac{(1+j\alpha)}{4}.\end{aligned}\tag{30}$$

These three spectral components represent the optical carrier, as well as the lower and upper optical sidebands of the electric field spectra at the output of the light emitter. Such an optical signal with carrier and the two sidebands is also referred to as optical double sideband (DSB) signal.

Each spectral component of eq. (30) travels at a slightly different velocity. The propagation constants of the two first order sidebands are:

$$\beta_{\pm p} = \beta_0 \pm \frac{2\pi pf}{v_g} - \frac{\pi\lambda^2 D p^2 f^2}{c},\tag{31}$$

with  $v_g$  being the group velocity. Using eqs. (29) and (31), the electric field at the output of the optical fiber with length  $L$  and dispersion  $D$  can be expressed as:

$$\left| \vec{\underline{E}} \right| = e^{j\omega_0 t} \cdot \sum_{-\infty < p < \infty} \underline{A}_p e^{j(2\pi pf t - \beta_p L)}.\tag{32}$$

Here, fiber absorption was not taken into account as it only stands for a constant factor. In general, the intensity component at frequency  $f$  is given by:

$$I_f = \frac{1}{2} \Re \left\{ \underline{A}_p \cdot \underline{A}_q^* \cdot e^{j(\beta_q - \beta_p)L} \right\}.\tag{33}$$

By inserting eqs. (30) and (31) into (32), the component at frequency  $f$  of the light intensity can be found by:

$$I_f = I_0 m \sqrt{1 + \alpha^2} \left| \cos \left( \frac{\pi \lambda^2 D L f^2}{c} + \arctan(\alpha) \right) \right|.\tag{34}$$

Experimentally, this frequency response can be measured using a high-frequency light source, a fiber with dispersion coefficient  $D$ , and a high frequency photodetector. As can be seen from eq. (34), resonance frequencies will appear each time the argument of the cosine function equals  $\pi/2 + u\pi$  with  $u$  being an integer. This is a result of the interference between two different beating

products, the beating between the lower sideband and the carrier as well as the beating of the upper sideband with the carrier. If the phase difference between those two beating products equals  $\pi$ , destructive interference occurs at the photodetector and the frequency response exhibits a minimum.

From eq. (34), it can be seen that the resonance frequencies  $f_u$  follow the following law:

$$f_u^2 L = \frac{c}{2D\lambda^2} \left(1 + 2u - \frac{2}{\pi} \arctan(\alpha)\right). \quad (35)$$

According to the above equation, fiber dispersion and modulator chirp can be experimentally characterized by measuring the resonances in the frequency response of an analogue fiber-optic link with a fixed fiber length  $L$ .

### 3.2.1 Optical double sideband (DSB) signals

In the following, the maximum product of fiber length times modulation frequency squared for standard single mode fiber (SMF) will be experimentally investigated. Further, it will be experimentally shown for a millimeter-wave fiber-optic transmission link that by adjusting the chirp value  $\alpha$  of the intensity modulator, a distinct extension of the maximum fiber-length and a reduction of the dispersion penalty can be achieved. This technique is well-known in digital optical communications (see for example [116]). However, it represents the first experimental study of a modulator's chirp value at 60 GHz mm-wave frequency and its optimization in order to extend the fiber length and reduce the dispersion penalty in an mm-wave fiber-optic system.

The modulator used for the following experiments is a high-speed waveguide InGaAsP electro-absorption modulator (EAM) [117]. The optical insertion loss is 7 dB and the polarization dependence is less than 0.5 dB. As discussed above, if the optical DSB spectrum generated by the EAM is transmitted over fiber, each of the three spectral components experiences a different phase shift depending on the fiber dispersion coefficient  $D$ . Thus, the phase shift sets a limit to the maximum fiber-length, which is defined as the fiber length  $L$  where the RF beat signals after detection exhibit a phase shift of  $\pi$  and thus interfere destructively. This dispersion limited fiber-length  $L$  can be derived from equation (35) to be

$$L = \frac{c}{2D\lambda^2 f_{RF}^2} \left(1 - \frac{2}{\pi} \arctan(\alpha)\right), \quad (36)$$

where  $f_{RF}$  denotes the RF frequency,  $\lambda$  the optical wavelength and  $\alpha$  the modulator's chirp value. From eq. (36), the dispersion limited fiber-length  $L$  can be extended when the modulator exhibits a large negative chirp value  $\alpha$ . In principle, EAMs based on multiple-quantum wells (MQW) exhibit negative chirp values if they are either operated at wavelengths just above the excitonic resonance or driven with a large reverse bias. In these cases, the refractive index change due to the quantum confined Stark effect (QCSE) is negative and thus the chirp value which is proportional to the refractive index change is also negative.

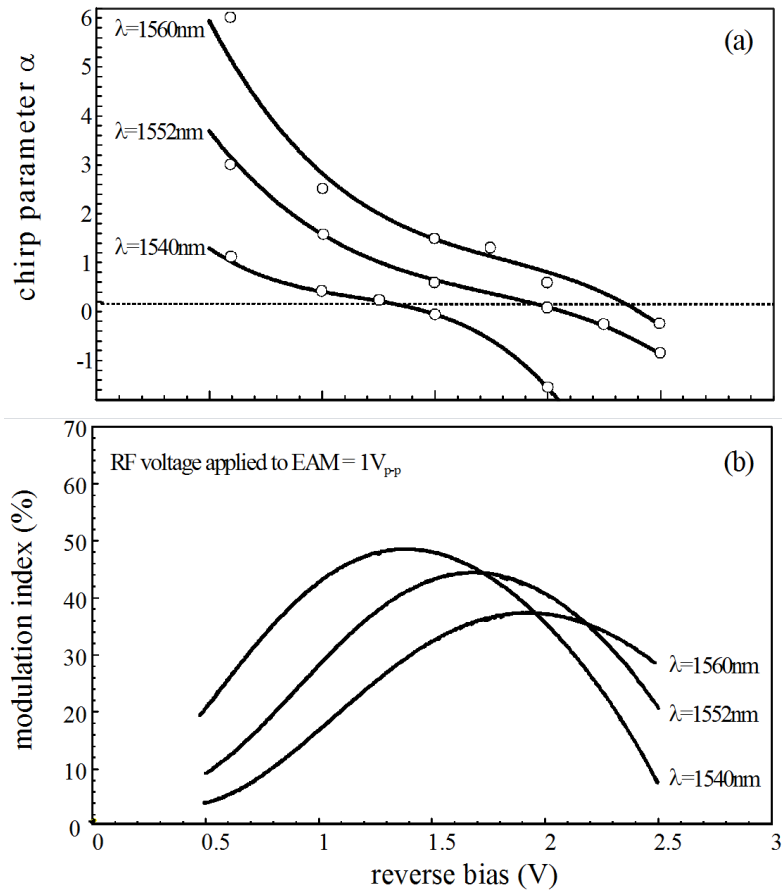


Fig. 3.3 Chirp value (a) and modulation index (b) of high-speed EAM versus reverse bias [118].

To experimentally determine the chirp value  $\alpha$  of the EAM at mm-wave frequencies, the frequency-domain method described above was used. In Fig. 3.3, the chirp value is shown versus the applied reverse bias voltage at different wavelengths. As can be seen, the chirp value varies between +5.5 and -1.5 depending on the optical wavelength and the applied reverse bias. This clearly demonstrates that the EAM's chirp is not independent of the bias condition and thus, optimum system performance must be identified by adjusting both, the wavelength of the light source and the modulator's reverse bias. The small signal modulation index shown in Fig. 3.3(b) was determined from DC modulation characteristics for an applied RF peak-to-peak voltage of 1 V<sub>p-p</sub>, which corresponds to an applied RF power of 4 dBm. From there it can be seen that the

maximum modulation index of  $m = 48\%$  is achieved at 1540 nm wavelength and even for a negative chirp value of -1 the modulation index is still  $m = 42\%$ .

Since this work is concerned with the fiber distance extension, an experimental test-bed of a 60 GHz fiber-optic transmission system was set-up (see Fig. 3.4). This set-up includes two 156 Mb/s channels each using a NRZ (PRBS,  $2^{23}-1$ ) in a DPSK format at IF's of 2.6 and 3.0 GHz. These signals are frequency multiplexed and up-converted by a 57 GHz local oscillator in the transmitter. The mm-wave modulated optical carrier generated by the high-speed EAM is transmitted through non-dispersion shifted fiber having a dispersion coefficient of  $\sim 17$  ps/nm/km at 1540 nm wavelength. The electrical mm-wave signal is recovered by a photodetector with a 3 dB cutoff frequency of  $f_{3\text{dB}} = 50$  GHz.

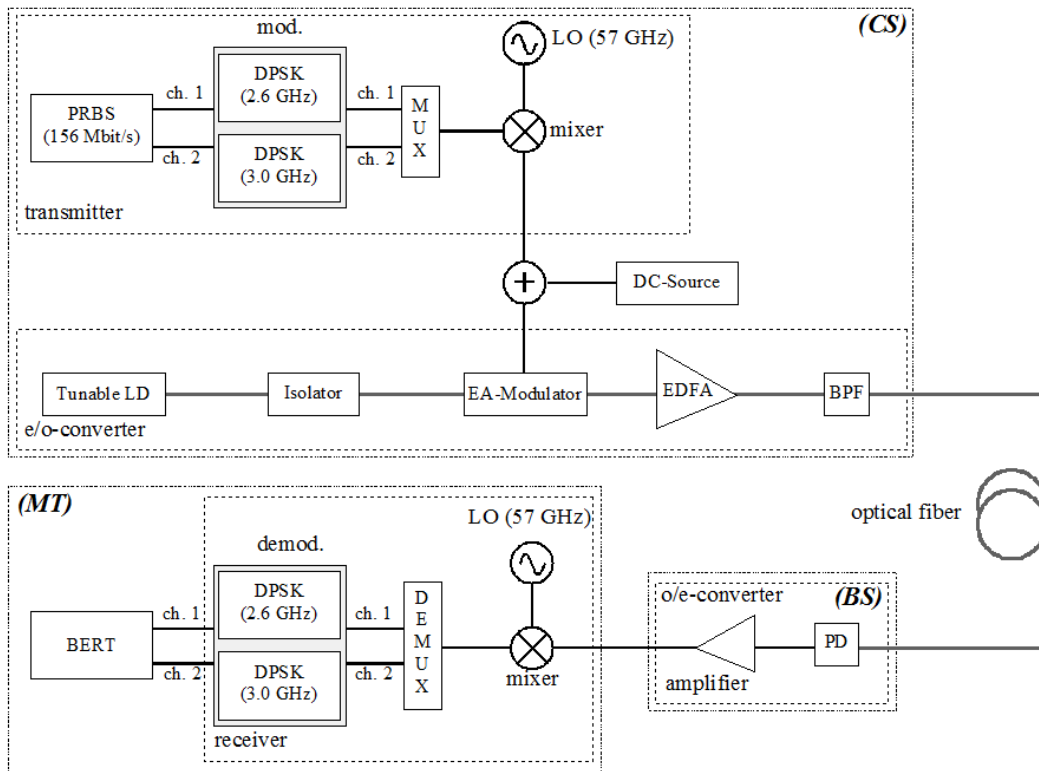


Fig. 3.4 Experimental set-up of a 60 GHz fiber-optic link [118].

In Fig. 3.5, the measured bit-error rate (BER) of channel 1 is shown versus the modulator's chirp parameter at different optical wavelengths. The fiber length used in this experiment was 503 m, the received optical power at the PD input was fixed to -12 dBm and the RF voltage applied to the EAM was 1 V<sub>p-p</sub>.

As can be seen, the BER drastically depends on the precise adjustment of the chirp value. As an example, operating at 1540 nm with a chirp of about -0.5 reduces the BER by about four orders of magnitude compared to a chirp-free modulation.

In order to demonstrate the extension of the fiber-optic transmission distance using chirp adjustment, the minimum received optical power at the PD required for  $\text{BER} = 10^{-10}$  was measured versus the fiber length. These measurements were performed at 1540 nm wavelength for a chirp value of  $\alpha = -1.45$  and  $\alpha = 0.9$  corresponding to a reverse bias of -2 V and -0.75 V, respectively.

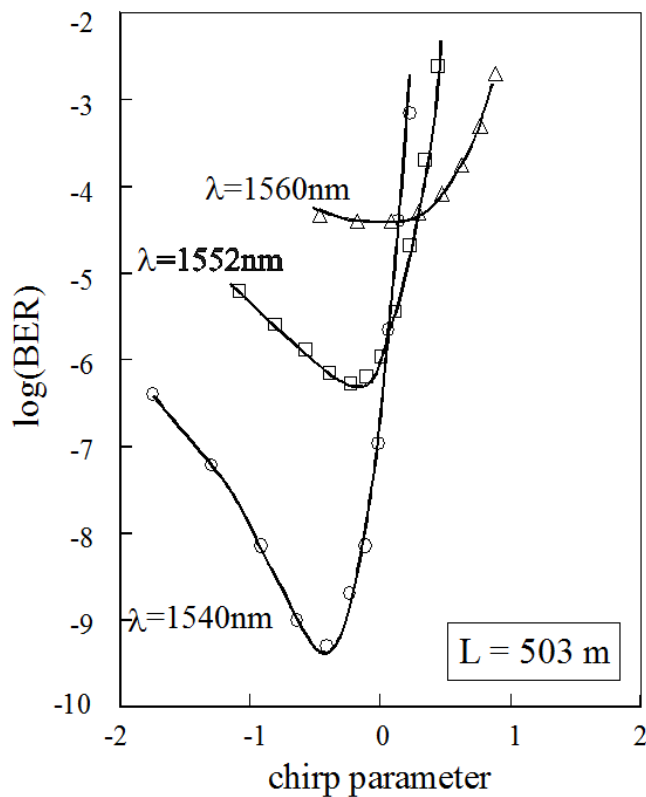


Fig. 3.5 BER versus chirp parameter for fixed received optical power of -12 dBm [118].

The experimental results shown in Fig. 3.6 clearly indicate a distinct extension of the maximum fiber length from 600 m at  $\alpha = +0.9$  to about 1600 m at  $\alpha = -1.45$ . These lengths are also in good agreement to theoretical values calculated from eq. (36) (see also arrows in Fig. 3.6). The maximum admissible fiber length for a  $\text{BER} = 10^{-10}$  that was achieved equals 1409 m, corresponding to a system bandwidth as high as  $5072.4 \text{ GHz}^2\text{km}$ . From the viewpoint of effective power management, the smallest optical power required for  $\text{BER} = 10^{-10}$  is about -12 dBm. It is achieved at 550 m fiber length, where optimum interference of the RF beat signals

after detection occur for the given chirp value of  $\alpha = -1.45$ . It should be noted that the optimum chirp value  $\alpha$  is shifted to larger negative values for a longer fiber distance.

To determine the sensitivity of the optical receiver we measured the BER of both channels versus the received optical power using 503 m of non-dispersion shifted fiber at 1540 nm wavelength. The results are presented in Fig. 3.7 where also the optical spectrum of the DSB signal generated by the EAM is plotted.

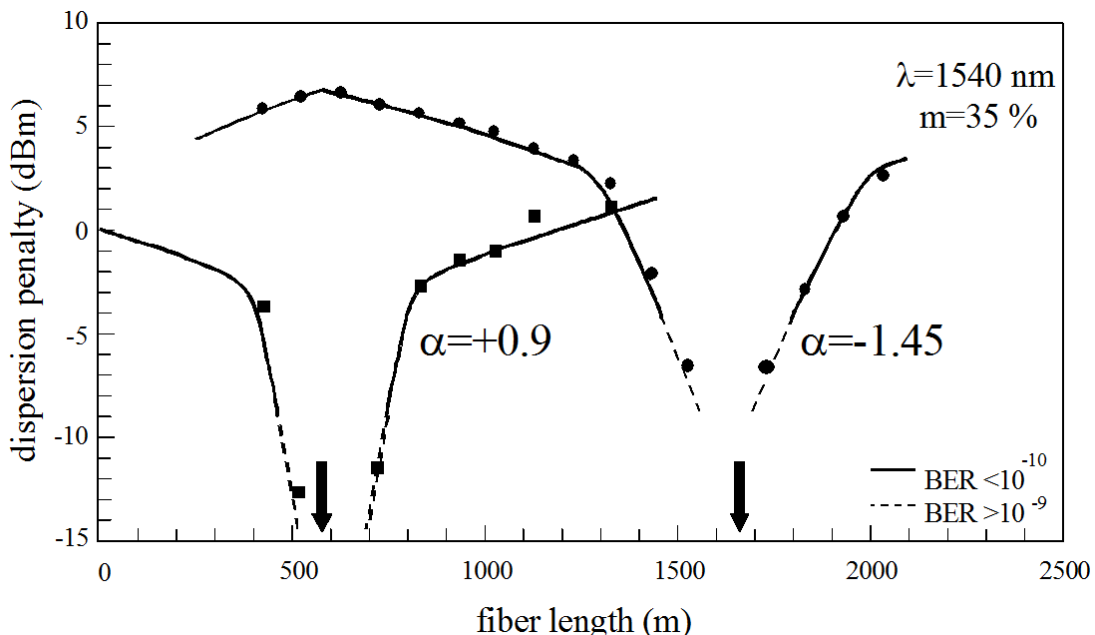


Fig. 3.6 Minimum required received optical power for  $\text{BER} = 10^{-10}$  versus fiber length.

As can be seen from Fig. 3.7, a BER of  $10^{-10}$  is achieved for both channels and no error floor was observed. The slight difference in required optical power for  $\text{BER} = 10^{-10}$  between both channels is due to a larger phase noise of channel 2. From the optical spectrum shown in Fig. 3.7, no significant higher order optical sidebands were observed. This result in addition to IM3 measurements indicate that this set-up probably allows an upgrade to more than two IF channels.

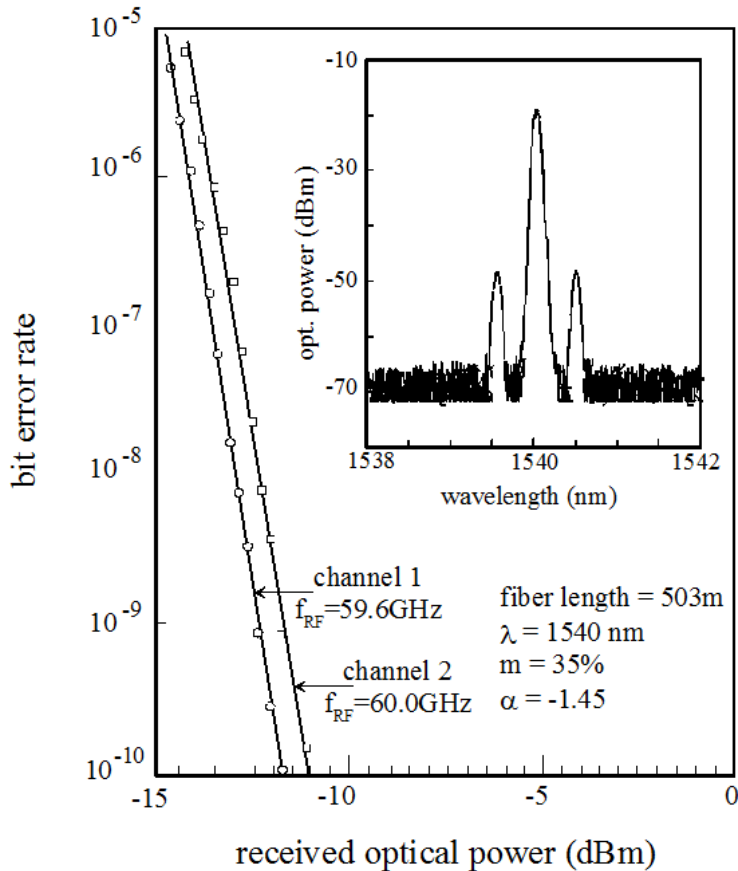


Fig. 3.7 BER versus received optical power and optical DSB spectrum.

The above experiment reveals that for a 60 GHz modulation frequency a maximum fiber length of 1409 m can be achieved for low error rate transmission ( $\text{BER} = 10^{-10}$ ) using non-dispersion standard SMF. This length is achieved without the need for any dispersion compensation technique or more complex modulation formats and this length is also expected to be sufficient not only for most indoor or inter-building applications, but also for broadband wireless application scenarios in mobile backhauling. However, other applications might require much longer fiber spans and thus, from a general system's point of view, it is necessary to predict the fiber length at which the received power is attenuated by a certain figure as compared to the case of no dispersion. Usually, a 3 dB penalty in the received electrical power is taken as reference. For determining this dispersion induced 3dB power penalty  $DIPP_{\text{DSB}}$  for a chirped optical DSB signal with a carrier frequency  $f$ , it can be generally stated that

$$P_{el}(f) \sim i_{ip}^2(f) \sim P_{opt}^2(f) \sim I_f^2. \quad (37)$$

Using eqs. (34) and (39), the  $DIPP_{DSB}$  can be expressed as

$$DIPP_{DSB} = 20 \cdot \log \left\{ \sqrt{1 + \alpha^2} \cdot \cos \left( \frac{\pi \lambda^2 D L f^2}{c} + \arctan(\alpha) \right) \right\}. \quad (38)$$

Using the following identity

$$\sqrt{1 + \alpha^2} \cos(\arctan(\alpha)) = 1, \quad (39)$$

the length of the fiber  $L_{3dB}$  after which the received electrical power  $P_{el}(f)$  at the carrier frequency  $f$  suffers a dispersion induced power penalty of 3dB can be determined to be:

$$L_{3dB} \cdot f^2 = \frac{c}{\pi \lambda^2 D} \left[ \arccos \left( \frac{1}{\sqrt{2} \cdot \sqrt{1 + \alpha^2}} \right) - \arctan(\alpha) \right]. \quad (40)$$

From the above equation, the fiber length causing a 3 dB power penalty when transmitting chirped 1.55  $\mu\text{m}$  optical DSB signals via standard SMF with dispersion  $D = 17 \text{ ps/nm/km}$  are indicated versus the carrier frequency. As can be seen from Fig. 3.8, for chirp free ( $\alpha = 0$ ) optical 60 GHz DSB signals the maximum fiber length is about 500 m. When the signal is pre-chirped ( $\alpha < 0$ ), e.g. by an EAM operating closer to the excitonic resonance, longer fiber spans up about 2 km are possible. For positive chirped ( $\alpha > 0$ ) DSB signals, which is the usual case in normal fiber-optic RF transmission systems using standard MZM direct modulated lasers, the maximum fiber length is significantly reduced, down to below 100 m for  $\alpha = 2$ . This once again clearly shows the importance of considering the chirp-value when designing a fiber-optic RF transmission link.

As already stated above, fiber lengths of several 100 meters are sufficient for many applications including mobile backhauling, but for applications calling for much longer spans, either dispersion compensating techniques or more dispersion tolerant modulation formats must be applied, such as optical double sideband with suppressed carrier (DSB-SC) modulation. The next section will discuss the dispersion induced penalties for DSB-SC optical modulation.

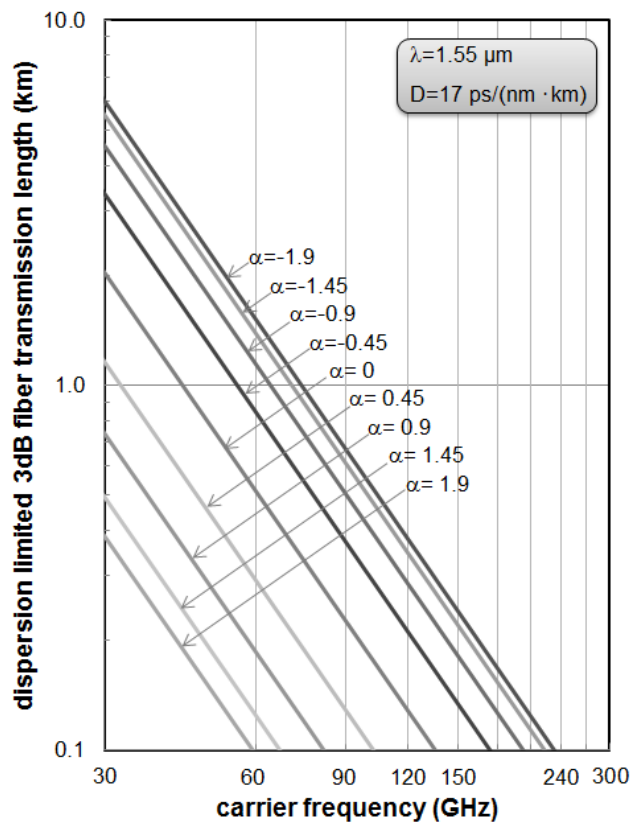


Fig. 3.8 Dispersion limited (3dB penalty) SMF transmission length for chirped mm-wave modulated (DSB) optical signals at  $1.55 \mu\text{m}$  wavelength.

### 3.2.2 Optical double sideband signals with suppressed carrier (DSB-SC)

In the previous section, it has been theoretically and experimentally demonstrated that the output intensity in an IMDD fiber-optic link with DSB modulation varies with the cosine of the RF frequency squared and the fiber length squared. This is due to the fiber's chromatic dispersion and it leads to significant restrictions in the fiber length, e.g. for a chirp free modulation the first cancellation already occurs at around 500 m of standard SMF. Although the length can be extended to a few kilometers [118], the length limitation is not acceptable in many applications including mobile backhauling and other outdoor wireless applications (see chapter 5).

Physically, the observed power fluctuations in an IMDD link can be explained from the frequency spectrum of a DSB-SC signal. The two RF beating products (lower sideband with carrier and carrier with upper sideband) propagate at different speeds through standard SMF

because of chromatic dispersion. When being detected, they cancel out each other whenever the phase difference gets an odd multiple of  $\pi$ . This is why at certain fiber lengths and modulation frequencies, substantial power penalties occur, as can be seen from Fig. 3.6.

According to the above discussion, it would thus be beneficial generating an optical double-sideband signal that has no optical carrier in order to cope with fiber dispersion. This way, only one beating product exists (lower sideband to upper sideband). Assuming complete carrier suppression, the Fourier coefficients according to eq. (30) can be expressed as

$$\begin{aligned}\underline{A}_{-1} &= \sqrt{I_0} m \frac{(1+j\alpha)}{2} \\ \underline{A}_0 &= 0 \\ \underline{A}_{+1} &= \sqrt{I_0} m \frac{(1+j\alpha)}{2}\end{aligned}\tag{41}$$

and the propagation constants of the lower and upper sidebands are

$$\begin{aligned}\beta_{-1} &= \beta_0 - \frac{2\pi f}{v_g} - \frac{\pi\lambda^2 D p^2 f^2}{c} \\ \beta_{+1} &= \beta_0 + \frac{2\pi f}{v_g} - \frac{\pi\lambda^2 D p^2 f^2}{c}.\end{aligned}\tag{42}$$

The output intensities can then be determined according eq. (33) to be

$$\begin{aligned}I_f &= \frac{1}{2} \Re \left\{ \underline{A}_0 \cdot \underline{A}_{-1}^* \cdot e^{j(\beta_0 - \beta_{-1})L} + \underline{A}_0 \cdot \underline{A}_{+1}^* \cdot e^{j(\beta_{+1} - \beta_0)L} \right\} = 0 \\ I_{2f} &= \frac{1}{2} \Re \left\{ \underline{A}_{-1} \cdot \underline{A}_{+1}^* \cdot e^{j(\beta_{+1} - \beta_{-1})L} \right\} = \frac{1}{2} \Re \left\{ I_0 m^2 \frac{1-\alpha^2}{4} \cdot e^{j(\frac{4\pi f}{v_g})L} \right\}.\end{aligned}\tag{43}$$

From eq. (43) one can firstly observe that the intensity at the modulation frequency  $f$  becomes zero. Secondly, for de-correlated optical signals, i.e. for incoherent detection, the exponential term in eq. (43) can be neglected and thus, the output intensity at the spectral component with twice the modulation frequency becomes a constant. It does neither depend on the modulation

frequency nor on the fiber length. In other words, no dispersion penalties are observed in IMDD links employing DSB-SC modulation with strong carrier suppression. A similar derivation could be made for optical single sideband (SSB) modulation.

### 3.2.3 Optical combs

There exist several techniques for generating optical combs, i.e. an optical signal consisting of multiple longitudinal modes with a constant beat frequency between the longitudinal modes. An all-optical technique to generate an optical comb that has been used in this work and was described in section 2.1.2 is to use a passive mode-locked laser diode (MLLD). Generally, i.e. independent of the generation approach, it can be stated that due to chromatic dispersion, each mode runs at a different speed through optical fiber and consequently, all the beat notes exhibit different phases after being transmitted, which results in power fluctuations with respect to fiber length or beat note frequency. To study this in more detail, it is necessary to theoretically describe the output electrical field of an MLLD. As has been shown in [60], the electrical field of a MLLD can be expressed as

$$\underline{E}(t) = \sum_p \hat{E}_p \cdot e^{j\{2\pi(\frac{c_0}{\lambda_0} + p \cdot f_{RF}) + \phi_p\}}, \quad (44)$$

where  $\lambda_0$  is the highest optical wavelength,  $\hat{E}_p$  is the amplitude of the  $p^{\text{th}}$  longitudinal laser mode, and  $\phi_p$  is the relative phase of the  $p^{\text{th}}$  mode. The difference frequency between the longitudinal modes, i.e. the free-spectral range of the MLLD, is denoted as  $f_{RF}$ . Assuming that the longitudinal modes have the same polarization (which usually is the case) and further assuming TEM modes, we can state from eq. (4) that the optical intensity is proportional to

$$I_{opt} \approx \Re\{\vec{E} \times \vec{H}^*\} \approx \Re\{\vec{E} \times \vec{E}^*\}. \quad (45)$$

Thus, the generated photocurrent at the fundamental beat frequency  $f_{RF}$  is given by

$$i_{ph}(f_{RF}) = \eta_{OE,RF} \cdot \sum_{p+1} \hat{E}_p \hat{E}_{p-1} \cdot e^{j(2\pi \cdot f_{RF} + \Delta\phi_{p,p-1})}, \quad (46)$$

where  $\eta_{OE,RF}$  denotes the opto-electrical conversion efficiency at the beat frequency  $f_{RF}$ , while  $\Delta\phi_{p,p-1}$  is the phase difference between the  $p^{\text{th}}$  and  $(p-1)^{\text{th}}$  longitudinal mode. As was shown in section 3.2.1 (see especially eq. (31)), each longitudinal mode exhibits another relative phase after propagation through a dispersive fiber. Consequently, the phase of the different beat notes  $\Delta\phi_{p,p-1}$  varies depending on e.g. the fiber length and chromatic dispersion (see eq. (31)). Therefore, during the heterodyne detection process in the photodiode, some beat notes might be in phase with others whereas others might be out of phase, thus interfering destructively. As the total power converted from a mode-locked laser source is obtained thanks to the beating of all the couples of optical modes having a beat frequency  $f_{RF}$  during the photodetection process, it is clear that if there is a phase difference between the optical modes it will also affect the electrical beat notes and thus the power of the sum of all the beat notes. If the phase dispersion in the optical spectrum is compensated using the group index dispersion of an optical fiber, it is possible to minimize the phase dispersion between all the electrical beat notes and hence to maximize the generated power at the fundamental beat frequency  $f_{RF}$ .

To demonstrate this, the electrical power at the output of a photodetector was measured using a mode-locked laser as input signal to the photodetector. Here, the electrical power was measured using an Agilent E4448A ESA coupled to a V-band (50-75 GHz) HP 11974V preselected harmonic mixer. The measurements were performed after propagation through different lengths of standard single-mode fiber. The results of these measurements are presented in Fig. 3.9 (squares).

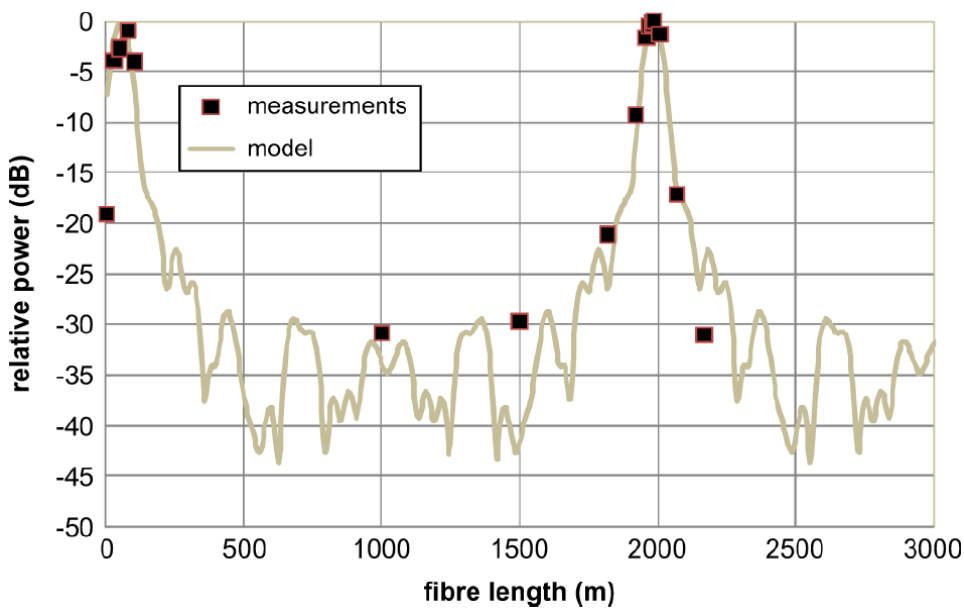
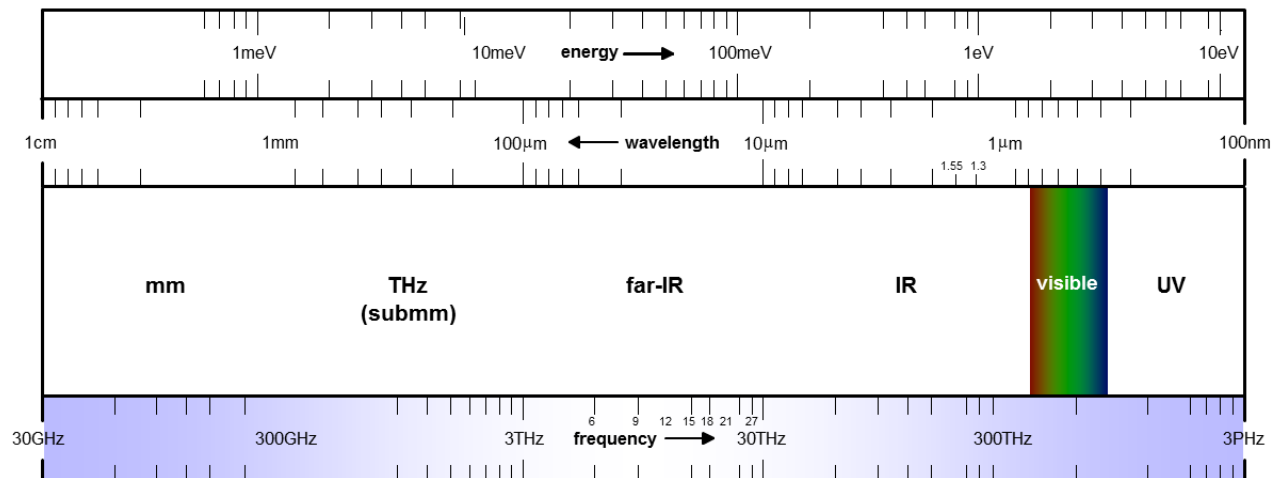


Fig. 3.9 Corrected photodetected electrical power as a function of fiber length.

It can be seen that it is possible to increase the electrical power generated by detecting the MLLD's output signal by about 20 dB just by adding 78 m of standard single-mode optical fiber. This way, the phase difference between the different beat modes is compensated up to a certain extent, resulting in a significantly higher output power. However, the above experiment also shows that when transmitting optical combs with a free-spectral range in the millimeter-wave region, the fiber length must be carefully designed to achieve optimum performances.

## 4 Photonic Millimeter-Wave and THz Transmitter and Transceiver

Today, the term terahertz is commonly applied to sub-millimeter-wave (submm-wave) energy that fills the wavelength range of 1000 - 100  $\mu\text{m}$  (300 GHz - 3 THz). Below 300 GHz, we enter into the millimeter-wave (mm-wave) regime covering the wavelength region of 10-1 mm (30-300 GHz). Beyond 3 THz and up to 30 THz (100-10  $\mu\text{m}$ ) we enter the far-infrared (far-IR), but the exact border between sub-millimeter and far-infrared is still rather blurred since the frequency range between 3 and 10 THz is a more or less unclaimed territory. Above 30 THz there is the infrared region covering the wavelength span between 10 and 1  $\mu\text{m}$  (frequency 30 - 300 THz). In Fig. 4.1, the commonly assigned terms for the various frequency bands of the electromagnetic spectrum between 30 GHz and 3 PHz are indicated.



*Fig. 4.1 The electromagnetic spectrum between 30 GHz and 3000 THz. The term THz region is commonly applied to the submm-wave frequency range which extends from 300 GHz up to about 3 THz.*

So far, the mm-wave and the submm-wave or THz frequency regimes have been of interest for some more or less niche applications requiring such high frequency ranges. Today, however, we notice a significantly increasing interest in mm-wave and THz technologies. This has last but not least been stimulated by some recent space and earth exploration experiments such as the Atacama large millimetre array (ALMA) telescope project [119]. Yet today, with the evolution of mm-wave and THz technology, more and more key applications with potentially large market volumes appear on the horizon, some are even already in the phase of being regulated and standardized. This includes communication applications such as 60 GHz broadband short-range wireless (IEEE 802.3c), 100 Gb/s Ethernet (802.3ba) and even Terahertz communications (IEEE 802.15.THz), but also sensing and imaging applications such as T-ray imaging for security

applications or mm-wave and THz signal generation in instrumentation and aerospace applications. An excellent overview on potential applications – mainly within the THz frequency band can be found in the review paper by *Peter Siegel* [120]. More information on applications can also be found in recent and emerging THz research networks and research projects such as the “Terahertz Science and Technology Network” in the USA, the “THz technology forum” in Japan and in various white papers published by key European projects including “Teranova” and “IPHOBAC”.

However, despite the growing number of new mm-wave and THz applications, the deployment of mature and compact continuous-wave (cw) sources in that frequency range is just beginning to emerge. Consequently, one of the key scientific and technological challenges that must be tackled is the development of ultra-wideband and tunable local oscillators (LO) operating in the mm-wave and THz frequency regimes. When comparing the currently existing high-frequency LO technologies, it is noticed that all electronic solutions such as Gunn diodes, IMPATT diodes, resonant tunneling diodes (RTD) or frequency doublers and triplers are widely used in the microwave and lower mm-wave regions. On the other hand, all optical sources, such as p-doped Ge lasers or Quantum Cascade Lasers (QCLs) are employed in the far-IR, leaving a gap in the higher mm-wave and THz frequency ranges. For this frequency range, there is almost no compact power source available so far. In addition, purely electrical LO sources such as Gunn diodes with subsequent frequency multiplier chains suffer from their poor frequency coverage and limited tunability. To overcome these technological limitations of all-electronic LOs, there has been increasing interest in developing photonic LOs (PLOs) capable of operating in these high-frequency bands. Photonic LOs exhibit a number of unique advantages such as ultra-wideband tunability, compactness and the ability to operate over a broad temperature range. Thus, photomixing has attracted a lot of interest, and according to a recent study initiated by the European Space Agency (ESA), photomixing is considered to be one of the most promising candidates for the generation of mm-wave and THz signals [121].

The recently invented photonic techniques (heterodyning, OIL, OPLL etc.) and technologies (external modulation, MLLD etc.) for the generation of such high-frequency LO signals in the optical domain, as well as the theory of optical heterodyning such signals in a photodiode or photomixer have already been discussed in chapter 2. The transport of such optical mm-wave and THz signals has been elucidated in chapter 3. This chapter will focus on recent achievements in ultra-wideband photonic mm-wave and THz transmitter technologies and will report on some key application oriented demonstrations. Here, the term transmitter shall refer to a high-frequency photodiode or photomixer integrated with some passive or active circuitry, as well as a respective output connector. Depending on the operational frequency range, the output connector might either be a simple coplanar waveguide (CPW) output, a rectangular waveguide (WR) or a

coaxial output connector. Especially for THz transmitter, the output might be realized in form of integrated antenna structures.

#### 4.1 Millimeter-Wave and Terahertz Photomixer

The key component in a high-frequency mm-wave or THz transmitter is the photodiode or photomixer. The most important requirement for this kind of component is a high responsivity at mm-wave or THz frequencies, not necessarily a large 3 dB-bandwidth. The physical effects determining the photomixers high-frequency performances are usually represented by time constants describing the dynamics of the photo-generated carriers. Most important are the transit time and the carrier lifetime. Conventional lumped photomixers are further limited by RC time constants. At very high frequencies ( $>100$  GHz), also electrical wave propagation effects must be considered and further on, propagation losses become more significant.

Looking at the various types of photomixers, the conventional vertically illuminated photomixer, such as the *pn* or the *pin* photomixer, exhibit a tradeoff between quantum efficiency and bandwidth. For short transit times the absorbing layer of a conventional *pn*-PD or *pin*-PD needs to be thin which on the other hand results in a low quantum efficiency and a large capacitance. Thus, the RC time constant is large, preventing conventional vertical PD for having a high quantum-efficiency at very high frequencies.

A promising approach for achieving a high-efficiency at high frequencies is to utilize an uni-travelling carrier (UTC) concept [122]. In the UTC-PD the absorbing layer is p-doped and therefore only the minority carriers, i.e. the electrons, travel across the depletion layer. Due to the much higher drift velocity of electrons and due to the fact that electrons can travel at overshoot velocity, the space charge effect which is dominated by electrons is significantly reduced. This principle allows high-saturation currents. The bandwidth of a UTC-PD is restricted by transit time effects mainly determined by the diffusion time of electrons travelling in the p-doped absorbing layer and of course it is also limited by the RC time constant. Recently, high bandwidths UTC PDs have been demonstrated and in terms of the bandwidth-efficiency product, UTC PDs have been shown to exhibit better performances than conventional pin-diodes [123].

To circumvent the transit time limitation one can also utilize a material with a very short carrier lifetime. For several years, research has been carried out to grow GaAs layers at low temperatures. Due to the low growth temperature, the GaAs layers contain lots of impurities which capture free carriers and thus reduce the carrier lifetime. Recently, low temperature grown

GaAs operating around 850 nm wavelength were utilized for high-frequency signal generation in the THz range [124], work on LT-InGaAs and other LT-materials for  $1.55\mu\text{m}$  is underway.

Edge-coupled or waveguide photomixers can overcome some of the above discussed limitations by enabling longitudinal optical wave propagation perpendicular to the vertical transport of the photo electrical carriers. In principle, this concept allows for a long but narrow absorption layer having both, a low transit time and a high quantum efficiency. On the other hand, the detector's RC time constant becomes significantly large due to the long absorbing layer, leading to the well-known lumped element RC time limitation.

In all approaches discussed above, the RF responsivities are mainly determined by transit time and RC time constants and thus, the photomixers' responsivity decrease with frequency with  $f^4$ . To overcome the RC time limitation of lumped photomixers, distributed or travelling-wave type photomixers have been investigated since the early 1990's. In a travelling-wave photomixer the photo-absorption process occurs in a distributed manner along the length of the device such that it contributes to the overall electrical signal in the contact transmission line. Thus, travelling-wave photomixers are not limited by the normal RC time constant since electrically the device is not a lumped element with a concentrated capacitance but an electrical waveguide (typically microstrip or coplanar) with a given characteristic impedance. The responsivity is therefore mainly determined by its transit time and electrical wave propagation losses. Although travelling-wave photomixer exhibit a couple of challenges that need to be solved, they do offer a great advantage: for high power THz signal generation, namely the prospective to independently optimize its quantum efficiency and saturation photocurrent. The various physical effects determining the high-frequency performance of a pin travelling-wave photomixer are discussed in more detail in [125-127].

In the following sections, photonic transmitter modules based upon travelling-wave photomixer structures are reported yielding either quasi optical free space radiation of the generated (sub)mm-wave signals or guided transmission within a coaxial or rectangular metallic waveguide. In detail, broadband (DC-110 GHz), wideband (30 GHz - 0.3 THz), narrow band 0.46 THz slot antenna integrated travelling-wave photomixers and ultra-wideband rectangular waveguide and bow-tie antenna coupled TWPD that enable (sub)mm-wave generation up to 1 THz will be presented.

### 4.1.1 100 GHz broadband travelling-wave photomixer

A sketch of a travelling-wave photodetector (TWPD) or optical heterodyne mm-wave generation investigated is shown in Fig. 4.2. The detector consists of an optical channel waveguide and an electrical transmission line. The optical heterodyne signal launched into the optical channel waveguide is gradually absorbed, resulting in a distributed current generation along the detector's length that contributes to the overall current propagating along the electrical transmission line of the TWPD. The traveling-wave detector differs from a lumped element in a non RC time limited response exhibiting superior high-frequency performances which has recently been demonstrated experimentally [40, 128, 129].

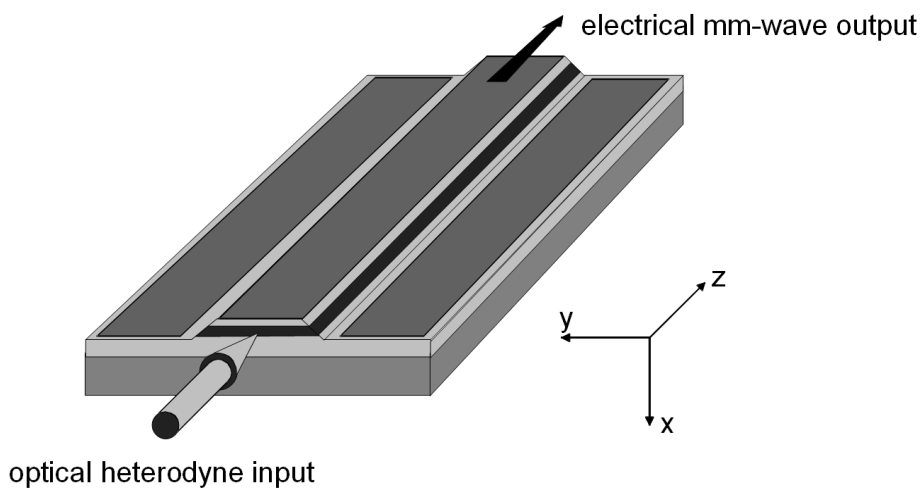


*Fig. 4.2 Schematic diagram of the fabricated  $1.55\mu\text{m}$  TWPD.*

A cross-section including the relevant geometrical parameters of the TWPD layer structure studied in this section is shown in Fig. 4.3. The waveguide structure was grown on InP:S substrate by metal organic vapor phase epitaxy. The optical core is embedded in the intrinsic region of a p-i-n diode. The absorptive region of the optical core consists of a multiple quantum well (MQW) section. A small strain is applied to the wells and the barriers of the MQW section to reduce the splitting of the valence band degeneracy resulting in identical electro-absorption properties for both, the TM and TE modes. This way, the waveguide core of the TWPD exhibits a polarization insensitive absorption coefficient at  $1.55\mu\text{m}$  wavelength. In detail, the waveguide core mainly consists of ten periods of 10 nm 0.3% tensile strained InGaAs quantum wells separated by 9 nm thick 0.2 compressively strained  $1.15\mu\text{m}$  InGaAsP barriers. To increase fiber-to-chip coupling efficiency, the overall thickness of the optical core is increased by transparent  $1.15\mu\text{m}$  quaternary InGaAsP layers adjacent to the MQW-region. The waveguide cladding layers consist of p- and n-doped InP, together with 50 nm of non-intentionally doped InP layers adjacent to the core. The non-intentionally doped InP sections prevent diffusion of the dopants

into the waveguide core and therefore increase the total thickness of the intrinsic region to  $d_i = 409$  nm. On top of the upper cladding a thin p-doped lattice matched InGaAs contact layer finalizes the optical waveguide structure.

The technological realization of the optical waveguide together with the hybrid microstrip/coplanar transmission line consists of a self-aligned etching process and two metallization steps for the p- and n-type ohmic contacts. At first e-beam evaporation of the p-type TiPtAu center contact is performed which is also used as a mask for the subsequent etching processes of the waveguide mesa. Selective wet-chemical etching of the contact layer, the top cladding and the optical waveguide region is performed, followed by the GePtAu metallization to form the n-type ground contact of the electrical waveguide.

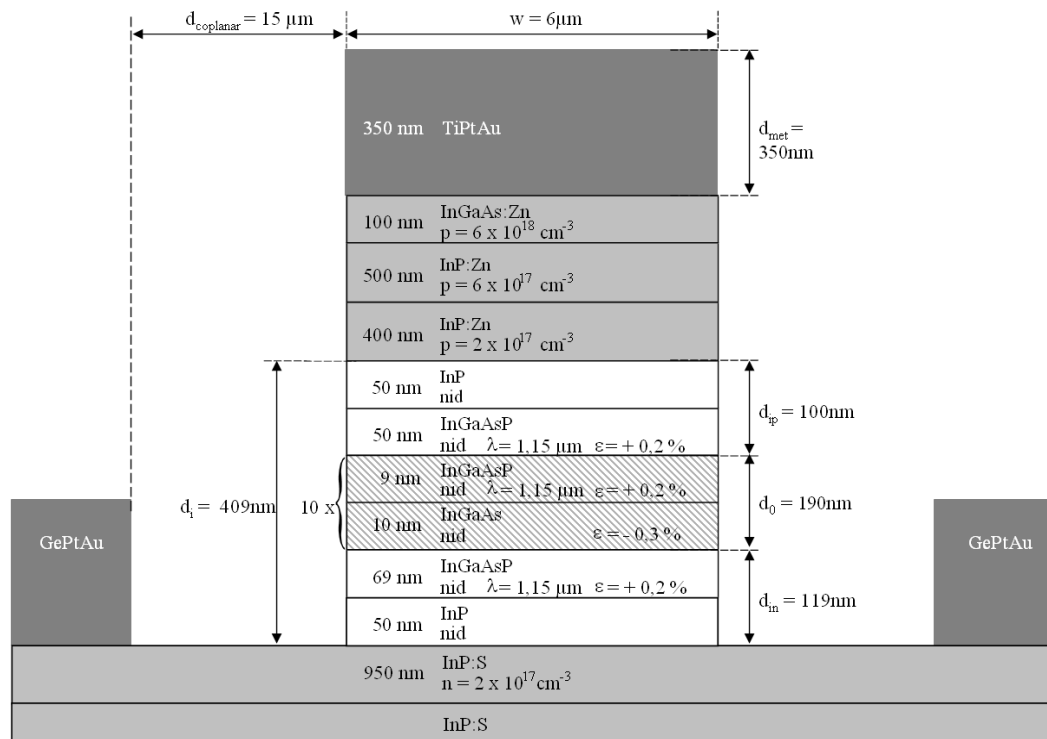


Fig. 4.3 Detailed cross section of the fabricated TWPD.

In order to study the detector's high-frequency limitations and to further improve the design of the TWPD with respect to higher frequency operation, it is inevitable to identify the relevant physical effects limiting the frequency response of the TWPD and to study the impact of design variations on the detector performance. For this purpose a theoretical analysis is developed in the following including all relevant phenomena of the photo-generated carriers, together with optical and electrical wave propagation effects. Recently, several groups reported on theoretical studies

on the high-frequency and high-current limitations of TWPD. A time domain model describing the picosecond pulse response of a TWPD has been reported in [130]. An analytical description of a travelling-wave photodetector in frequency domain can be found in [131]. This model describes the photo-generated current source per unit length and also includes wave propagation effects. However, this work did not consider velocity mismatch effects. Furthermore, the limitation due to the transit time was reduced to a single time constant similar to [122]. Other groups employed frequency domain models using a frequency independent distributed current source per unit length inside the electrical transmission line [132]. The model presented here uses a quasi-static equivalent circuit for the electrical transmission line with a distributed current source which is more accurately as the dynamics of the photo-generated carriers are considered.

At first, a theoretical analysis based upon the carrier continuity equations is used to describe the frequency dependent distributed photo current generated at any point along the detector. This current includes the intrinsic effects such as the transit time limitation due to the propagation through the intrinsic layers. Next, a model based upon the transmission line method (TLM) is used in order to describe the contribution of the distributed photo current to the total electrical power delivered to the load impedance. Limiting effects due to the electrical wave propagation along the hybrid coplanar/microstrip transmission line of the TWPD are included in the TLM model. To verify the reliability of the developed model, the theoretical calculations are compared with the experimental results and the limiting contributions of the different physical effects are identified.

Fundamentally, the photo-generated carrier transport in the TWPD waveguide structure can be described by the continuity equation. By neglecting the transversal carrier transport and assuming harmonic time dependence, the one-dimensional (1-D) complex continuity equations for the electron and hole densities  $n(x)$  and  $p(x)$  are given by

$$j\omega \cdot n(x) = D_n \cdot \frac{\delta^2}{\delta x^2} n(x) - \frac{\delta}{\delta x} [n(x) \cdot v_n(x)] - R_c + G_c \quad (47)$$

$$j\omega \cdot p(x) = D_p \cdot \frac{\delta^2}{\delta x^2} p(x) - \frac{\delta}{\delta x} [p(x) \cdot v_p(x)] - R_c + G_c . \quad (48)$$

The first term in the continuity equations describes the carrier diffusion with the electron and hole diffusion constants represented by  $D_n$  and  $D_p$ . These diffusion constants are functions of carrier velocity and electric field and it has been shown [133] that the carrier diffusion constants get very small in value for high electric fields in excess of 20 kV/cm. Assuming that the typical

thickness of a high-frequency p-i-n detector is well below 1 μm and assuming further that a reverse voltage of a few volts is applied, strong electric fields well above 20 kV/cm occur. Thus, for calculating the photo-generated current we can neglect carrier diffusion in the intrinsic region of the reverse biased TWPD. The second term in eqs. (47) and (48) describes the respective carrier drift in the presence of an electric field with  $v_n(x)$  and  $v_p(x)$  representing the electron and hole velocity, respectively. The carrier recombination rate represented by  $R_c$  can also be neglected for our purposes, since the carrier lifetime in InGaAsP strained MQWs is in the order of a few nanoseconds [134] which is about three orders of magnitude larger than the average transit time of the investigated structure. The last term  $G_c$ , representing the carrier generation rate, is a function of the optical intensity at any point along the detector and it can be determined to be

$$G_c = G_0 \cdot \exp(-\gamma_{opt} \cdot z) \quad (49)$$

with

$$G_0 = \frac{\eta \cdot \lambda}{h \cdot c} \cdot \alpha_{opt} \cdot I_{opt} . \quad (50)$$

Here,  $\eta$  denotes the external quantum efficiency,  $\gamma_{opt}$  is the complex propagation constant of the optical heterodyne input signal and  $I_{opt}$  represents the optical intensity. It should be noted that the carrier generation rate is a function of the longitudinal coordinate  $z$  due to the optical wave propagation determined by the complex heterodyne optical propagation constant  $\gamma_{opt}$ .

Since diffusion can be neglected as discussed above, the electron and hole current densities in the absorbing layer are given by

$$\mathbf{J}_n(x) = -q \cdot v_n(x) \cdot n(x), \quad (51)$$

$$\mathbf{J}_p(x) = -q \cdot v_p(x) \cdot p(x). \quad (52)$$

Here, it is assumed that electrons and holes in the intrinsic region travel at constant saturation velocity  $v_n$  and  $v_p$ , an assumption neglecting carrier escape times, which is valid and appropriate for reverse biased TWPDs with strong internal electric fields. Although there exists some uncertainty about the absolute carrier escape times in reverse-biased MQW structures,

experimental investigations have been published demonstrating that the carrier escape times drastically decrease with the bias field indicating that carrier escape times for strong reverse-biased structures are below 1 ps [135, 136].

Introducing eqs. (49)-(52) into the continuity eqs. (47), (48), we derive two first order differential equations with constant coefficients describing the carrier densities in the absorbing layer

$$\frac{dJ_n}{dx} = -\frac{j\omega}{v_n} \cdot J_n - q \cdot G, \quad (53)$$

$$\frac{dJ_p}{dx} = +\frac{j\omega}{v_p} \cdot J_p + q \cdot G. \quad (54)$$

To solve the above differential equations we make use of the fact that electrons only travel in positive  $x$ -direction and thus, the electron carrier density at  $x = 0$  needs to be equal to zero. Similarly, we can state that the hole current density is equal to zero at  $x = d_0$ :

$$J_n(x=0) = 0 \quad (55)$$

$$J_p(x=d_0) = 0. \quad (56)$$

By using the two boundary values in eqs. (66) and (68), we can solve the differential eqs. (53) and (54) and derive the electron and hole current densities in the absorbing layer:

$$J_n = \frac{q \cdot G \cdot v_n}{j\omega} \left[ e^{-j\omega \frac{x}{v_n}} - 1 \right] \quad (57)$$

$$J_p = \frac{q \cdot G \cdot v_p}{j\omega} \left[ e^{-j\omega \frac{d_0 - x}{v_p}} - 1 \right]. \quad (58)$$

In a similar way, we can now proceed to find the current densities in the adjacent non-absorbing intrinsic layers. For simplicity, we only consider the hole current density in the following, the procedure for deriving the electron current density is similar. Due to the fact that there is no photon absorption in these two layers, the continuity equation for holes eq. (48) becomes quite simple

$$j\omega \cdot p = -\frac{1}{q} \cdot \frac{d}{dx}(J_p). \quad (59)$$

This leads to the following simple differential equation for the carrier density:

$$\frac{d}{dx}(J_p) = \frac{j\omega}{v_p} \cdot J_p. \quad (60)$$

The required boundary values to solve eq. (72) are given by the consistency of the current density at the boundary. From eq. (58) it follows that

$$J_p(x=0) = \frac{q \cdot G \cdot v_p}{j\omega} \cdot \left[ e^{-j\omega \cdot \frac{d_0}{v_p}} - 1 \right] \quad (61)$$

and we derive the hole current density in the non-absorbing intrinsic layer

$$J_p = \frac{q \cdot G \cdot v_p}{j\omega} \cdot \left[ e^{-j\omega \cdot \frac{d_0}{v_p}} - 1 \right] \cdot e^{j\omega \frac{x}{v_p}}. \quad (62)$$

By summing the electron and hole current contributions from the active and the the non-absorptive intrinsic regions, one gains the total photo current per unit length generated at any point  $z$  along the TWPD [127]:

$$i'(z) = \frac{w}{d_{in} + d_{ip} + d_0} \cdot \frac{q \cdot G_0 \cdot \exp(-\gamma_{opt} \cdot z)}{j\omega} \cdot (\Psi_1 + \Psi_2 + \Psi_3 + \Psi_4) \quad (63)$$

with

$$\begin{aligned}
 \Psi_1 &= v_n \cdot \left[ \frac{v_n}{j\omega} \cdot \left( 1 - e^{-j\omega \frac{d_0}{v_n}} \right) - d_0 \right] \\
 \Psi_2 &= v_p \cdot \left[ \frac{v_p}{j\omega} \cdot \left( 1 - e^{-j\omega \frac{d_0}{vp}} \right) - d_0 \right] \\
 \Psi_3 &= \frac{v_n^2}{j\omega} \cdot \left[ 1 - e^{-j\omega \frac{d_{in}}{v_n}} \right] \cdot \left[ e^{-j\omega \frac{d_0}{v_n}} - 1 \right] \\
 \Psi_4 &= \frac{v_p^2}{j\omega} \cdot \left[ 1 - e^{-j\omega \frac{d_{ip}}{v_n}} \right] \cdot \left[ e^{-j\omega \frac{d_0}{vp}} - 1 \right].
 \end{aligned} \tag{64}$$

Here,  $w$  represents the width of the detector and  $d_{in}$  and  $d_{ip}$  are the thicknesses of the intrinsic but non-absorbing layers. Equation (75) not only comprises the carrier transport and generation within the intrinsic absorptive layer of the TWPD, but also the carrier transport through the adjacent non-absorptive intrinsic regions of the waveguide core.

Next, a model describing the contribution of the distributed current source to the overall electrical wave propagating along the transmission line of the TWPD is developed. The type of transmission line formed in this TWPD is a slow-wave hybrid coplanar/microstrip waveguide [137]. Generally, such transmission lines require “full-wave” analysis for rigorous modeling [135]. However, for our purposes the quasi-TEM analysis using a quasi-static equivalent circuit model as shown in Fig. 4.4 satisfactorily describes the millimeter-wave properties of the TWPD transmission line. Here, the photo-generated current per unit length is represented by the current source  $i'(z)$ .  $R'$  and  $L'$  are the resistance and the inductance of the metal center conductor per unit length, respectively.  $R_s'$  represents the semiconductor losses associated with transverse current flow in the doped cladding layers and  $C_i'$  and  $G_i'$  are the capacitance and the conductance of the intrinsic core layer per unit length. The air capacitance which is typically very small in value is neglected. By transforming the current source  $i'(z)$ , we can convert the equivalent circuit into a form where the active current source is parallel to the completely passive electrical transmission line of unit length represented by its characteristic impedance  $Z_0$  and propagation constant  $\gamma_{el}$  [127]. For the transformed current source  $i_0'(z)$  and the relevant microwave properties of the TWPD, we obtain

$$i_0'(z) = \frac{i'(z)}{1 + R_s' G_i' + j\omega C_i' R_s'} = i_0 \cdot \exp(-\gamma_{opt} \cdot z). \quad (65)$$

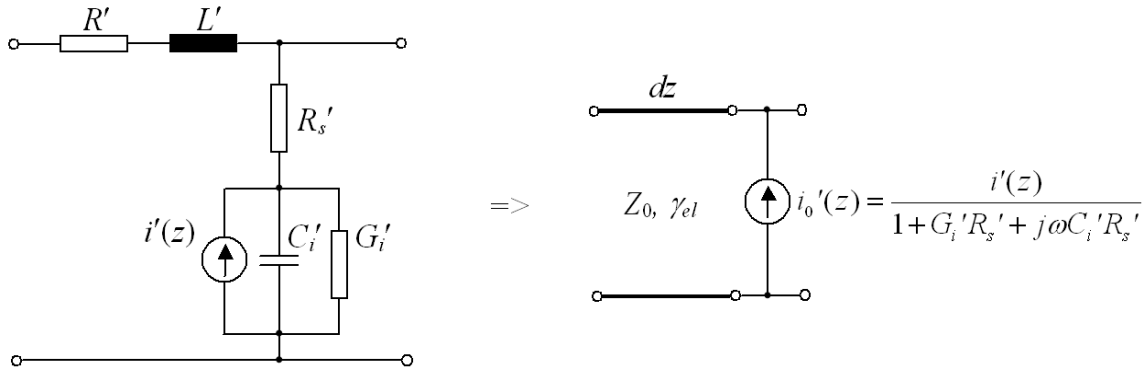
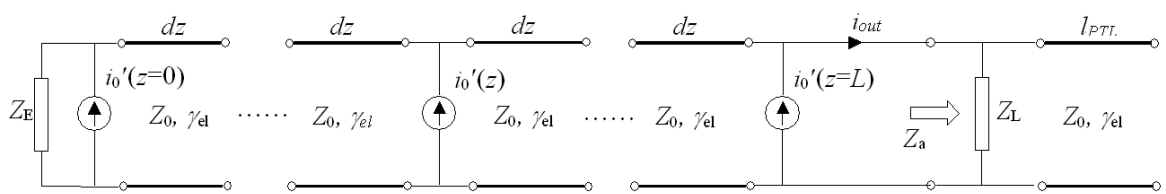


Fig. 4.4 Quasi-static equivalent transmission line circuit for unit length TWPD.

The contribution of the distributed photo-generated current  $i_0'(z)$  at any point of the detector to the overall current propagating along the transmission line can be described by the transmission line model (TLM) as shown in Fig. 4.5. Here,  $Z_E$  represents the impedance at the input port and  $Z_L$  is the load impedance of the coplanar probes at the output port. In order to increase the output power of a travelling-wave PD delivered to the load impedance, it is a fundamental requirement to reduce the mm-wave reflections at the output port. However, in millimeter-wave measurements using commercially available coplanar probes the load impedance  $Z_L$  is fixed to  $50 \Omega$  impedance which is significantly larger than the typical characteristic impedance  $Z_0$  of ultra-high frequency TWPDs of typically  $10 - 20 \Omega$ . To overcome this impedance mismatch in the experiment an open ended long ( $l_{PTL} = 450 \mu\text{m}$ ) passive transmission line with a characteristic impedance  $Z_0$  is used in parallel to the load impedance  $Z_L$ . This way the impedance mismatch at the output port is reduced, keeping in mind that the power delivered to  $Z_L$  is of course not the total power generated by the TWPD.



*Fig. 4.5 TLM model describing the distributed current generation along the TWPD.*

Based on the TLM model, the RF output power delivered to the load impedance  $Z_L$  can be analytically determined by

$$P_{out,el} = \frac{i_0^2 Z_L}{8} \cdot (\Gamma_1 - \Gamma_2 - \Gamma_3) \quad (66)$$

with

$$\begin{aligned} \Gamma_1 &= \frac{1}{\gamma_{el} - \gamma_{opt}} (\exp(-\gamma_{opt}l) - \exp(-\gamma_{el}l)) \\ \Gamma_2 &= \frac{r_a}{(1 - r_a r_e \exp(-2\gamma_{el}l)) \cdot (3\gamma_{el} - \gamma_{opt})} \cdot (\exp(-\gamma_{opt}l) - \exp(-3\gamma_{el}l)) \\ \Gamma_3 &= \frac{r_e}{(1 - r_a r_e \exp(-2\gamma_{el}l)) \cdot (\gamma_{el} + \gamma_{opt})} \cdot (\exp(-\gamma_{opt}l - 2\gamma_{el}l) - \exp(-\gamma_{el}l)) \end{aligned} \quad (67)$$

and with

$$r_e = \frac{Z_E - Z_0}{Z_E + Z_0} \quad (68)$$

$$r_a = \frac{Z_a - Z_0}{Z_a + Z_0} \quad (69)$$

representing the reflection coefficients at the input and output ports, respectively.

The presented frequency domain model allows considering the relevant limiting intrinsic effects, such as transit times limitations and limitations due to propagation effects such as, microwave losses and the mismatch between the optical group velocity and the electrical phase velocity. By applying this model to the investigated TWPD, the contribution of the different effects on the total roll-off at high-frequencies can be identified and the impact of design variations of the high-frequency performance can be studied in detail.

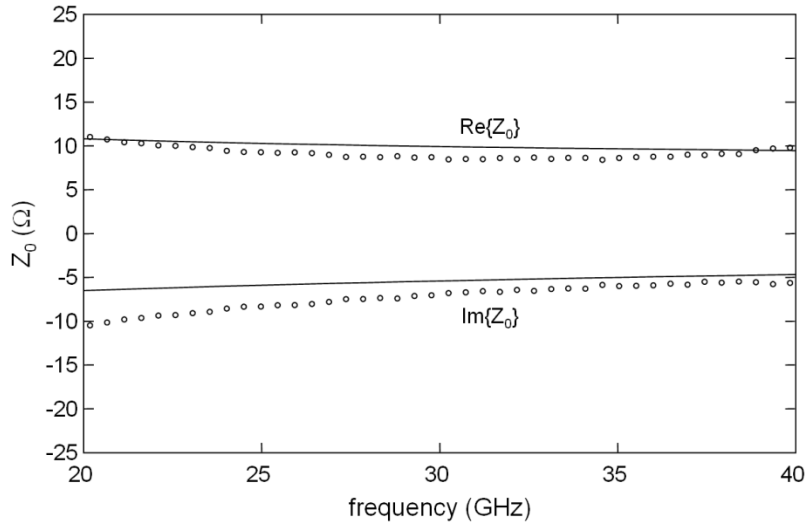


Fig. 4.6 Experimentally (circles) and numerically (solid lines) determined characteristic impedance of the hybrid coplanar/microstrip transmission line.

In order to numerically calculate the generated power, the circuit parameters of the TWPD equivalent circuit must be determined first. Generally, these parameters are frequency dependent but for frequencies in excess of 20 GHz, the parameters  $L'$ ,  $R'_s$ ,  $C'_i$  and  $G'_i$  are considered to be constant. Only  $R'$  increases with the square root of frequency due to the skin effect. In good approximation,  $C'_i$  can be determined by  $C'_i = \epsilon_0 \epsilon_r \cdot w / d_i$ , resulting in 1.7 pF/mm for the investigated TWPD structure. The constant conductor resistance per unit length at frequencies below 10 GHz is given by  $R' = \rho_{Au} / (w \cdot d_{met})$ , resulting in 18.5 Ω/mm. For frequencies in excess of 10 GHz,  $R'$  is considered to increase with the square root of the frequency. The series resistance of the doped semiconductor layers for a 6 μm wide rib waveguide with 15 μm separation between the center and the ground electrode is approximately  $R'_s \sim 0.25 \Omega \cdot \text{mm}$ . The parallel conductance  $G'_i \sim 20 \text{ mS/mm}$  and the transversal inductance  $L' \sim 0.1 \text{ nH/mm}$  were experimentally determined from S-parameter measurements. With all the equivalent circuit parameters known, the complex characteristic impedance  $Z_0$  and the complex electrical propagation constant  $\gamma_{el}$  of the TWPD transmission line can be calculated. The theoretically determined complex characteristic impedance for microwave frequencies is shown in Fig. 4.6 and is compared with experimental values obtained from on-wafer S-parameter measurements. As can be seen, there is

a good agreement between the experimental and theoretical data indicating that the approximations used to determine the equivalent circuit parameters are appropriate.

In Fig. 4.7, the theoretically determined characteristic impedance and the propagation constant are plotted up to 200 GHz millimeter-wave frequency.

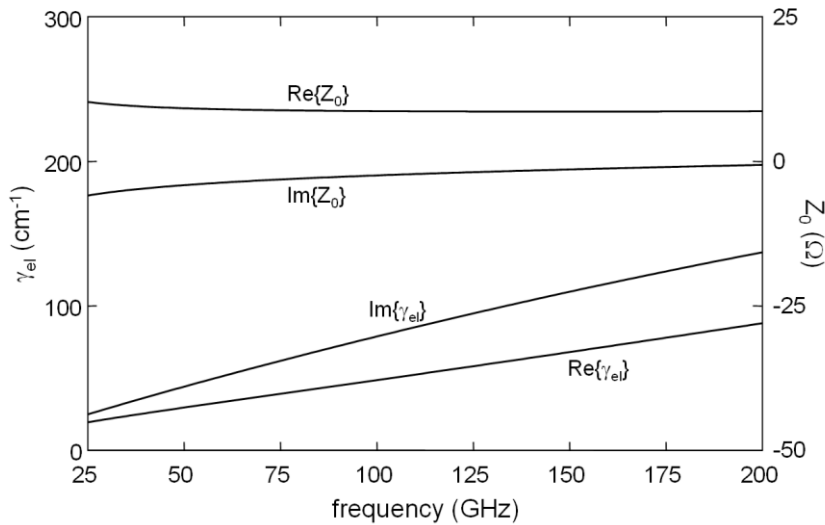


Fig. 4.7 Theoretically determined characteristic impedance and electrical propagation constant of the hybrid coplanar/microstrip transmission line.

For measuring the frequency response of the fabricated TWPD, an optical heterodyne set-up with two 1.55  $\mu\text{m}$  cw laser diodes is used. The beat frequency  $f_{\text{RF}}$  of the generated RF signal can be tuned by varying the wavelength of one of the lasers while keeping the wavelength of the second laser fixed (see also section 2.1). A schematic of the experimental set-up can be found in [40]. The linear polarized optical output signals of two free-running external cavity laser diodes are combined using a 3 dB optical coupler. The polarization state of both lasers is adjusted to each other by tuning the polarization state of the tuned laser using a polarization controller. The combined optical heterodyne signal is amplified by a high-power erbium doped fiber amplifier (EDFA). A variable optical attenuator is employed for performing power dependent measurements. A second polarization controller is used to adjust the input polarization heterodyne optical signal to determine the polarization dependence of the RF output signal. Optical input power to the TWPD is monitored by coupling 5 % of the optical heterodyne signal to a dual-purpose optical spectrum analyzer/power meter. The TWPD is reverse biased, using a DC voltage source with internal current monitoring. A cleaved optical single mode fiber is used for fiber-to-chip coupling. For on-wafer measurements over the wide frequency span up to 160 GHz, different calibrated coplanar probes are used. For frequencies up to 50 GHz the

generated electrical power is directly measured using a mm-wave spectrum analyzer. Measurements at frequencies within the U-, W-, F- and G-band are performed utilizing the calibrated external mixers.

The active waveguide section of the TWPD measured was 50  $\mu\text{m}$  long with a width of 6  $\mu\text{m}$ . The device exhibits a DC responsivity of 0.2 A/W at a reverse bias of 7 V and a maximum breakdown voltage in excess of 9 V. Frequency response measurements were performed keeping a fixed optical wavelength of 1.54  $\mu\text{m}$ , while tuning the other laser towards larger wavelengths. A reverse bias of 7 V was applied to the TWPD and the overall optical input power was set to +15 dBm (+12 dBm per carrier).

The measured frequency response from 25 GHz to 160 GHz is shown in Fig. 4.8. As can be seen, a flat and broadband frequency response is achieved with a total signal roll-off from 25 to 160 GHz of about 10 dB. To our knowledge, this is the first time optical heterodyne cw mm-wave generation using a photodetector is demonstrated up to 160 GHz. The different physical phenomena contributing to the overall roll-off of the TWPD are discussed in detail in section IV.

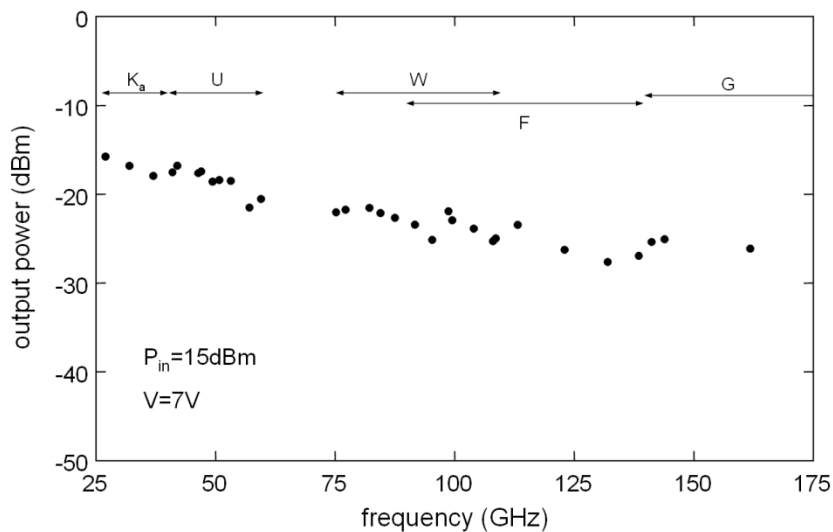


Fig. 4.8 Broadband K<sub>a</sub> to G-band mm-wave generation using the TWPD. The associated frequency bands of the applied coplanar probes and mixers are shown.

In Fig. 4.9, the measured mm-wave output power at a beat frequency of 110 GHz is plotted versus the optical input power. A maximum mm-wave power level of -11.5 dBm is achieved representing the highest mm-wave power level ever reported for 1.55  $\mu$ m waveguide photodetectors. Furthermore, it should be noted that the power delivered to the 50  $\Omega$  probe is measured. The total power generated by the TWPD is about 8 dB larger, as will be explained in the next section. No saturation effects are observed up to electrical power levels of -13 dBm where electrical mm-wave power exhibits the expected quadratic dependence on the optical input power. At electrical power levels in excess of -13 dBm, saturation effects can be observed.

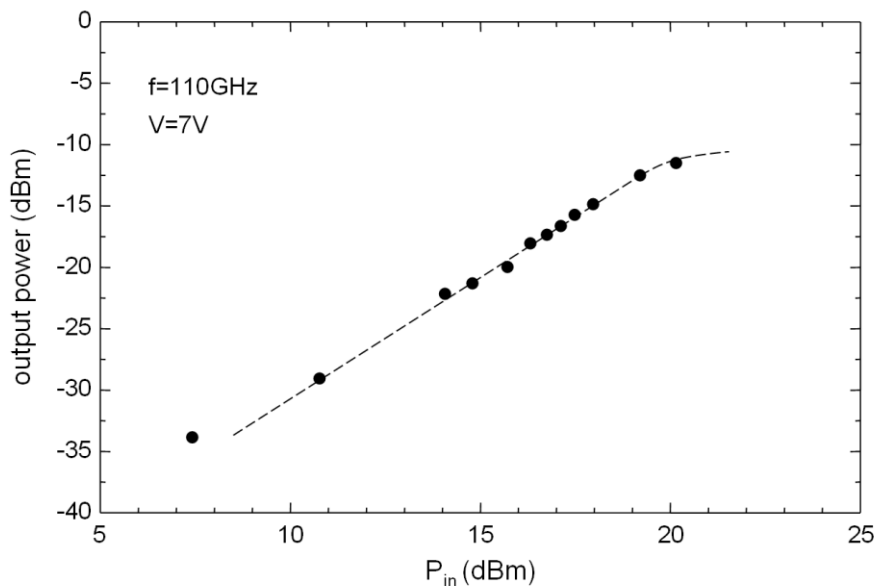


Fig. 4.9 Generated mm-wave power at 110 GHz versus the optical input power.

The power conversion efficiency of the investigated TWPD is bias dependent as can be seen from Fig. 4.10. Here, the measured mm-wave power at a beat frequency of 132 GHz is shown versus the applied reverse bias. Clearly, the generated power gets smaller if the reverse bias is reduced below 4 V. Previous experiments have already shown that the nonlinear saturation behavior of ultrahigh frequency p-i-n photodetectors under high power illumination can be overcome by applying a large external bias [40, 129, 133]. Physically, the nonlinear power dependence is mainly attributed to a reduced carrier velocity in the intrinsic waveguide core of the detector. The photo-generated carriers induce a space charge field reducing or even screening out the applied bias field at low biases and thus resulting in a significantly reduced carrier velocity [133]. According to equations given in [131], the generated space charge field in the investigated TWPD can be estimated to be in the order of 20-30 kV/cm. Thus, for reverse

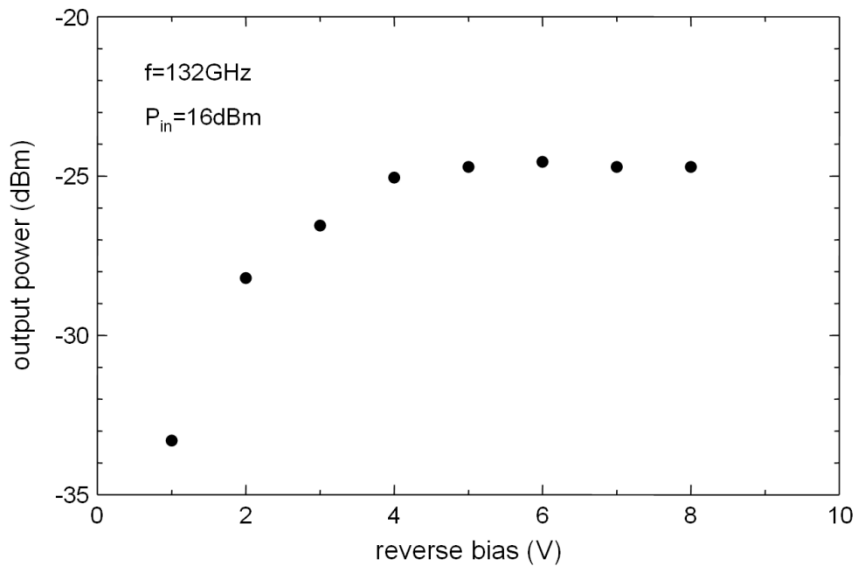


Fig. 4.10 Generated mm-wave power at 132 GHz versus the applied reverse bias.

voltages below 4 V the space charge field screens out the applied bias field, leading to saturation effects due to reduced electron and hole velocities.

Also, the dependence of the conversion efficiency was investigated. For this purpose, the polarization angle of the linear polarized input signal was rotated using a half-wave plate inside the second polarization controller. In Fig. 4.11, the measured mm-wave power at a beat frequency of 132 GHz is shown versus the relative polarization angle of the heterodyne signal. As can be seen, the maximum polarization penalty is only 1.3 dB, which can be attributed to the

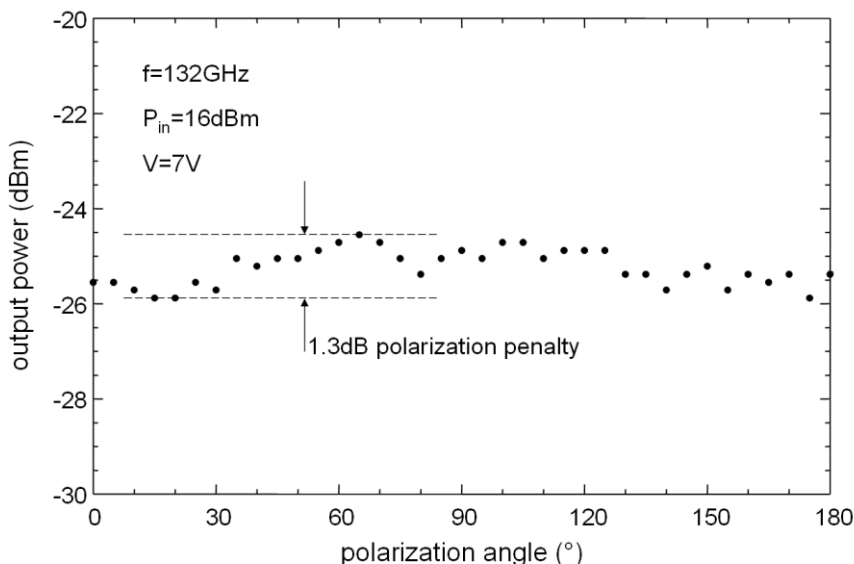


Fig. 4.11 Generated mm-wave power at 132 GHz versus the polarization angle.

polarization insensitive design of the absorption region by using strained QWs as discussed above.

Finally, in Fig. 4.12, the theoretically calculated power delivered to the load impedance  $Z_L$  is compared with the experimental data already presented in Fig. 4.8. The excellent agreement between measured and simulated data with a maximum variation of only 3 dB proves the accuracy and reliability of the analytical model. The total roll-off for a frequency span from 20 GHz to 200 GHz is 13.1 dB. For future design optimizations with respect to a higher electrical output power, it is of great importance to identify the physical reasons causing this roll-off. By identifying the contributions of the different physical phenomena considered in the developed model, we can state that the total roll-off is composed of a 6.5 dB penalty due to transit time effects and a 1.1 dB penalty due to intrinsic effects resulting from carrier transport in the doped sections of the TWPD. The remaining penalty of 5.5 dB originates from propagation effects, namely microwave losses and velocity mismatch. In order to further improve the TWPD performance one has to address primarily the penalty caused by transit time and wave propagation effects. A more detailed discussion on the optimization of the p-i-n TWPD design for high-power (sub-)millimeter-wave generation will be presented elsewhere.

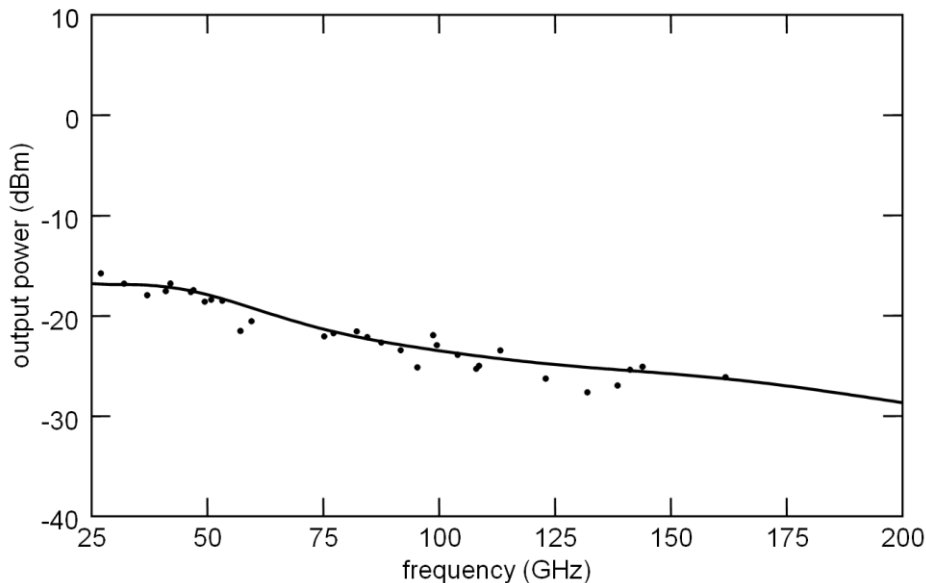


Fig. 4.12 Experimentally (circles) and numerically (solid line) determined broadband mm-wave generation using the TWPD.

As discussed above, the measured and calculated power shown in Fig. 4.12 represents the power delivered to the probe. It does not represent the total power generated by the TWPD. Referring to Fig. 4.7, the absolute value of the characteristic impedance at 110 GHz is  $Z_0 = 9 \Omega$ . Thus, the

total power generated by the TWPD is estimated to be 8.16 dB larger than the measured power delivered to the probes.

#### 4.1.2 300 GHz wideband travelling-wave TW photomixer

In this section, we report on a compact antenna-integrated photonic mm-wave transmitter employing a travelling-wave (TW) photomixer based upon an InP-based pin double waveguide structure.

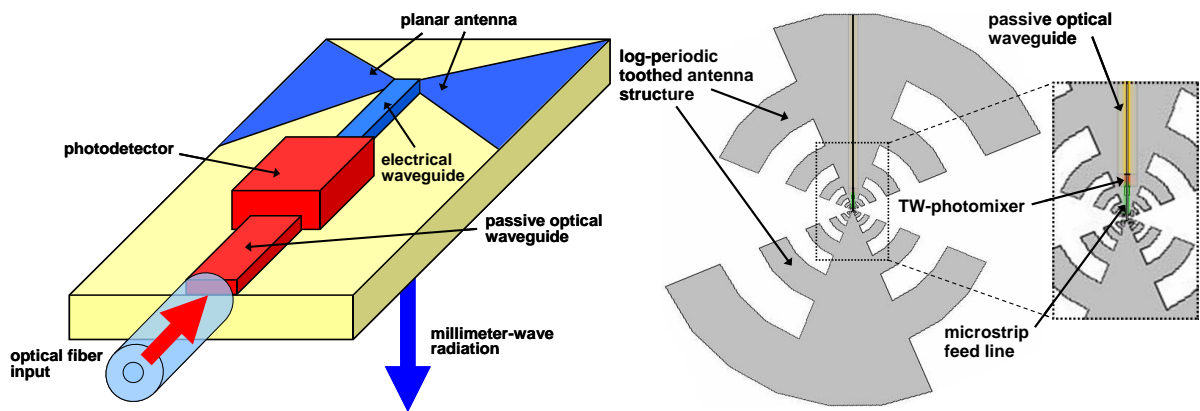


*Fig. 4.13 Operation principle (left hand) and schematic structure of the developed component comprising passive optical waveguide, photomixer, low-loss antenna feed and a broadband LPTA-structure (right hand).*

Fig. 4.13 shows a schematic of the antenna-integrated photomixer. An optical heterodyne signal is coupled via a single mode fiber (SMF) into a passive optical waveguide (POW) which further guides the optical signal to the antenna integrated photomixer operating within the whole mm-wave range (i.e. 30-300 GHz). After photomixing of the optical heterodyne signal, the converted electrical signal is coupled to an electrical coplanar waveguide connecting the photomixer to the feeding point of a planar antenna. Due to the large difference in the dielectric constant between air and semiconductor substrate, the generated mm-wave is mainly (~92 %) radiated through the substrate. For efficient beam-forming and coupling to free-space, an additional hemispherical Silicon lens is used as reported in [138]. To achieve a wide frequency tuning range, the photomixer was integrated with a broadband planar log-periodic toothed antenna (LPTA), as can be seen in Fig. 4.13.

The cross section of the InP layer structure used for the photomixer is schematically shown in Fig. 4.14. Our approach comprises a travelling-wave pin waveguide structure using a partially p-doped absorbing layer and a partially non-absorbing intrinsic layer. This structure, in conjunction with a thin absorber in the drift region, is expected to exhibit high photocurrent saturation without compromising the frequency response [139, 140]. Another key benefit is the applied travelling wave principle which differs from a lumped element in a non-RC time limited response, exhibiting superior high-frequency performances. This was already demonstrated e.g. in [125, 141, 142].

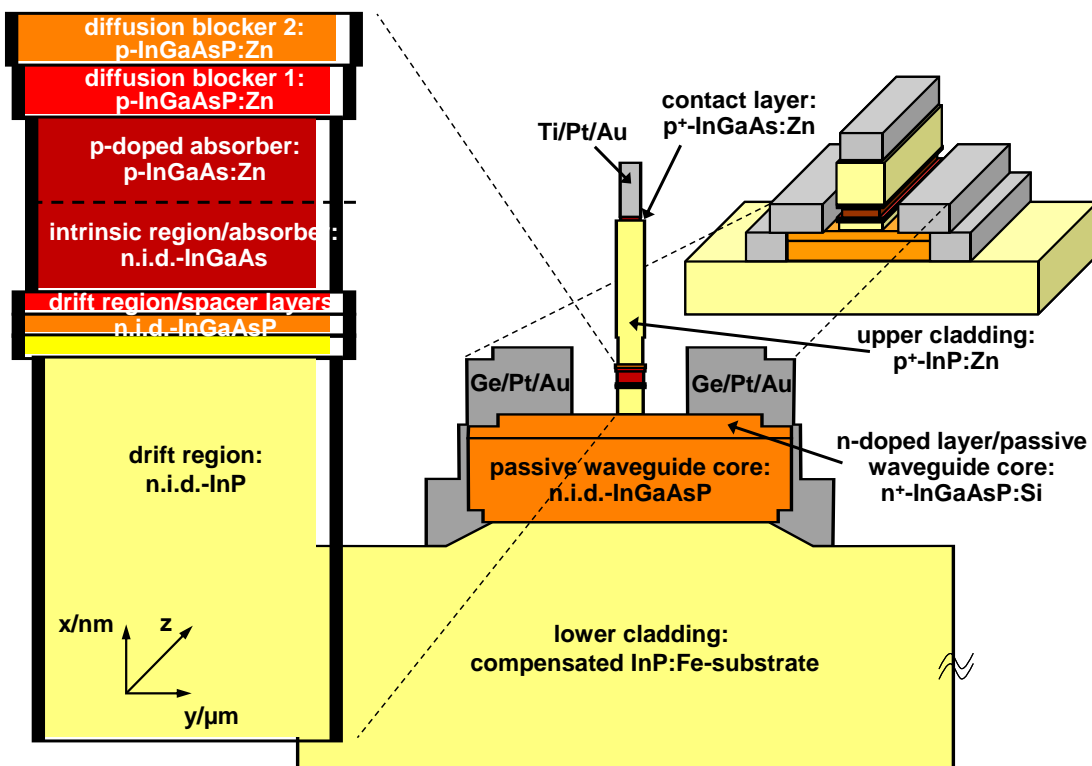
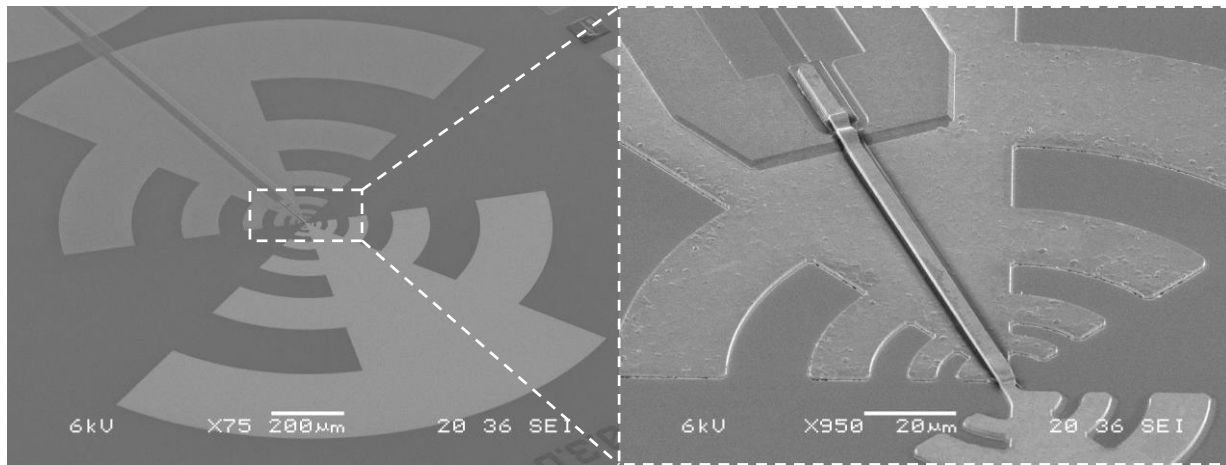


Fig. 4.14 Schematic cross section (middle) of the developed travelling-wave photomixer, enlarged active section (left hand) and 3-dimensional model (right hand).

In detail, the active core consists of a partially p-doped absorbing InGaAs layer (50 nm) and of a non-intentionally doped absorbing InGaAs layer (50 nm). The drift region featuring three InGaAsP spacer layers and the InP layer are located below the intrinsic absorber. The thickness of the non-absorbing InP drift layer is 220 nm.

This layer ensures that the applied field is dropped across the whole drift region. By varying the thickness of this layer, the overlap of the optical mode with the absorber can be adjusted. As a result, a lower overlap factor and thus a longer absorption profile and in turn a more uniform distribution of photo-generated carriers along the length of the active photomixer section is achieved. This reduces saturation effects at the front facet and enhances the overall photocurrent



*Fig. 4.15 SEM-Photographs of the developed photonic transmitter chip. Top view of the fabricated antenna-integrated photomixer (left hand) and close-up view of the center of the LPTA structure with microstrip circuitry, active photomixer section and passive optical waveguide (right hand).*

saturation of the photomixer. For guiding the optical heterodyne signal from the SMF to the active section which is located at the feeding point of the antenna, an additional strip-loaded InGaAsP/InP POW consisting of two InGaAsP layers has been grown underneath the active waveguide which is shown in Fig. 4.13 and Fig. 4.14. BPM CAD simulations were carried out to calculate the overall optical coupling efficiency from a lensed SMF to the active photomixer. Here, it was found that the maximum efficiency is as high as 73%, provided a proper geometrical design is applied. Photoluminescence wavelength for the non-absorbent core was determined to be  $1.21\text{ }\mu\text{m}$  at room temperature which indicates that the photomixer can be operated not only at  $1.55\text{ }\mu\text{m}$  but also at  $1.3\text{ }\mu\text{m}$ .

Fig. 4.15 shows the realized antenna-integrated photomixer comprising of a  $2\times 2\text{ mm}^2$  log-periodic antenna and an approx.  $1\text{ mm}$  long POW for optical feed, extending from the front surface to the active photomixer section. The photomixer, exhibiting a  $100\text{ }\mu\text{m}$  microstrip feed line between the active photomixer section and the antenna center, is positioned close to the antenna center for low electrical losses between photomixer output and antenna feeding point. Calculated results show an input return loss around -20 dB up to 300 GHz for the integrated electrical waveguide circuitry.

The pattern and directivity of the integrated planar LPTAs were studied using FEM and FDTD. It was found that the directivity increases from 8 dBi at 30 GHz up to 25 dBi at 300 GHz and that the input antenna impedance is in the order of  $74\text{ }\Omega$  [138].

For measuring the power generated by the fabricated device from 30-300 GHz, a set of narrow-band waveguide-coupled Schottky diode power detectors (WR22, WR15, WR10, WR8, WR5,

WR3) with attached horn antennas was used. The measured relative frequency response of the fabricated antenna integrated photomixer is shown in Fig. 4.16. As can be seen from that figure, the received power drops only by approximately 16 dB over the full frequency range of 30-300 GHz which is traced back to the travelling wave concept. Additionally, we investigate the polarization dependency between the receiving horn antennas and the transmitter modules. Experimentally, a maximum polarization dependent variation of the output power of 3-5 dB was found.

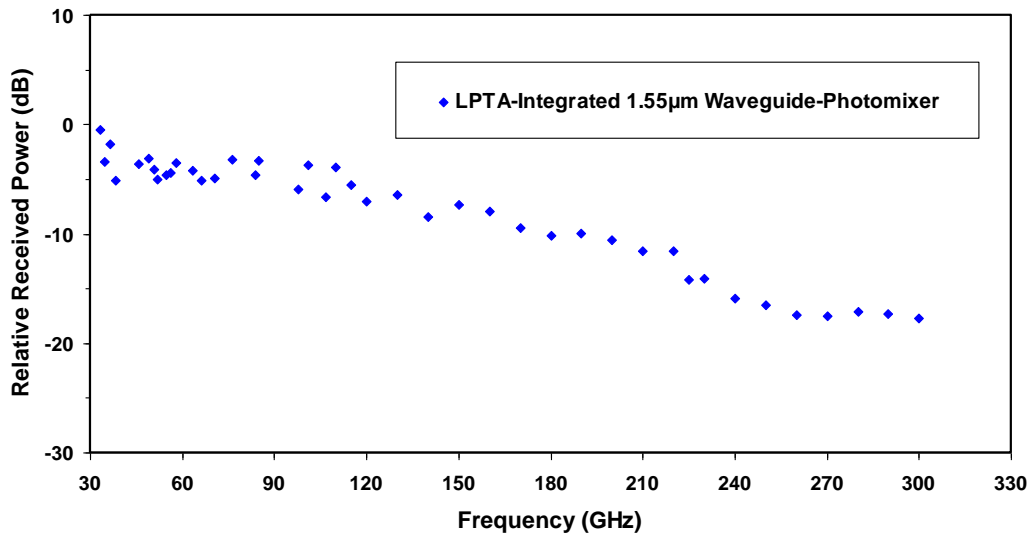
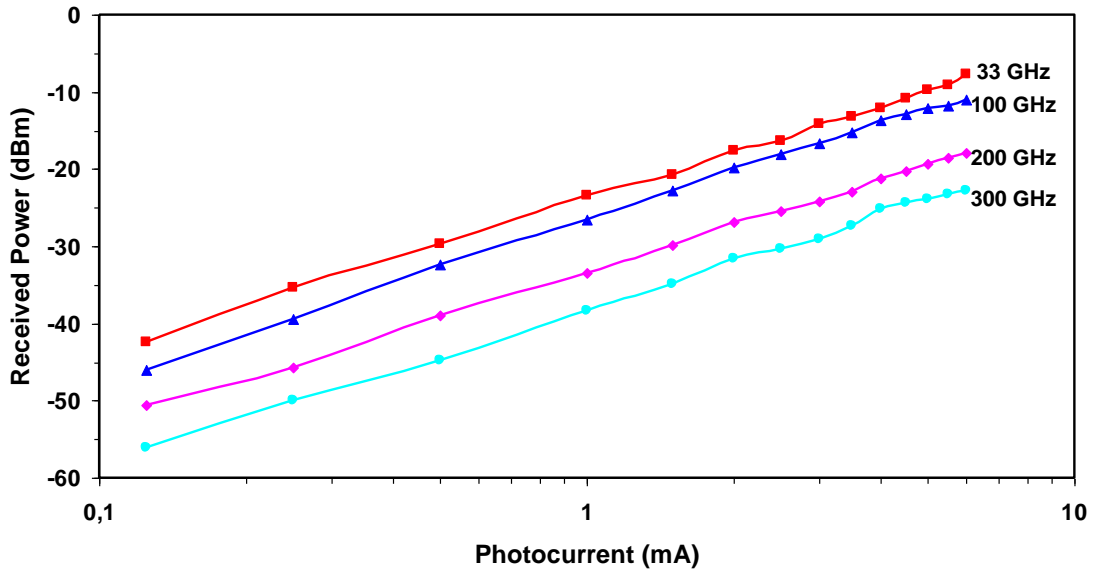


Fig. 4.16 30-300 GHz characterization of the developed photomixer using a set of narrow-band Schottky diode power detectors.

For comparison, all chips were measured at a photocurrent level of only 1 mA. Here, the maximum power received in the Schottky detectors was -23.3 dBm at 33 GHz, -26.6 dBm at 100 GHz, -33.4 dBm at 200 GHz and -38.3 dBm at 300 GHz.

As can be extracted from Fig. 4.23, the received power increases linearly with the photocurrent up to 6 mA. Thus, approx. 15.6 dB higher output power levels are achieved when operating at 6 mA. Currently, the maximum photocurrent is limited to 6 mA due to the POW and a lack of a high-output power EDFA, for PDs without the POW photocurrent levels of 30 mA have been achieved.

For packaging the antenna-integrated photomixer, a quasi-optical transmitter module with an



*Fig. 4.17 High-power chip-level measurements of an LPTA-integrated photomixer at a DC-bias level of -2V and a photocurrent up to -6 mA at 33 GHz, 100 GHz, 200 GHz and 300 GHz.*

SMF input was constructed, comprising techniques for an efficient antenna beam generation, which was already reported in [138]. This module consists of a high-resistive (HR) silicon spacer and a hemispherical HR silicon lens for focusing the generated THz beam and is shown in Fig. 4.18. The package also features two DC pins for biasing the antenna-integrated photodetectors, as well as means to couple the SMF to the POW of the antenna-integrated PD chip.

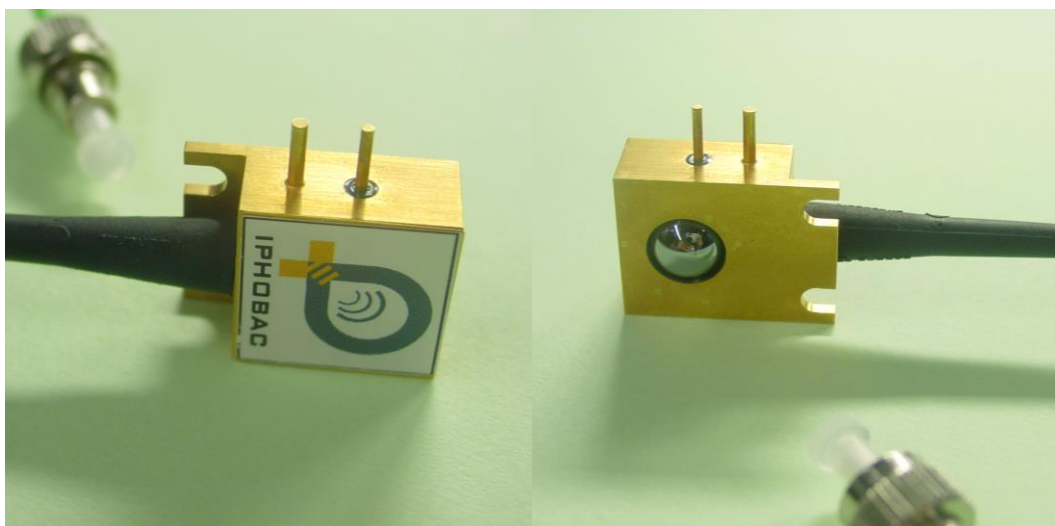


*Fig. 4.18 Top view of a packaged antenna-integrated photomixer (left hand) and bottom view (right hand) showing the quasi-optics for efficient radiation pattern generation.*

### 4.1.3 460 GHz antenna integrated travelling-wave TW photomixers

This section reports on an integrated resonant 460 GHz photonic transmitter module employing an ultra-broadband travelling wave (TW) waveguide InP photodetector which is monolithically integrated with a resonant dipole antenna. Optical heterodyne submm-wave generation at 460 GHz is experimentally reported. At first, the configuration of the monolithically integrated photonic transmitter chip and the hybrid transmission module is described. Next, the ultra-broadband performance of the developed  $1.55\text{ }\mu\text{m}$  photodetector is experimentally investigated and finally, the classical solid state Gunn oscillator and tripler chain of an astronomical

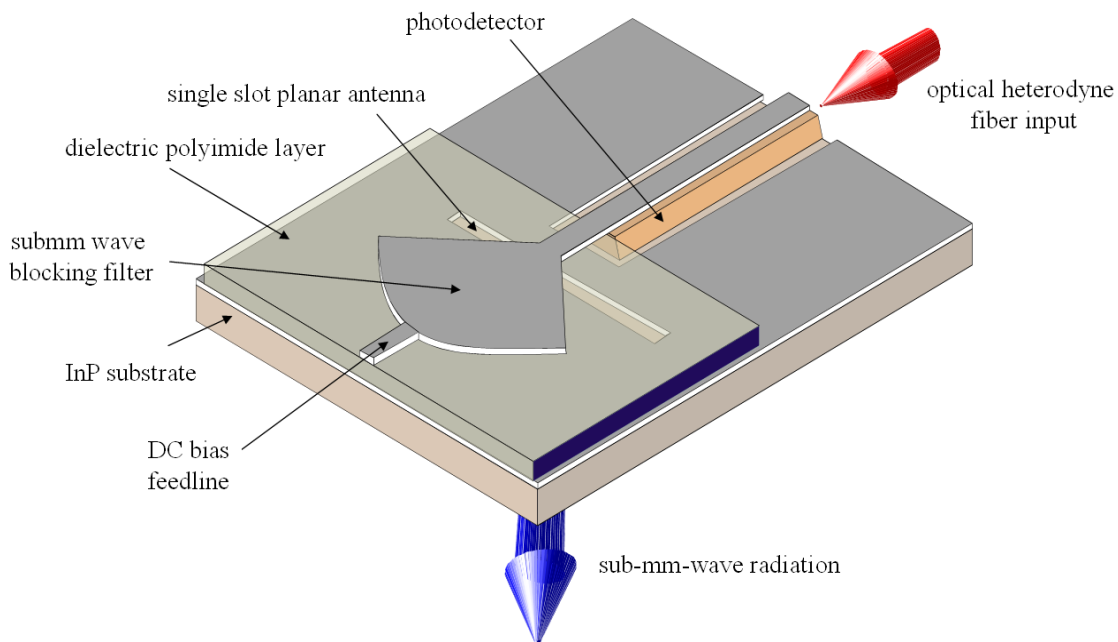


*Fig. 4.19 Schematic drawing of the integrated 460 GHz photonic transmitter.*

heterodyne receiver is completely replaced by the photonic transmitter module. In the experiment, the photonic module is used to generate a 460 GHz submm-wave local oscillator (LO) signal which is further utilized to pump the superconductor-insulator-superconductor (SIS) junction of the astronomical receiver. It is shown that the photonic transmitter module meets the LO power requirements for such an astronomical receiver.

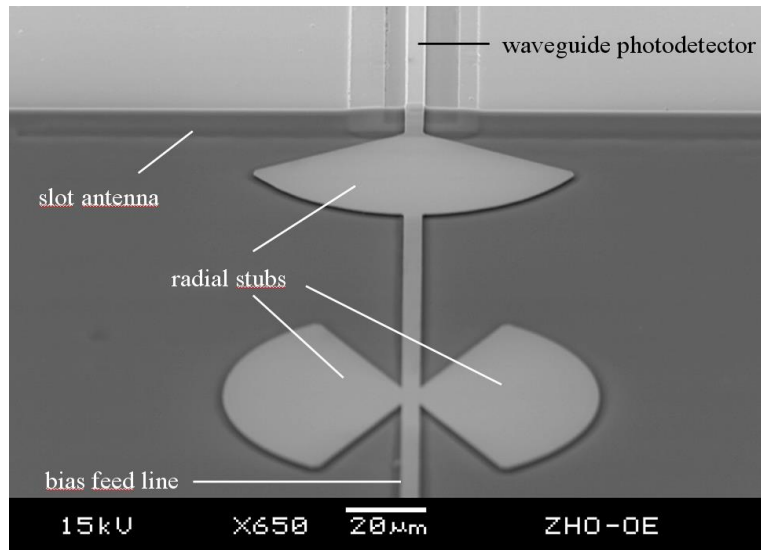
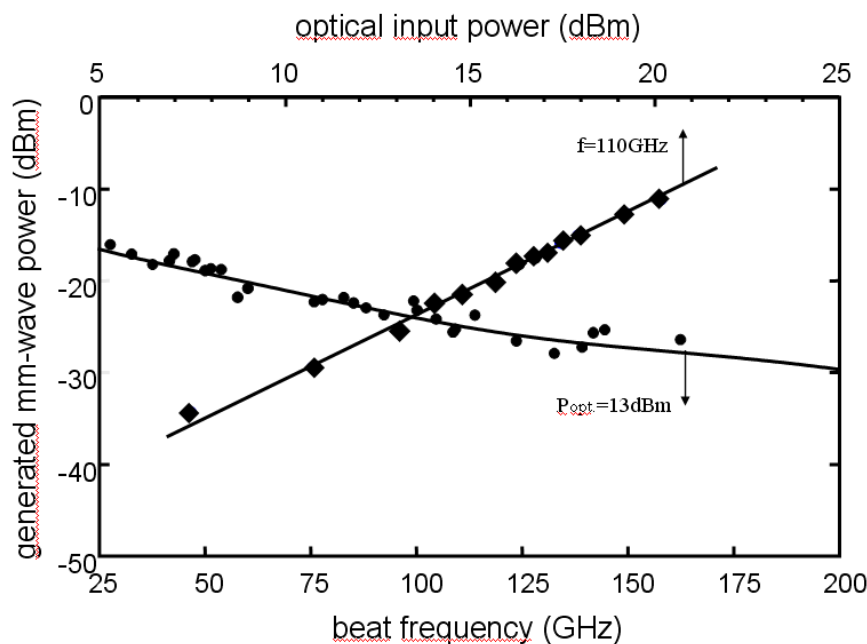


Fig. 4.20 SEM picture of waveguide photodetector with integrated slot antenna and bias-T circuitry.

A sketch of the integrated photonic transmitter module is shown in Fig. 4.19. The module contains an ultra-broadband waveguide InP-based TW photodetector designed for operation at  $1.55 \mu\text{m}$  wavelength which is similar to the photodetectors presented in the sections above. The InP-based waveguide structure of the *p-i-n* detector consists of a quaternary InGaAsP passive core and a 100 nm thin ternary InGaAs absorbing layer adjacent to the p-doped top InAlAs cladding layer. The bottom cladding layer was realized using an n-doped InP layer. The waveguide photodetector was monolithically integrated with a planar full-wave slot antenna resonant at 460 GHz. Furthermore, a passive bias-T was integrated employing radial stubs as low-pass filters. The SEM picture in Fig. 4.20 shows a top view of the waveguide photodetector with the integrated planar slot antenna, as well as the radial stubs and the bias feed line. Finally, the integrated photodetector chip was mounted on a hemispherical silicon lens with a diameter of 10 mm. This lens couples the antenna to free space, producing a near Gaussian submm-wave beam that can be re-imaged on any receiver optics. Details on the antenna geometry, bias-T circuitry and mixer block will be presented elsewhere.

The frequency response of the TW photodetector was characterized using an experimental set-up for optical heterodyning. A description of the set-up, allowing for frequency response measurements up to 170 GHz, can be found in [125]. For those measurements, cleaved rib waveguide detectors without antenna and bias-T were fabricated and tested using commercial coplanar on-wafer probes to contact the detectors. The length and width of the investigated devices were 50  $\mu\text{m}$  and 6  $\mu\text{m}$ , respectively. The detector exhibits a DC responsivity of 0.2 A/W at a reverse bias of 7 V and a maximum breakdown voltage in excess of 9 V.



*Fig. 4.21 Generated mm-wave power versus beat frequency and versus optical input power at a beat frequency of 110 GHz.*

Fig. 4.21 shows a typical broadband frequency response from 25 GHz to 160 GHz with a total signal roll-off of about 10 dB between 25 and 160 GHz. It also shows the measured mm wave output power at a fixed beat frequency of 110 GHz versus the optical input power. The maximum mm wave power level achieved is as high as -11.5 dBm. It should be noted that the measured power levels only indicate the power delivered to the coplanar 50  $\Omega$  probe. Due to the impedance mismatch between the electrical characteristic impedance of the photodetector ( $Z_{PD} = 9 \Omega$ ) and the probe we expect the total power generated by the TWPD to be about 8 dB larger [125].

Fig. 4.22 shows the photonic LO configuration in which the photonic transmitter module is used to pump an astronomical 460 GHz SIS-receiver. Two semiconductor lasers with a beat frequency of 460 GHz are used for optical heterodyne generation of the sub-mm signal in the photonic transmitter. The silicon lens transforms the sub-mm signal into a near Gaussian beam that is imaged on the receiver optics (lens and horn) and the SIS junction. All receiver components are at liquid helium temperature. For comparison, a 460 GHz solid state oscillator chain consisting of a Gunn oscillator with a subsequent tripler was first used to pump the SIS-junction. The output power of the solid state oscillator was adjusted for optimum sensitivity (i.e. lowest noise temperature) of the SIS-receiver, and the corresponding DC bias curve of the SIS-junction was recorded (solid line in Fig. 4.23). Hereafter, the solid state oscillator signal was replaced by the LO signal generated by the photonic transmitter module. Different DC bias curves of the SIS-junction were recorded as a function of laser input power level, i.e. as a function of the detector's photocurrent. As can be seen from Fig. 4.23, for a photocurrent of about 20 mA the sub-mm

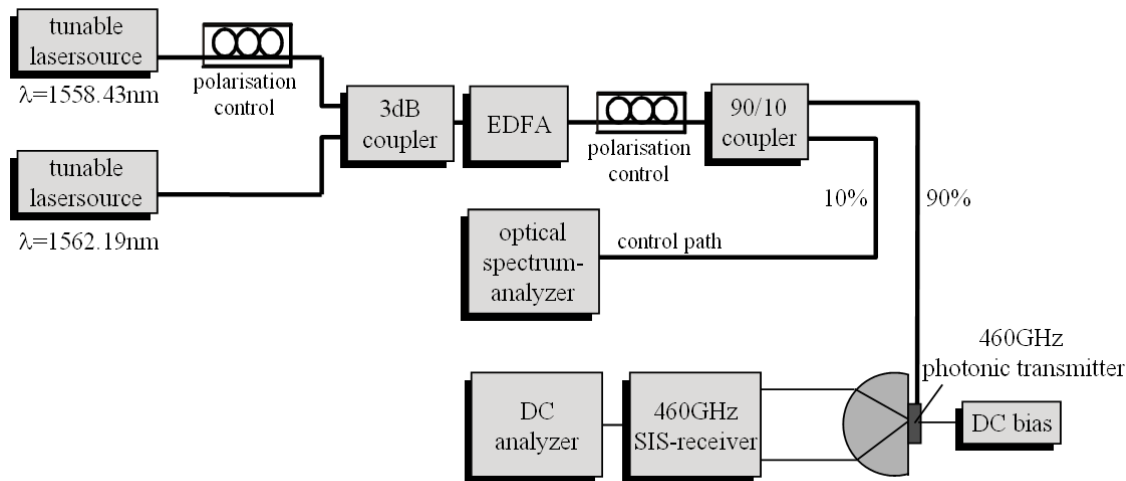


*Fig. 4.22 Set-up for 460 GHz sub-mm wave generation and transmission into the SIS-junction of an heterodyne astronomical receiver.*

wave power generated by the photonic LO is sufficient for optimal pumping of the SIS-junction. Thus, the developed photonic transmitter fulfills the power requirements of a local oscillator for SIS-receivers at this high sub-mm wave frequency. In fact, the generated power is not at the limit yet; the photocurrent of the detector can be increased to a maximal value of about 60 mA.

To my knowledge, at the time of publication this was the first time an InP-based photonic LO has been successfully employed to replace a solid state oscillator at sub-mm wave frequency. A fact offering promising perspectives for a distinct simplification and cost reduction, e.g. of astronomical heterodyne receivers for large telescope arrays like ALMA [143]. It should be noted that the photodetector itself is a broadband device and thus, the operating frequency band

of the photonic transmitter is defined by the resonant antenna. Experiments employing photonic transmitters at even higher frequencies up to 1 THz will be carried out in the very near future.

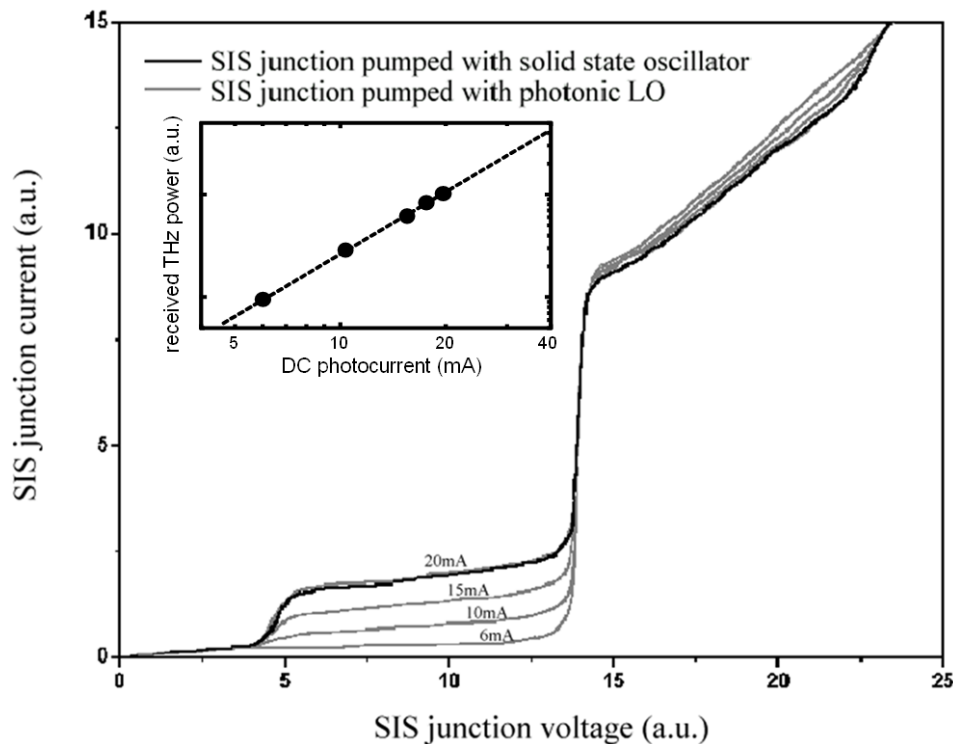


*Fig. 4.23 DC bias curves of the SIS-junction as a function of optical pump power. Inset: sub-mm signal power versus DC-photocurrent.*

#### 4.1.4 1000 GHz ultra-wideband antenna and WR integrated photomixer

To investigate the THz performance of photonic transmitters utilizing waveguide photomixers, the fabricated TWPD were integrated with an impedance matching CPW circuit having a  $50\ \Omega$  output and they connected to a WR10 rectangular waveguide using a CPW-WR transition. The output of the WR10 waveguide was free-space coupled to a Golay cell for measuring the generated power up to THz frequencies (see Fig. 4.22). Here, neither impedance matching stubs nor any imaging quasi optical lenses were employed. Fig. 4.24 shows the measured relative output power versus sub-mm wave frequency up to 1 THz.

As can be seen, below the cut-off frequency ( $< 59$  GHz) of the  $TE_{10}$  mode, no power is detected since no mode can propagate within the WR10 at such low frequencies. Furthermore, it can be observed that the

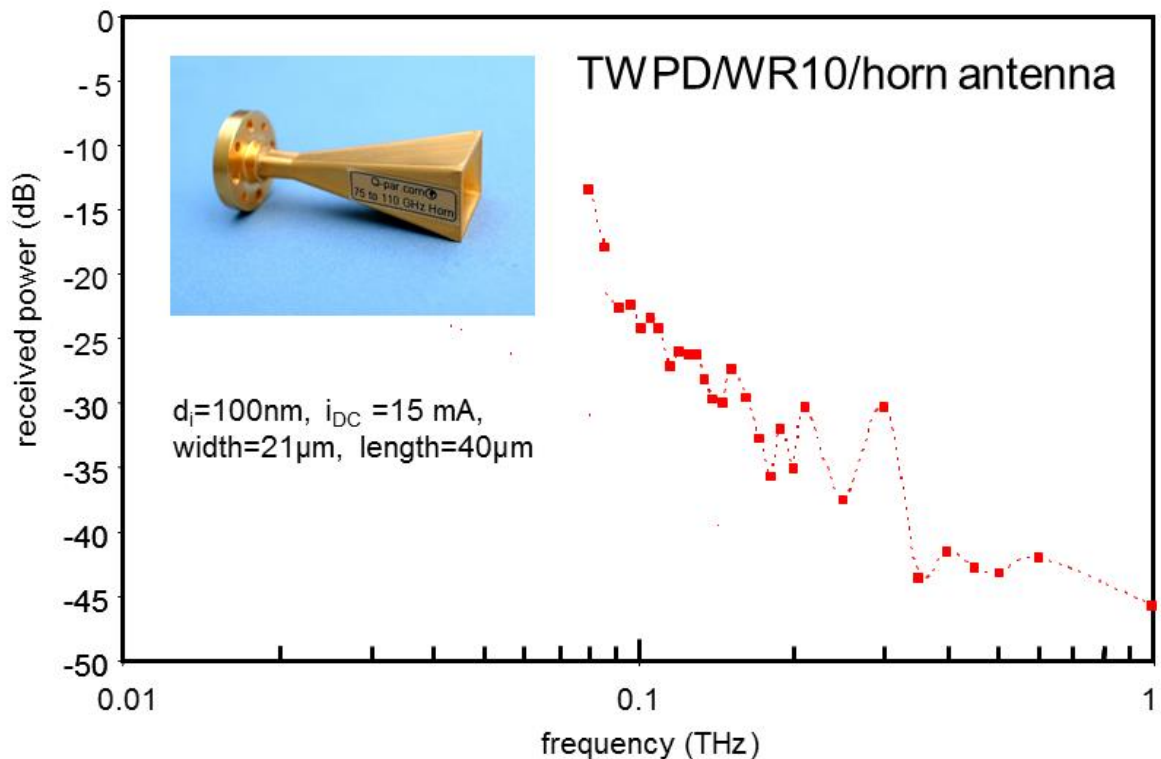


Fig. 4.24 Measured THz output power of a WR10 integrated 1.55  $\mu\text{m}$  TWPD.

measured power decreases with  $f^{-4}$ . This decrease is considered to be caused by the TWPD time constants, but also by a reduced coupling efficiency from the CPW to the higher order modes of the WR waveguide, as well as to increasing waveguide losses.

Table 4.1 Calculated cut-off frequencies of the various  $\text{TE}_{mn}$  and  $\text{TM}_{mn}$  modes in WR8 and WR5 waveguides.

$\text{TE}_{mn}, \text{TM}_{mn}$ waveguide modes	$\text{TE}_{10}$	$\text{TE}_{20}$ $\text{TE}_{01}$	$\text{TE}_{11}$ $\text{TM}_{11}$	$\text{TE}_{21}$ $\text{TM}_{21}$	$\text{TE}_{30}$	$\text{TE}_{31}$ $\text{TM}_{31}$
Cut-off frequencies in WR8	73.8	147.6	165.1	208.8	221.5	266.2
Cut-off frequencies in WR5	115.8	231.6	258.9	327.5	347.4	417.5

To further study the coupling efficiencies of the CPW to higher order WR modes, the TWPD were integrated with WR8 and WR5 rectangular waveguides. This is because WR8 and WR5

both exhibits a fewer number of higher order modes up to 400 GHz as compared to a WR10 waveguide. In Table 4.1, the calculated cut-off frequencies are listed.

The measured output power of these waveguide coupled transmitters is shown in Fig. 4.25. As can be seen, for both waveguide types a step-like frequency response is observed where the different steps appear in the vicinity of the cut-off frequencies of the higher-order modes. This implies that not only the frequency dependence of the TWPD causes the total roll-off of  $f^{-4}$  observed in Fig. 4.24, but also the frequency dependent coupling efficiencies from the CPW output of the TWPD to the higher order modes in the WR8 and WR5 waveguides.

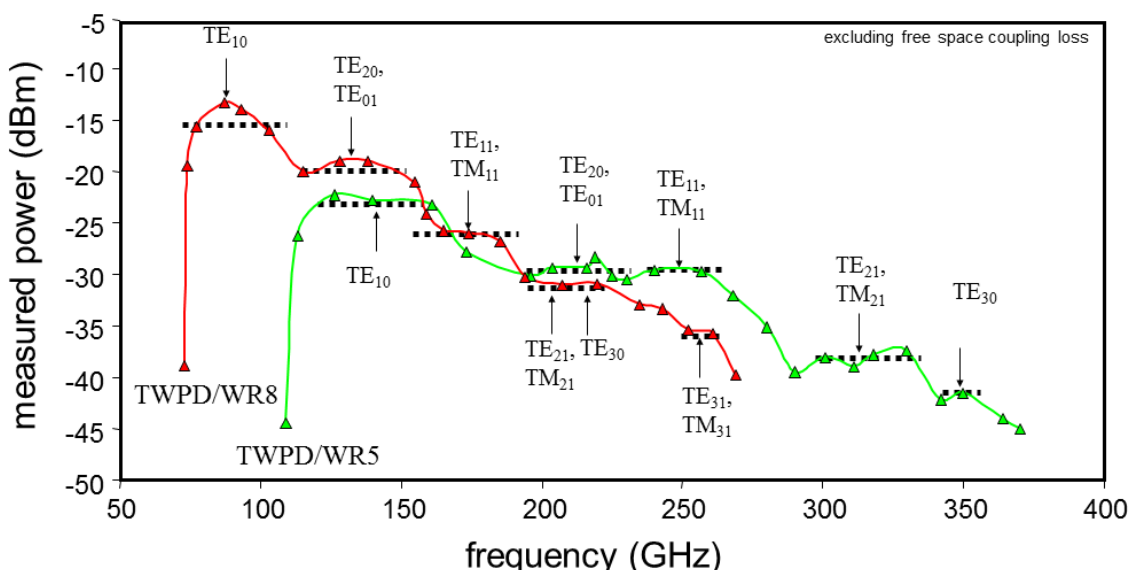


*Fig. 4.25 Measured frequency response of waveguide (WR8 & WR5) integrated photonic transmitter employing 1.55  $\mu$ m TWPD.*

To further study the THz performance of the fabricated TWPDs and in order to circumvent the frequency dependent coupling efficiencies to higher order waveguide modes, the TWPDs were monolithically integrated with broadband planar bow-tie planar antenna structures.

Fig. 4.26 shows the measured output up to 1 THz for a 115  $\mu$ m long and 3 mm wide TWPD that was monolithically integrated with a 30  $\Omega$  broadband bow-tie antenna. As can be seen, there is no power generated below  $\sim$ 20 GHz which represents the lower cut-off frequency of the integrated planar bow-tie antenna defined by the antennas dimensions. Within the frequency range from 25 - 100 GHz the frequency response remains reasonably flat, indicating that not only the TWPD quantum efficiency and the impedance of the CPW output of the TWPD are reasonable flat in that frequency range but also the input impedance of the integrated bow-tie

antenna appears to be constant. At frequencies above 100 GHz up to 1 THz, the generated power drops with  $f^3$ , i.e. the decrease with frequency is somewhat “better” as compared to the WR integrated TWPD.

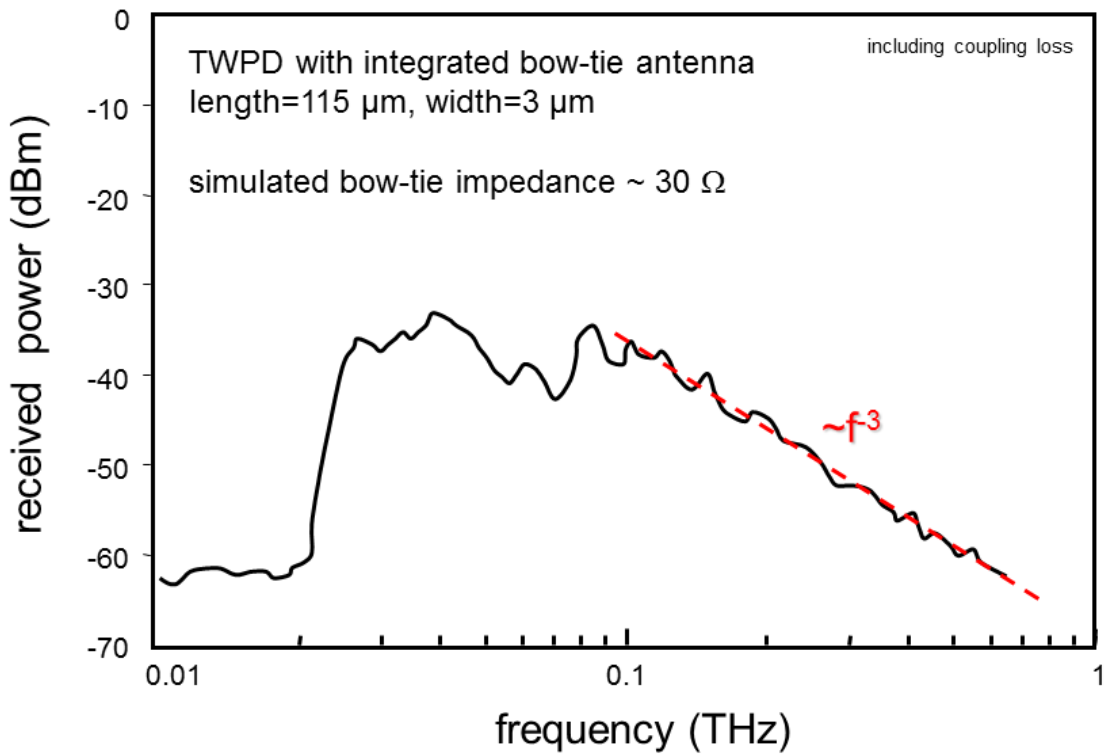


Fig. 4.26 Measured received power from an TWPD integrated with a planar bow-tie antenna. The THz power has been measured using a Golay cell.

#### 4.2 60 GHz Electro-absorption transceiver (EAT)

An optical key function in a full-duplex photonic-wireless communication network is the optical transceiver function for performing bi-directional and full-duplex conversion between the wireless and the optical domain. Several approaches for realizing such transceiver functionality exist; the most straight forward approach of course is integrating a laser for wireless-to-optical conversion and a photodetector for optical-to-wireless conversion. Within the research projects *R-EAT 1* and *R-EAT 2* funded by the Deutsche Forschungsgemeinschaft, a monolithically integrated transceiver component for full-duplex o/e- and e/o-conversion has been developed simultaneously. This work was continued in the European IPHOBAC project (annex I). The following section describes the development of a monolithically integrated reflective electro-

absorption transceiver (R-EAT), as well as some fundamental component characterizations and system experiments. In section 5.5.1, the use of an EAT in a full-duplex mm-wave photonic wireless system is reported.

With respect to dual-function (o/e- and e/o-converter) photonic components, *Wood et al.* from British Telecom previously reported on a dual-function vertical Fabry-Perot multiple-quantum-well (MQW) modulator for bi-directional digital fiber-optic transmission [144] and *Welstrand et al.* [145] demonstrated a waveguide electro-absorption device as a modulator/detector element for analog fiber-optic links. However, in both cases, the electrical bias had to be adjusted to achieve either efficient optical modulation or detection. This requires a bias control circuitry and only allows half-duplex transmission. Full-duplex optical transmission using an MQW EA waveguide device in a frequency-division-multiplexed fiber-wireless system is reported in [146–148], but the approach reported here requested some significant compromises with respect to the component’s layer structure which allowed only moderate maximum data rates up to 120 Mb/s. A solution to that problem was achieved in this work by developing a reflective electro-absorption transceiver (R-EAT) employed in a looped-back configuration.

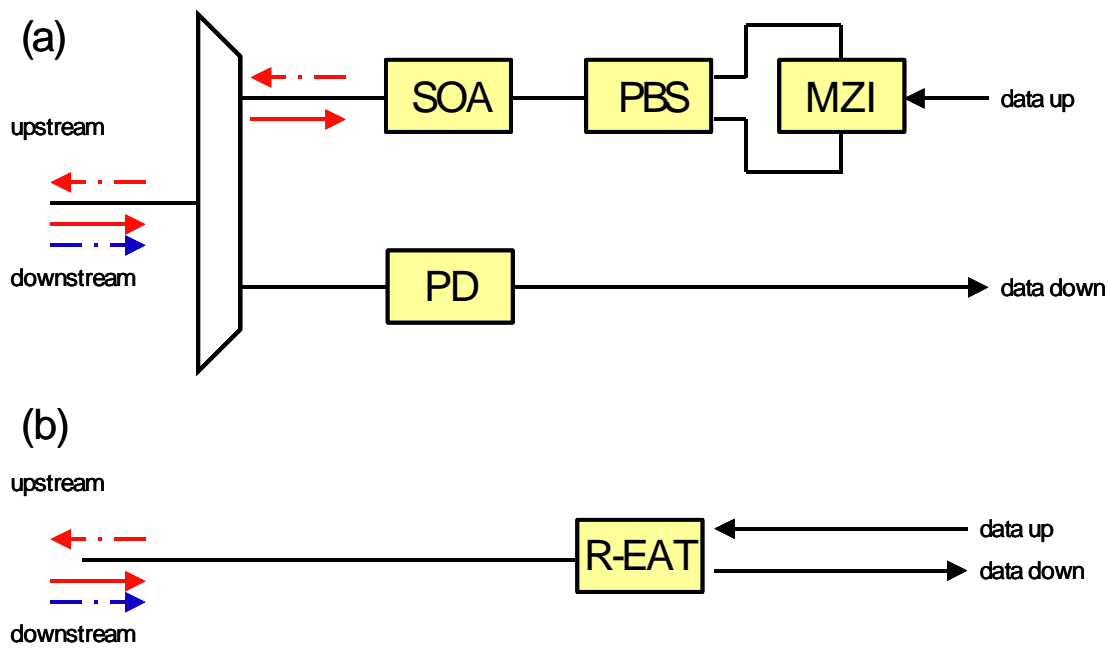


*Fig. 4.27 Schematic set-up of a full-duplex transceiver function using individual optical components (upper, a) and the developed monolithic integrated R-EAT component (b) which fulfills the same function.*

Schematically, the functionality of an R-EAT in a looped-back configuration is shown in Fig. 4.27. For down link transmission, modulated light at a wavelength  $\lambda_1$  (dashed blue arrow) is

detected by the R-EAT and simultaneously, un-modulated light at wavelength  $\lambda_2$  (solid red line) is modulated with the uplink data and reflected back into the fiber by the R-EAT. This way, full duplex communication is established. In that context, the term lopped-back configuration refers to the fact that no laser is integrated in the transceiver element but the R-EAT “just” modulates the incoming continuous-wave (cw) light. It is worth mentioning that the term “electro-absorption transceiver” and its respective abbreviation “EAT” was first introduced in this work in [149] and is now widely used worldwide, e.g. in 2008 and as a result of the *IPHOBAC* project, first EAT and R-EAT components were commercialized by *CIP Technologies Ltd.* [150].

As mentioned above, a “straight forward” optical transceiver would usually consist of a hybrid integrated laser and a photodetector. In this work, the idea was to develop a reflection type transceiver consisting of a single optical waveguide section with a sinlge fiber-chip coupling at the front facet and a high-reflective back facet coating. This concept relies on the physical phenomena of the wavelength dependent electro-absorption effect in multiple quantum well (MQW) structures. The fundamental absorption close to the first order quantum well transition wavelength in the MQW structure is rather small but can be substantially increased due to the quantum confined Stark effect (QCSE) by an electric field. On the contrary, the fundamental absorption at smaller wavelengths can be as large as  $10^2\text{-}10^4\text{ cm}^{-1}$  and it remains high, even in the presence of an electrical field [151, 152]. This physical phenomenon allows to efficiently detect (by fundamental interband absorption processes) modulated light with a wavelength somewhat smaller than the first order QW transition and to simultaneously modulate light with a wavelength close to the first order QW transition. The term “electro-absorption transceiver” thus refers to the underlying physical mechanism employed.

First, a simulation tool entitled “InGaAsP” was developed for designing the active MQW layer of the R-EAT in such a way that light at  $1.3\text{ }\mu\text{m}$  is absorbed, whereas efficient modulation occurs at  $1.55\text{ }\mu\text{m}$  wavelength. For achieving efficient modulation at  $1.55\text{ }\mu\text{m}$  wavelength, it was decided to grow a *pin* double hetero-structure waveguide layer with an active intrinsic  $\text{In}_{1-x}\text{Ga}_x\text{As}_y\text{P}_{1-y}$  MQW layer on InP substrate. With the developed simulation program it is possible to calculate the absolute energy positions of the conductance and valence band edges, the effective masses of the electrons and of the light and heavy holes in dependence of the material composition.

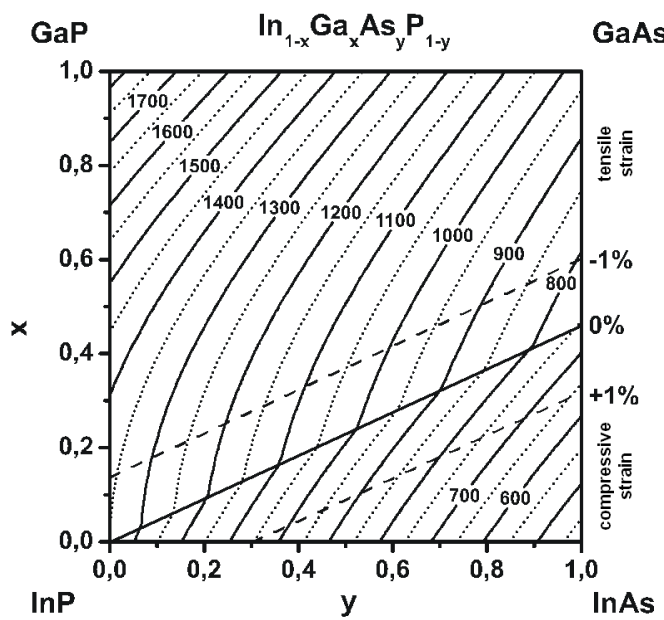


Fig. 4.28 Band gap energies in meV depending on the Gallium concentration  $x$  and the Arsenide concentration  $y$ . Indicated are also relations for lattice matched InGaAsP on InP as well as for -1% tensile and +1% compressive strained bulk InGaAsP on InP.

structure was grown using metal organic vapour phase epitaxy (MOCVD) by the project partner *Fraunhofer Heinrich-Hertz Institut (FhG-HHI)*.

The optical mode evolution in the double hetero-structure waveguide was investigated using a commercial simulation tool BPM-CAD from *OptiWave Inc.* which is based upon the beam-propagation method (BPM). Fig. 4.29 shows the simulated confinement factors for the fundamental and first order TE- and TM-modes as a function of the ridge height. As can be seen from Fig. 4.29, the strip-loaded waveguide with a maximum ridge height of about 650 nm ensures single-mode operation.

Fig. 4.28 shows the calculated band gap energies in meV for bulk  $\text{In}_{1-x}\text{Ga}_x\text{As}_y\text{P}_{1-y}$  grown on InP as a function of the Gallium content  $x$  and the Arsenide content  $y$ . The modeled band gap energies were compared to available data in the literature [153]. Here, a very good agreement was found within the strain region between -1% to +1% with a maximum deviation of the band gap energies below 10 meV, only. Using the additionally developed programs QW-Sim and R-EAT, the QW energy levels, the fundamental absorption in the MQW structure, the absorption change due to the QCSE and the behavior of the optical cavity of the R-EAT were simulated [154]. Finally, the designed InGaAsP/InP double hetero

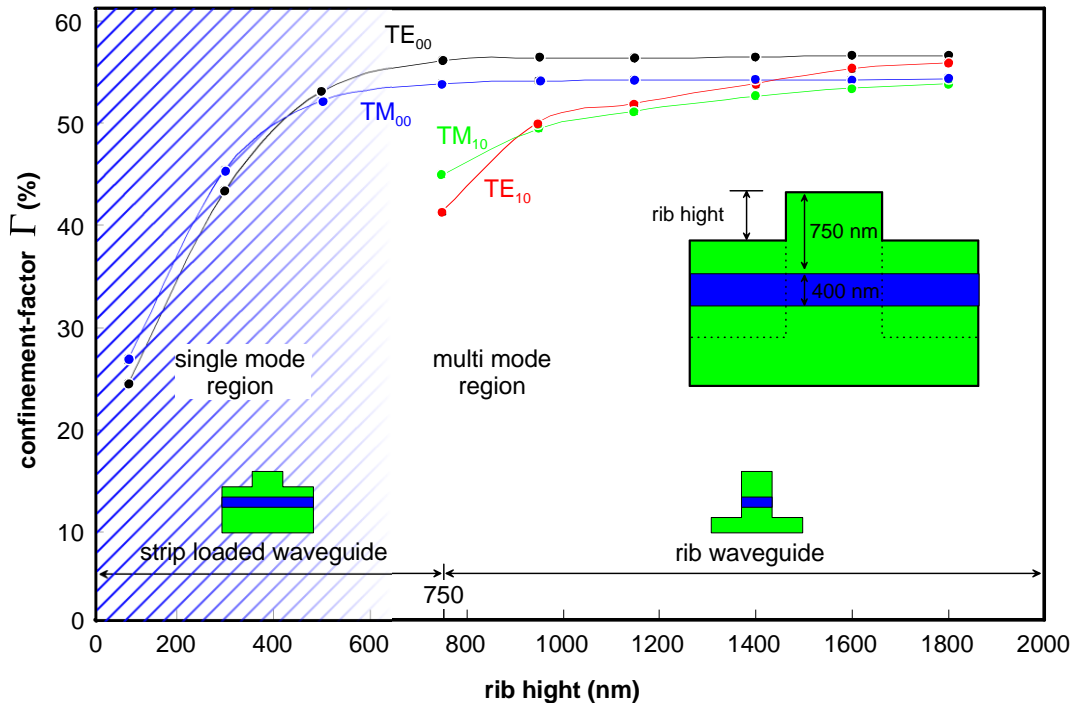


Fig. 4.29 Optical confinement factor for fundamental and first order TE and TM modes as a function of the rib height. The inset schematically shows the cross section of the double hetero structure waveguide layer.

To simulate the modulation and detection performance of the R-EAT, a further model based upon the transfer-matrix method was developed. Here, the R-EAT is considered as a quasi-one-dimensional electroabsorptive Fabry-Perot resonator (FPR) with a length  $L$  and a front and back intensity reflectivity  $R_f$  and  $R_b$ , respectively. The absorption and reflection coefficients of the active materials  $\alpha$  and  $n$  were also considered. Given that the absorption coefficient is not too large, multiple interferences between the front and the back facets occur, which is studied by using the developed model.

The power reflectivity  $R$  at the front facet, as well as the power transmittivity  $T$  at the rear facet can be derived using the Airy-functions [155]

$$R = \frac{P_{out}}{P_{in}} = \eta^2 \frac{(\sqrt{R_f} - \sqrt{R_b} \exp(-\Gamma \alpha L))^2 + 4\sqrt{R_f R_b} \exp(-\Gamma \alpha L) \sin^2(\beta L)}{(1 - \sqrt{R_f R_b} \exp(-\Gamma \alpha L))^2 + 4\sqrt{R_f R_b} \exp(-\Gamma \alpha L) \sin^2(\beta L)} \quad (70)$$

$$T = \frac{P_{trans}}{P_{in}} = \eta^2 \frac{(1 - R_f)(1 - R_b) \exp(-\Gamma \alpha L)}{(1 - \sqrt{R_f R_b} \exp(-\Gamma \alpha L))^2 + 4\sqrt{R_f R_b} \exp(-\Gamma \alpha L) \sin^2(\beta L)}. \quad (71)$$

Here,  $\Gamma$  denotes the optical confinement factor as shown in Fig. 4.29,  $\eta$  the fiber-chip coupling efficiency,  $\alpha$  the absorption coefficient and  $n$  the refractive index. The voltage dependency of  $\alpha$  and  $n$  is considered using the following approximations

$$\alpha = \alpha_{on} + \Delta\alpha \quad (72)$$

$$\beta = \frac{2\pi}{\lambda} (n_{on} + \Delta n) . \quad (73)$$

In the following the refractive index variation was neglected and the field-induced absorption changes were modeled using the following approach

$$\Gamma\Delta\alpha = CV^n. \quad (74)$$

Here, the constants C and n are depending on the operating conditions, as well as on the applied voltage.

The multiple propagation in the cavity of the R-EAT results in the fact that the reflective approach improves the modulation performances of the R-EAT as compared to those of a single path EA modulator (EAM) having the same length. This can be easily demonstrated using the developed model. For an ideal single-path modulator with input and back facet reflectivities of 0%, the extinction ratio can be derived from eq. (71) to be

$$E_r^{EAT} = 10 \cdot \log(\exp(-\Gamma\Delta\alpha L)) \sim -4.34 \cdot \Gamma\Delta\alpha L [dB]. \quad (75)$$

Contrary, the extinction ratio for an ideal reflective type R-EAT with a front reflectivity  $R_f = 0\%$  and a back reflectivity of  $R_b = 100\%$  is

$$E_r^{R-EAT} = 10 \cdot \log(\exp(-\Gamma\Delta\alpha L)^2) \sim -8.68 \cdot \Gamma\Delta\alpha L [dB]. \quad (76)$$

Thus, for the same length and for the same absorption changes, the extinction ratio is twice as large or, in other words, the required voltage swing according to eq. (74) is somewhat smaller, as can be seen from eq. (74)

$$\frac{V^{R-EAM}}{V^{EAM}} = \frac{1}{\sqrt[n]{2}}. \quad (77)$$

A drawback of the reflective approach is seen in the spectral modulation performance, especially in the on-state, i.e. when no voltage is applied and the absorption is at its minimum. In that case, the spectral response of the R-EAT cavity results in an unwanted spectral modulation of the reflected light with a maximum power variation  $\Delta L$  given by the following equation:

$$\begin{aligned} \Delta L = 10 \cdot \log & \left( \left( \frac{\sqrt{R_f} - \sqrt{R_b} \cdot \exp(-\Gamma \alpha L)}{\sqrt{R_f} + \sqrt{R_b} \cdot \exp(-\Gamma \alpha L)} \right)^2 \right) + \\ & + 10 \cdot \log \left( \left( \frac{1 - \sqrt{R_f R_b} \exp(-\Gamma \alpha L)}{1 + \sqrt{R_f R_b} \exp(-\Gamma \alpha L)} \right)^2 \right). \end{aligned} \quad (78)$$

In Fig. 4.30 (left), the maximum power variation  $\Delta L$  of the light reflected at the front facet is shown as a function of the front facet reflectivity and the on-state single-path loss for a back facet reflectivity of 95%. As can be seen, to suppress the unwanted power spectral variation, the front facet reflectivity should be as small as possible. Given the fact that the on-state single-path loss typically is about 1-2 dB because of light scattering at the rough ridge edges, the front facet

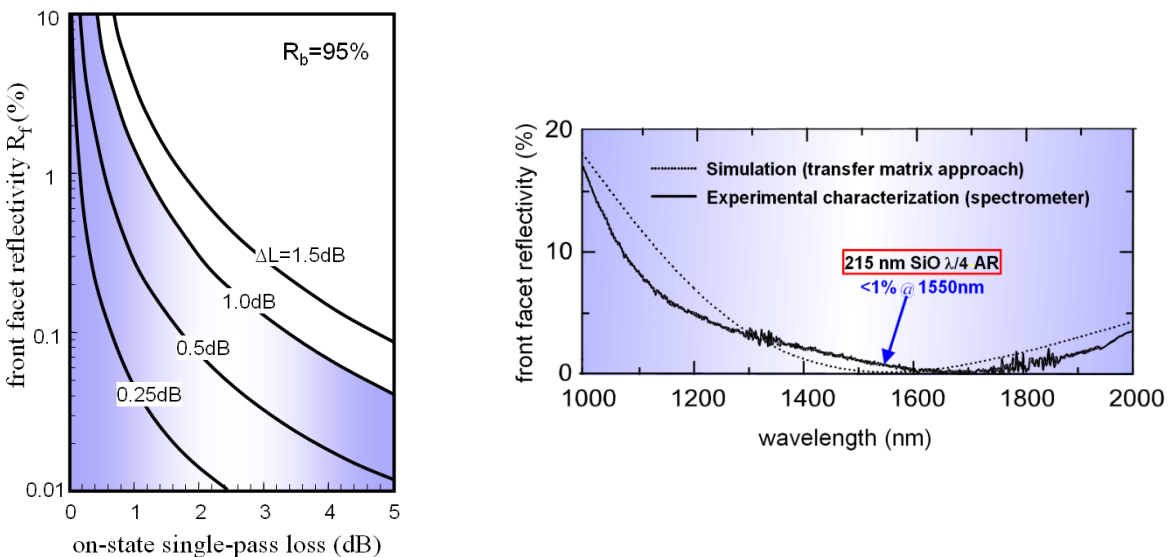


*Fig. 4.30 Maximum power variation  $\Delta L$  of the light reflected at the front facet as a function of the front facet reflectivity and on-state single-path loss for a back facet reflectivity of 95% (left). Measured front facet spectral reflectivity after AR coating, using a 215 nm thick  $\text{SiO } \lambda/4$  layer.*

reflectivity must not be larger than 1%. To achieve this, the front facets were AR-coated using a 215 nm thick SiO  $\lambda/4$  layer. As can be seen from Fig. 4.30 (right), the front facet reflectivity was below 1%, as necessary.

The technological processing of the R-EAT chip was carried out within the clean room facilities of *Universität Duisburg-Essen*. The photolithographic masks were designed and digitalized using AutoCAD R14, the Chromium masks were fabricated using a HeCd-Laser lithograph process. Since the minimum resolution was in excess of 1  $\mu\text{m}$ , standard contact lithograph and wet chemical etching were used for the chip fabrication process. Also, the Ti/Pt/Au and Ge/Ni/Au metal contacts were fabricated using contact lithograph and electron-beam evaporation in an ultra-high vacuum chamber. Schematic drawings and scanning electron microscopic (SEM) photos can be seen in Fig. 4.31. A special V-groove technology was developed for fiber-chip coupling [156, 157].

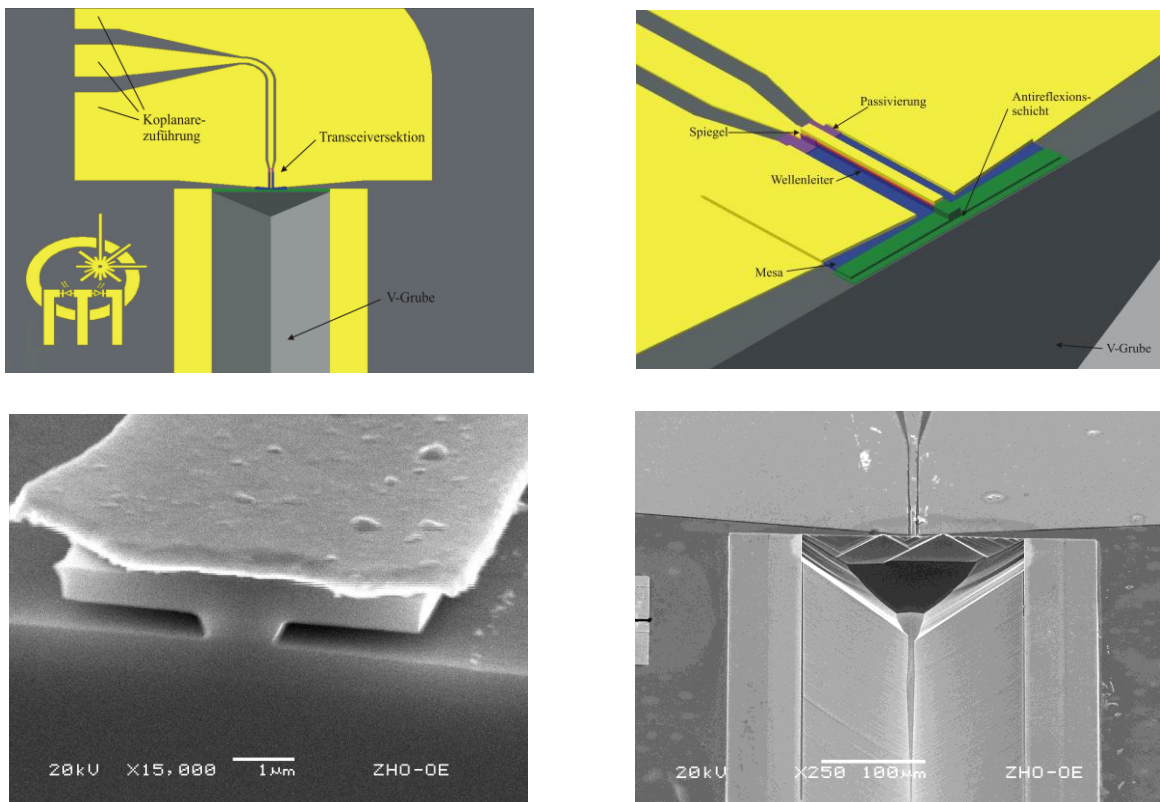


*Fig. 4.31* Schematic top view of the R-EAT showing the V-groove in front of the active R-EAT section supporting the fiber-chip coupling and the bended coplanar 50  $\Omega$  transmission lines, ensuring high-frequency operation (top left), close-up drawing of the R-EAT front facet with anti-reflection (AR) coating (top right), SEM photo of the T-shaped front facet (bottom left), and SEM picture of the front facet with V-groove (bottom right).

The active section of the fabricated R-EAT is typically about 100  $\mu\text{m}$  long, the average reflectivity of the AR-coated front facet was  $R_f = 0.6\%$  at a wavelength of 1.55  $\mu\text{m}$ . The reflectivity of the high-reflective (HR) coated back facet is about ~96% at 1.55  $\mu\text{m}$  wavelength. This way, the maximum spectral input power variation was below 1 dB.

The fabricated R-EAT typically exhibits a 100  $\mu\text{m}$  long EA section, the average the reflectivity of the anti-reflection ( $\lambda/4$ -SiO<sub>x</sub>) coated front facet was as low as 0.6% at a wavelength of 1.55  $\mu\text{m}$ . The reflectivities of the high-reflection coated back facet (SiO<sub>x</sub>/Au) were typically in the order of ~96% at 1.55  $\mu\text{m}$  wavelength. Because of this, the maximum variation of the spectral insertion loss was reduced to below 1 dB. For high-frequency operation, the active EA section of the R-EAT was connected via CPW structures. For electrical passivation of the center conductor, a polyimide passivation layer was used [154]. Fiber coupling of the active EA section to an SMF has been achieved using an special InP V-groove technology and ball lenses [156-158]. In comparison to coupling the EA section to cleaved SMF, the coupling efficiency could be improved by 6.4 dB.

As designed, the operating optical input wavelength region is around 1.55  $\mu\text{m}$ , precisely it was found to be 1.52-1.57  $\mu\text{m}$ . At a reverse DC bias of only 2.5 V, a maximum modulation contrast in excess of 12 dB has been achieved at 1.55  $\mu\text{m}$  wavelength and a maximum responsivity of 0.37 A/W at 1520 nm wavelength [154]. The maximum modulation speed for the transmit and receive function was higher than 3.5 GHz. A further improvement of the modulation contrast up to 10 GHz appears feasible when using an additional electrical impedance matching circuitry.

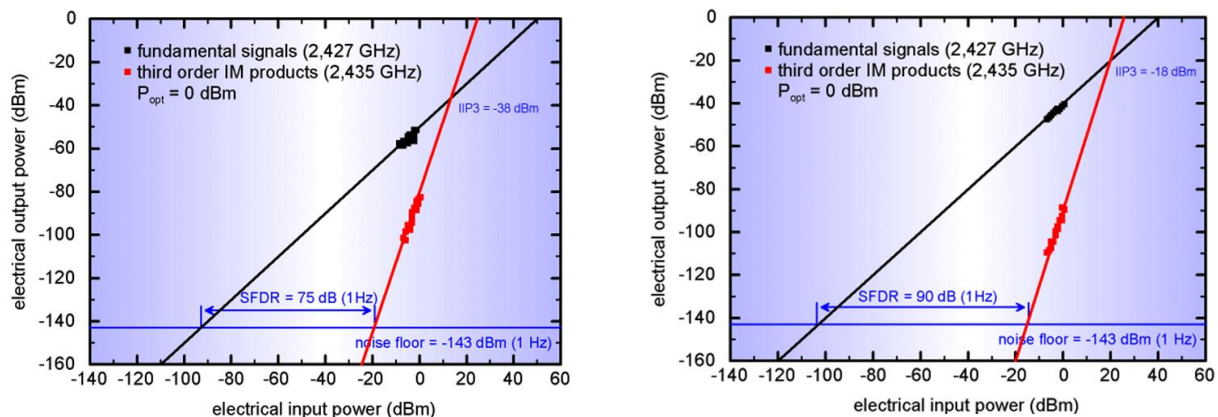


Fig. 4.32 Fundamental and third order output power versus electrical input power for transmit (left) and receive (right) operation.

In order to experimentally verify the system compatibility of the fabricated R-EAT, the components were used for different fiber-optic transmission systems.

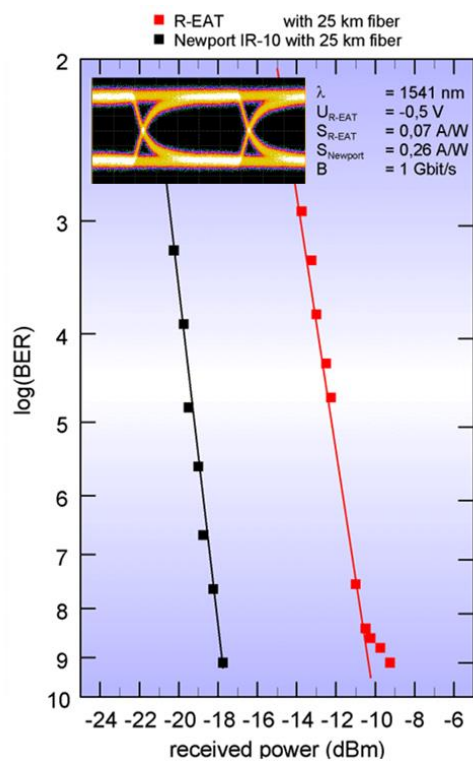


Fig. 4.33 Bit error rate versus received optical power for a 1 Gb/s ASK signal using either the R-EAT as receiver or a commercial PD.

In [159], the simultaneous transmission of a 1 Gbit/s base band signal and a full-duplex WLAN signal at 2.4 GHz was successfully achieved. The receiver sensitivity of the R-EAT was below -9 dBm for 1Gbit/s (NRZ,  $2^{31}-1$ ,  $\text{BER} < 10^{-9}$ ) ASK signal. The measured spurious free dynamic ranges (SFDR) for transmit and receive operations were measured to be 75 dB/Hz and 90 dB/Hz in a 1 Hz bandwidth, respectively. Furthermore, the fabricated R-EATs were successfully employed for base band transmission up to 5 Gbit/s. The usage of R-EAT in broadband millimeter-wave photonic wireless systems will be discussed in detail in section 5.5.1.

## 5 Broadband Photonic Millimeter-Wave Wireless Systems

This section puts a focus on today's importance of broadband fixed wireless communications and the role and advantages Microwave Photonics can bring to this application field. At first, it will be shown that there is a great economical need for broadband wireless systems that could offer much higher data rates than today's wireless systems. Next, new broadband wireless architectures based upon advanced photonic technologies and components will be presented and discussed. Experimentally, world record performances in terms of maximum wireless data capacity and spectral efficiency will be reported in this section.

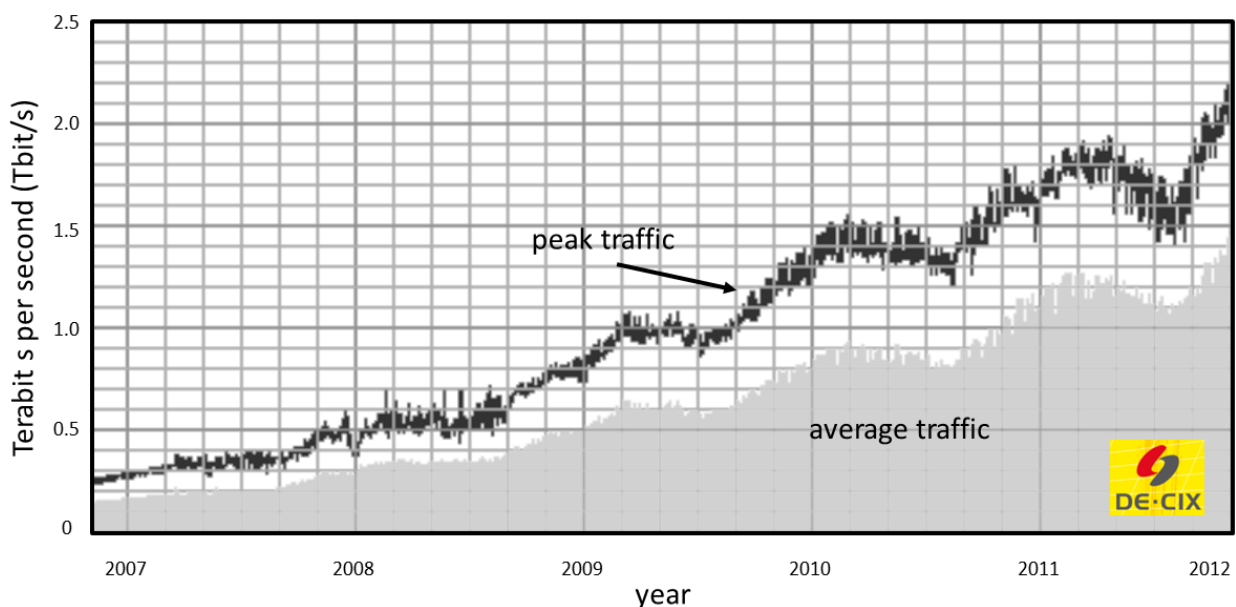


Fig. 5.1 Average internet traffic and peak internet traffic at the worldwide leading internet exchange note (DE-CIX) located in Frankfurt am Main [160]. Courtesy from DE-CIX.

The total throughputs of today's communication systems continue to increase at a more or less constant rate which is not at the least driven by the raising demand in multimedia services and the ever increasing number of new applications. This can be seen e.g. from internet traffic. For instance, the worldwide leading Internet exchange note; the German Internet Exchange (DE-CIX) located in Frankfurt am Main, frequently reports new traffic records [160]. DE-CIX is connecting all major German internet services providers, many international ISPs and organizations like the National Research Network and DFN. Fig. 5.1 shows the peak and average traffics at DE-CIX. As can be seen, average traffic has quadrupled within two years; from about 95 Gbit/s in June 2007 up to 380 Gbit/s in June 2009. Also, the peak traffic has quadrupled in

that time period. It is noteworthy mentioning that the highest peak traffic in 2009 has already approached the 1 Tbit/s margin.

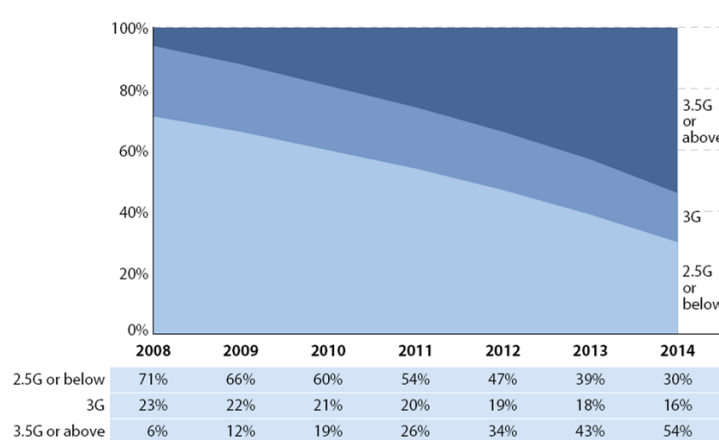


Fig. 5.2 Distribution of handsets by network generation for Western Europe [161].

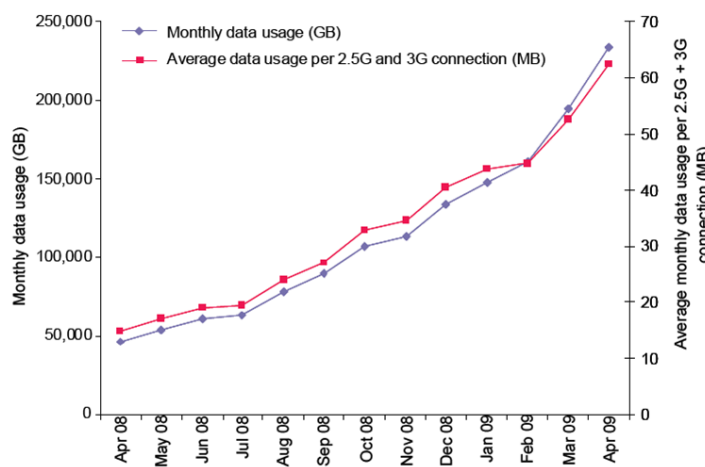


Fig. 5.3 Mobile data use in Hong Kong [162].

is now underway to replace electronic transport systems even in the shorter-reach access networks.

Obviously, the ever increasing internet traffic has required frequent advances of the maximum data capacities of the underlying physical transport layer. With respect to wired internet access, this has been made possible by using fiber-optic communication technologies which have played a crucial role in enabling broadband internet access. Fiber-optics is advantageous compared to copper and other wired technologies whenever high aggregate data rates or long transmission distances are involved. Consequently, as optoelectronic component and integration technologies have matured, fiber-optic communications has gradually replaced electronic solutions in the long-haul intercontinental and continental links as well as in many metropolitan area networks. With massive fiber-to-the-home (FTTH) deployments in Asia, the US and some countries in Europe, fiber-optic communications

## 5.1 Applications and worldwide markets

The emergence of the many new “bandwidth hungry” multimedia applications is not only influencing the capacity of fiber-optic communication systems. Also mobile data service is booming today, and there is no doubt that wireless networks will face a capacity crunch soon.

Indeed, a 2008 market study from the ICT advisory brand of the Datamonitor Group OVUM forecasts mobile broadband (or mobile internet) users in excess of 2 billion worldwide by 2014 [163] (just under one third of the total earth population!) – an increase of about 1100% as compared to figures in 2008. For Europe, the forecasted number varies a lot from one study to the other and ranges between 140 and 440 million users in 2014 [161, 164, 165]. Whatever is the most realistic forecast, the growth in data usage that mobile operators will have to face in the near future is enormous.

Currently worldwide mobile data and internet traffic is doubling about every 18 months and operators encourage subscribers to migrate from previous generation mobile standard GSM with a bandwidth of a few hundred kilobits per second over HSPA to LTE, offering a peak bandwidth of up to 150 Mbit/s. This rapid migration from traditional voice only subscription to broadband enabled ones is illustrated for Western Europe in Fig. 5.2. In densely populated areas, the traffic increase is even stronger. For example in Hong-Kong [162], the mobile internet traffic has quadrupled in only one year, reaching an average of 60 MB in mid-2009 per user per month (Fig. 5.3). This in turn has caused quality of service issues as users have started to use peer-to-peer file exchanges via their mobile broadband connections. This trend is certainly going to continue and even probably be reinforced in the coming year as the difference between fixed broadband and mobile broadband services/usages is decreasing [165]. Indeed, the market price for mobile broadband is decreasing faster than its fixed counterpart with ever increasing data rates available leading to people switching their internet habits and usages from DSL to mobile.

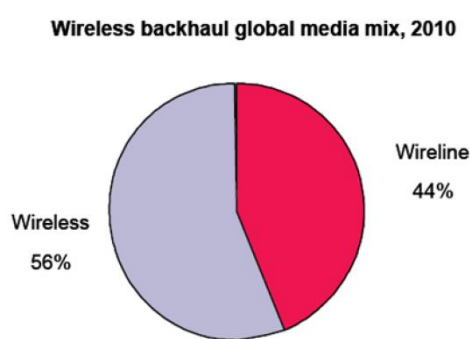
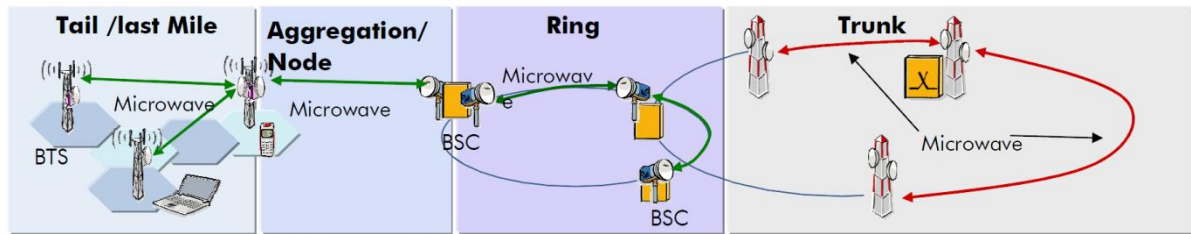


Fig. 5.4 Wireless backhaul global mix in 2010 [166].

The combination of all these factors, i.e. the worldwide trend towards more mobile broadband services and a higher number of users using these broadband services, induces a very strong predicted growth on data capacity to be transported over the wireless backhaul networks for mobile telephony. In [164], it is forecasted that mobile telephony downlink traffic per month and per 10 million users will increase over the capacity of 3G+ mobile standard by 2012. This traffic metric is directly linked to the one that the wireless backhaul network will have to carry in the coming years.

This exploding capacity requires new paradigms for the wireless backhauling systems in mobile networks. Today, the backhaul in mobile network is primarily constructed with microwave point-to-point links. On average over all operators, the proportion of wireless links in the mobile



*Fig. 5.5 Schematic architecture of a wireless system. Courtesy from Alcatel-Lucent.*

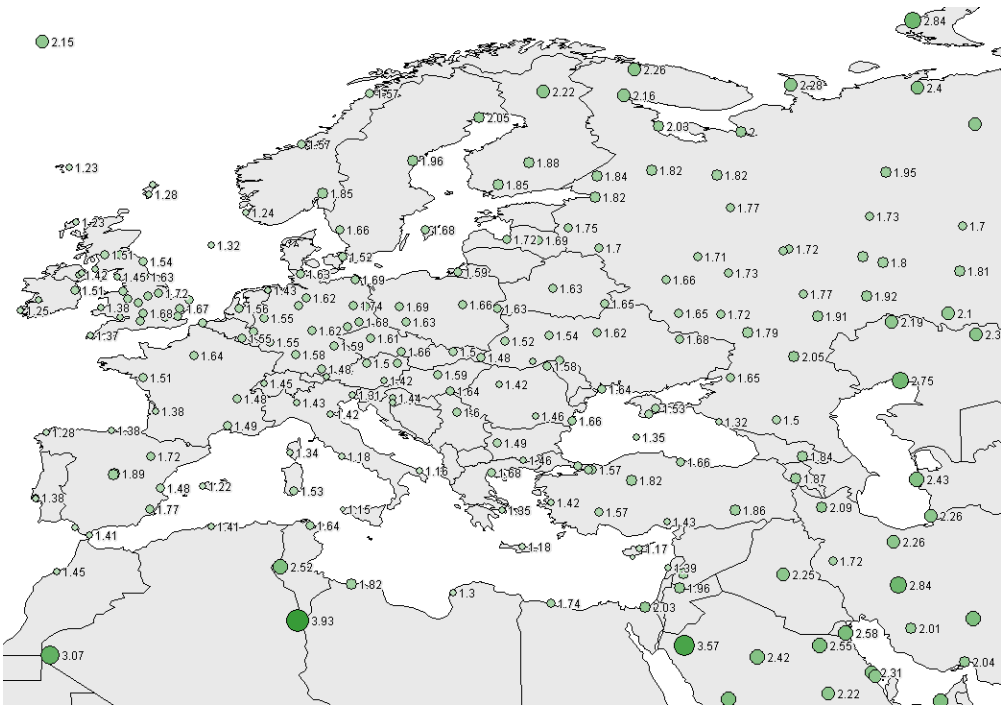


*Fig. 5.6 Example of the average hop length variation across Europe, North Africa and western parts of Russia calculated with ITU rain model in km for 1 Gbit/s and 99.999% availability. Courtesy from Alcatel-Lucent.*

backhaul network is around 56% (Fig. 5.4) [166]. The main driver to install wireless connections for mobile backhauling is the reduced necessary investments compared to installing a new cable between the base station and the backhaul network connection point. Furthermore, the evolution of mobile standards towards higher bandwidth, as well as the necessity to reduce the power radiated by base stations in the future will require the densification of the base station installations. This will lead to an important extension of the backhaul network towards denser points of presence and shorter links, around 2 km long (see Fig. 5.6). This is completely compatible with the capabilities of mm-wave radio links. In this prospect, it is vital for future wireless backhauling that high capacity wireless links approaching today 1 Gbit/s and in the near future 10 Gbit/s are being developed (especially as the traffic from many cells will be aggregated when transported to the nearest point of presence). This is seen as an enabler for a major market [167]. Future wireless backhauling for broadband access in rural areas where fixed lines are

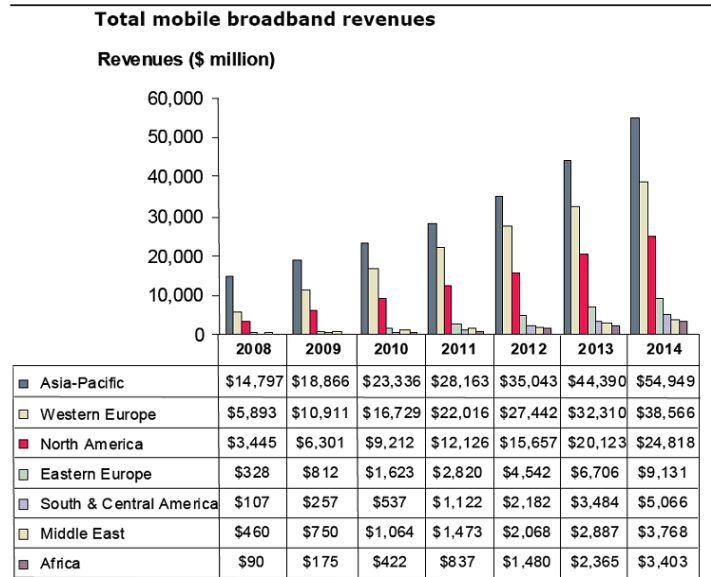
unavailable (fiber extension) will even require radio systems offering today 10 Gbit/s and 40 Gbit/s in the future.

The current limitation in capacity is likely to become a bottleneck in wireless networks soon. When looking at the architecture of a typical wireless system architecture depicted in Fig. 5.5, it becomes clear that with increasing rates in the last mile, e.g. due to the evolution of mobile systems, the backhauling fixed wireless systems e.g. in the aggregation part of the networks will have to handle much higher capacities in the future, requiring gigabit or even multi-gigabit per second wireless systems.

But those future “Gigabit Wireless” systems would not only be useful and necessary for mobile backhauling. Broadband wireless systems are also expected to play an important role in future internet access for providing an alternative technology to FTTH deployments. Such an alternative is strongly required. Even when assuming 1 Mio. FTTH access note deployments a year, which is far from reality, it would last for about 40 years to connect all households in Germany. Obviously, an alternative fast deployable access technology would be very beneficial, especially for remote areas.

Other scenarios requiring an almost instant deployment are e.g. disaster recovery or bridging failed out Gigabit Ethernet fiber-optic links. For such applications, Gigabit wireless links would also offer an attractive alternative to existing fiber-optic but also to free-space optic communication systems, provided the capacities of wireless systems can eventually cope with those of fiber-based communication systems.

As stated above, mobile backhauling is one of the key markets for broadband millimeter-wave wireless systems fuelled by mobile broadband expected revenues where tremendous growth is forecasted. For instance (Fig. 5.7), OVUM forecasts that mobile broadband revenues will have doubled by 2013 with a total market of over 110 billion dollars [163]. It is key for operators to be able to respond to the increasing service demand over mobile telephony as this market growth is today compensating for the stagnant more traditional market for voice and messaging services [163].

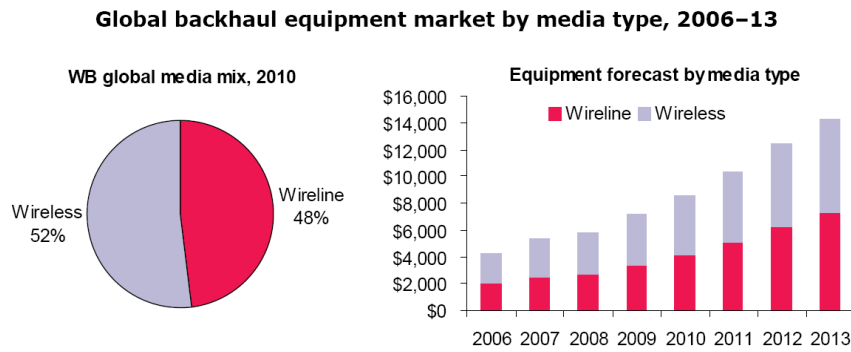


Source: Ovum

*Fig. 5.7 Revenue from mobile broadband per geographic region for years 2008 to 2014 [163].*

In [168], it is forecasted that a traffic higher than 140 Mbit/s is to be available at each base station by 2012. This will result on an increase of the number of base stations and associated backhaul links in urban areas of developed countries (which represents one fifth of the actual 2.3 Million cell sites as reported in [168]) by a factor that operators already estimate between 5 and 10 compared to the actual situation [169]. As immediate obvious consequence, this will reduce the distance between one base station to the other which is today on average as small as 1 to 2 km for urban and sub-urban areas and will potentially lead to reduced radio emission levels for the users and to higher energy efficiency for the operators (see also Fig. 5.6).

This booming mobile telephony market pushes the market for mobile wireless backhaul equipment by 19% year-on-year for 2008 [170]. The forecast for the mobile backhaul equipment market is shown in Fig. 5.8. The market was evaluated in 2008 to be 5.8B\$ with 54% share for wireless, while for 2013, it is estimated to be 14.3B\$ with 49% share for wireless. Similar trends are forecasted in [168] and [170]. This decline in the share of the market for wireless backhaul systems is partly due to the need for increased capacity and the perceived limited bandwidth offered by today's wireless systems.



Source: Ovum

Fig. 5.8 Global mobile backhaul equipment market by media type for 2006-2013. Market data on the right hand side graph is in million dollars [171].

The time frame needed for this increase will obviously depend on the success of those new services (which is already much higher than expected a year ago), but also on the capability of operators to invest and to get a rapid return on investment despite the low increase of revenues linked to a data rate increase. Without risk of error, it can be stated that this has to be accomplished before the next ten years, and operators will not be able to wait for the arrival of fiber (with the appropriate bit rate  $>100$  Mbps) to all their future potential base station sites but must find other backhaul solutions potentially representing a lower TCO (Total Cost of Ownership) portion than the 25% that laying new cables represents today on the actual networks.

For this reason, today, point-to-point broadband wireless systems operating in the millimeter-wave bands have become a real chance due to their larger channel capability as compared to microwave wireless systems, their easy licensing rules, their gaseous attenuations which are in the same range as for microwave frequencies and due to the fact that they have been hardly used up to now enabling the definition of engineering rules to maximize their usage. Unfortunately, the few actual millimeter-wave products available on the market are not in line with most operators' expectations for a large deployment due to their relatively high cost per link and poor spectral efficiencies (~0.5-1.0 bit/s/Hz). If one adds to that the actual apparent limitation of those commercial wireless systems in reaching higher data rates like 10 or even 40 Gbit/s, which would be necessary in the future, operators may decide to opt anyway for the installation of an optical infrastructure for mobile backhauling, hence leading to massive investments and delay in implementing successfully the necessary evolution of future mobile networks.

In summary, the major outdoor applications that can potentially be addressed by broadband wireless systems can be summarized as follows:

- Millimeter-wave mobile backhauling
- Fiber-extension
- Wireless access
- Short-range secure wireless transmission
- Fast-deployable wireless systems, e.g. for disaster recovery
- Fiber-repair

## 5.2 Worldwide regulations and standardizations

In view of the future market for broadband wireless as discussed in the section above, regulatory bodies in Europe, Japan, the United States, and other countries have allocated frequency bands in the millimeter-wave frequency range for such services. For enabling future “Gigabit Wireless” systems, larger channel bandwidths allowing more simple modulation formats (e.g. OOK) and thus the use of simple and cost effective transmitters and receivers, were necessary. Because of the congestion in the microwave bands, millimeter-wave bands were allocated. Especially the 60 GHz band has been regulated for unlicensed use and the 71-76 GHz and 81-86 GHz bands are allocated for licensed use.

In this section, the issued and proposed frequency allocations and main specifications for radio equipment in a number of countries worldwide will be summarized. As those regulations were issued already in view of a potential market before any technical system was available, it is obvious that they are frequently adapted by regulatory bodies for harmonization reasons, but also for technical and safety reasons. Thus, the following summary reflects the actual situation in some key countries while intense efforts in other countries are currently underway.

As the general objective of this work is in realizing RoF systems providing gigabit or even multi-gigabit per second data speeds, only the regulations and standardizations in the millimeter-wave range offering sufficient bandwidth will be covered. Therefore, regulations for wireless services in frequency bands below 57 GHz offering a maximum channel bandwidth of 56 MHz (50 MHz in North America) will not be looked at. For Europe, more information on those microwave point-to-point systems operating in bands between 1 GHz and 58 GHz can be found in a single multi-part regulation [172].

### 5.2.1 Unlicensed wireless services in the 60 GHz band

The 57-64 GHz band has been set for license-free usage of fixed wireless services in many parts of the world. In 2000, the Ministry of Public Management, Home Affairs and Posts and Telecommunications (MPHPT) in Japan issued 60 GHz radio regulations for unlicensed utilization in the 59-66 GHz band [173]. The maximum transmission bandwidth within the 60 GHz band was limited by MPHPT and must not exceed 2.5 GHz. The maximum transmit power and antenna gain are 10 dBm and 47 dBi, respectively. In 2001, the United States Federal Communication Commission (FCC) allocated 7 GHz in the 57-64 GHz band also for unlicensed use of wireless services. These allocations were last modified in 2008 [174], specifying a maximum transmit power (for emission bandwidth greater than 100 MHz) and a maximum equivalent isotropic radiated power (EIRP) of 27 dBm and 43 dBm, respectively. In contrary to Japan, the bandwidth in the US is not limited, i.e. the use of a total bandwidth of 7 GHz is permitted. The 60 GHz regulations in Canada regulated by Industry Canada Spectrum Management and Telecommunications (IC-SMT) is harmonized with the US [175]. With respect to regulation, the situation in Europe is somewhat more complex. In 2005 (revised in 2009), the Electronic Communications Committee (ECC) within the Commission for European Post and Telecommunications (CEPT) released recommendations for a European-wide frequency band for fixed services using the 64-66 GHz band [176]. In 2007, the European Telecommunication Standards Institute (ETSI) released technical specifications for wireless systems operating in the 60 GHz range [177]. Based upon these specifications, the Bundesnetzagentur (BNetzA) in Germany allocated the 59-63 GHz band for unlicensed fixed wireless services but limited the maximum bandwidth to 2 GHz. Finally and very recently, in 2009, ECC released new recommendations for fixed wireless services in the 57-64 GHz range [178]. These recommendations provide power limits for radio equipment being used for short distance (approx. 1 km), high capacity wireless links operating at 57-64 GHz, in conjunction with the 64-66 GHz band specified in [176]. According to these recommendations, maximum transmit power, maximum EIRP and minimum antenna gain are 10 dBm, 55 dBm, and 30 dBi, respectively. Also in 2009, the Australian Communications and Media Authority (ACMA) provided power limits for data communication wireless transmitters operating in the 57-66 GHz region [179] and in South Korea, the 57-64 GHz is allocated for unlicensed use [180].

Table 5.1 summarizes important worldwide regulations for wireless services in the 60 GHz band. As can be seen from that table, the maximum permitted bandwidth in the 60 GHz band is significantly larger than for any microwave wireless system [172]. In many parts of the world, there is no channel segmentation in place and aggregation of the total bandwidth is permitted, resulting in a maximum usable bandwidth of up to 7 GHz, in some places even 9 GHz are possible. This huge bandwidth allows for the deployment of cost effective single channel

wireless systems with rather simple modulation schemes (e.g. OOK) providing gigabit per second speeds. Even 10 gigabits per second are feasible with single channel systems using a more complex modulation scheme (e.g. 8-QAM).

### 5.2.2 Licensed wireless services in the 71-76 GHz and 81-86 GHz bands

In the United States, the FCC made a historic ruling in 2003 [181], opening up 12.9 GHz of spectrum at frequencies much higher than had been commercially available before. In detail, FCC allocated the 71-76 GHz, 81-86 GHz and 92-95 GHz except the 94-94.1 GHz portion which is for exclusive Federal Governmental use. These regulations were last modified in 2005 [182]. Canada has adopted the same bands with the same technical specifications and licensing regimens as the USA in 2005 [183]. Also in 2005, the ECC within the Commission for European Post and Telecommunications released a European-wide frequency channel plan for fixed service systems in these bands, which was last modified in 2009 [184]. In 2006, the European Technical Standards Institute (ETSI) released technical specifications covering the 71-76 GHz and 81-86 GHz bands [185]. Similar specifications are also effective or proposed for the United Kingdom [186] and Australia [187].

Of particular interest is the 10 GHz of bandwidth at 70 and 80 GHz bands. Designed to coexist together, the 71 to 76 GHz and 81 to 86 GHz allocations allows up to 5 GHz of full duplex transmission bandwidth; enough to transmit a gigabit of data even with the simplest modulation schemes. With more spectrally efficient modulations, full duplex data rates of 10 Gbit/s can be envisaged.

Table 5.2 summarizes relevant worldwide regulations and recommendations for radio equipment to be used in those frequency bands. As can be seen from that table, for the E-band altogether nineteen 250 MHz channels are defined within each 5 GHz band in Europe (four 1.250 MHz channels in North America), with a 125 MHz guard band at the bottom and the top of the band. Also, aggregation of any number of channels, from 1 to 19, is permitted. Standards also permit pairing, i.e. using one RF channel in the 70 GHz for down- and another RF channel in the 80 GHz band for uplink transmission.

Table 5.1 Worldwide frequency allocation for unlicensed wireless services in the 60 GHz band.

Region	Unlicensed frequency range	Channel segmentation	Maximum bandwidth	RF tolerance	Modulation	max. Tx power	EIRP	min. antenna gain	Reference(s)
Europe	57-66 GHz	various seg. 240 MHz LGB 120 MHz UGB	8,640 GHz		Various incl. OOK, OFDM-16QAM	10 dBm	55 dBm	30 dBi	[178], [188]
Germany	59-63 GHz		2 GHz (min. 150 MHz)	not spec.	not spec.	not spec.	40 dBm	35 dBi	[189]
USA	57-64 GHz	not spec.	7 GHz (min. 100 MHz)		not spec.	27 dBm	43 dBm	not sepc.	[174]
Canada	57-64 GHz	not spec.	7 GHz (min. 100 MHz)		not spec.	27 dBm	43 dBm	not spec.	[175]
Japan	59-66 GHz		2.5 GHz <sup>+-</sup> 500 ppm		10 dBm			max. 47 dBi	[173]
Australia	57-66 GHz		9 GHz		not spec.	13 dBm	43 dBm <sup>1</sup> 51.7 dBm <sup>2</sup>	not spec.	[179]
Korea	57-64 GHz		7 GHz		10 dBm				[180]

1,2 In Australia, two different maximum EIRP levels are defined; for indoor max. EIRP is 43 dBm, for outdoor use it is 51.7 dBm.

Table 5.2 Worldwide frequency allocations for licensed wireless services in the 71-76 GHz and 81-86 GHz frequency bands.

Region	Licensed frequency range	Channel segmentation	Maximum bandwidth	RF tolerance	Modulation	max. Tx power	EIRP	min. antenna gain	Reference
Europe	71-76 GHz	19x250 MHz 125 MHz LGB 125 MHz UGB	4.75 GHz <sup>+</sup>	+/- 150 ppm	Various incl. OOK, 128-QAM	30 dBm	75 dBm	43 dBi	[184], [185]
	81-86 GHz	19x250 MHz 125 MHz LGB 125 MHz UGB	4.75 GHz <sup>+</sup>	+/- 150 ppm	Various incl. OOK, 128-QAM	30 dBm	75 dBm	43 dBi	[184], [185]
USA Canada	71-76 GHz	4x1250 MHz	5 GHz*	not spec.	Various incl. OOK min. 0.125 bit/s/Hz	27 dBm 1.5 mW/Hz	85 dBm	43 dBi	[181], [182], [183]
	81-86 GHz	4x1250 MHz	5 GHz*	not spec.	Various incl. OOK min. 0.125 bit/s/Hz	27 dBm 1.5 mW/Hz	85 dBm	43 dBi	[181], [182], [183]
	92-94 GHz	no segmentation	2 GHz*		min 1 bit/s/Hz.				[181], [182], [183]
	94.1-95 GHz	no segmentation	0.9 GHz*		min. 1 bit/s/Hz				[181], [182], [183]
Australia	71-76 GHz	no segmentation 125 MHz LGB 125 MHz UGB	4.75 GHz <sup>+</sup>			t.b.d.	t.b.d.	t.b.d.	[187]
	81-86 GHz	no segmentation 125 MHz LGB 125 MHz UGB	4.75 GHz <sup>+</sup>			t.b.d.	t.b.d.	t.b.d.	[187]

LGB and UGB stand for lower and upper guard band, respectively.

+ In Europe and Australia, 70 and 80 GHz bands can be aggregated resulting in a total bandwidth of 8.5 GHz.

\* In the USA and Canada it is permitted to aggregate all 70-80-90 GHz bands resulting in a total bandwidth of 12.9 Hz.

### 5.2.3 Industrial standardization efforts

With respect to the 60 GHz band, the first international industry standard that covered the 60 GHz band is the IEEE 802.16 Standard for local and metropolitan area networks. This standard is for line of sight (LoS) wireless access systems. It was first published in 2001 and revised in 2004; its actual 2<sup>nd</sup> revised version IEEE 802.16-2009 was published in May 2009 [190]. In Japan, two standards related to the 60 GHz band were issued by the Association of Radio Industries and Business (ARIB) in 2001, that is the ARIB-STD T69 [191] and the ARIB-STD T74 [192]. The former is the standard for millimeter-wave video transmission equipment while the second one is for high-speed wireless LAN. Both standards cover the 59-66 GHz range defined in Japan. Both standards were updated in 2005. In 2005, the IEEE 802.15.3c task group (TG3c) was established to develop a millimeter-wave alternative physical layer for the existing IEEE 802.15.3 Standard for wireless personal area networks (WPAN). However, the IEEE 802.15.3c group was somehow outpaced by ECMA International, a European association for standardizing information and communication systems. At the end of 2008, ECMA published a standard for high-rate unlicensed 60 GHz wireless systems for WPAN [188]. This standard covers video streaming and WPAN applications in the 10 meter range, video and data LoS applications over shorter range (1-3 meters), and data applications over PtP LoS wireless links at less than 1 meter range.

## 5.3 Rationale for using photonics for future broadband wireless systems

This section will explore the generic advantages of using Microwave Photonics and more specifically Radio-over-Fiber (RoF) techniques for future broadband fixed wireless systems operating in the millimeter-wave frequency range.

Generally, the term “Radio over Fiber” (RoF) refers to a technology whereby light is modulated by a radio frequency (RF) signal and transmitted over an optical fiber link to facilitate wireless systems. Although radio transmission over fiber is used for multiple purposes, such as in cable television (CATV) networks and in satellite base stations, the term RoF is usually applied when this is done for broadband wireless networks.

In RoF systems, wireless signals are transported in optical form between a central station (CS) which is also called base station controller (BSC) and one or a set of radio base stations (BS) or radio transceiver stations (BTS) before being radiated through the air. Each base station is adapted to communicate over a radio link with at least one receiving station or at least one user's mobile station.

RoF transmission systems are usually classified into three main approaches or categories: baseband over fiber, IF over fiber, or RF over fiber (see Fig. 5.9). This is differentiated, depending on whether the transported radio signal can be directly transmitted after o/e-conversion (RF or radio over fiber) or requires electrical IF to RF or even baseband to RF up-conversion after o/e-conversion before being transmitted via air. Since RF over fiber allows for the most compact BSs and thus the lowest [193, 194], only this approach will be studied in the following.

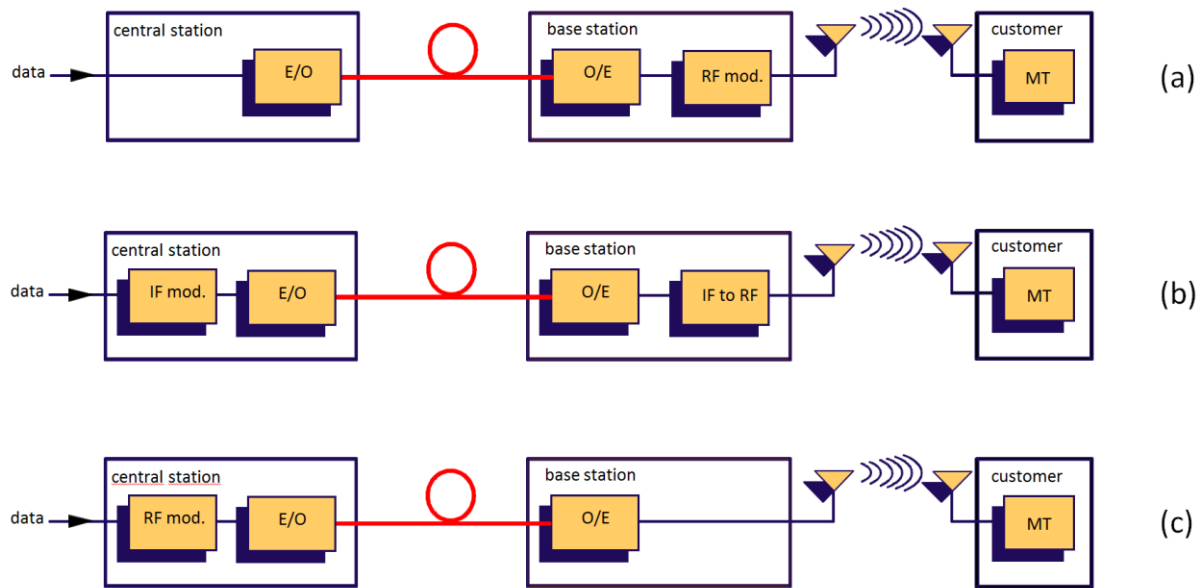


*Fig. 5.9 Schematics of photonic techniques for signal generation and transmission of Gb/s wireless signals. Baseband over fiber with baseband to RF up-conversion in the BS (a), intermediate frequency (IF) over fiber with IF to RF up-conversion in the BS (b), and RF over fiber (RoF) (c).*

In comparison to electronic baseband or RF transmission systems, RoF generally has the edge whenever high aggregate bit rates and/or long transmission distances are involved. Both advantages are deeply rooted in physics: First, the high optical carrier frequencies allow for high-capacity systems at very small relative bandwidths. For example, a mere 2.5% bandwidth at a carrier frequency of 193 THz (1.55 μm wavelength) opens up a 5 THz chunk of continuous communication bandwidth. Such “narrow-band” systems are much easier to design than baseband or RF systems with a large relative bandwidth. To further emphasize this: The cost for an optical modulator (Mach-Zehnder type) for performing a 10 Gbit/s modulation of a millimeter-wave carrier, e.g. at 60 GHz or 70/80 GHz, in the optical domain is about a few 100€. On the contrary, doing the same in the electrical domain is not just much more expensive, it is almost impossible with current electronic technology.

Besides the ability to process high bandwidth signals, another key advantage of RoF is that it allows transporting high-frequency RF signals at low loss. Today's optical telecommunication fibers can transmit an RF signal, e.g. 60 GHz, with less than 0.2 dB/km loss, the loss of a coaxial V-cable for 60 GHz is 6000 dB/km; more than four orders of magnitude larger. Obviously, this leads to very different system configurations. Whereas in all-electronic RF wireless systems all high-frequency electronics must be located in immediate proximity to the antenna, RoF systems enable centralizing costly electronics and optics required for high-frequency generation, modulation and processing in the BSC. This opens a path for so-called remote radio antennas reducing cost as it becomes possible to support more than just one antenna with the same centralized equipment.

Another cost advantage of photonic wireless systems expected by mobile system vendors (private discussions with Nokia Siemens Networks) is due to the fact that a photonic approach can generally address different carrier frequencies with only just small variations. This is due to the fact that the photonic approach offers much wider bandwidth, i.e. in the photonic domain the actual RF carrier frequency can vary over large frequency ranges. Thus, it appears at least possible to provide a photonic wireless system that could operate at microwave as well as millimeter-wave frequencies.

Furthermore, RoF greatly simplifies the configuration of BS, since each base station has only to perform optical to RF conversion and vice versa. Apart from the above mentioned three major advantages, other considerations sometimes come into play, such as the absence of electromagnetic interference or the low weight of optical fiber.

It is noteworthy to mention that to the authors' knowledge the recent demonstrations of broadband wireless systems with capacities in the ten gigabit range were all performed using photonic techniques.

The following summarizes the key advantages of using RoF for broadband millimeter-wave wireless systems as discussed in this section:

- RoF provides broadband modulation capabilities at low-cost
- RoF enables the centralization of costly mm-wave components in the BSC
- RoF allows low-loss RF signal transport over fiber and thus enables remote antenna sites
- RoF can potentially address different frequency bands
- RoF is immune to electromagnetic interference
- RoF utilizes low weight optical fiber

## 5.4 Link model for broadband photonic mm-wave wireless transmission

It is a challenge to design a wireless communication system that performs better than the state-of-the-art, especially when the requirements call for very high data rates and high carrier frequencies. Not only the wireless channel for broadband communication introduces several major impairments, the optical transmission of the radio signal over fiber also introduces several limitations. Even when limiting only to LoS PtP wireless links, several radio channel impairments, such as spectral bandwidth limitations, free-space path loss, noise, rain and fog attenuation, interferences, multi-path fading and various other factors weaken, delay, and distort the transmitted signal. On top of that, fiber-optic impairments like chromatic dispersion distort the radio signal when being transmitted over fiber as discussed in chapter 3. Obviously, not all of these impairments and their impacts on the systems' performance can be discussed in full detail within this work. However, as the focus of the work reported in this chapter is in developing a very high data rate photonic wireless system, a focus will be put on those impairments that have a major impact on the maximum wireless transmission rate. Knowing those impairments is an unconditional requirement for the development of photonic wireless systems operating at millimeter-wave carrier frequencies.

### 5.4.1 Wireless transmission capacity

Generally, the maximum transmission capacity of any wireless system per antenna polarization is determined by the well-known Shannon-Hartley theorem. This theorem or law gives a theoretical maximum bit rate that can be transmitted with an arbitrarily small bit error rate (BER), with a given average signal power over a channel with a bandwidth  $B$  which is affected by additive white Gaussian noise (AWGN), which is the case for most wireless as well as for most amplified optical transmission systems. Here, “arbitrarily” small BER means that, provided the conditions of the theorem are met, for any given BER, however small, we can find a coding technique that achieves this BER; the smaller the given BER, the more complicated will be the technique. The maximum achievable bit rate or capacity  $C$  in the case of a binary input channel is defined by the Shannon-Hartley theorem [195, 196] that states:

$$C = B \cdot \log_2 \left( 1 + \frac{S}{N} \right) \text{in bit/s} , \quad (79)$$

where S/N is the mean square signal to noise ratio. To avoid calculating the logarithm to the base 2, the maximum capacity  $C$  can be written as:

$$C = \frac{1}{\log_{10}(2)} B \log_{10} \left( 1 + \frac{S}{N} \right) \approx 3.32 \cdot B \log_{10} \left( 1 + \frac{S}{N} \right). \quad (80)$$

Assuming we transmit average signal per bit energy of  $E_b$  (Joules per bit) and the AWGN single sided power spectral density is  $N_0$ , we can re-write eq. (80) to

$$C = 3.32 \cdot B \log_{10} \left( 1 + \frac{E_b R}{N_0 B} \right), \quad (81)$$

where  $R$  is the data rate. If  $R$  is not too close to  $C$  or the BER is not too low, the transmitter and receiver may be fairly simple. Otherwise, more and more complex modulation and coding formats must be considered to achieve the required performance. If  $R$  is greater than  $C$ , it is not impossible to find a solution for a relatively high BER, but reducing that BER will lead to a situation where targets cannot be achieved. Thus, for any real technical system, the system's bit rate  $R$  must always be smaller than the maximum theoretical capacity  $C$ . Knowing that, eq. (81) becomes

$$\frac{R}{B} \leq 3.32 \cdot \log_{10} \left( 1 + \frac{E_b R}{N_0 B} \right). \quad (82)$$

The solid line in the following Fig. 5.10 depicts the maximum spectral efficiency  $R/B$  a communication system can accomplish according to the Shannon-Hartley theorem for a given signal-to-noise ratio (SNR) per bit ( $E_b/N_0$ ). Fig. 5.10 visualizes the theoretically available spectral efficiencies for four different modulation schemes, namely on-off keying (OOK), phase shift keying (PSK), quadrature amplitude modulation (QAM), and pulse position modulation (PPM). The required SNR per bit figures for the different modulation schemes are extracted from [197] for a  $\text{BER} = 2 \cdot 10^{-3}$ . This BER level was chosen as it reflects the minimum requirement, provided that modern forward-error-correction (FEC) with a typical overhead of about 7% is applied. Note that the data given in Fig. 5.10 represent theoretical limits; additional noise sources, nonlinearities and hardware implementation difficulties prevent the formats from operating at their theoretical limits, both in terms of spectral efficiency and sensitivity.

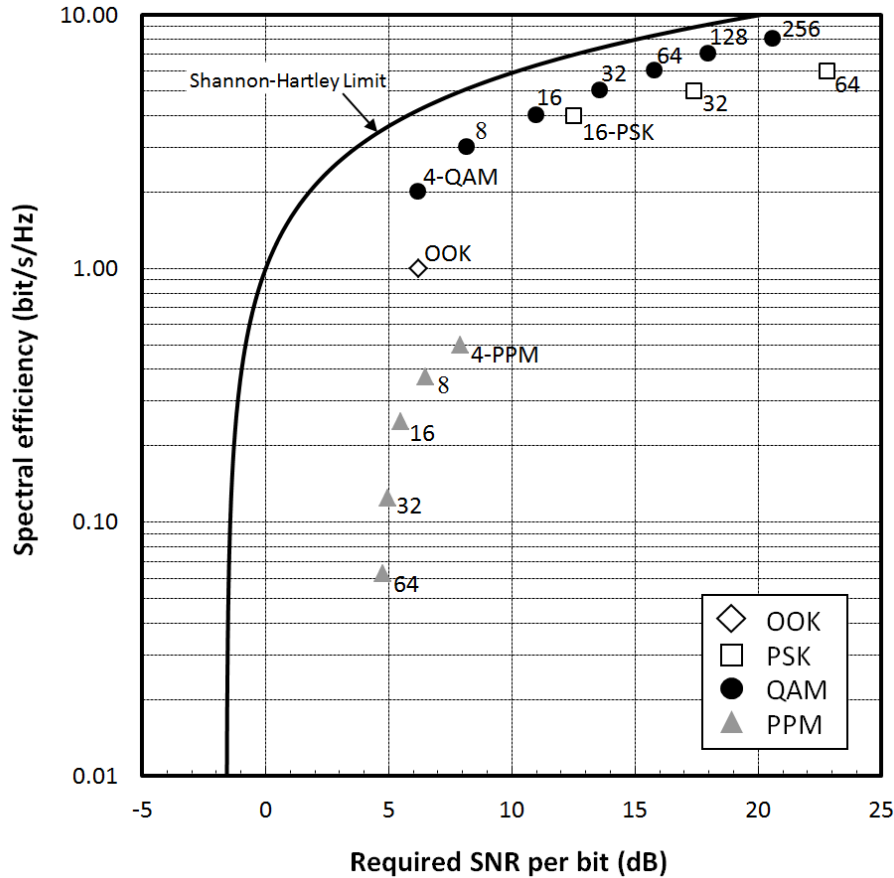


*Fig. 5.10 Spectral efficiencies for different modulation schemes: on-off keying (OOK), phase shift keying (PSK), quadrature amplitude modulation (QAM), and pulse position modulation (PPM). Required SNR per bit for the various modulation formats are all given for a BER =  $2 \cdot 10^{-3}$  [197]. The solid line represents the maximum spectral efficiency according to the Shannon-Hartley theorem, as given in eq. (82).*

As can be seen from Fig. 5.10, pulse position modulation (PPM) with  $M$  non-overlapping time slots per symbol significantly improves the sensitivity, i.e. reduces the signal-to-noise (SNR) ratio at the expense of an expanded signal bandwidth by  $M/\log_2(M)$  and thus a reduced maximum spectral density as compared to OOK, for example. Therefore, PPM is very suitable for sensitivity constrained communication systems, such as long reach free space optical communications. However, for capacity constrained systems, such as wireless systems, other modulation formats like  $M$ -ary orthogonal PSK or QAM modulation with  $M > 2$  offering a higher spectral efficiency as compared to OOK are more appropriate than PPM. Although both, QAM and PSK with the same number of modulation states  $M$ , offer the same spectral efficiency, the sensitivity requirements for QAM are less stringent, e.g. a 64-PSK modulation requires about 10 dB higher SNR than a 64-QAM signal. Thus, QAM modulation is widely used for wireless systems, e.g. for 802.11a/g WLAN.

Generally,  $M$ -QAM is a multilevel modulation format using a combination of phase and intensity modulation in which each symbol can be interpreted as a complex phasor with its in-phase (I) and quadrature-phase (Q) coordinates. The symbols can be either arranged in different circles (Star QAM) or can be positioned in a square (Square QAM). Fig. 5.11 schematically shows the constellation diagrams of some selected modulation formats including OOK, 8-PSK as well as some square-type QAM modulation formats.

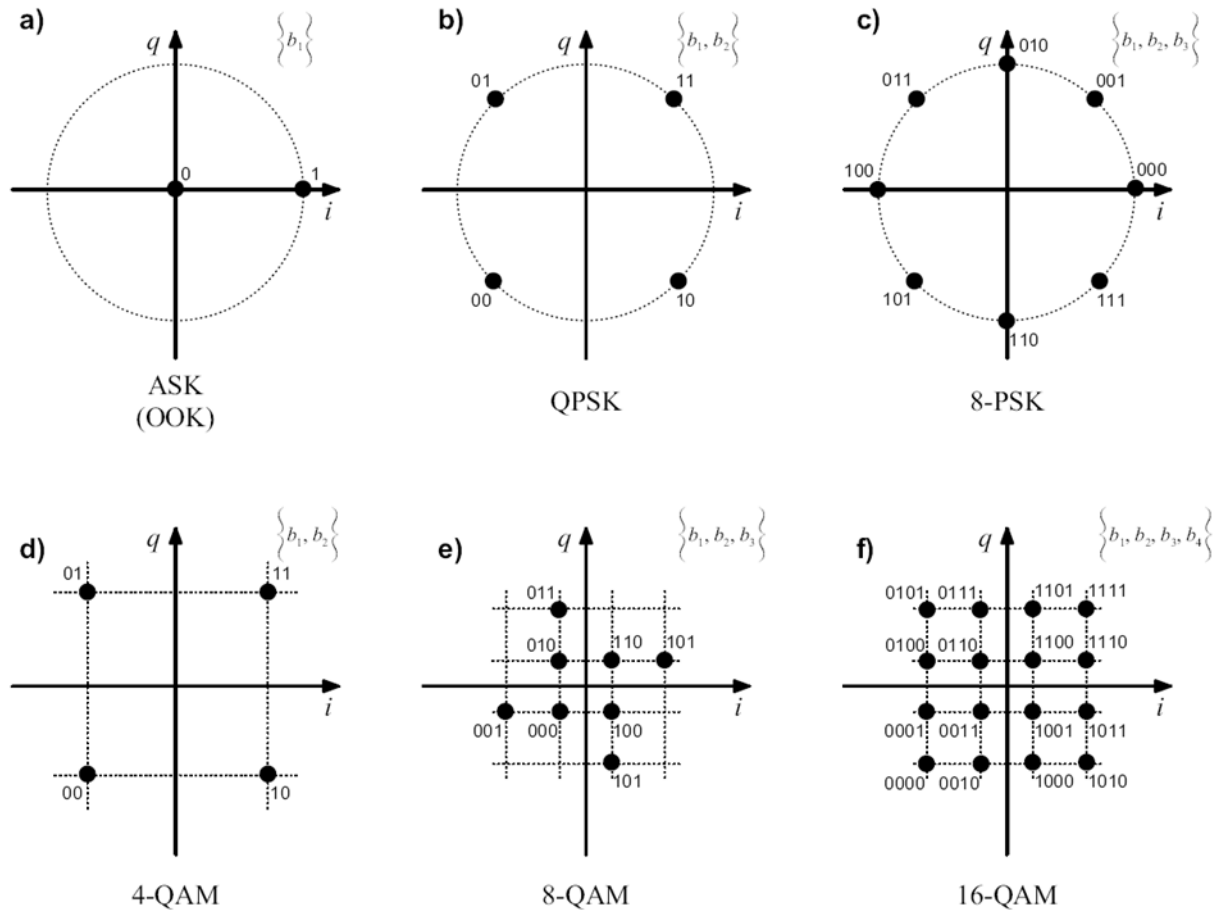


*Fig. 5.11 Constellation diagrams for different modulation formats showing the normalized vector coordinates for each symbol point and its bit mapping. Constellation is shown for conventional amplitude shift keying (ASK) which is usually denoted as on-off keying (OOK) (a). Also, constellations of higher modulation formats are shown, including quadrature phase shift keying (QPSK) (b), 8-ary phase shift keying (8-PSK) (c) as well as higher order square quadrature amplitude modulation (QAM).*

As mentioned above, conventional short-haul fixed wireless systems operating mostly in the microwave region (6-38 GHz) offer capacities from a few Mbit/s up to a few 100 Mbit/s. These maximum capacities are determined by the RF channel bandwidth permitted by the regulatory agency and the spectral efficiency of the modulation format used. For example, a system operating in the 23 GHz frequency band may use up to 56 MHz RF channel bandwidth (50 MHz in North America) which is limited by regulation. In such a 56 MHz channel, a simple modulation scheme like QPSK (4-QAM) with a maximum theoretical spectral efficiency of

2 bit/s/Hz (see Fig. 5.10) yields a maximum theoretically achievable throughput of ~90 Mbit/s considering an FEC with 6% overhead and a typical band roll-off of 10% (private discussions with Alcatel-Lucent Wireless Business Unit, Milano). In Fig. 5.23, the throughput capabilities of typical (FEC with 6% overhead, 10% band roll-off [198]) short-haul wireless systems is shown with respect to the given RF channel bandwidth and the modulation scheme used.

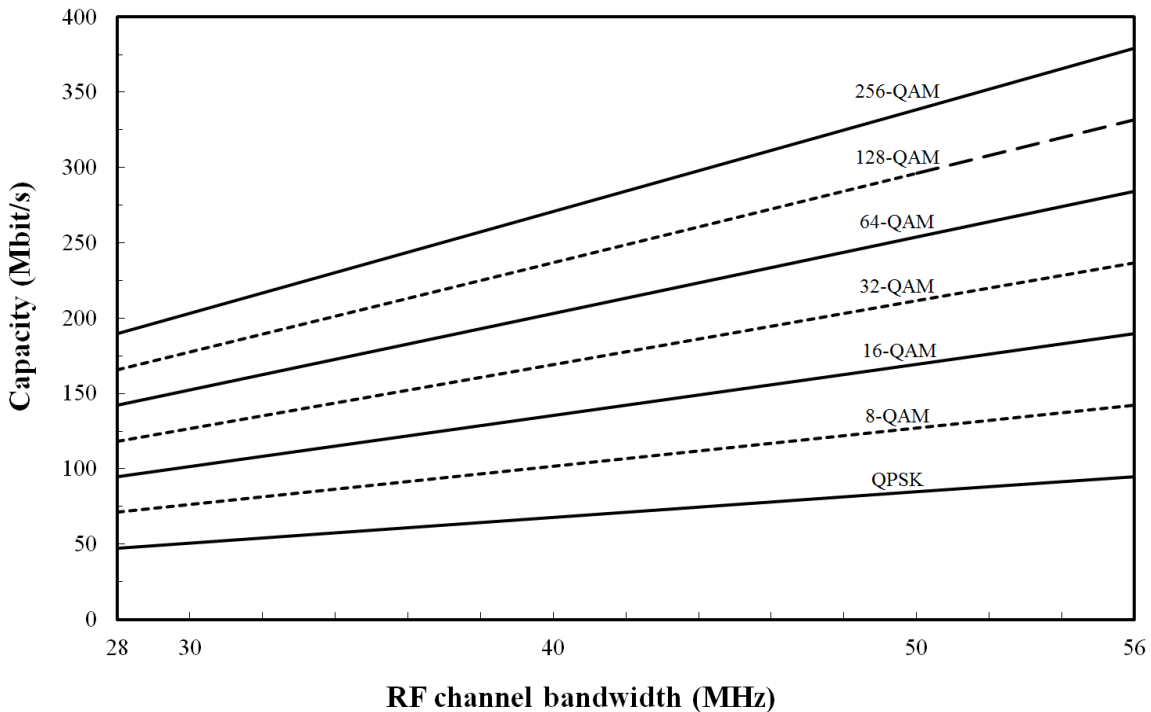


*Fig. 5.12 Throughput versus RF channel bandwidth for different modulation schemes. Calculation considers an FEC with 6% overhead and a typical band roll-off of 10%.*

As can be seen from Fig. 5.12, a typical microwave wireless system with only one radio equipment (one transmitter and one receiver), maxes out at about 400 Mbit/s even when using a complex 256-QAM modulation scheme. Today, in fact, a 56 MHz channel is used to transmit 311 Mbit/s (see for instance EN 302 062). Thus, if one aims at carrying a full-duplex 1 Gbit/s Ethernet signal, altogether 8 RF channels (for FDD) and 4 radios (i.e. 4 receiver and 4 transmitter units) would be required which is not only a problem due to high equipment and licensing cost but also because of the congestion in the microwave bands [199]. There are simply not enough free channels available in many locations, especially those with a dense population.

This situation is somewhat more relaxed in the millimeter-wave range. As discussed above, the available spectrum in the mm-wave region that had been opened up by regulatory agencies for wireless services is about 7 GHz in the 60 GHz band and 2 times 5 GHz in the 70/80 GHz bands. Thus, even for rather simple modulation formats like ASK (direct-detection OOK in the optical

domain) having a comparably low spectral efficiency of up to 1 bit/s/Hz, it would be possible to develop a Gigabit wireless link. Even 10 Gbit/s wireless links appear to be feasible when using higher-order modulation formats with higher spectral efficiencies.

### 5.4.2 Wireless channel model

As discussed above, the maximum theoretically achievable link capacity is primarily determined by the RF channel bandwidth and the modulation efficiency. The key parameter deciding upon the quality of the receipt signal and thus the key parameter determining the technically achievable throughput is the signal-to-noise (SNR) figure at the receiver, i.e. after the receiving antenna. Of course, with increasing channel bandwidth or with increasing wireless path length, the signal-to-noise (SNR) ratio at the receiver decreases and consequently, the SNR at the receiver and the receiver's sensitivity set an upper limit to the link's maximum capacity. In order to determine the SNR, it is necessary to study the environmental impairments, such as signal attenuation by propagation phenomena and weather conditions (e.g. rain). Also, technical impairments such as the antenna's gain, will be investigated in this section. Thereafter, the impairing optical, electrical and atmospheric noise contributions will be studied to allow describing the signal transport in the optical as well as in the wireless domain.

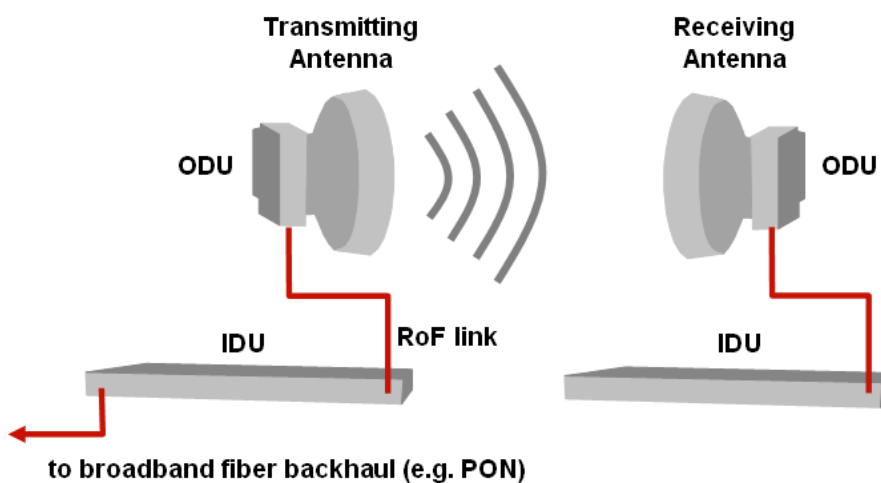


*Fig. 5.13 Illustration of the key components for a point-to-point (PtP) line of sight (LoS) wireless link using RoF transport between the indoor-units (IDU) and the outdoor units (ODU), i.e. the antennas.*

Fig. 5.13 illustrates the key components of a PtP LoS wireless link. It typically consists of an indoor unit (IDU) housing the photonic baseband and the RF up-conversion modules. In the IDU, the optical baseband signal is processed and up-converted to the radio frequency before it

is sent, using RoF transport to the outdoor units containing the o/e conversion unit and the antenna. The data signal is then transmitted over air within an RF channel that can vary according to the wireless standard used.

### Free-space wireless path loss

As discussed above, the radio channel places strong limitations on the performance of wireless communication systems because the transmission principles in wireless communications are quite complex. The transmission path between the transmitter and the receiver can vary from a simpler line of sight (LoS) to one that is severely obstructed by buildings, foliage and the terrain. Also, unlike in wired connections, wireless radio channels performance may vary with time. In this section, a model for the free-space wireless path loss is developed to support the system modeling and to allow for a theoretical investigation of environmental and technical impairments limiting the wireless capacity. As the main interest in this work is in high-capacity E-band PtP wireless links with LoS propagation, the discussion will be limited to those impairments that have a major impact on the capacity of such links. A typical realistic scenario for a broadband PtP link is shown in Fig. 5.14.

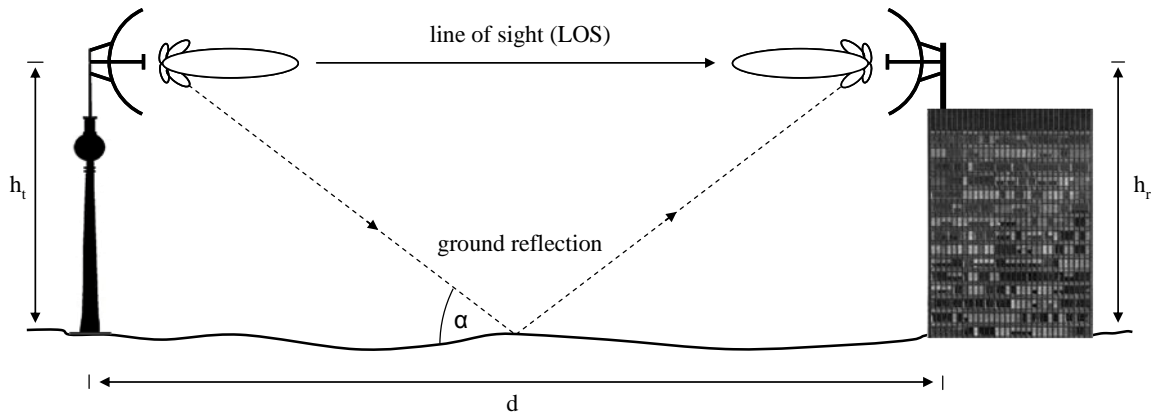


Fig. 5.14 Schematic of a point-to-point wireless link with line of sight (LoS) propagation path.

For a broadband wireless link used for mobile backhauling the antennas would typically be mounted either on an antenna tower or a high building. The height would thus vary between a few tens to a few hundreds of meters. The wireless distance very much depends on the channel frequency used. As this work is focusing on E-band (60-90 GHz) wireless, the expected average wireless path length would be approximately 2 km (see Fig. 5.6) for mobile backhauling and for last mile wireless access.

For developing a consistent RoF link model, it is at first necessary to calculate the wireless signal power detected by the receiving antenna which is set at a given distance  $d$  from the transmitting antenna. For doing so, the average power density (in units of  $\text{W/m}^2$ ) at the receiving antenna site must be determined which can be done using Maxwell's theory. Here, the averaged power density is given by the time averaged pointing vector

$$\langle \vec{S}(r) \rangle = \frac{1}{T} \int_0^T \vec{S}(r) dt = \frac{1}{T} \int_0^T (\vec{E} \times \vec{H}) dt = \frac{1}{2} \operatorname{Re} \left\{ \vec{E} \times \vec{H}^* \right\}. \quad (83)$$

Assuming an isotropic antenna, the wireless signal would be radiated as ball-like waves in all directions and consequently, all spectral field components of the Poynting vector would be different from zero. However, as the average wireless distance between two antennas is expected to be around 2 km (e.g. for wireless backhauling), the distance would be much larger than the free space wavelength. Also, the maximum antenna dimension (typically the reflector diameter for a high-gain E-band antenna is around  $D_{max} \sim 0.5\text{-}2 \text{ m}$ ) is small compared to the antenna distance. Given that the distance  $d$  between the antennas fulfills the following requirement

$$d > 2 \cdot \frac{D_{max}^2}{\lambda}, \quad (84)$$

it can be assumed that the receiving antenna is located within the Fraunhofer region, i.e. far-field conditions apply. For example, when operating at a 60 GHz carrier frequency (i.e. a free space wavelength of  $\lambda \approx 0.5 \text{ cm}$ ) with high-gain 45 dBi antennas (as requested by regulations) having a typical diameter of  $D_{max} \approx 1 \text{ m}$ , the distance must be larger than 400 m which is reasonable to assume in a typical scenario. If far-field conditions apply, the electrical and magnetic fields at the receiving system can be considered as plane transversal electromagnetic (TEM) waves having no radial components. Therefore, the resulting Poynting vector only has a radial component  $S_r$  which can be described as

$$\langle S_r(\vartheta, \phi) \rangle = \frac{1}{2} \frac{|E_\vartheta(\vartheta, \phi)|^2 + |E_\phi(\vartheta, \phi)|^2}{Z_0} d. \quad (85)$$

Here,  $Z_0$  represents the free space wave impedance

$$Z_0 = \sqrt{\frac{\mu_0}{\epsilon_0}} = 120 \cdot \pi \approx 377 \Omega. \quad (86)$$

Using eq. 54, the total transmitted power  $P_t$  can be calculated to be

$$P_t = \int_0^{2\pi} \int_0^{\pi} \langle S_r(\vartheta, \phi) \rangle \cdot r^2 \cdot \sin \vartheta \cdot d\vartheta d\phi. \quad (87)$$

In case of an isotropic transmitting antenna, the power density  $\langle S_r(\vartheta, \phi) \rangle$  at a distance  $r$  from the radiating source is constant, i.e. it is independent of  $\vartheta$  and  $\phi$ , and according to the above equation the total transmitted power  $P_t$  can be expressed as

$$P_t = 4\pi \cdot r^2 \cdot S_r. \quad (88)$$

Of course, in a PtP wireless link directive antennas must be used instead of isotropic ones. Assuming that the maximum lobe efficiency of the transmitting antenna is pointing exactly towards the receiving system, which certainly is the case in a real system, then the power density  $S_r$  at a distance  $r$  from the radiating source is given by

$$S_r = \eta_t \cdot \frac{P_t}{4\pi r^2} \cdot D_t. \quad (89)$$

Here,  $D_t$  denotes the antennas' directivity and  $\eta_t$  is the transmitting antennas' efficiency, accounting for conduction and dielectric losses of the antenna. Typically, for parabolic antennas the efficiency ranges from 55% to 70% [200]. The antennas' gain which is often given in the specification sheets is defined by

$$G_t = \eta_t \cdot D_t. \quad (90)$$

In order to calculate the total power detected by the receiving antenna, typical geometrical and environmental circumstances of a wireless PtP E-band backhauling link must be taken into account. As already discussed above, in a typical E-Band PtP LoS scenario, the antenna's heights  $h_t$  and  $h_r$  would be in the order of 50 – 300 m and the average distance between the two antennas is approximately 2 km. Furthermore, as discussed in section 5.2.2, very high-gain ( $\sim 45$  dBi)

“pin-pointing” type antennas must be used to fulfill the regulative requirements. Usually, dish-like antennas with a high-gain parabolic reflector, such as Cassegrain antenna, are used in those cases. In this case, the antenna’s gain can be approximately calculated according to the following equation [200]:

$$G = \eta \left( \pi \cdot k / \gamma \right)^2, \quad (91)$$

where  $\gamma$  denotes the half power beam width (HPBW),  $\eta$  is the antenna’s net efficiency and  $k$  depends on the shape of the reflector and the method of illumination. Typical values for the net efficiency and the  $k$ -factor are  $\eta \approx 0.55$  and  $k = 70^\circ$ , respectively [200]. Thus, the gain can be expressed directly in terms of the half power beam width  $\gamma$

$$G \approx 27.000 / (\gamma^\circ)^2, \quad (92)$$

where  $\gamma^\circ$  is expressed in degrees. From this well-known engineering approximation for parabolic antennas, we can estimate the HPBW of a 45 dBi antenna to be around  $0.92^\circ$ . Considering further that the angle for ground reflection according to Fig. 5.14 is about  $5.7^\circ$  for a 100 m high antenna tower, it can be seen that the power density transmitted towards the ground is very low and thus, ground reflection can be neglected in the first instance.

Because of that, one can assume only LoS propagation for calculating the total received power, reflections from the ground or other large objects, as well as diffraction from edges and corners of terrain or buildings can be neglected in the first instance. Also, scattering from foliage or other small objects is negligible. However, attenuation from the atmosphere and from rain scattering must be considered.

Consequently, in the case of two antennas ideally pointing to each other, the received power  $P_r$  can be calculated from the power density at the receiving antenna site

$$P_r = \iint_{A_E} \vec{S}_r(\nu, \phi) dA_E \approx S_r \cdot A_E \quad . \quad (93)$$

Here,  $A_E$  denotes the effective area of the receiving antenna which is given by

$$A_E = \eta_r \cdot \left( \frac{\pi \cdot d_{\text{ant}}^2}{4} \right) = \eta \cdot \frac{\lambda^2}{4\pi} \cdot Dr, \quad (94)$$

where  $d_{\text{ant}}$  represents the diameter of the parabolic antenna. For a sufficient long distance  $d$  between the transmitting and receiving antennas, i.e. for far-fields conditions, the power density can be considered as being constant over the receiving antennas aperture and thus, the received power can be calculated using eq. (89) to be

$$P_r = P_t \cdot \frac{\eta_t D_t}{4\pi \cdot d} \cdot A_E \cdot \left| \vec{a}_t \cdot \vec{a}_r^* \right|^2 \cdot \exp(-\alpha_{pl} \cdot d). \quad (95)$$

Here,  $a_t$  and  $a_r$  denote the polarization vectors of the transmitting and receiving antennas, respectively, taken in the appropriate direction. The total absorption coefficient of the intervening medium is denoted as  $\alpha_{pl}$ . By introducing eq. (94) into eq. (95), the total received power can be expressed as

$$P_r = P_t \cdot \frac{\eta_t D_t}{4\pi \cdot d} \cdot \frac{\eta_r D_r}{4\pi \cdot d} \cdot \lambda^2 \cdot \left| \vec{a}_t \cdot \vec{a}_r^* \right|^2 \cdot \exp(-\alpha_{pl} \cdot d). \quad (96)$$

If impedance mismatch of the transmitting and receiving antenna is also considered, the received power can be expressed as:

$$P_r = P_t \cdot (\eta_t D_t) \cdot (\eta_r D_r) \cdot \left( \frac{\lambda}{4\pi \cdot d} \right)^2 \cdot \left( 1 - |\Gamma_t|^2 \right) \cdot \left( 1 - |\Gamma_r|^2 \right) \cdot \left| \vec{a}_t \cdot \vec{a}_r^* \right|^2 \cdot \exp(-\alpha_{pl} \cdot d). \quad (97)$$

Here,  $\Gamma_t$  and  $\Gamma_r$  represent the reflection coefficients of transmitting and receiving antennas, respectively.

For a lossless, linear and isotropic medium and for ideal, i.e. reflection-free, antennas that are pointing to each other in a perfect way, the above equation can be simplified to the well-known Friis transmission formula [201]

$$P_r = P_t \cdot G_t \cdot G_r \cdot \left( \frac{\lambda}{4\pi \cdot d} \right)^2. \quad (98)$$

For calculating the frequency dependent free-space path loss for an ideal line of sight (LoS) wireless link in decibel, the Friis equation can be expressed as

$$L_{Free-Space} = G_T + G_R - 92.45 - 20 \cdot \log(d) - 20 \cdot \log(f) . \quad (99)$$

Here,  $G_T$  and  $G_R$  represent the antenna gain in dBi, the distance  $d$  is given in km and the frequency  $f$  in GHz. As can be seen, the free-space loss increases quadratically with the wireless carrier frequency  $f$ . This can also be interpreted as a reduction of the antenna area of the receiving antenna with rising frequency. In Fig. 5.15, the free-space path loss  $L_{Free-Space}$  is shown for some important wireless frequencies, assuming isotropically radiating antennas.

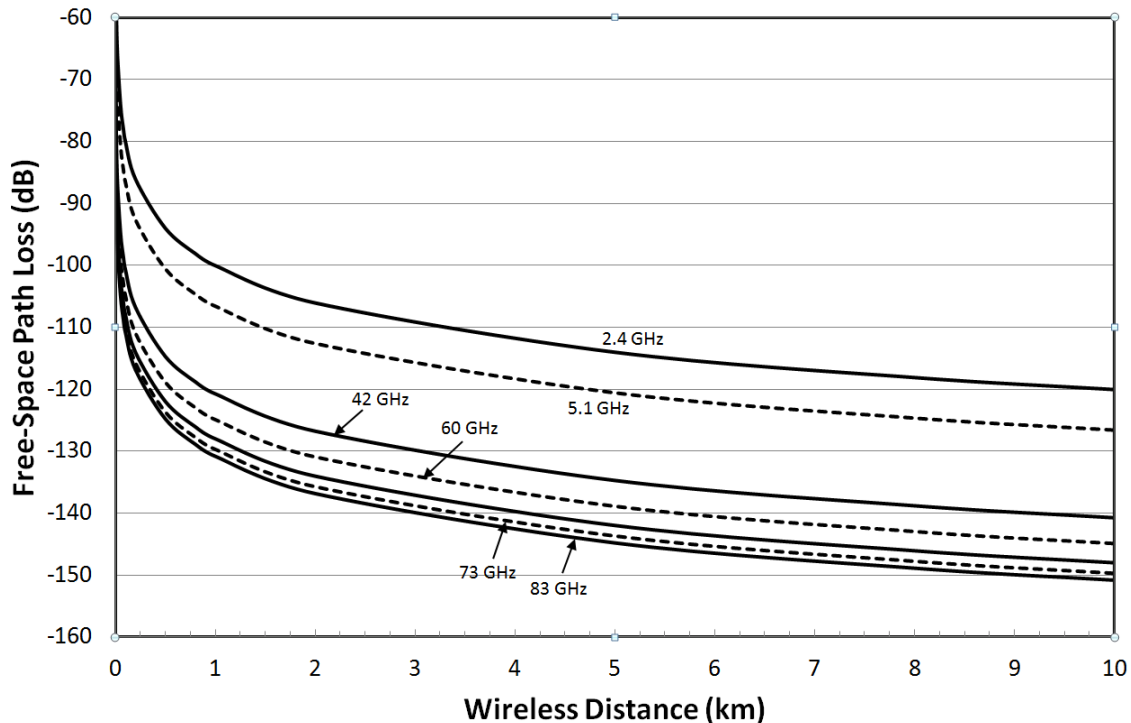


Fig. 5.15 A point-to-point wireless link with line of sight (LoS) propagation path.

As can be seen from Fig. 5.15, even for comparably short distances of about 500 m, the free-space loss of a millimeter-wave carrier ( $> 30$  GHz) is already in the range of 100 dB and higher. Since the free-space loss scales with  $1/f^2$ , the path loss in a 2.4 GHz WLAN system is about 30 dB lower than for an E-band (70/80 GHz) wireless link, but those wireless systems are used in

quite different applications. More important is the comparison between a microwave PtP link operating at 26 GHz and an E-band PtP link. Here, the free-space path loss of the E-band system is “only” about 10 dB larger, a fact that of course has to be taken into account when designing an E-band link, but not at all a fundamental limitation.

### **Atmospheric attenuation in the millimeter-wave regime**

In microwave wireless systems, transmission loss is accounted for mainly by the above discussed free space loss, gaseous attenuation is negligible for most cases. However, in the millimeter-wave bands, additional loss factors including gaseous losses and rain attenuation in the transmission medium must be considered.

While propagating through the atmosphere, millimeter-waves are absorbed by molecules of oxygen, water vapor and other gaseous atmospheric constituents. These losses are greater at certain resonance frequencies, coinciding with the mechanical resonant frequencies of the gas molecules. In general, the atmosphere comprises of different gases including  $N_2$ ,  $O_2$ ,  $H_2O$ ,  $CO_2$ ,  $SO_2$ , inert gases and several pollutants. Many of these gases exhibit molecular resonance frequencies, i.e. absorption lines, in the millimeter-wave range. Near 60 GHz, many oxygen absorption lines merge together at sea-level pressures, forming a single, broad absorption band.

For frequencies up to about 1000 GHz, the atmospheric attenuation can be most accurately described at any value of pressure, temperature, and humidity by means of a summation of the individual resonance lines from oxygen and water vapor, together with small additional factors for the pressure-induced nitrogen attenuation above 100 GHz and a wet continuum to account for the excess water vapor-absorption found experimentally [202]. Fig. 5.16 shows the atmospheric attenuation from 0 to 1 000 GHz for a pressure of 1013 hPa and a temperature of 15° C for the cases of a dry atmosphere with a water content of 1 g/m<sup>3</sup> and a water-vapor density of 7.5 g/m<sup>3</sup>. The later one represents 59% humidity at a temperature of 15°C.

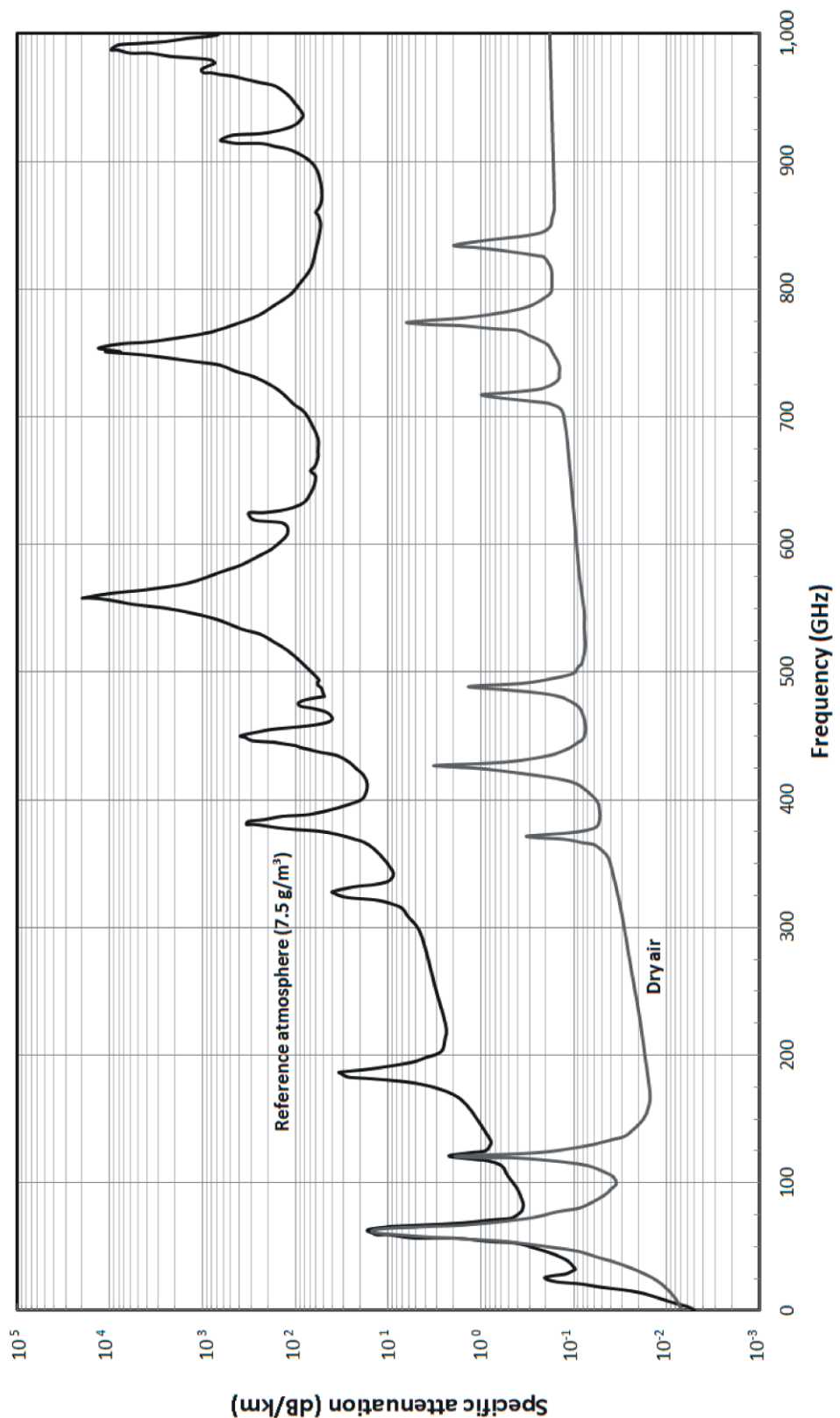


Fig. 5.16 A point-to-point wireless link with line of sight (LoS) propagation path.

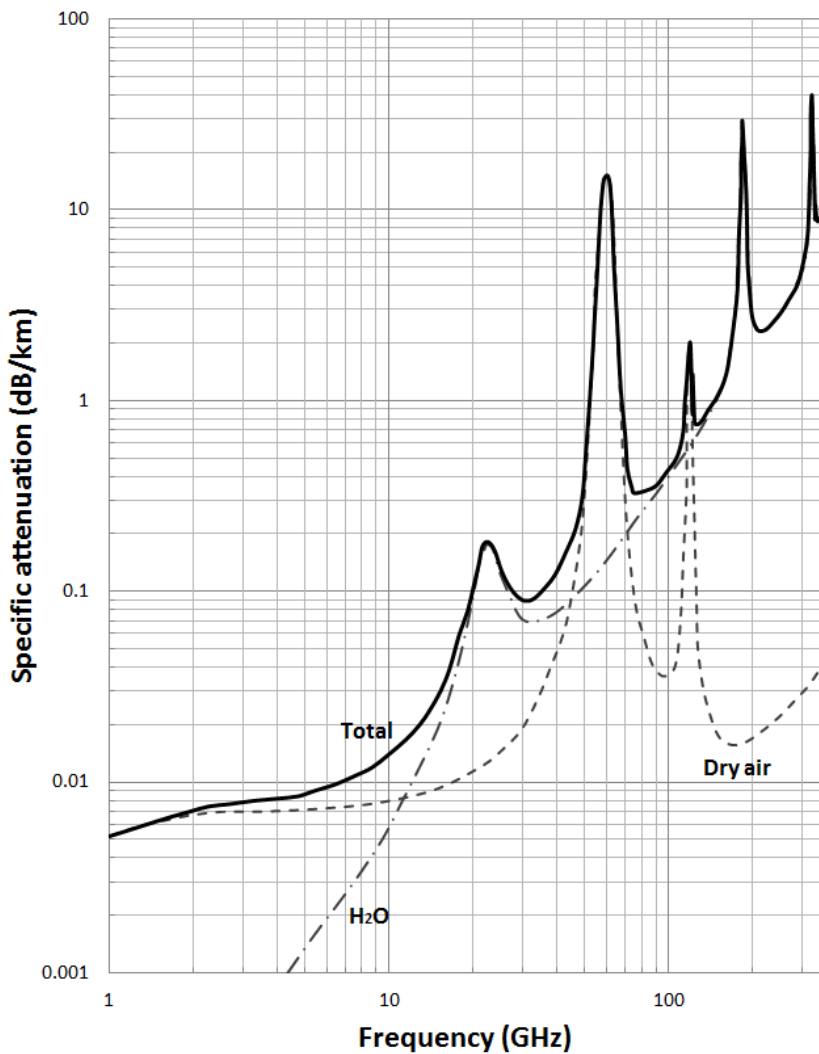


Fig. 5.17 Specific attenuation from 1 to 350 GHz for dry air at sea-level (air pressure of 1013 hPa, temperature of 15°C) and for water vapor with a density of 7.5 g/m<sup>3</sup>.

and, therefore, shorter propagation distance. For current technology, the important absorption peaks occur at 24 and 60 GHz. The spectral regions between the absorption peaks provide windows where propagation can more readily occur. The transmission windows are at about 35 GHz, 94 GHz, 140 GHz and 220 GHz.

### Rain attenuation in the millimeter-wave regime

While losses due to free-space propagation and atmospheric gases can be predicted in an accurate way, the attenuation due to rain, which is mainly dependent on the rain amount, but also on the size of the rain drops, is much more complex. It is especially difficult to assess the

For lower frequencies up to 350 GHz and altitudes from sea level to 5 km, a good approximation for the atmospheric attenuation is found by considering only the specific attenuation of dry air and water vapor. The absolute difference between these results and more precise figures considering the different gaseous absorption sources is generally less than 0.1 dB/km and reaches a maximum of 0.7 dB/km near 60 GHz [202]. Fig. 5.17 shows the specific attenuation for a water content of 1 g/m<sup>3</sup> and 7.5 g/m<sup>3</sup>. It shows several peaks that occur due to absorption of the radio signal by water vapor ( $H_2O$ ) and oxygen ( $O_2$ ). At these frequencies, absorption results in high attenuation of the radio signal

intensity of the rainfall (i.e. the rain rate in mm/h) in specific regions, although a large set of empiric datasets is available [203-205]. Even many cities have microclimates where temperature and rain rates differ significantly from one area to another.

The ITU has published a model that allows calculating the specific attenuation millimeter-wave experience due to rainfall. Fig. 5.18, shows the specific rain attenuation between 1-1000 GHz for different rain rates [206].

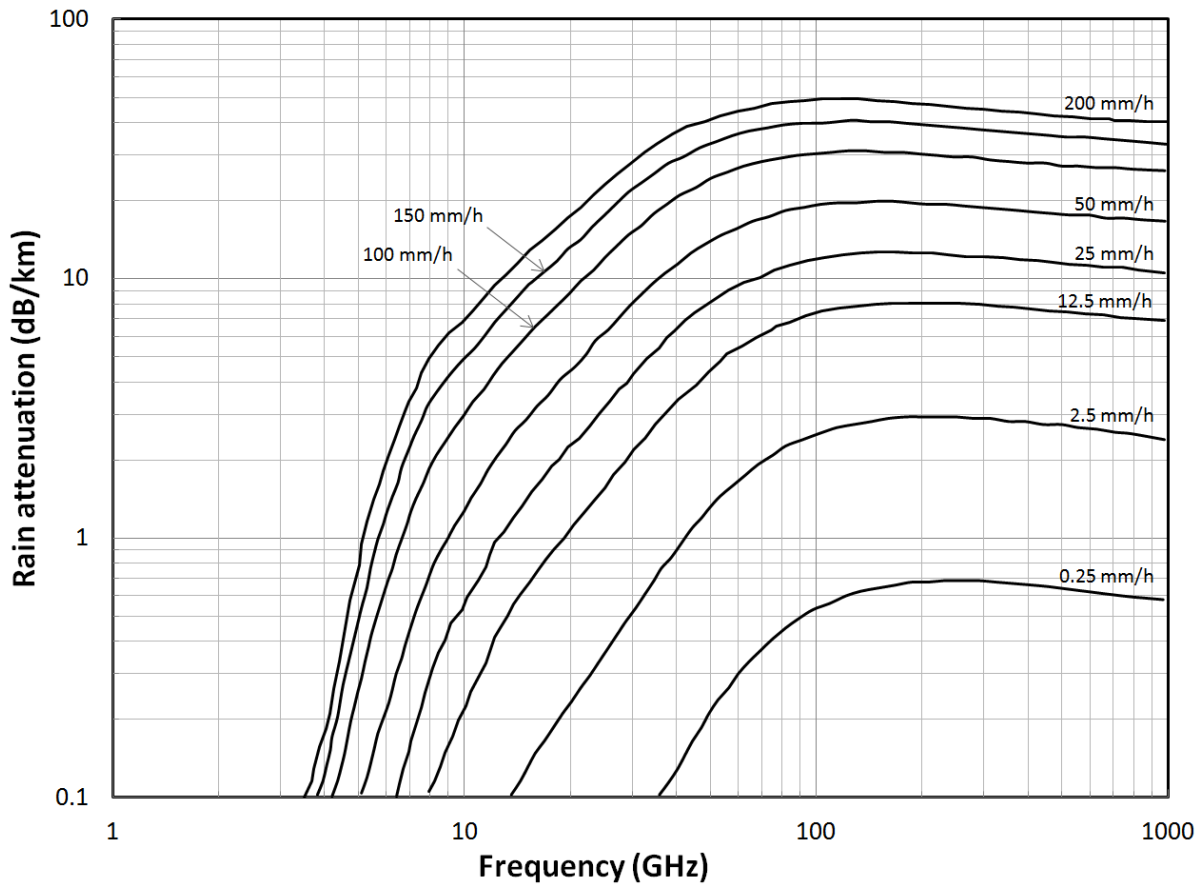


Fig. 5.18 A point-to-point wireless link with line of sight (LOS) propagation path.

As can be seen from Fig. 5.18, for microwave frequencies below 10 GHz, rain attenuation can almost be neglected. Here, rain attenuation is below 2 dB/km, even for heavy rainfall with precipitation amounts of 50 mm/h. At higher frequencies, however, rain attenuation significantly contributes to the overall losses. In the E-band (60-90 GHz) for example, rain attenuation reaches figures of 20 dB/km for precipitation amounts of 50 mm/h. Consequently, rainfall is the dominant factor when designing a millimeter-wave wireless link for the 70 GHz and 80 GHz bands, where atmospheric attenuation is below 1 dB/km. Only in the 60 GHz band and for moderate rainfall up to 5 mm/h, atmospheric attenuation dominates. This is because several

oxygen absorption lines merge together, resulting in a maximum gaseous attenuation of up to 16 dB/km.

### Total wireless path loss for E-band wireless PtP links

The total path loss  $L_{TotalPath}$  is further calculated by adding the specific attenuation coefficients for free-space path loss  $L_{Free-Space}$ , gaseous attenuation  $L_{Gas}$ , and rain attenuation  $L_{Rain}$  discussed above.

$$L_{Total Path} = L_{Free-Space} + L_{Gas} + L_{Rain} \quad (100)$$

The following figures show the total path loss within the E-band for different path lengths and different precipitation amounts.

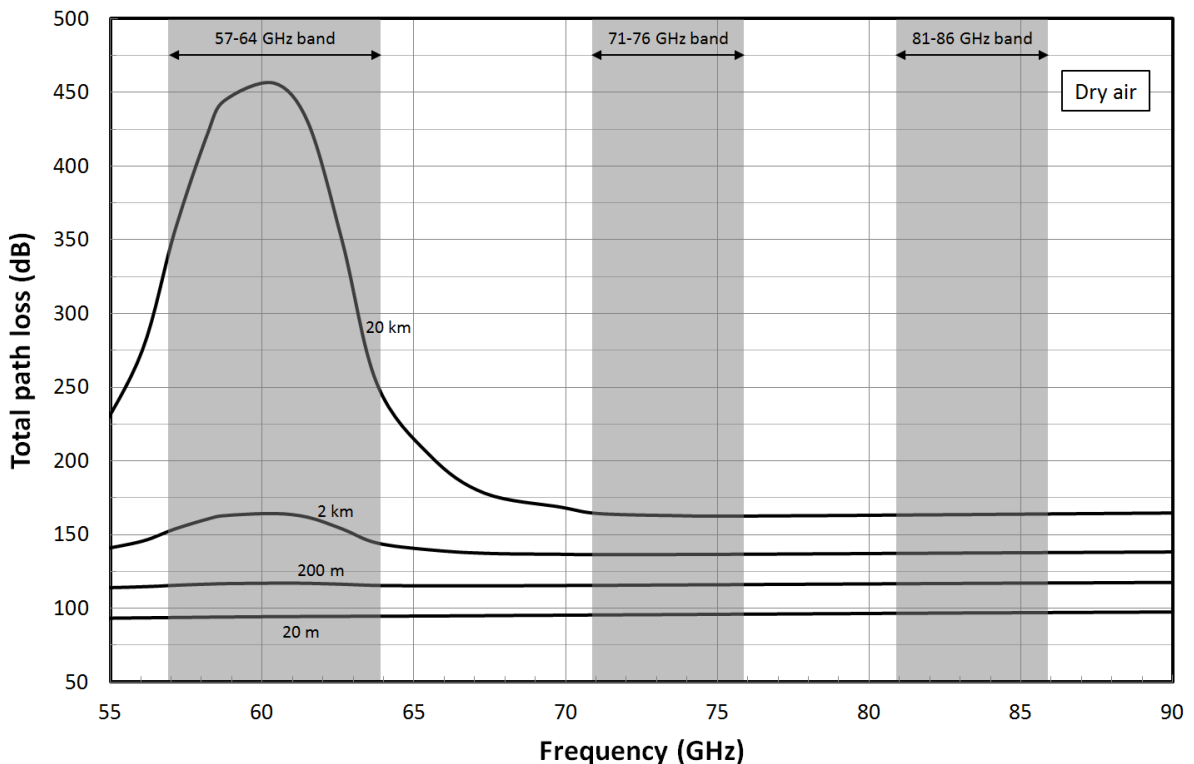


Fig. 5.19 A point-to-point wireless link with line of sight (LoS) propagation path.

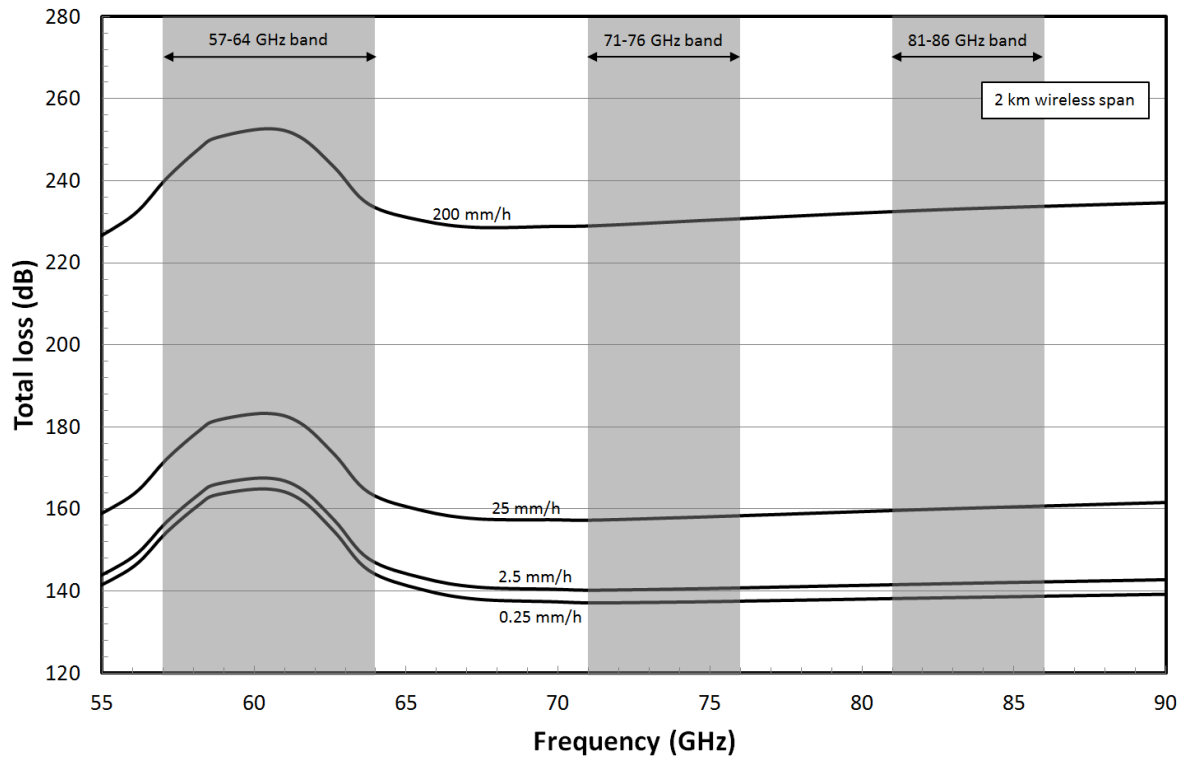


Fig. 5.20 A point-to-point wireless link with line of sight (LoS) propagation path.

### 5.4.3 Noise modeling

This section discusses the relevant noise sources contributing to the overall noise in a photonic wireless link. This includes thermal noise, shot noise, noise from optical sources and amplifiers, such as relative intensity noise (RIN), noise from amplified spontaneous emission (ASE) and atmospheric noise.

#### Thermal noise

Thermal noise consists of additional current fluctuations that occur when a voltage is applied and a macroscopic current starts to flow. It can be modeled by a current source in parallel with the resistor. The root mean square value of the current source is found to be

$$\langle i_{th}^2 \rangle = \frac{4 \cdot k \cdot T \cdot B_{el}}{Z_{ref}}, \quad (101)$$

where  $k$  is Boltzmann's constant in joules per kelvin,  $T$  is the resistor's absolute temperature in kelvins,  $z_{ref}$  is the resistor value in ohms, and  $B_{el}$  is the bandwidth in hertz in which the noise is accumulated.

In a cascaded scenario with several resistors in series, the noise generated at the reference resistor can transfer noise to the remaining circuit. The maximum noise power transfer happens with impedance matching, i.e. when equivalent resistance  $z_{out}$  of the remaining circuit is equal to the noise generating resistance  $z_{ref}$ . In this case, the noise power transfer to the circuit is given by

$$\begin{aligned} N_{el,th} &= k \cdot T \cdot B_{el} \Big|_{z_{out}=z_{ref}} \\ N_{el,th}^{dBm} &= 10 \cdot \log_{10} \left( \frac{k \cdot T \cdot B_{el} \Big|_{z_{out}=z_{ref}}}{1 \text{ mW}} \right) \\ &\approx -174 \text{ dBm} \Big|_{z_{out}=z_{ref}, B=1 \text{ Hz}, T=290 \text{ K}} , \end{aligned} \quad (102)$$

where  $N_{el,th}$  and  $N_{el,th}^{dBm}$  are the noise power in Watt and in dBm, respectively. As can be seen, thermal noise power at room temperature within a bandwidth of 1 Hz is -174 dBm.

### Shot noise

A fundamental limit to the optical intensity noise as observed in many situations is given by *shot noise*. Shot noise is a quantum noise effect related to the discreteness of photons and electrons. It results from statistical quantum fluctuations, that is, variation in the number of photons detected by a photodetector at a given optical intensity. Thus, it can be interpreted as arising from the random occurrence of photon absorption events in a photodetector, not as noise in the light field itself, such as relative intensity noise (RIN) which is further discussed below. In addition to photon shot noise, there can be additional shot noise from the dark leakage current in the photodetector; this noise is sometimes known as "dark shot noise" or "dark-current shot noise". Like thermal noise, photon shot noise and dark current noise exhibit Gaussian probability density distributions, and the resulting noise power is described as

$$\begin{aligned} N_{el,shot} &= \langle i_{shot}^2 \rangle \cdot z_{ref} + \langle i_{dark}^2 \rangle \cdot z_{ref} \\ &= 2 \cdot q \cdot B_{el} \cdot (P_{opt,in} \cdot \eta_{OE,DC} + I_{dark}) \cdot z_{ref} , \end{aligned} \quad (103)$$

where  $I_{dark}$  denotes the dark current. The terms  $\langle i^2_{shot} \rangle$  and  $\langle i^2_{dark} \rangle$  represent the mean-squared values of the photon shot noise and the dark noise current.

### Relative intensity noise

Intensity noise of a laser results partly from quantum noise (associated with laser gain and resonator losses) and partly from technical noise sources, such as excess noise of the pump source, vibrations of resonator mirrors, thermal fluctuations in the gain medium, etc. The resulting intensity noise also depends on the operation conditions; in particular, it often becomes weaker at high pump powers, where relaxation oscillations are strongly damped.

In the context of intensity noise (optical power fluctuations) of a laser, it is common to specify the relative intensity noise (RIN), which is the power noise normalized to the average power level. The optical power of the laser can be considered to be

$$P_{opt}(t) = \overline{P_{opt}} + \delta P_{opt}(t), \quad (104)$$

with an average value and a fluctuating quantity  $\delta P$  with zero mean value. The relative intensity noise is then that of  $\delta P$  divided by the average power. The relative intensity noise can then be statistically described with a power spectral density (PSD)

$$S(f) = \frac{2}{\overline{P_{opt}}^2} \int_{-\infty}^{+\infty} \delta P(t) \delta P(t + \tau) e^{j\omega\tau} d\tau \quad (105)$$

which depends on the noise frequency  $f$ . It can be calculated as the Fourier transform of the autocorrelation function of the normalized power fluctuations  $\delta P(t)$ , but for real lasers it is usually measured with a photodiode and an electronic spectrum analyzer. The factor of 2 in the formula above leads to a one-sided PSD. The units of the RIN PSD are  $\text{Hz}^{-1}$ , but it is common to specify a laser's RIN by using its RIN noise figure  $NF_{rin}$  given in 10 times the logarithm to base 10 of the RIN in  $\text{dBc/Hz}$ .

For an analog optical link employing a laser with a RIN figure  $NF_{rin}$ , the noise power resulting from the laser's RIN after o/e-conversion can be calculated as follows:

$$\begin{aligned} N_{el,rin} &= \langle i_{rin}^2 \rangle \cdot z_{ref} \\ &= 10^{NF_{rin}/10} \cdot B_{el} \cdot I_{ph}^2 \cdot z_{ref} \\ &= 10^{NF_{rin}/10} \cdot B_{el} \cdot (P_{opt,in} \eta_{OE,DC})^2 \cdot z_{ref} . \end{aligned} \quad (106)$$

Here,  $I_{ph}$  is the generated photocurrent,  $\langle i_{rin}^2 \rangle$  the mean-squared value of the RIN-induced photocurrent, and  $z_{ref}$  the reference impedance. The generated photocurrent can further be expressed in terms of the optical input power  $P_{opt,in}$  and the photodetector's DC conversion efficiency.

It should be stated, however, that unlike shot or thermal noise, the RIN frequency spectrum is not flat over the frequencies of interest. Fig. 5.21 is a plot from *Coldren and Corzine* (1995) that shows the calculated RIN spectrum for a typical waveguide diode laser. As can be seen, the RIN spectrum is constant at low frequencies, peaks at the relaxation resonance frequency and then falls to the shot noise level above resonance. In the RIN dominated portion of the spectrum, i.e. less than the relaxation peak, the noise power should vary at the square of the laser power, as can be seen from eq. (106). For frequencies larger than the relaxation peak of the peak, i.e. in the shot noise dominated region, the noise power only varies linearly with the laser power. Indeed, over the range of optical powers from 0.25 mW to 4 mW we would expect a 24 dB change in the RIN noise power but only a 12 dB change in the shot noise power. From Fig. 5.21 we see 22 dB and 11 dB, respectively.

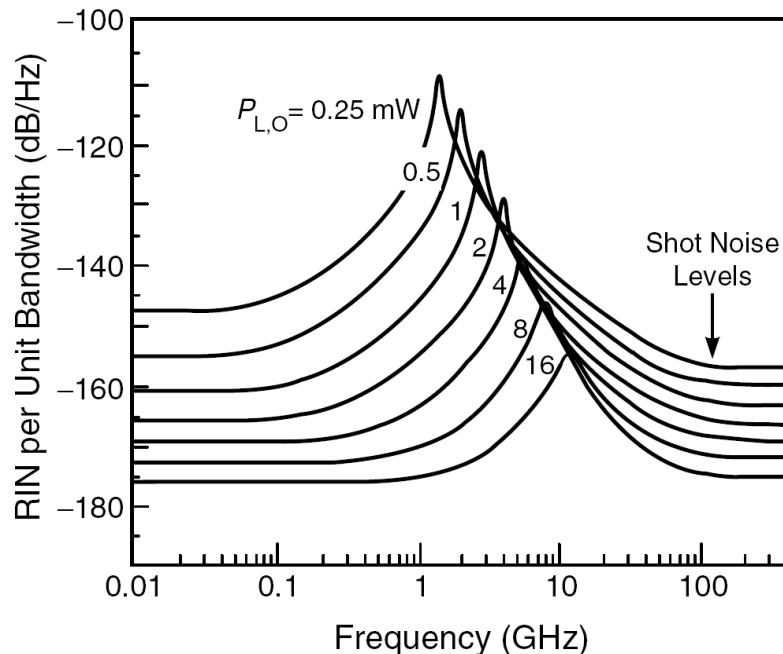


*Fig. 5.21 RIN vs. frequency for an in-plane diode with the laser's average optical power as a parameter [207].*

From the above discussion, it can be concluded that the calculation of the frequency-independent RIN noise calculation at the photodetector's output using eq. (106) with an average RIN noise figure  $NF_{rin}$  is an approximation which is reasonable only for the RIN dominated frequency spectrum. In other words, the laser output power should be well in the mA-range, given that the GHz-modulation bandwidths are considered here. Furthermore, for modulation bandwidths well in the GHz-range the excess RIN noise at the relaxation frequency must be taken into account instead of simply using the usually given RIN noise figure which is typically specified at low offset frequencies from the optical carrier.

### Amplified spontaneous emission noise

The amplified spontaneous emission noise originates from optical amplifiers, such as EDFA, which do not only amplify the desired signal (stimulated emission) but also generate a significant amount of amplified spontaneous emission. In the absence of an input signal, the noises detected by a PD are thermal noise, ASE-ASE and ASE-shot noise. When a signal is present, the noise is increased by signal-shot noise and signal-ASE beat noise contributions.

Generally, an EDFA is described as a linear amplifier with an optical gain  $G_{opt}$  in conjunction with a Gaussian noise source due to amplified spontaneous emission (ASE) acting over the optical bandwidth of interest. The resulting optical noise bandwidth is here determined by the gain spectrum of the EDFA but may be further limited by optical multiplexers or filters, as well

as the responsivity of the photodetector at certain wavelengths. This leads to the above mentioned additional noise contributions, mainly ASE-ASE, signal-ASE beating, and ASE-shot noise.

According to the well-known standard field-beating theory [208], describes the ASE noise as a Gaussian noise with a narrow-band (bandwidth  $B_{\text{opt}}$ ) white spectrum of double-sideband spectral density  $\frac{1}{2} hf(G_{\text{opt}} - 1) \rho_{\text{sp}}$ , where  $\rho_{\text{sp}}$  denotes the spontaneous power density,  $hf$  the photon energy and  $G_{\text{opt}}$  the gain of the amplifier. Using this approach, the noise figure  $NF_{\text{opt}}$  of an optical amplifier, such as an EDFA, can be expressed as [209]

$$NF_{\text{opt}} = \frac{2 \cdot \rho_{\text{sp}}}{hf \cdot G_{\text{opt}}} . \quad (107)$$

Assuming that the amplifier's gain is high, i.e.  $G_{\text{opt}} \gg 1$ , and assuming further that the receiver's electrical bandwidth is significantly smaller than the optical bandwidth  $B_{\text{opt}} \gg B_{\text{el}}$  (which is valid for most practical systems), the noise power due to ASE-ASE beating can be described as [210]

$$\begin{aligned} N_{\text{el,ase-ase}} &= \langle i_{\text{ase-ase}}^2 \rangle \cdot z_{\text{ref}} \\ &= 4 \cdot \eta_{\text{OE,DC}}^2 \cdot \rho_{\text{sp}}^2 \cdot B_{\text{opt}} \cdot B_{\text{el}} \cdot z_{\text{ref}} \\ &= (\eta_{\text{OE,DC}} \cdot G_{\text{opt}} \cdot NF_{\text{opt}} \cdot hf)^2 \cdot B_{\text{opt}} \cdot B_{\text{el}} \cdot z_{\text{ref}} , \end{aligned} \quad (108)$$

where  $\eta_{\text{OE,DC}}$  is the photodetector's DC conversion efficiency and  $z_{\text{ref}}$  the reference output impedance of the photodiode. The term  $\langle i_{\text{ase-ase}}^2 \rangle$  denotes the variance of the noise current at the photodetector due to ASE-ASE beating. The generated noise power while the signal is beating with the ASE noise can be described as [210]

$$\begin{aligned} N_{\text{el,sig-ase}} &= \langle i_{\text{sig-ase}}^2 \rangle \cdot z_{\text{ref}} \\ &= 4 \cdot \eta_{\text{OE,DC}}^2 \cdot G_{\text{opt}} \cdot P_{\text{opt,in}} \cdot \rho_{\text{sp}} \cdot B_{\text{el}} \cdot z_{\text{ref}} \\ &= 2(\eta_{\text{OE,DC}} \cdot G_{\text{opt}})^2 \cdot NF_{\text{opt}} \cdot P_{\text{opt,in}} \cdot hf \cdot B_{\text{el}} \cdot z_{\text{ref}} , \end{aligned} \quad (109)$$

where  $\langle i_{sig-ase}^2 \rangle$  denotes the variance of the photocurrent induced by beating of the signal with ASE noise. Finally, the noise contribution due to ASE-shot noise is given by

$$\begin{aligned} N_{el,ase-shot} &= \langle i_{ase-shot}^2 \rangle \cdot Z_{ref} \\ &= 4 \cdot \eta_{OE,DC} \cdot q \cdot \rho_{sp} \cdot B_{opt} \cdot B_{el} \cdot Z_{ref} \\ &= 2 \cdot \eta_{OE,DC} \cdot q \cdot G_{opt} \cdot NF_{opt} \cdot hf \cdot B_{opt} \cdot B_{el} \cdot Z_{ref} , \end{aligned} \quad (110)$$

where  $\langle i_{ase-shot}^2 \rangle$  denotes the variance of the photocurrent induced by ASE-shot noise.

### Atmospheric noise

Anything that absorbs electromagnetic energy is also a radiator. Constituents of the atmosphere that cause attenuation, such as water vapor, oxygen and rain, radiate signals which are noise-like. When these signals impinge on a receiver antenna, they degrade system performance. For low elevation angles, i.e. for horizontal wireless links, the dominant noise will be mostly from terrain. For higher elevation angles, also sky noise emanating from atmospheric constituents and other sources will be picked-up.

The terrain and sky noise entering a wireless receiver from the antenna is commonly referred to as the antenna noise temperature and it depends on the elevation angle. The antenna noise figure  $NF_{antenna}$  in decibel and the antenna temperature  $T_a$  in Kelvin are related as follows:

$$NF_{antenna} = 10 \cdot \log_{10} \left( \frac{T_a}{T_0} + 1 \right), \quad (111)$$

where  $T_0$  represents the reference noise temperature of 290 K.

Fig. 5.22 shows the antenna noise temperature as a function of the carrier frequency for horizontal (elevation angle = 0°), as well as for an elevation angle of 10°. As can be seen, the noise peaks at the millimeter wave gaseous molecule resonance bands, e.g. at around 20 GHz and 60 GHz. For an absolute horizontal wireless transmission in the 60 GHz band, the antenna noise temperature and noise figure are 290 K, and 3.01 dB, respectively.

However, for non-ideal horizontal or for wireless transmission within the E-band, i.e. 71-76 GHz and 81-86 GHz, the antenna noise temperature and noise figures are somewhat lower. As an

example, for horizontal transmission within the 81-86 GHz regime, the antenna temperature and noise figure are approximately 130 K and 1.6 dB.

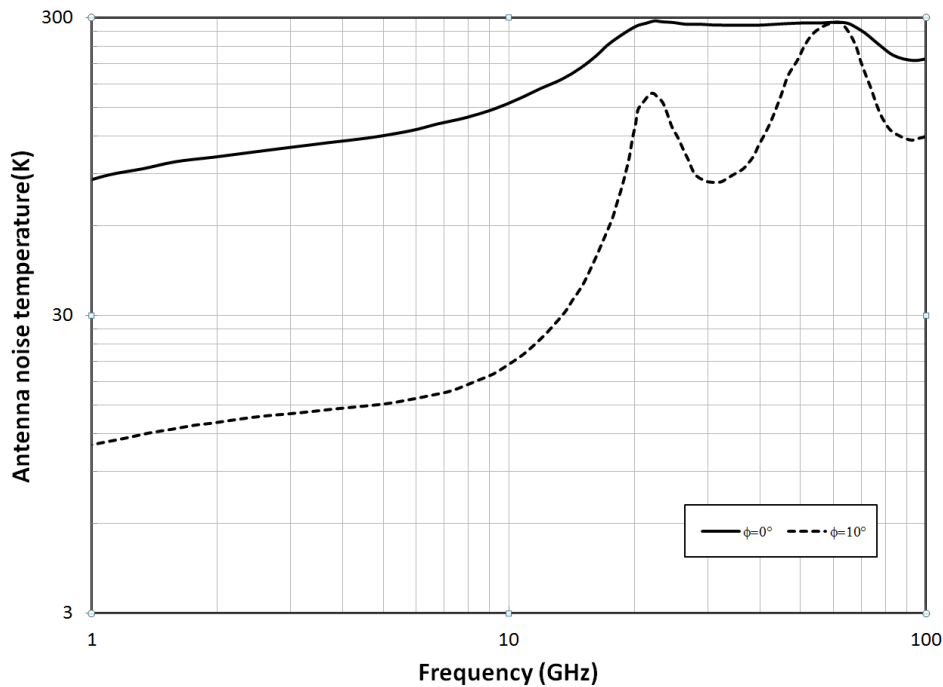


Fig. 5.22 Antenna noise figure vs. carrier frequency in the microwave and millimeter-wave region. Noise temperature is indicated for horizontal ( $\phi = 0^\circ$ ) wireless transmission, as well as for an elevation angle of  $10^\circ$  [211, 212].

## 5.5 Advanced photonic millimeter-wave wireless system demonstrations

As discussed in the previous chapters, future broadband wireless links will operate in the millimeter-wave region and must be capable of handling data rates well in the Gbit/s range. This will require transmitting and processing much wider frequency spectra as it is common in today's wireless systems. This causes enormous challenges for pure electronic systems; not only does the RF carrier frequency demand the development of efficient, low-loss, ultra-high frequency local oscillators and RF up- and down-converters. Even more of a problem is the development of broadband electronic RF modulators or mixers that exhibit the required linear performances over an extreme wide frequency range for processing the wideband signals to be transmitted.

It has been shown in chapter 5.3 that photonics provides some inherent advantages in that respect. Not only would photonics enable the low-loss transport of the high-frequency RF signals, it would also allow making use of broadband optical modulation techniques. Broadband modulation techniques have been widely used in fiber-optic communications. Adapting these techniques in order to fulfill the needs of wireless applications truly is a challenge, but it is possible.

In the following sections, key demonstrations will be shown to prove the applicability of photonics

- to generate high-frequency RF carrier for wireless applications,
- to process wideband signals at mm-wave carriers for multi-gigabit wireless systems,
- to transport wideband signals at mm-wave carriers via optical fibers at low loss,
- to convert wideband signals at mm-wave carriers from the optical to the electronic domain for wireless transmission.

In all these demonstrations,  $1.55\text{ }\mu\text{m}$  wavelength will be used for the optical fiber transmission in order to make use of cost-efficient photonic technologies developed for fiber-optic communications. The wireless signals will be in the 60 GHz band. At first, in section 5.5.1, a full-duplex photonic wireless system will be presented that makes use of a novel photonic electro-absorption transceiver (EAT) component developed for wireless systems using sub-carrier multiplexing (SCM) for full-duplex operation in the 60 GHz band. This system allows full-duplex operation in the 60 GHz band with data rates which are well in hundreds of megabits per second range. By utilizing a looped-back configuration and a dual-wavelength approach, this was the first system achieving full-duplex operation using photonics at the time of publication. In section 0, a much faster photonic wireless system is presented. Based upon a cascaded external modulation approach for RF carrier generation and data modulation and by making use of optical on-off keying (OOK) modulation format, this system is aimed at wireless transmission with data rates well exceeding the gigabit per second range. At the time of publication this system represented a record in wireless data rate times wireless transmission distance, which resulted in more than 100 press releases world-wide including renamed magazines, such as the US-based Science Daily or the Russian Pravda (see e.g. [35]). Finally, in section 5.5.3, a super-broadband 60 GHz photonic wireless system is demonstrated. By making use of spectrally efficient photonic modulation schemes, such as 8-QAM OFDM and 16-QAM OFDM, this system achieved not only a high spectral efficiency but especially a maximum data rate exceeding the ten gigabit per second range. Both, the spectral efficiency and the maximum throughput represent current record figures. To the knowledge of the author, it is the fastest wireless transmission system ever demonstrated.

### 5.5.1 156 Mbit/s full-duplex 60 GHz photonic wireless system

For the successful implementation of future broadband photonic wireless systems in mass-market applications such as mobile backhauling, a cost-effective infrastructure is a necessity. Considering the general architecture of a full-duplex wireless link, the remote wireless base station (BS) is connected to the central station (CS) via fiber. This approach allows to also connect a number of BS to a single CS, i.e. centralizing the equipment in the CS, which contributes to cost reduction. Obviously, the cost of each wireless BS is a critical factor and consequently, much research has been directed towards reducing the costs and complexity of the BSs in a photonic wireless system, e.g. by replacing the uplink laser transmitter in the BS with an optical intensity modulator in a so-called “looped-back” configuration [149, 151, 152]. This not only reduces total power consumption of the BS but also simplifies temperature and bias control and thus further reduces the cost. Even greater cost savings could be accomplished by employing dual-function electro-optic devices in the BS that provide optical modulation, as well as detection functionality and therefore allows for bi-directional fiber-optic transmission.

Previously, *Wood et al.* [144] reported on a dual-function vertical Fabry-Perot multiple-quantum-well (MQW) modulator for bi-directional digital fiber-optic transmission, and *Welstrand et al.* [145] demonstrated a waveguide electro-absorption (EA) device as a modulator/detector element for analog fiber-optic links. However, in both cases, the electrical bias had to be adjusted to achieve either efficient optical modulation or detection. This requires a bias control circuitry at the BS and only allows for half-duplex (bi-directional but not simultaneously) transmission. Full-duplex optical transmission using an MQW EA waveguide device in a frequency-division-multiplexed fiber-wireless system is reported in [146], [147], [148].

In this section, a novel 1.55  $\mu\text{m}$  InGaAsP/InP EA MQW waveguide device as described in section 4.2 was used as a dual-function modulator/photodetector. This electro-absorption transceiver (EAT) device is shown to be an attractive solution for full-duplex fiber-optic transmission [118, 149, 151, 152, 213-218]. To achieve optimum EAT modulation and detection performance, a dual-lightwave approach was used. The advantage of using two wavelengths in conjunction with an EA transceiver is experimentally confirmed by a distinct improvement of the RF up- and downlink insertion loss. Employing the EA transceiver in a looped-back configuration, full-duplex point-to-point fiber-optic transmission of subcarrier-multiplexed (SCM) signals is demonstrated for the first time.

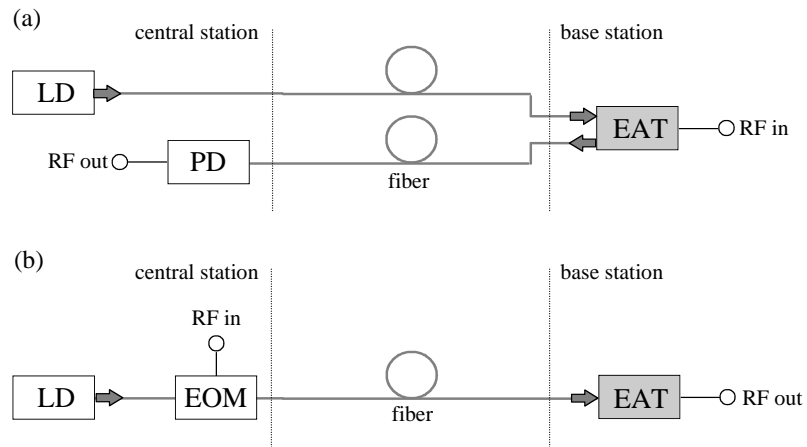


*Fig. 5.23 Schematic of RoF down- and uplink transmission using an electro-absorption transceiver (EAT). Uplink transmission is based upon an EAT device as an optical modulator in a looped-back configuration (a), downlink transmission is achieved employing the same EAT as a photodiode (b).*

For experimental verification, the up- and downlink RF insertion loss of the analog fiber-optic down- and uplink employing a 60 GHz EAT (see Fig. 5.23) was measured. These measurements were performed as a function of optical wavelength for different reverse bias applied to the transceiver. Optical input power of the transceiver and RF subcarrier frequency were 0 dBm and 5 GHz, respectively. For comparison, we also measured the downlink RF insertion loss using a commercial InGaAs PD (New Focus, Model 1014) with a specified sensitivity of 0.35 A/W. The measured up- and downlink RF insertion losses are shown in Fig. 5.24.

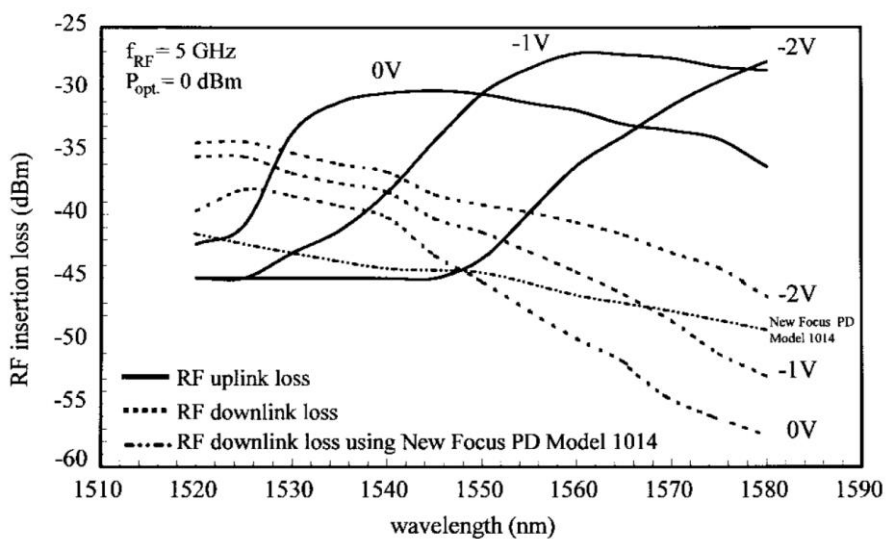


*Fig. 5.24 RF up- and downlink insertion loss versus optical wavelength at different reverse voltages applied to the EAT.*

As can be seen, the optimum wavelength for minimum uplink RF insertion loss (solid lines) strongly depends on the applied reverse bias; e.g. at -1V bias, a minimum uplink RF insertion loss of -28 dB is achieved at 1560 nm wavelength. The dependence of the uplink RF insertion loss on the optical wavelength and the applied reverse bias is due to a trade-off between transmission loss on the one hand and modulation index on the other hand. For smaller wavelengths, the uplink insertion loss is increased because of a larger transmission loss whereas at larger wavelengths it is increased due to a reduced modulation index. In contrast, the optimum wavelength for minimum downlink RF insertion loss (dotted lines) is almost independent of the applied reverse bias. Experimentally, a minimum downlink RF insertion loss of -34 dB is achieved at a wavelength of 1525 nm and -2V reverse bias.

Fig. 5.24 clearly demonstrates the advantage of employing the dual-lightwave technique in conjunction with the transceiver. By way of comparison, if the EAT is operated at one particular wavelength, e.g. 1550 nm and -1 V reverse bias instead of using two wavelengths (1525 nm for downlink and 1560 nm for uplink transmission), the uplink insertion loss is increased by 3.5 dB and the downlink insertion loss even by 6.5 dB. From Fig. 5.24, we also determine the detection responsivity of the transceiver by comparing the downlink RF insertion loss of the transceiver with the RF insertion loss achieved when a PD with a specified responsivity of 0.35 A/W at 1525 nm is used (dashed line) instead of the transceiver. As can be seen, at 1525 nm and -1 V reverse bias the RF insertion loss of the fiber-optic link employing the EAT is reduced by 7 dB as compared to the link employing the InGaAs PD. Thus, the transceiver exhibits a remarkable responsivity of 0.8 A/W.

To further illustrate the principle of operation of the EAT, different optical spectra are shown in Fig. 5.25. In Fig. 5.25(a), the optical input spectrum to the EAT consisting of the modulated optical downlink signal at 1532 nm and the cw optical uplink carrier at 1560 nm is shown. The spectra of the modulated optical downlink signal can be seen in Fig. 5.25 (b). The optical output spectrum of the EAT only consists of the modulated uplink signal at 1560 nm that is depicted in Fig. 5.25(c). As elucidated by Fig. 5.25(a)-(c), the mm-wave modulated optical downlink signal is detected by the EAT while the cw optical uplink carrier is simultaneously intensity modulated. This way, full-duplex fiber-optic mm-wave transmission was achieved.

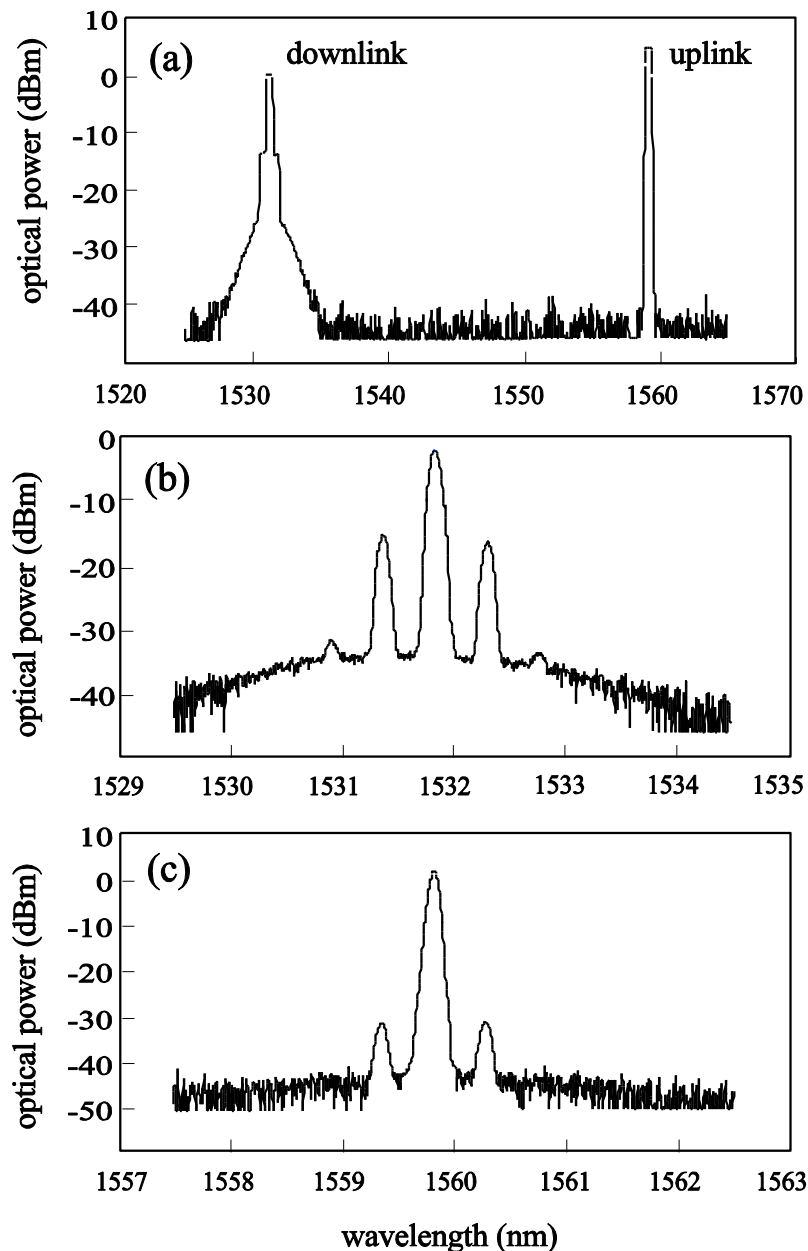
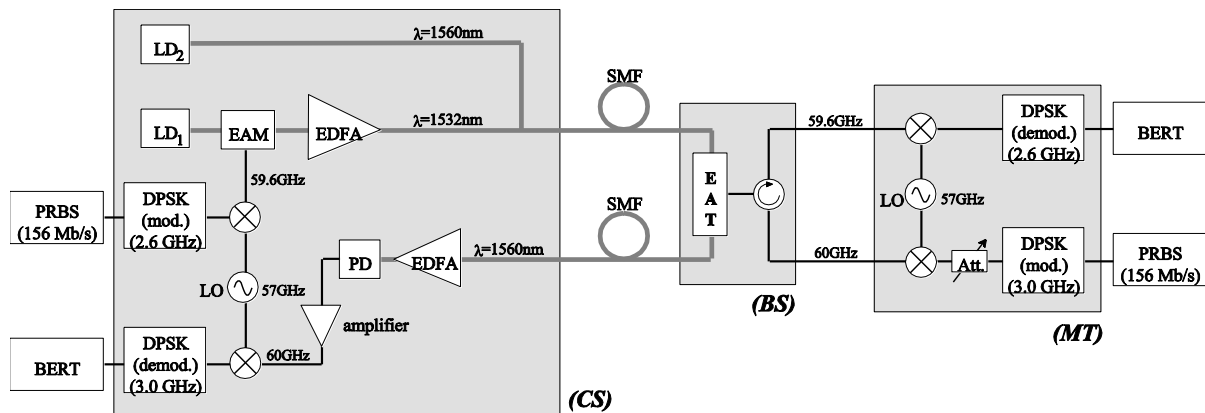


Fig. 5.25 Optical input spectrum of the EAT (a) and spectra of the mm-wave modulated optical downlink (b) and uplink signals (c).

The experimental set-up of the developed full-duplex 60 GHz RoF transmission system is shown in Fig. 5.26. It consists of a CS which is connected to a BS via non-dispersion shifted standard single mode fiber (SMF). For measurement purposes, the mobile terminal (MT) is directly linked to the base station, omitting the wireless path. For downlink transmission, 155.52 Mb/s differential phase shift keyed (DPSK) data centered at an intermediate frequency (IF) of 2.6 GHz is up-converted to 59.6 GHz mm-wave frequency by a local oscillator (LO) in the CS. The optical downlink carrier at 1532 nm (generated by LD<sub>1</sub>) is intensity modulated with the mm-wave downlink signal using a high-frequency electro-absorption modulator (EAM). The optical downlink signal is then amplified by an Erbium-doped fiber amplifier (EDFA) and transmitted to

the BS. In the BS, the optical downlink signal is detected by the EAT. The received mm-wave signal is down-converted to IF and demodulated in the MT to recover the 155.52 Mb/s data and extract the clock signal. For uplink transmission, 155.52 Mb/s DPSK data centered at an IF of 3 GHz is up-converted to 60 GHz mm-wave frequency by the LO in the MT. The optical uplink carrier at 1560 nm (generated by LD<sub>2</sub>) is intensity modulated with the mm-wave uplink signal by the EAT in the BS. The resulting optical uplink signal is then transmitted back to the CS where it is detected by a high-frequency photodiode (PD). The received mm-wave signal is amplified, down-converted to IF and demodulated to recover the downlink data and clock.



*Fig. 5.26 Experimental set-up for full-duplex analog RF fiber-optic transmission of a 256 Mb/s PRBS (downlink) and 56 Mb/s PRBS (uplink) signal. Frequencies used for up- and downlink subcarrier were 3 GHz and 10 GHz, respectively.*

For experimental verification of full-duplex broadband transmission and to avoid any correlation between the up- and downlink signals, two PRBS sources generating 155.52 Mb/s ( $2^{31}-1$ ) NRZ OOK signal and two bit error rate testers (BERT) were used simultaneously as indicated in Fig. 5.26. The DC voltage applied to the EAM and the EAT were -1.4 V and -2 V, respectively. The gain of the receiver EDFA in the CS was +9 dB. The measured up- and downlink bit error rates (BER) with respect to the received optical signal power are shown in Fig. 5.27 (a) and (b), respectively. As can be seen, a BER of less than  $10^{-9}$  was achieved in both directions. As this BER is by far better than what is required when forward error correction (FEC) is applied (most fiber-optic systems employ FEC with a 7% overhead improving the BER from  $2 \cdot 10^{-3}$  up to the  $10^{-15}$  level [219]), higher data rates at the expense of a reduced net bit rate are feasible. In addition to the above demonstration of a symmetrical (with respect to the data rate) RoF wireless system, a similar RoF wireless has been demonstrated for asymmetrical transmission with a maximum data rate of 256 Mbit/s for downlink and 56 Mbit/s for uplink transmission. Also in this case, a  $\text{BER} \sim 10^{-10}$  without FEC was achieved and no error floor was observed.

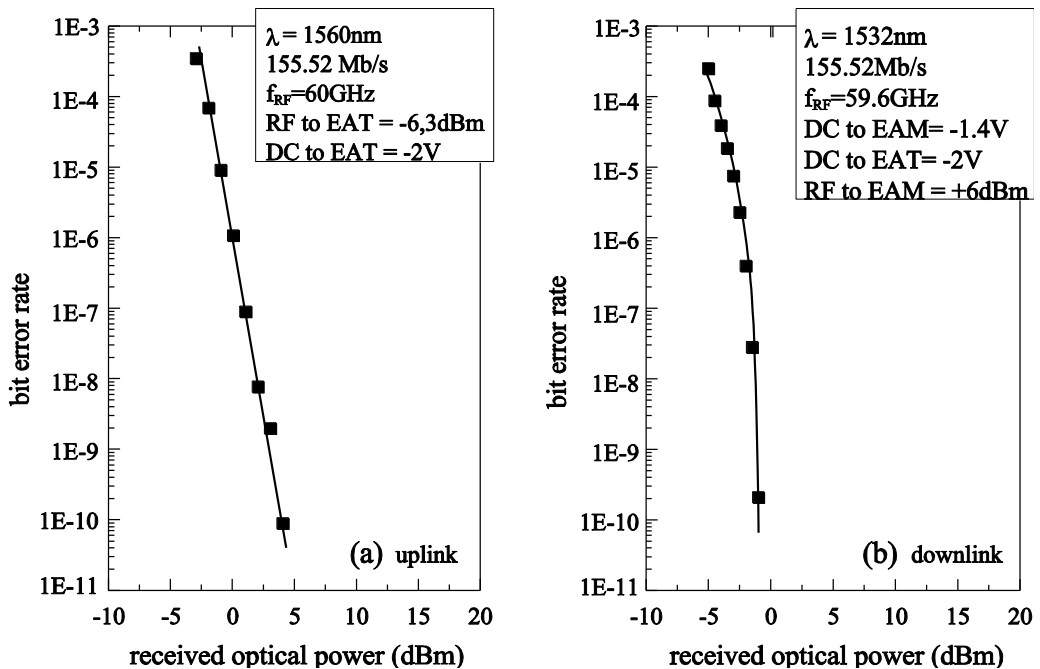


Fig. 5.27 Measured bit error rates (BER) with respect to received optical power for uplink (a) and downlink (b) transmission.

The above transmission experiments clearly show that the EAT device in a looped-back configuration in conjunction with a dual-lightwave technique is an excellent approach for full-duplex RF subcarrier fiber optic transmission. At first, the number of necessary optoelectronic components in the BS is reduced to just one photonic transceiver device. Additionally, the RF insertion loss of the EA-transceiver is comparable or even better than those of conventional laser-detector arrangements, and by employing the dual-lightwave technique, the up- and downlink RF insertion loss is further improved by 3.5 dB and 6.5 dB, respectively. Finally, the EAT enables full-duplex transmission which was also the first demonstration of a full-duplex 60 GHz RoF system in general.

### 5.5.2 10 Gbit/s broadband 60 GHz photonic wireless system

The key technology trend in wireless communications is the increase in data rate needed to fulfill the expanding broadband requirements as discussed in chapter 5.1. Especially for outdoor fixed wireless access (FWA) and mobile backhauling mm-wave wireless systems operating within the E-band (60 to 90 GHz) or F-band (90 to 140 GHz) are likely to be the offering throughputs in the multi-gigabit range. Nevertheless, the potential of 60 GHz for broadband 10 Gb/s transmissions over relevant distances has not been exploited yet, but could be beneficial in terms of costs and component availability. In this section, a broadband 60 GHz wireless photonic link system for short- to medium-range broadband wireless data transmission is studied. Here, the challenge is to develop photonic technologies and techniques that are capable to process data signals with multi-gigahertz bandwidth. The investigated system is based upon advanced mm-wave photonic

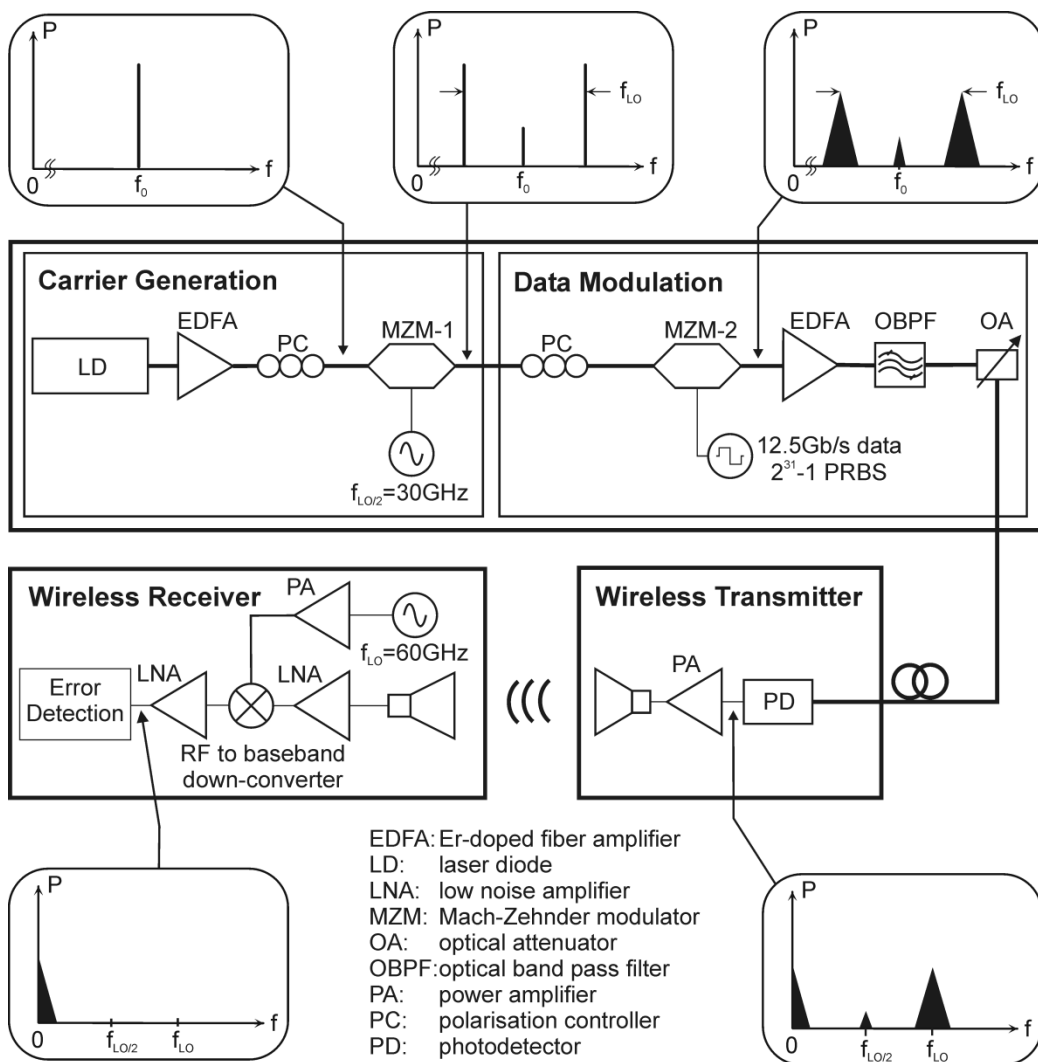
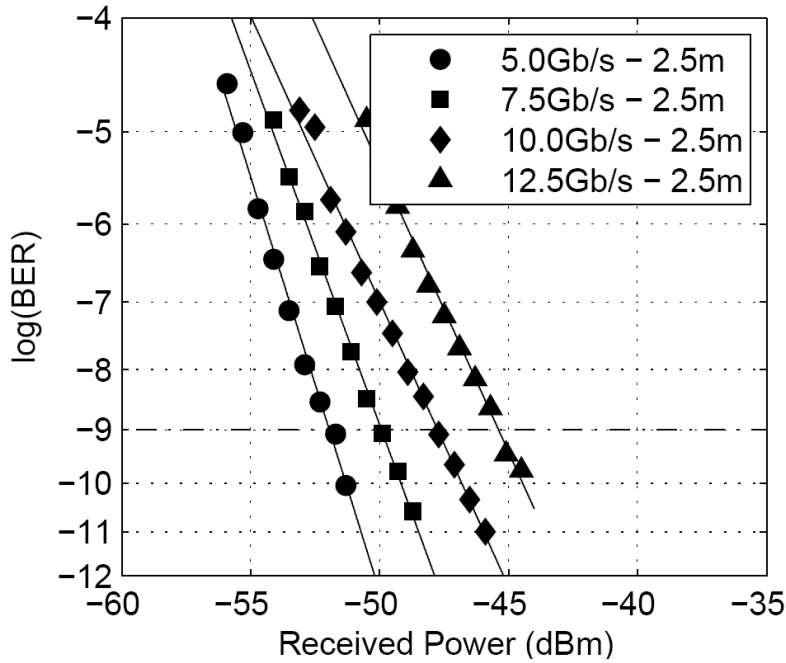


Fig. 5.28 Schematic of the constructed 60-GHz RoF link consisting of an optical mm-wave carrier generation (DSB-SC) unit and a subsequent broadband data modulation (OOK).

components and radio-over-fiber (RoF) techniques. The key technical innovation in the system set-up shown in Fig. 5.28, is the cascaded modulator approach for optical mm-wave carrier generation and subsequent broadband modulation. As bandwidth limitations are much less stringent in the mm-wave range, the system makes use of an optical on-off-keying (OOK) format for broadband modulation of the optically generated mm-wave carrier.

Fig. 5.28 shows the configuration of the 60-GHz radio-over-fiber testbed. In general, the system consists of an optical carrier generation unit and a subsequent broadband data modulation, a wireless RoF transmitter, and a wireless receiver. For optical mm-wave carrier generation, light from an external cavity laser source at a wavelength of about 1550 nm is modulated using a single-drive Mach–Zehnder modulator (MZM-A) biased at V to generate an optical double-sideband signal with suppressed carrier (DSB-SC). The modulator is driven by a sinusoidal source with a frequency and phase noise level of  $f_{\text{LO}}/2 = 30$  GHz and 67 dBc/Hz at 10 kHz offset, respectively. An optical carrier suppression of approximately 26 dB is achieved. Due to low  $V_{\pi}$  of the MZM (3.5 V at 30 GHz), no additional driver amplifier is necessary. The optical 60-GHz carrier is further modulated (MZM-B) with non-return to zero on-off-keying (NRZ-OOK) data. In the testbed, a pseudorandom binary sequence (PRBS) with a word length of  $2^{31}-1$  was applied to the modulator, which is biased to the quadrature point. The data-modulated mm-wave signal is amplified by an erbium amplifier and further coupled to an optical attenuator for adjusting the optical power. After 50 m fiber-optic transmission to the wireless RoF transmitter via a standard single-mode fiber (SMF), the optical mm-wave signal is o/e-converted by an experimental 70 GHz photodetector with a dc responsivity of 0.59 A/W. The applied maximum optical input power was fixed to 10 dBm during the experiments. This corresponds to an RF output power of 7.5 dBm which was measured with a WR15-coupled power sensor. For the transmission experiments described below, different wireless transmitter configurations were used. For short-range in-door wireless transmission up to 11 m no amplifier was used in the wireless RoF transmitter, but the RF signal generated by the photodiode was directly coupled to a standard 23 dBi horn antenna. For medium-range wireless out-door transmission, an additional amplifier was implemented between the PD and horn antenna to boost the RF signal level up to 19.2 dBm. The gain and noise figure of the power amplifier are 32 and 10 dB, respectively.

To experimentally investigate the system's performance for short-range broadband wireless transmission, the wireless signal was transmitted within a laboratory environment, allowing a maximum wireless path length of about 11 m. No endeavours have been made to avoid multipath propagation. At first, the receiver sensitivity was investigated for a wireless path length of 2.5 m and BER measurements were performed for data rates of 5, 7.5, 10, and 12.5 Gb/s.



*Fig. 5.29 Measured BER as a function of received power level for multi-gigabit broadband wireless data transmission over 2.5 m.*

The measured receiver sensitivities can be seen in Fig. 5.29 showing the measured BER as a function of received power level for multi-gigabit broadband wireless data transmission over 2.5 m. As can be seen, no error floor was observed down to a BER of  $10^{-11}$ . For a BER of  $10^{-9}$  (NRZ, word length  $2^{31}-1$ ), the measured receiver sensitivities for 5, 7.5, 10, and 12.5 Gb/s are -51.8, -50.1, -47.6, and -45.4 dBm, respectively. The measured power penalties (at  $\text{BER} = 10^{-9}$ ) for 5 Gb/s versus 7.5 Gb/s, 7.5 Gb/s versus 10 Gb/s, and 10 Gb/s versus 12.5 Gb/s are 1.9, 2.0, and 2.4 dB, respectively. According to the bandwidth ratios, receiver sensitivity penalties of approximately 1.8, 1.1, and 0.96 dB are expected, respectively. As can be seen, the measured sensitivity penalty for 5 Gb/s versus 7.5 Gb/s agrees quite well with this expectation, but for higher data rates the measured penalties are slightly larger than expected even when considering some measurement fluctuations. This is expected to be due to the limited bandwidth of the LNA in the RoF receiver which has a 3-dB bandwidth of about 10 GHz.

Next, the system performance was tested for up to 50 m medium-range wireless spans. From bit error rate (BER) measurements shown in Fig. 5.30, broadband wireless transmission up to 50 m is demonstrated. No error floor was observed in the BER measurements for data rates up to 5 Gb/s. Although for higher data rates BER some error floor is observed, transmission of 12.5 Gb/s up to 50 m is demonstrated with BER below the required FEC level of  $2 \cdot 10^{-3}$ . To the knowledge of this author, this was the first demonstration of  $> 10$  Gb/s broadband wireless transmission over reasonable wireless path lengths at the time of publication in 2008 [59, 220].

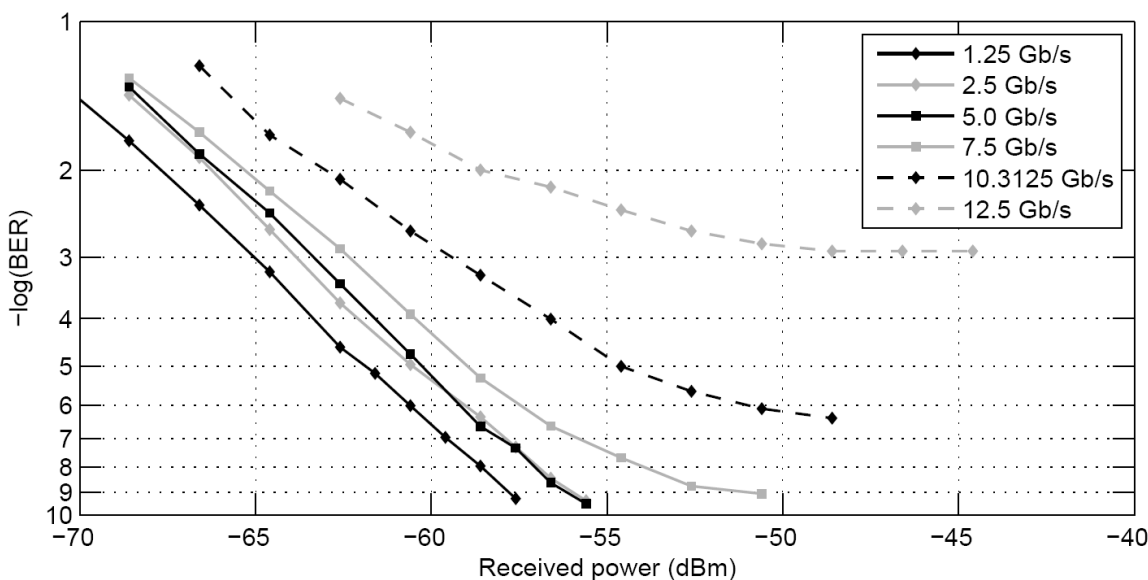


*Fig. 5.30 Measured BER as a function of received power for different bit rates up to 12.5 Gb/s and wireless distances up to 50 m.*

Based upon the experimental system results, the potential of extending the wireless path length up to the km range (for 12.5 Gb/s at 60 GHz) by using high gain antennas and RF amplifiers with suitable bandwidth was studied theoretically. Based upon the measured receiver sensitivities and by using the link model developed in chapter 5.4, the received power was calculated for the case of high-gain 50 dBi receive and transmit antennas. Fig. 5.31 shows that the maximum wireless distance to achieve a BER of  $10^{-9}$  is approx. 2000 m for 99% link availability (drizzle with 2 mm/h) and approx. 400 m for 99.999% (heavy rain with 85 mm/h) link availability.

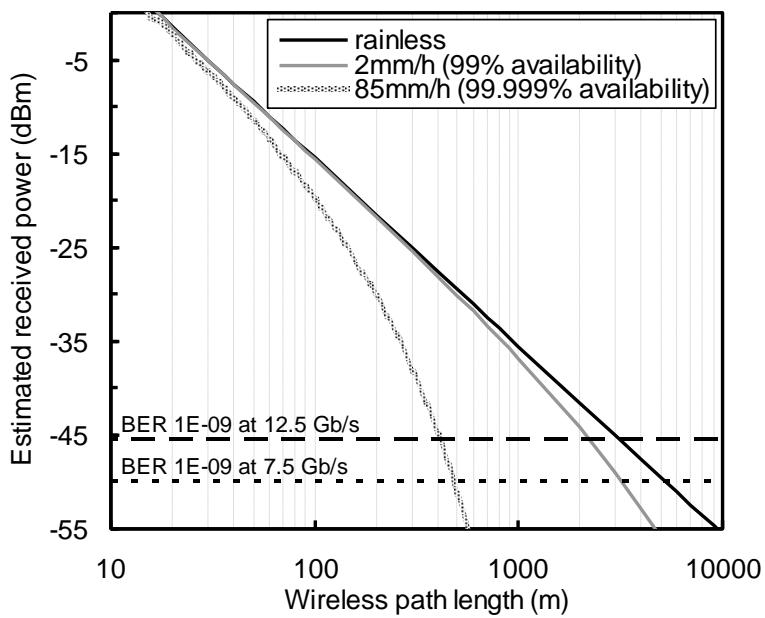


Fig. 5.31 Maximum wireless path lengths for 50 dBi gain antennas under different weather conditions.

### 5.5.3 27 Gbit/s super-broadband 60 GHz photonic wireless system

At the time of publication in 2008, the achievements presented in the above section represented world record figures in terms of data rate times wireless span for broadband millimeter-wave wireless systems. This can also be seen as an indication that photonic wireless systems have the edge over electrical RF systems whenever high aggregate bit rates are involved. However, it should be mentioned that the spectral bandwidth of the radio signal in the above mentioned 10 Gbit/s OOK photonic wireless system is approximately  $2^{3/4}$  times the *data rate*, since a double-sideband signal was transmitted and since the bandwidth of each sideband of the NRZ baseband signal is approximately 0.75 times the *data rate*. Thus, the total occupied bandwidth for a 10.3125 Gbit/s is about 15.5 GHz. As discussed in section 5.2.1, this clearly exceeds the maximum allowable aggregate bandwidth in the 60 GHz band which is limited by regulatory agencies worldwide to 7 GHz (see section). In other words, although technically feasible, the system presented in section 0 is not in accordance with existing regulations. The maximum data rate the above described OOK photonic wireless system could be used for, considering a total bandwidth of 7 GHz in the 60 band would be about 4.6 Gbit/s. This is still by far faster than any of today's commercial fixed wireless system offers (see also section 5.4.2), and it would even

support the current industrial endeavors in developing full duplex Gbit/s systems requiring a total capacity of about 2 Gbit/s (TDD).

Nevertheless, it is clear that the maximum capacity the OOK photonic wireless system can offer is not sufficient for the development of a full duplex 10 Gbit/s wireless system. For a full-duplex 10 Gbit/s (i.e. a total capacity of 20 Gbit/s) operating in the 60 GHz band with a maximum bandwidth of 7 GHz, a spectral efficiency of at least 2.86 bit/s/Hz would be required. This is very close to the theoretical limit for an 8-QAM modulation which is of 3 bit/s/Hz (see Fig. 5.10).

To achieve this goal, i.e. a total capacity exceeding 20 Gbit/s, a system using a 8-QAM OFDM (orthogonal frequency division multiplex) and 16-QAM OFDM modulation was developed. OFDM is a multi-carrier modulation format in which a high bit-rate digital data stream is split into several narrowband channels at different frequencies (using sub-carriers) [221]. The sub-carriers are modulated e.g. by PSK or QAM and are then up-converted to the millimeter-wave carrier. This is similar to FDM (frequency division multiplexing) or subcarrier multiplexing, except for the stringent requirement of orthogonality between the sub-carriers. OFDM is considered as an advanced modulation technique for future broadband wireless systems as it provides increased robustness against frequency-selective fading and narrowband interference. OFDM is also efficient in dealing with multi-path delay spread, and it can combat optical chromatic dispersion [221-223]. These advantages together with the ability to use higher level modulation formats with increased spectral efficiencies have resulted in the fact that OFDM technology is widely adopted today, e.g. in wireless systems such as IEEE 802.11a/g (WiFi) and IEEE 802.16 (WiMAX) [224].

The configuration of the 60 GHz photonic wireless testbed that has been constructed for demonstrating broadband wireless transmission with a maximum capacity of at least 20 Gbit/s is shown in Fig. 5.32. In general, the system consists of an optical mm-wave carrier generator unit with a subsequent broadband data modulation, a photonic wireless transmitter and a coherent wireless receiver.

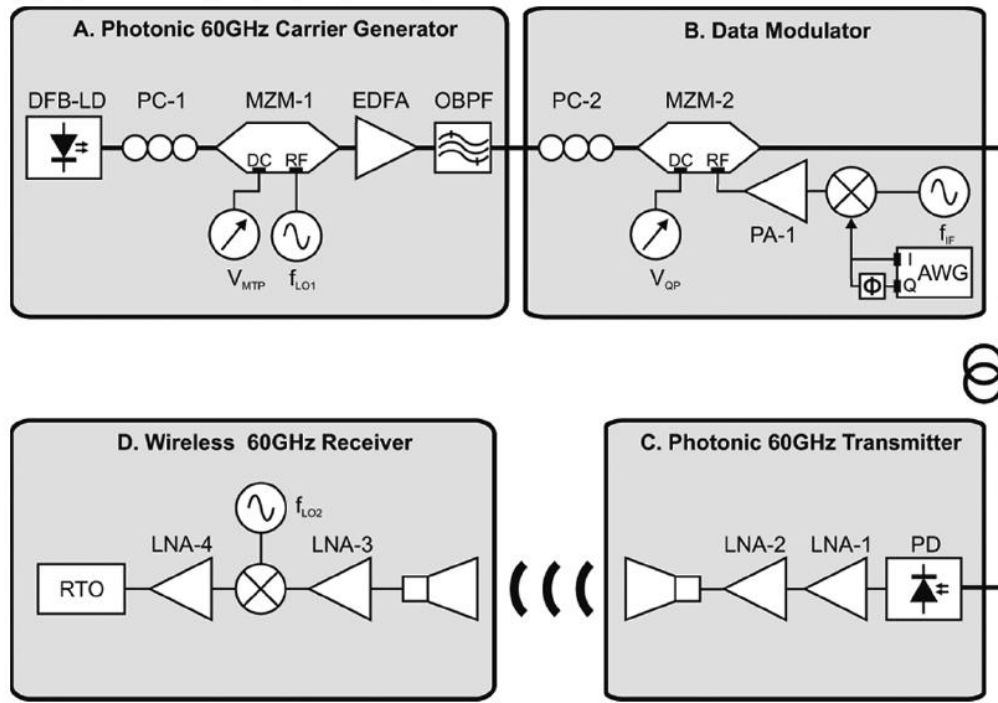


*Fig. 5.32 Schematic of the compact 60 GHz photonic wireless link consisting of an optical mm-wave carrier generator based upon external modulation, a subsequent broadband OFDM data modulation, a photonic wireless transmitter and a wireless coherent receiver. The configuration for wireless and back-to-back experiments is further indicated in the figure.*

For optical mm-wave carrier generation, light from a DFB laser source at a wavelength of 1548.9 nm is modulated using a single-drive 35 GHz bandwidth Mach-Zehnder modulator (MZM-1) which is biased to the minimum transmission point (MTP) for generating an optical double-sideband signal with suppressed carrier (DSB-SC). A polarization controller is used to minimize the polarization dependent losses. The modulator is driven by a sinusoidal source with a frequency of  $f_{LO1} = 34.7$  GHz, thus creating a double-sideband RF carrier with a frequency of 69.4 GHz. With an applied power of +13 dBm, the optical carrier suppression is measured to be approximately 19 dB. To compensate for the modulation losses while operating at MTP, an EDFA was implemented, followed by an optical band-pass filter to remove ASE noise. The signal power of the data-modulated optical mm-wave carrier is approximately +14 dBm at this stage.

Photonic data modulation is also performed by external modulation. The DC-bias is set to the quadrature point to achieve a quasi-linear modulation of the optical signal in conjunction with a sufficiently low power of the modulating data signal. A polarization controller is used before the modulator to minimize the polarization dependent loss.

The applied OFDM signal under test is created on a computer using Matlab® with an FFT block size of 2048 data subcarriers, 34 pilots and 5 null subcarriers. Total signal bandwidth is set to 7 GHz, while applying QAM-modulation for each data subcarrier. Signal generation is performed by a Tektronix AWG7102 10 GS/s dual-output arbitrary waveform generator (AWG), where the I- and the Q-component of the OFDM signal are combined and applied to a mixer. A sinusoidal microwave source is applied to the LO input of the mixer to up-convert the signal to an IF carrier frequency of 8.5 GHz. The LO power level is +24 dBm. The up-converted OFDM signal is amplified by a 18 dB gain power-amplifier (PA-1) to a level of approx. 3.5 dBm and applied to the RF electrode of MZM-2.

After fiber-optic transmission to the wireless ROF transmitter, the optical mm-wave signal is o/e converted by a 70 GHz photodetector. The converted mm-wave signal is amplified by LNA-1 with a gain of  $G = 20$  dB and a noise figure of  $NF = 6$  dB and LNA-2 ( $G = 18$  dB,  $NF = 6$  dB) to a transmit power of approx. -1 dBm and coupled to a 23 dBi gain horn antenna. Considering carrier and intermediate frequency, the OFDM signal is centered at  $f_{RF} - f_{IF} = 60.9$  GHz, giving a consumed bandwidth of 57.4 - 64.4 GHz. This does not quite exactly meet the worldwide regulatory specifications of 57 - 64 GHz (see section 5.2.1). This is due to the insufficient bandwidth of LNA-2.

The wireless receiver consists of an identical 23 dBi horn antenna. After amplification by a low-noise amplifier LNA-3 with a gain of  $G = 18.6$  dB and a noise figure of  $NF = 4.5$  dB, the signal is coupled to a low-loss custom design balanced mixer for down-conversion. The LO frequency  $f_{LO2}$  is 53.2 GHz and down-converts the mm-wave signal to an intermediate frequency centered around 7.7 GHz. This signal is further amplified by LNA-4 ( $G = 22$  dB,  $NF = 4$  dB) to a power level of approximately +5 dBm and coupled to an Agilent DSO91304A 13 GHz bandwidth real time oscilloscope (RTO) with a sampling speed of 40 GS/s to capture the IF signal. Finally, OFDM demodulation and EVM evaluation are performed offline using Matlab®

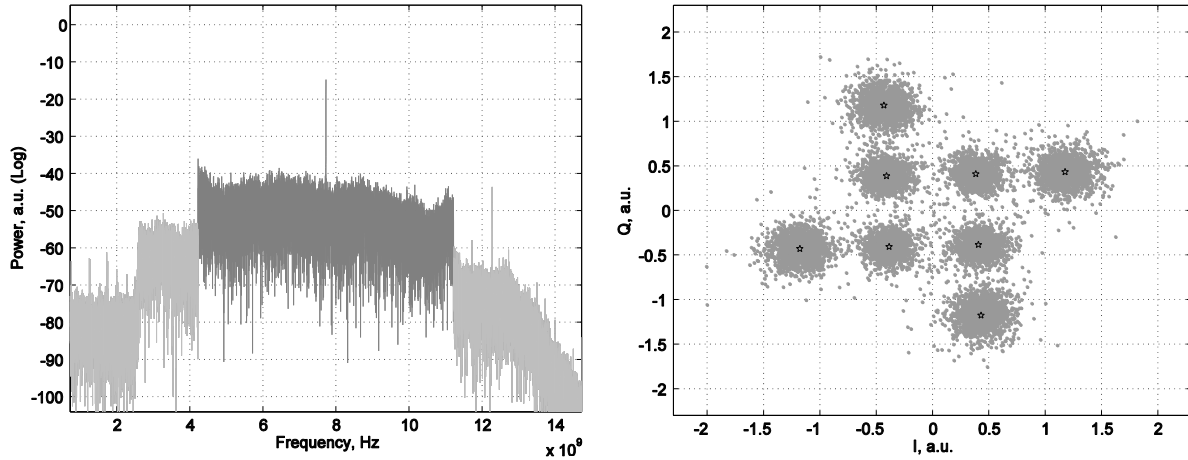


*Fig. 5.33 Received spectrum and constellation diagram obtained after photonic up-conversion, 10 m of fiber-optic and 2.5 m of wireless transmission. The 7 GHz bandwidth OFDM signal with 8-QAM subcarrier modulation gives a data transmission rate of 20.28 Gbit/s.*

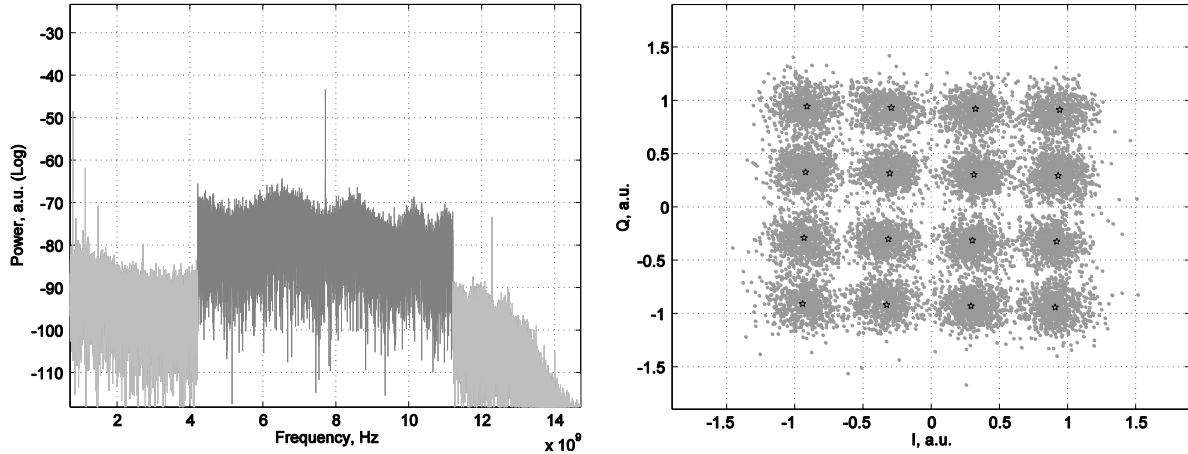


*Fig. 5.34 Received spectrum and constellation diagram obtained after photonic up-conversion, 10 m of fiber-optic and 2.5 m of wireless transmission. The 7 GHz bandwidth OFDM signal with 16-QAM subcarrier modulation gives a data transmission rate of 27.04 Gbit/s.*

For evaluating the system performance, we have performed experiments in a laboratory environment with a fiber-optic transmission span of 10 m and a wireless path length of 2.5 m. The data subcarriers of the 7 GHz bandwidth OFDM signal are modulated with either 8- or 16-QAM OFDM signals, corresponding to transmitted data rates of 20.28 and 27.04 Gbit/s, respectively. For the measurements, transmitter and receiver are placed at a height of approximately 90 cm above floor level. The received spectrum and constellation diagram for 20.28 Gbit/s photonic-wireless transmission using 8-QAM subcarrier modulation are shown in Fig. 5.33. The measured mean EVM is 18.8% for an SNR of 18.9 dB. From the EVM, a BER of  $2.2 \cdot 10^{-4}$  can be computed, which is below the forward error correction (FEC) limit of  $2.2 \cdot 10^{-3}$  [197].

We further demonstrated 16-QAM modulated OFDM transmission, which corresponds to a data rate of 27.04 GHz at a bandwidth of 7 GHz. The received spectrum and the constellation diagram are shown in Fig. 5.34. The measured mean EVM is here 17.6 % for a SNR of 21.5 dB. From the EVM, a BER of  $4.2 \cdot 10^{-3}$  can be computed, which is slightly above the FEC limit [197].

In summary, with the above presented broadband photonic wireless 60 GHz transmission system and by using an 8-QAM and a 16-QAM OFDM modulation format, record spectral efficiencies up to 3.86 bit/s/Hz have been achieved. Experiments have been carried out with 10 m fiber-optic and 2.5 m wireless transmission. For 8-QAM OFDM modulation, a data rate of 20.28 Gbit/s has been achieved with a measured mean EVM of 18.8 % and a SNR of 18.9 dB resulting in a BER of  $2.2 \cdot 10^{-4}$ . For 16-QAM OFDM modulation, a record throughput of 27.04 Gbit/s has successfully been achieved. In that case, the measured mean EVM and SNR were 17.6 % and 21.5 dB, respectively, resulting in a BER of  $4.2 \cdot 10^{-3}$  which is slightly above the FEC limit. Also, the wireless span of 2.5 m was limited by the laboratory environment. The transmit power and antenna gain used in the experiments were -1 dBm and 23 dBi, respectively. By increasing the transmit power and antenna gain, one can expect to be able to extend the wireless span up to a few 100 m given the measured wireless receiver sensitivity.

## 5.6 State of the art in broadband photonic wireless demonstrations

As discussed above, broadband wireless is widely considered as the third wireless revolution, following cellular phones in the 1990s and Wi-Fi in the 2000s. It is viewed by many carriers and cable operators as a disruptive technology. However, at present, there is no broadband wireless system offering 10 Gigabit per second connections commercially available although there are remarkable research activities being carried out in this field. Most of the leading companies and research institutes in broadband wireless are located in the USA, Japan and Europe. Noticeable is the fact that most solutions reported or proposed for 10 Gbit/s broadband wireless systems employ photonic technologies.

Today, various companies offer commercial series broadband wireless link products up to 1.25 Gbit/s, potentially supporting full-duplex 1 Gigabit Ethernet. Such products are available from Comotech [225], E-Band Communications [226], Loea [227], Elva-1 [228], Rayawave [229], Gigabeam [230], Proxim Wireless [231] and others. Most of those systems operate within the E-band at around 60 GHz or around 70 and 80 GHz and are usually equipped with interfaces for fiber or copper. The spectral efficiency offered by those commercial systems often does not comply with actual regulations – at least not for Europe. Also, the systems do not offer low cost-per-bit. Broadband wireless systems offering > 1.5 Gbit/s connectivity are being announced, e.g.

by Asyrmatos [232] or Gigabeam [230]. Most of those so-called super-broadband wireless systems also operate in the E-band, although the Asyrmatos product also considers operation in frequencies around 94 GHz and 140 GHz. To the best of the author’s knowledge, none of these 10 Gbit/s wireless systems is commercially available at the moment.

Looking at the academic achievements and developments, broadband millimeter-wave wireless systems have attracted a lot of interest during the last decade. However, although research on mm-wave wireless links has been carried out for about a decade now, it is just within the last years that broadband wireless links with capacities in the Gbit/s range could be successfully developed. However, in many if not in most publications, only RoF signal transport over fiber omitting the wireless transmission is demonstrated. As shown in Fig. 5.15, wireless transmission, even for short distances, requires the systems’ power budget to be 100-130 dB better. Obviously, this has a great impact on the required systems’ performances and thus, only those RoF demonstrations including the wireless transmission are discussed further.

Early RoF demonstrations were made by *Stöhr, Kuri and Kitayama* at NiCT, Japan, already in 1998 and 1999 by demonstrating the first full-duplex 60 GHz millimeter-wave photonic wireless links using external optical RF modulation and coherent detection [213, 215-217, 233, 234] (see also section 5.5.1). Based upon a novel optical transceiver approach and by employing subcarrier multiplexing (SCM) (see also section 5.5.1 below), this system allowed a maximum downlink transmission data throughput of 256 Mb/s and an uplink throughput of 56 Mb/s [149, 151]. The same authors also demonstrated 156 Mb/s wireless transmission over 5 m [234]. Here, the RF carrier frequency and data modulation format were 60 GHz and differential phase-shift keying (DPSK), respectively. In 1999, *Stöhr* et al. also demonstrated a WDM RoF system concept employing wavelength routing for addressing multiple BSs in a bus-type network and using SCM for full-duplex operation [151].

In 2003, *Seo* et al. demonstrated a 60 GHz RoF system employing also a WDM scheme for addressing multiple base stations in a star-type network architecture [235]. By using optical ON-OFF keying (OOK), a more simple modulation format as compared to DPSK which was used in [151, 152, 234], *Seo* et al. demonstrated a total data throughput of 2 times 622 Mb/s over 3 m wireless span.

More recent relevant research on broadband mm-wave wireless systems was conducted by a Japanese research group from NTT, who successfully constructed and employed photonic transmitters for wireless transmission with data rates up to 10 Gbit/s. Using OC-192 and 10 Gbit/s Ethernet formats, they demonstrated 10 Gbit/s wireless transmission over 300 m at 125 GHz carrier frequency using optical amplitude-shift keying (ASK) modulation format [236].

Latest work of the same research group focused on THz photonic wireless transmission systems. Records in terms of data throughput at THz carrier frequencies were demonstrated in [237, 238] by showing 8 Gbit/s and 2 Gbit/s over 0.5 m wireless at carrier frequencies of 250 GHz and 300 GHz, respectively.

Recently, in 2008, researchers at Battelle [239] built a photonic wireless system operating at 94 GHz for data rates up to 10.6 Gbit/s. They demonstrated wireless transmission over 6 m and claim to have been able to recover the 10.6 Gbit/s OOK data even after 800 m wireless transmission.

Very recently, in 2009, researchers from UDE reported on a photonic wireless system using an externally modulated 58.8 GHz MLLD as optical source and an incoherent receiver based upon an envelope detector. In [240], they reported on uncompressed HDTV transmission with a data rate of 1.48 Gbit/s over 10 m wireless span. Later results using the same system revealed maximum data throughputs of up to 5 Gbit/s being transmitted over 25 m wireless span [57, 241]. Later in 2009, *Gonzalez* et al. from TUD also employed an incoherent receiver (envelope detector) and demonstrated up to 10 Gbit/s over 1.5 m wireless span [242].

With respect to data rates and spectral efficiency, the *NEC Laboratories* in Princeton and the *Georgia Institute of Technology*, USA, achieved a remarkable result in 2008. Although operating in the microwave range at 24 GHz, their system was capable of delivering up to 16 Gbit/s over 6 m wireless span using an 16QAM-OFDM modulated signal with a spectral efficiency of 3.2 bit/s/Hz [243]. The same group at Georgia Tech. also developed integrated schemes for RoF-based optical-wireless services in WDM-PON systems to serve both, fixed and mobile users with a converged optical platform [244]. Also, researchers at *Corning Inc.* in the US published broadband 14 Gbit/s radio-over-fiber transmission (without wireless) in the 60 GHz band using an OFDM signal [245]. The same group has also achieved wireless transmission using the same system (personnel visit).

As can be seen from the above discussions as well as from Table 5.3 which summarizes the recent key achievements in RoF photonic wireless systems, most of the reported systems do not comply with regulations. In most cases, either the used spectral bandwidth is too large with respect to regulations or the used carrier frequency does not comply with regulations. One of the few systems that potentially comply with regulations was demonstrated by researchers from UDE and France Télécom in 2009 (see section 5.5.3). Here, for the first time to the author's knowledge, wireless transmission with a data throughput of up to 27 Gbit/s was demonstrated within the 60 GHz band. In order to be compliant with regulations, the total bandwidth had to be

limited 7 GHz. This was achieved by using a 16QAM-OFDM signal. This way, it was possible to increase the spectral efficiency up to 3.86 bit/s/Hz which also represents a world record figure.

Table 5.3 Summary of key achievements in photonic millimeter-wave wireless systems

Year	RF carrier frequency (GHz)	Wireless span (m)	Modulation format	Data rate (Gbit/s)	Spectral efficiency (bit/s/Hz)	Org.	Ref.
1998	60	0 (BtB)	DPSK	0.256 (down.) 0.056 (up.)	< 0.5	UDE, NiCT	[149], [151], [152]
1999	60	5	DPSK	0.156	< 0.5	NiCT, UDE	[234]
2006	120	200	ASK	10.3125	0.61	NTT	[236]
2008	94	6	OOK	10.6	< 0.5	Battelle	[239]
2008	60	50	OOK	12.5	< 0.5	UDE	[220, 240, 246]
2008	24	5	16QAM-OFDM	16	3,2	Georgia Tech.	[243]
2009	58.8	25	OOK	5	< 0.5	UDE	[240]
2009	30	1.5	OOK	10	< 0.5	TUD	[242]
2009	60	5	OOK	10	< 0.5	Georgia Tech.	[247]
2009	60	BTB	QPSK-OFDM	14	2	Corning, NCTU	[245]
2009	250	0,5	OOK	8	0.56	NTT	[238]
2009	300	~0,5	OOK	2		NTT	[237]
2009	60	2.5	16QAM-OFDM	27.04	3.86	UDE FT	[146],[57]
2010	60	10	8QAM-OFDM	21	3	ChiaTung, Corning	[248]
2011	60	3	Adaptive 8-32QAM-OFDM	31.4	4.48	ChiaTung, Corning	[249]
2011	60	1.2	DP-16QAM	100	~2.8	TUD	[250]
2012	220	0.5	QPSK	9.06	1.81	KIT, IAF	[251]

## 6 Microwave Photonics in Instrumentation and Sensing

In the previous chapter, the advantageous utilization of microwave photonic technologies and Radio-over-Fiber techniques in communication applications was shown. Advanced wireless communication systems based upon RoF techniques exhibiting world record performances were demonstrated. But Microwave Photonics is not only of particular interest in communications, it is also widely considered as an advanced high-frequency source technology for multiple applications in instrumentation, sensing, security, radar, and medical applications. The theoretical concepts discussed in chapter 2 and chapter 3, as well as the developed technologies shown in chapter 4 provide clear evidence that advanced, compact and potentially low-cost photonic-based high-frequency sources and sensors can be built. This includes highly stable and spectrally pure millimeter wave oscillators, ultra-wide tunable sources or wideband sensors for various applications. Such compact functional components are expected to have some inherent advantages as compared to other all-electronic or all-optical solutions. First of all, they would principally allow covering a huge frequency spectrum extending from DC all the way up to highest mm-wave frequencies or even THz frequencies. Currently, there is no other technology which is even envisaged to offer such a wide tunability. Obviously, a compact-size frequency-tunable mm-wave oscillator would have a great impact on multiple industrial sectors, including atomic and molecular spectroscopy (e.g. photonic spectrometer), mm-wave instrumentation (e.g. extremely wide frequency coverage mm-wave synthesizer), radio-astronomy (e.g. in tunable photonic LOs), security and radar (e.g. sources for mm-wave imaging), and last but not least in telecommunications (e.g. multi-service and ultra-wide band broadband wireless access). The next section will provide more details on some of the above mentioned applications. Thereafter, a photonic-based sensor and a photonic-based high-frequency source will be demonstrated. Namely, a microwave (300 MHz to 6 GHz) electrical-field sensor and a millimeter-wave photonic synthesizer with a wide frequency-tuning range from 75 GHz to 115 GHz will be shown.

### 6.1 Applications and worldwide markets

The various application fields that can potentially be addressed by photonic-based high-frequency sensors and sources are categorized in five major application fields of particular interest: communications, transport, instrumentation, security, and medical applications.

To get a better knowledge on the different application fields and to stimulate the growth of the emerging European industry in the field of photonic-based microwave and mm-wave components and functions, a survey has been conducted by University Duisburg-Essen and Optech-Net e.V. within the European IPHOBAC project. The survey is entitled “Millimetre-Wave Applications using Photonics”. The first version of the survey report was released in June 2007, an updated, more application-oriented survey was released in June 2008. A concise public summary report summing up the results of both survey versions was published in April 2010 [36].

In a first step, the technical needs and requirements of the European mm-wave industry were investigated by means of a questionnaire. In a second step, more application-driven requirements were revealed by means of an additional questionnaire, direct market analysis, and bilateral meetings with leading industrial players. The following presents a concise summary of the outcomes of this survey.

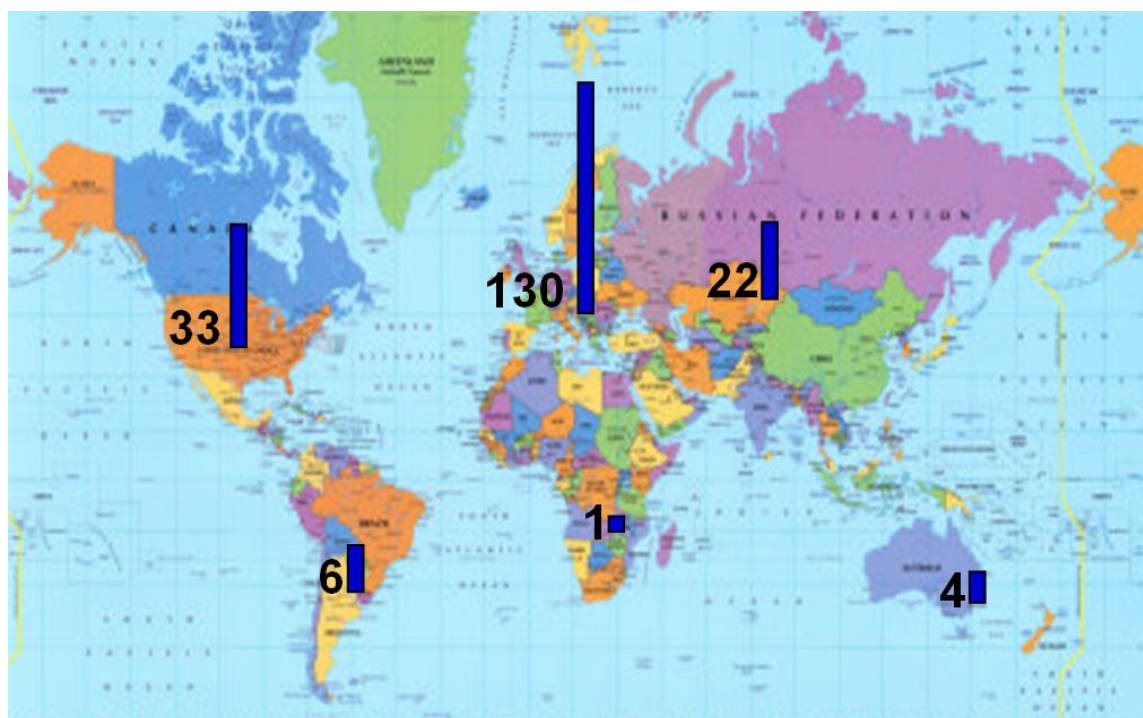


*Fig. 6.1 Origins of the 278 survey participants worldwide. The origins of 84 participants are unknown.*

In summary, until the end of 2009 altogether 278 participants had taken part in the IPHOBAC survey, of which about 200 indicated their country of origin. Even though the majority of respondents are from European companies and research organizations (two thirds of all participants), there was a fair amount of experts participating from non-European countries, predominately from the USA (see also Fig. 6.1), representing worldwide trends in the microwave

and mm-wave industry. The highest number of responders originated in the USA and Germany, followed by the United Kingdom, France, Italy, India, Belgium, Russia, Canada, and others.

With respect to photonic mm-wave components/functions, it is interesting to note that more than 80% of the respondents were particularly interested in utilizing a photonic solution for various reasons. This indicates that the majority is not only interested in the mm-wave function itself but also in using the underlying photonic technology. Only 19% indicated not to be interested in a photonic solution.

With respect to the technical requirements and specifications, different aspects were investigated. As to the required output power level it was found, for example, that almost half of the respondents would be satisfied with output power levels up to 0 dBm, more than 75% would be satisfied by power levels of up to 10 dBm. The most interesting frequency range was found to be DC-110 GHz, followed by the EHF frequency range of 30-300 GHz (see also Annex V).

The survey furthermore reveals that the most required individual photonic mm-wave component is the broadband photodetector operating from DC-110 GHz. Here, the high output power level is seen as key for commercial success with a power level of up to 0 dBm satisfying 42% of all requirements, a power level of up to 10 dBm would even satisfy the requirements of 77% of all respondents. With respect to the output connector, the highest interest was in having a coaxial W1 output connector (45%), followed by rectangular waveguide output connectors (28%). This reflects that the broadband and high-output power photodetector modules using a fiber-optic package with W1-coaxial output connectors and integrated bias-tee developed in the IPHOBAC project are of high interest. As for the cost, 71% would accept cost in the order of up to 1000 € and only 24% indicated to be willing to pay up to 10,000 €. This is somewhat unrealistic, as even the current cost for 40 GHz PDs exceeds the 1000 € level. In summary, the survey reveals a reasonably large market size for 100 GHz PDs – mainly for R&D applications and measurements. In that regard, it should be mentioned that such 100 GHz PD featuring a W1-coaxial output connector developed within the IPHOBAC project have become commercially available in the year 2010 from u<sup>2</sup>t Photonics AG ([www.u2t.de](http://www.u2t.de)) in Berlin and CIP Technologies in Ipswich ([www.ciphotronics.com](http://www.ciphotronics.com)).

Another important component is the integrated photonic mm-wave transmitter operating in the 30-300 GHz frequency range. From the survey, as well as from discussions and requests at international exhibitions, a great interest for these devices - mainly for THz wireless communications, but also for THz measurements - was found. For the time being, a market of a few tens of 30-300 GHz emitters with individual cost of about only 12-18 thousand euro is expected.

Summing up all survey results, photonic-based mm-wave applications and systems will most likely be of significant need in all stated application fields including communications, imaging, spectroscopy, instrumentation, measurement equipment, security, and radar applications. The highest interest was found for communications, where 112 experts see a significant demand for mm-wave applications and systems, followed by the fields of security and radar, where 82 specialists believe in a very high impact. In addition, mm-wave applications and systems are expected to play a stable role in imaging and spectroscopy (53), as well as in instrumentation and measurement equipment (39).

As regards more complex photonic-based systems, a specific function of particular interest is the integrated low-phase noise mm-wave source operating in a frequency range from DC to 110 GHz. Altogether one third of all the respondents have asked for such a fixed frequency source operating inside this range mainly for radar and sensor applications. Regarding the required phase noise levels, about three-fourth of the respondents would be satisfied with phase noise levels below -100 dBc/Hz at 10 kHz offset while 24% require a better phase noise level up to -140 dBc/Hz at 10 kHz offset.

In the following, some of the investigated application scenarios for fixed frequency and for frequency-tunable mm-wave sensors and sources will be briefly presented. Since applications in communications were already discussed in section 5.1, the following will concentrate on applications in instrumentation, transport, security, radar, and the medical field.

### **Enhanced Vision Systems (EVS) for transport vehicles**

The basic motivation for EVS on transport is increased safety, in particular during night and/or in low visibility conditions and also during approach, landing, takeoff, and ground operations. In addition to existing infrared systems, photonic-based mm-wave radar systems allow extending enhanced situation awareness to “all-weather” effectiveness. Moreover, in future systems, by determining the weight of potential obstacles in the approach path, this will allow autonomous approach and landing when opening a wide area of new applications.

The overall market size addressed by classical infrared systems will be more than 800 units per year after 2007, this represents a market of more than 100 M€. The world’s airlines are forecast to take delivery of more than 17,000 new passenger and freighter aircrafts over the next 20 years, equating to average annual deliveries of 866 aircrafts. It is expected that thanks to its “all-weather” effectiveness provided by mm-wave functions, addressable new markets will be at least 1% of the total market in 2012. Later on, since these new systems will replace the classical already installed ones, this market share will continue to increase.

### **High resolution automotive radars**

Strategy analysis predicts that short and long-range distance warning systems will become increasingly common features on passenger vehicles. Ultrasonic, camera, and radar technologies will be used extensively, but only radar systems will find significant application in both short and long-range systems. Market development of automotive radars is expected to accelerate now; more safety-oriented features are reaching the market, along with lower-cost, short-range devices. Short-range system sales will reach around 12 million units per year by 2007. For long-range systems, a worldwide market of approximately 2.5 million system units is expected by 2007. The market size of high-resolution radars is expected to reach 100,000 units in 2012 [36].

### **Measurement equipment**

Thanks to their low phase noise performances, their modulation bandwidth and also their size, mm-wave generator functions based upon Microwave Photonic technologies are intended to be used in instrumentation equipment, replacing all-electronic devices. The equipment concerned is all systems employing mm-wave generators. The worldwide market size is larger than 180 M€, an average of 5500 units.

### **Wireless Sensing Networks, Central Interrogating modules**

Future electronic sensors will have to be highly integrated and able to communicate to each other. Wireless short distance communication will allow building-up an ad-hoc network between several sensors. Several key applications have already been identified, such as distributed smart monitoring for transport applications, wireless sensor networks for health monitoring, and distributed intelligent control. This approach called Smart Dust has been initiated at Berkeley in 1999. But a lot of technical issues are still to be solved. This includes power consumption, size and weight, processing capabilities, communication links, and cost. Consequently, the use of photonic-based technologies will only be possible in medium term.

An application can be foreseen into the “central interrogating modules” responsible for collecting data from all the sensors of the network. These modules are bigger and the constraints are less critical. Among the main functionalities required for these modules, there are very high operating frequencies and frequency diversity. This can be addressed by the approaches studied here. In a rough analysis that takes into account the mobile station market forecast for the EU a total market of about 100,000 interrogating units per year are expected by 2012.

## Global security market

During the period 2000-2008, the global homeland security market grew by 600% from \$23 Billion by 2000 to \$140 Billion by 2008. It is forecasted that during the 2008-2018 period, the global home land security markets will grow by another 81% from a sum total of \$140 billion in 2008 to about \$254 billion in 2018. This means, the home land security market will grow from 0.25% of the global Growth Domestic Product in 2008 to about 0.36%. Most of this growth is expected to come at the cost of reducing traditional military outlays [36]. Overall, the global home land security market is robust and it is forecasted to grow over the next 10 years at an impressive annual growth rate of about 7-7.5%.

Amongst the Next Decade's Fastest Growing Market Sectors are the Information Technology systems, the Defending gas-oil energy facilities, and the Border Security domains which could benefit. In the following, we look at the possible market shares that can be expected in the related domains of high data rate short distance communications and fixed security radar for area surveillance.

### Point-to-point high rate short distance secure communications

The main application concerns crowd surveillance, especially during peace keeping or light crisis periods. The goal is to detect troublemakers through video surveillance by cameras located on vehicles or on policemen close to the vehicles (several ten meters). The video quality has to be of an excellent level since the trouble leaders are usually hidden by the crowd and their images are available only during short periods of time. Therefore, face recognition becomes difficult and a sufficient quality of image is needed. Indeed, the video stream data rate cannot be reduced or limited by using compression algorithms and can reach a couple of 100 Mb/s per channel. The use of mm-wave frequencies is of interest since it will allow delivering very high data rates over a short distance, with frequency reallocation, if necessary.

According to the IPHOBAC report [36], Thales provides a network encryption solution to be associated with mm-wave transmission (70/80 GHz) in order to provide a solution for securing data transmission including voice and video over wireless network. This is of interest for government entities, as well as for financial institutions that need to meet high level security standards. Licensed band 70/80 GHz mm-wave radio technology is also ideal for government and security installations that demand rapid deployment of temporary high-bandwidth wireless links for quick restoration of communications in the event of a natural disaster or other emergency.

The IT security market was estimated in 2007 at 32 billion euros with an annual growth rate of 18%, and the European market itself amounted a total of 12 billion euros.

### **Fixed security radar for area surveillance**

The market of the perimetric detection dedicated to the surveillance of industrial and sensitive areas (e.g. nuclear power stations or embassies) will represent a worldwide market of 1500 million euro in 2009. A third of this market is within Europe. It is forecast that the main boost in airport perimeter security will come from networking. A greater number of airports are switching to digital networks, making it essential to network all security solutions to the main command, control, and communications center. This could therefore enhance the need for optical solutions that easily allow using remote sensors connected to a central processing unit.

### **Health-care and medical applications**

Among the possible applications for photonic-based microwave and millimeter-wave components and systems are several applications in the health-care and medical domains. Today, the European Union population which is close to 400 million has an average age close to 36 years that will become 45 years in 2025. General ageing of the population will lead to an important number of senior citizens. Therefore, a significant increase of health expenses is expected and it is known that in average most of these expenses for seniors appear in the last two years of their lives. Therefore, health expense management is of importance, and to avoid an immense increase of cost, it is crucial to implement intelligent systems for automated health monitoring such as wearable diagnostic devices for providing a real time track of the health status at an earlier stage. As for wireless sensor networks, it is expected that the monitoring sensor itself will not take benefit from photonic-based solutions in a near or midterm. But the central interrogating modules responsible for collecting the data from all the monitoring sensors can probably take the benefit from photonic-based functions and systems. In a rough estimation, the targeted cost of an interrogating unit could be in the order of about 1000 € per unit, and it is expected that 100,000 citizens will require interrogating stations.

As regards market numbers, in 2005, medical techniques and life sciences represented 8% of the total photonic world market of 228 billion euros. Thus, the photonics world market for medical techniques and life sciences was about 18 billion € in 2005. This number is expected to grow to about 30 billion euros in 2015. European production represents about 30% of this market that is to say about 2.3 billion euros in 2005 and an expected 9 billion euros in 2015.

In the following, some medical applications where photonic-based microwave and millimeter-wave sensors and sources could be potentially used are listed:

### **Photonic mm-wave endoscope**

Microwave Photonics could potentially be used to construct an ultra-compact photonic mm-wave endoscope for intra-corporal, minimal invasive, local cell or tissue identification, thermal cancer treatment or cell activation. Absorption and reflection of mm-waves strongly depend on water and fat content and therefore on the composition of biological tissue. It has been reported that the use of mm-waves shows some advantages compared to classical infrared technology in terms of cancer detection and treatment. In that regard, even the activation of natural killer cells appear to be possible.

### **Photonic mm-wave radiator**

Photonic-based sources could potentially be used to construct a low power mm-wave radiator for extra corporal, local tissue exposure for pain therapy. In addition to classical acupuncture and laser induced acupuncture, there is some evidence that low power mm-wave radiation can be used to stimulate specific acupuncture points of the human body, supporting pain therapy. Additionally, studies reported in [36] show the successful application of low power mm-waves to support the healing and pain relief of various forms of ulcer.

### **Live surgery wireless video transmission system**

The high-capacity mm-wave wireless systems developed and discussed in chapter 5 have been shown to be useful for real-time, high-definition video transmission. Such a system is crucially needed during surgery in an operating theatre inside a hospital (telemedicine). It is obvious, that for such an application, high-definition video signals must be transmitted without compression as no latency is allowed. The fact that the wireless RoF systems developed represent the fastest wireless systems worldwide, with at least one order of magnitude higher data rates than conventional all-electronic systems open up an excellent opportunity for addressing such applications.

### **Short-range broadband indoor wireless system for mobile medical apparatuses**

The IPHOBAC technologies could potentially be used to construct a Multi-Gigabit Wireless LAN capable of bi-directionally transmitting medical data (high resolution X-Ray or MRT images, high definition videos from surgery or endoscopic analyses, histological data from

tissues, patient records and life signs like long-term ECG, EEG, etc.) between different mobile medical apparatuses.

### Wireless monitoring in home healthcare

The market for wireless monitoring in home healthcare is still nascent, but rapidly evolving. Among the most common conditions to monitor at home are irregular heartbeats or cardiac arrhythmia, high blood pressure, the glucose levels in diabetes, and high levels of lipids or fats in the blood. In Europe and North America, about 40 million people have cardiac arrhythmia, 200 million people have high blood pressure, 60 million people are diabetic, and about 180 million people have severe elevation of blood lipids. All these diseases are increasing as a result of people getting older and heavier, and all are major causes of high healthcare costs. *Berg Insight* estimates that 250 million people in the EU and the US suffer from one or several diseases that may require home monitoring. Although not everyone benefits from regular home monitoring, there will probably be 50 million people for whom wireless solutions available would be beneficial. According to Berg Insight, the market for home health monitoring of welfare diseases was worth approximately 11 billion \$ in 2008 and is growing about 10% annually.

## 6.2 Advanced microwave and mm-wave photonic sensors and oscillators

### 6.2.1 Microwave (300 MHz - 6 GHz) remote electro-optical EMC sensor

In many technical and medical domains, there is a great interest in small and remote sensors for measuring electromagnetic (EM) fields, e.g. for antenna measurements, automotive applications, EMC compliance testing or hyperthermia studies in biologic tissue. Although the requirements for any specific sensor of course vary between the different applications, it is obvious that electro-optical sensors for measuring EM fields offer a number of generic advantages if compared to all-electronic sensors: they provide electrical isolation which eliminates ground loops, and the optical fibers and dielectric components employed in electro-optical sensors produce minimal field distortion. In addition, electro-optic sensors do not suffer from the loss of phase information as there are no high impedance transmission lines used, in contrast to many all-electronic sensors. Furthermore, electro-optical sensors can be of small size, offer a wide dynamic range and a high sensitivity. Consequently, electro-optical field sensors have been studied for many applications.

For several years, there has been an increasing interest in EM field measurements related to electromagnetic compatibility (EMC) testing and the certification of electronic equipment. All

electronic systems and components are sensitive to EM radiation, but they also act as radiation sources themselves. Thus, for certifying the EMC of any electronic equipment, it is required to test both, the sensitivity of the equipment to EM fields and the power radiated by the equipment itself.

Of course, any EMC measurement relies on the existence of a sensor allowing precise measurements of the EM fields. In many applications, those sensors must not only offer a high sensitivity but also a wide frequency range of operation. As an example, all mobile terminal equipment is certified to fulfill the European norm “Considerations for evaluation of human exposure to electromagnetic fields (EMFs) from mobile telecommunication equipment (MTE) in the frequency range 30 MHz - 6 GHz” [252]. For measuring higher harmonics, the operational frequency range must be even wider.

With the objective to develop a sensor system that allows for frequency selective measurement of electrical fields up to 6 GHz, a hybrid integrated electro-optical sensor system has been developed. In order to provide minimum interference with the measured electric field, the sensor head was connected to the read-out unit via electromagnetic interference (EMI) free optical fibers. The key components within the sensor head are a planar antenna connected to a  $1.55 \mu\text{m}$  InGaAs/InAlAs waveguide electro-absorption (EA) modulator via a low-power GaAs MESFET transimpedance amplifier. In order to minimize interference with the electric field to be measured, any metallic parts in the sensor head had to be avoided as far as possible. Thus, the transimpedance amplifier was powered by optical means, using an array of photovoltaic cells on GaAs substrate for high-efficient power conversion at 850 nm wavelength. Fig. 6.2 shows a schematic of the realized sensor.

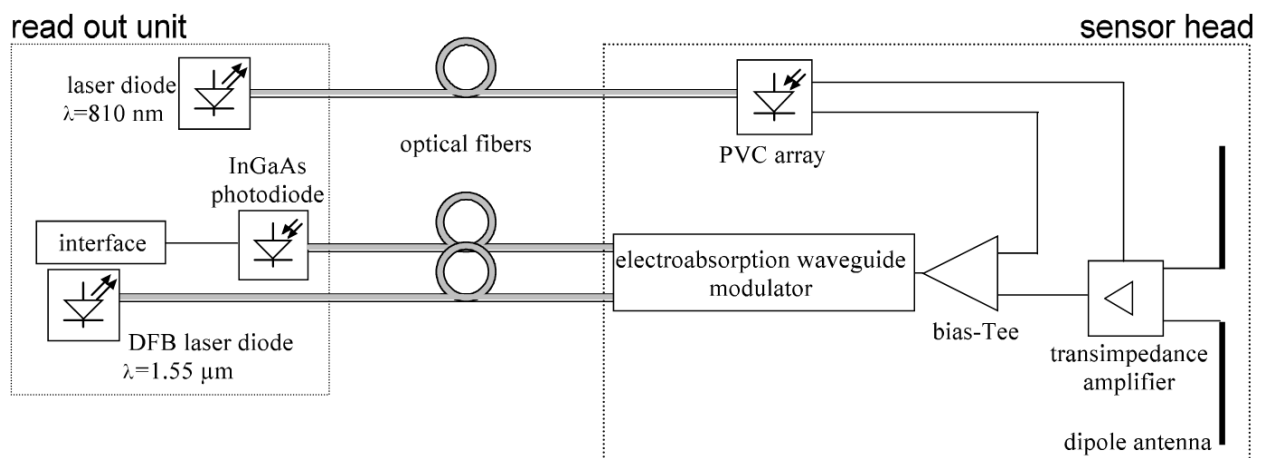


*Fig. 6.2 Sketch of the optically powered integrated electro-optical field sensor.*

In order to determine the theoretical electric field sensitivity of the sensor system, the minimum detectable voltage  $u_m$  of the modulator was determined from an analytic noise calculation where all contributing noise sources of the system were considered. In detail, relative intensity noise (RIN) of the signal laser diode, atmospheric noise, and amplifier noise together with thermal noise, dark current noise and shot noise contribute to the overall noise. The resulting minimum detectable voltage  $u_m$  can be expressed as [253]

$$u_m = \frac{\sqrt{B}}{a} \sqrt{\frac{2qI_D + \frac{4kT}{R_D}}{d^2 P_{LD}^2 S^2} + \frac{q}{dP_{LD}S} + \frac{10^{\frac{RIN}{10}}}{4} + 2v_u^2 kFT \cdot \frac{a^2}{\omega C_0} \cdot \frac{1}{1 + (\omega C_L R_L)^2}}. \quad (112)$$

Here,  $P_{LD}$ ,  $RIN$ ,  $I_D$  and  $S$  describe the output power and relative intensity noise of the laser diode and the dark current and sensitivity of the photodiode, respectively,  $a$  denotes the slope of the modulator transmission characteristic,  $R_L$  and  $C_L$  are resistance and capacitance of the modulator and  $d$  represents the fiber-chip-coupling loss. Finally, the amplifier and antenna are characterized by  $v_u$ ,  $F$  and  $C_0$ , which are the amplifier gain, the noise figure of the amplifier, and the capacitance of the dipole antenna, respectively. Furthermore,  $R_D$  determines the resistive load of the photodiode which depends on the equipment connected to the photodiode. Using eq. (119), the E-field sensitivity of the sensor system can then be derived from

$$|E| = 2 \cdot \frac{u_m}{v_u \cdot l}, \quad (113)$$

where  $l$  is the length of the dipole antenna.

Assuming a large resistive load for the photodiode  $R_D \rightarrow \infty$ , we calculated a field sensitivity of  $12.8 \cdot 10^{-6}$  V/m for a 1 Hz measurement bandwidth [254]. In general, however, the resistive load of the photodiode will be  $R_D = 50 \Omega$ , thus, the influence of thermal noise cannot be neglected. In order to theoretically determine the field sensitivity for that case, the following values of the EAM have been measured:  $a = 0.4 \text{ V}^{-1}$ ,  $R_L = 50 \Omega$  and  $C_L = 300 \text{ fF}$ . Together with the values for the dipole antenna of  $C_0 = 60 \text{ fF}$  and  $l = 8 \text{ mm}$ , as well as the transimpedance amplifier voltage gain and noise figure of  $v_u = 0.2$  and  $F = 3.16$ , respectively, the sensitivity of the sensor system was calculated using eq. (119) and eq. (120). Here, the values for the photodiode and the laser diode were taken from commercially available components and the fiber chip coupling efficiency was estimated to be  $d = 0.2$ . The resulting sensitivity versus the optical input power is shown in Fig. 6.3 for a frequency of 100 MHz. As can be seen, the sensitivity at low optical

power is mainly limited by thermal noise, and it is improved by increasing the optical power. However, for an optical input power in excess of 10 mW, no significant improvement of the sensitivity is achieved due to the noise floor summing up from the laser source, the amplifier and the antenna noise. For the realized sensor system, an optical input power of 4 mW was chosen, resulting in a theoretical electric-field sensitivity of 50  $\mu\text{V}/\text{m}$  for a measurement bandwidth of  $B = 1 \text{ Hz}$ .

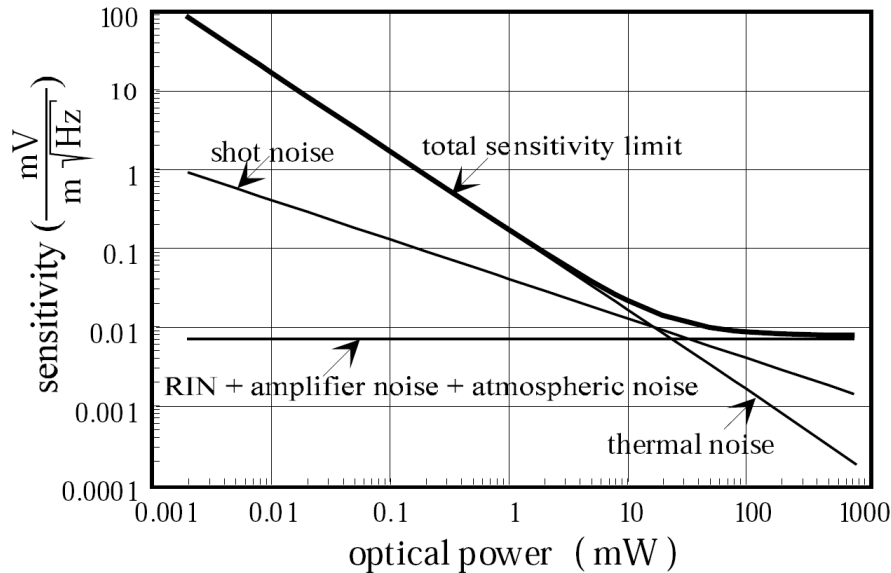


Fig. 6.3 Calculated sensitivity limit of the sensor system as a function of laser power.

A sketch of the realized sensor system that can accurately be described as an analog optical link based on an intensity modulation direct detection (IMDD) scheme was already shown in Fig. 6.2. In the realized sensor head, an electrically small dipole antenna (length  $l = 8 \text{ mm}$ ) was used to convert the measured electric field into a microwave voltage. Because of the impedance mismatch between the capacitive dipole antenna ( $C = 60 \text{ fF}$ ) and the EAM ( $R = 50 \Omega$ ,  $C = 300 \text{ fF}$ ), it was necessary to insert an impedance matching circuit between the antenna and the EAM. For achieving highest field sensitivity, this matching circuit was realized as a transimpedance amplifier (TIA) using a low-power GaAs MESFET technology.

Fig. 6.4 shows the frequency dependence of the voltage gain under operational conditions. A gain of -12.5 dB and a gain flatness of only  $\pm 0.07$  dB are achieved within the frequency range 0.1 GHz to 6 GHz. The power consumption of the amplifier is 40 mW at a voltage of 4 V. Further details of the MESFET TIA layout and dimensions can be found in [253].

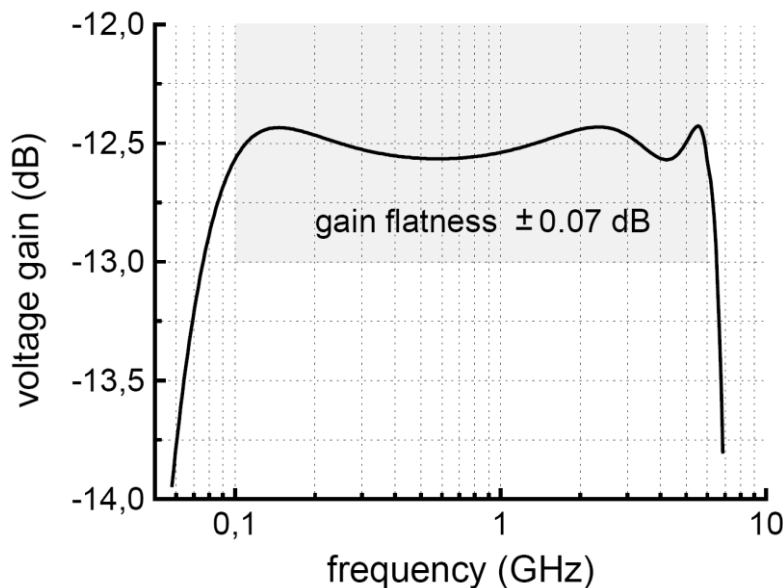


Fig. 6.4 Voltage gain of the GaAs MESFET transimpedance amplifier under operational conditions (the shaded frame indicates specification).

In the sensor, the TIA feeds the EAM which transfers the microwave voltage from the antenna into the optical domain. Next, the microwave modulated optical carrier is transmitted via a standard single mode fiber (SMF) to a high-speed photodiode located in the readout. After conversion back into the electrical domain, the measured signal is transferred to a general purpose interface, enabling the connection to almost any kind of measurement instrument. Generally, for frequency selective measurements an electrical spectrum analyzer will be connected to the interface.

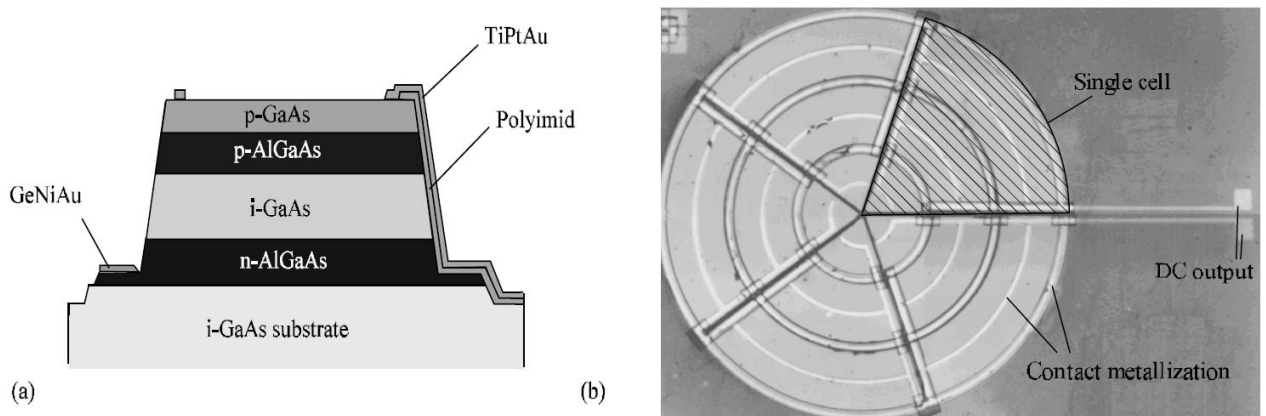


Fig. 6.5 Cross-section of single PVC (a) and photograph of a realized array of 5 PVCs (b).

In order to provide the necessary electrical power for driving the transimpedance amplifier and for reverse biasing the EAM by optical means, a photovoltaic cell (PVC) array was realized. The PVC array has been optimized for high power conversion efficiency at monochromatic illumination. Since almost no additional power consumption is expected from the EAM as it is a reverse biased device with a dark current of not more than  $100 \mu\text{A}$ , the total electrical power of 40-50 mW is required mainly to drive the transimpedance amplifier.

An optimum operating region for the high-efficiency PVC array is the wavelength range from 800 - 850 nm. This is because high power laser diodes for this wavelength range are available at reasonable prices, and the photovoltaic response of GaAs exhibits the optimum value within this wavelength range. Therefore, the PVC array was realized on GaAs substrate. The layer structure for the PVC was grown on semi-isolating intrinsic GaAs substrate and consists of a *pin* AlGaAs/GaAs double heterostructure with an additional thin GaAs cap layer. The *n*-contact is formed using a GeNiAu metallization while for the *p*-contact TiPtAu was used. The cross-section of the PVC is shown in Fig. 6.5 (a).

Both the modulator and the TIA were designed for optimum operation at a bias of 4 V. To achieve this output voltage from the PVC, it was necessary to connect five to six single photovoltaic cells in a series. For achieving the necessary output power, it was further necessary to develop an array of PVCs to reduce the thermal load per single cell. Furthermore, for having a uniform intensity distribution over the five PVC cells connected in series, a circular layout had been chosen for the PVC array. To enhance the efficiency, a SiO<sub>x</sub> had been deposited as anti-reflection coating. Furthermore, the thickness of the intrinsic GaAs region has been designed to be an odd multiple of half the wavelength. A photo of a fabricated PVC array with five cells in series is shown in Fig. 6.5 (b).

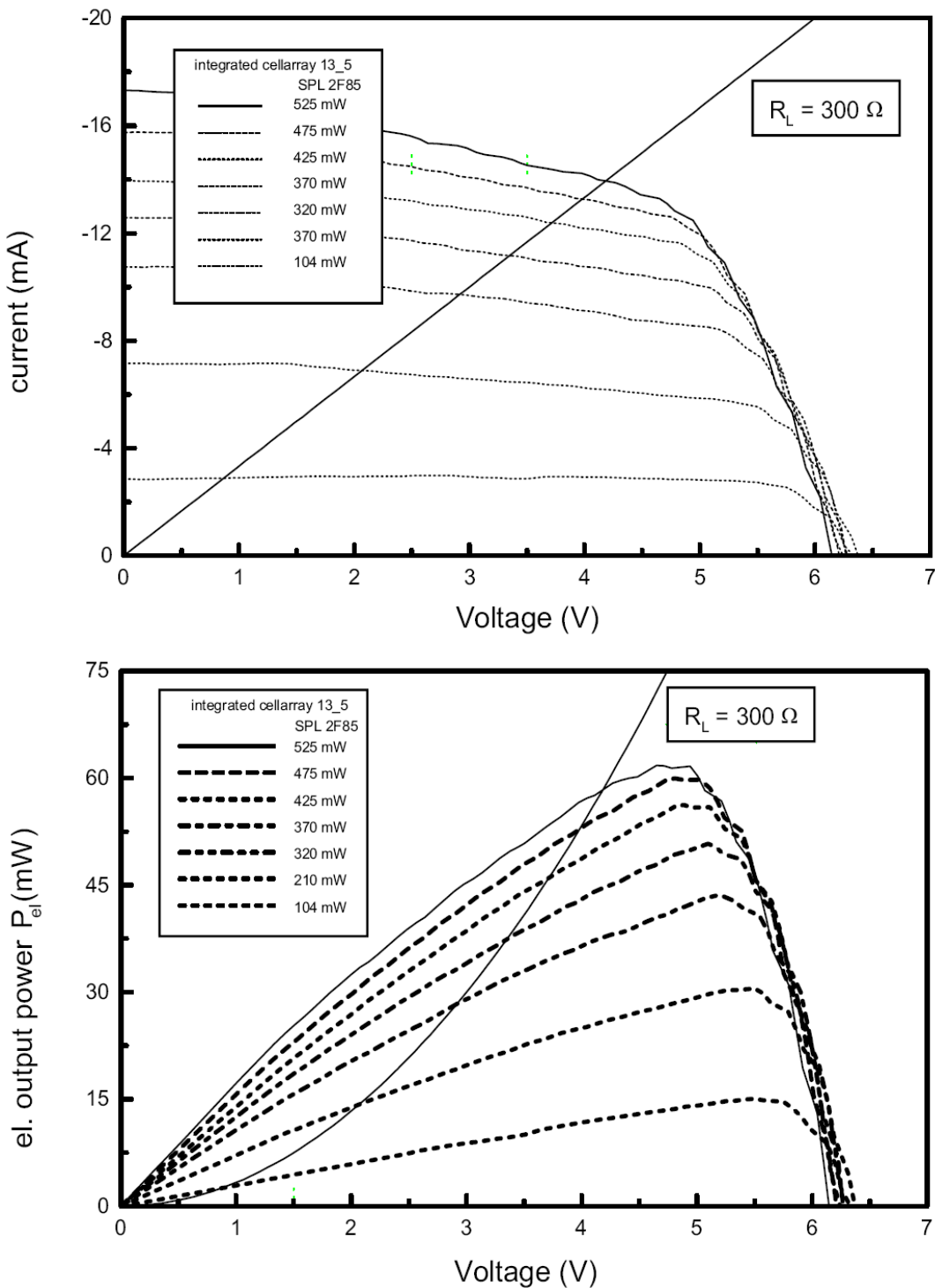


Fig. 6.6 Current-voltage (upper figure) and power-voltage (lower figure) of the fabricated PVC array consisting of six cells in series.

For characterizing the photovoltaic cell arrays, they were illuminated at 840 nm wavelength using direct vertical fiber-to-chip coupling. The measured I-V and P-V characteristics of a PVC array with six cells in series are shown in Fig. 6.6

The current-voltage characteristics for a PVC array with six serial AlGaAs/GaAs cells, shown in Fig. 6.6, exhibits an open-circuit voltage of  $\sim 6.2$  V. Also, a linear dependency of the short-circuit current with respect to the optical input power was found. Given that the DC input impedance of the TIA is about  $300\ \Omega$ , the I-V characteristic also shows that the required voltage to drive the TIA and the modulator of 4 V is achieved for optical input power levels in the range of 425-525 mW. Furthermore, the power-voltage characteristics reveal that the power conversion efficiency is close to optimum for the TIA load impedance of  $300\ \Omega$  and also the output power of 4 V

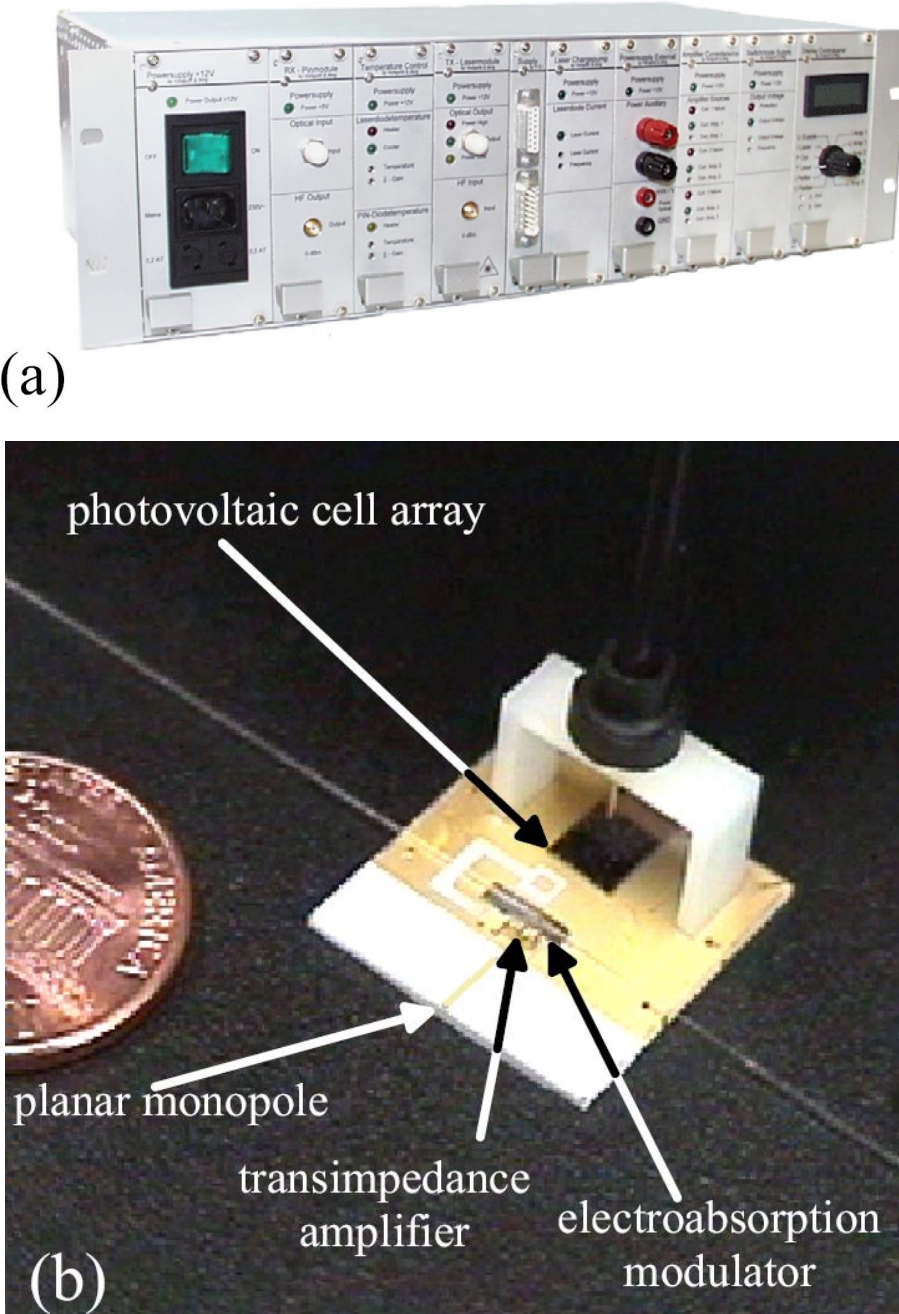


Fig. 6.7 Realized read-out (a) and sensor head (b).

required to drive the TIA and the modulator is achieved for optical input power levels between 425 and 525 mW. The achieved overall power conversion efficiency is in excess of 10%, allowing output power levels of up to about 60 mW which is even in excess of the required 40–50 mW to drive the TIA and the modulator.

The interference of the sensor with the electric field to be measured is of major importance in E-field measurement systems. In order to reduce this interference to a minimum level, the developed sensor system is split into a highly integrated, small-size sensor head and a remote read-out unit. The sensor head is connected to the read-out unit by use of optical fibers. The read-out unit contains a laser diode operating at  $1.55\mu\text{m}$  wavelength, providing the optical carrier for the looped-back transmission of the measured signal. The read-out unit also contains a second laser diode operating at 840 nm wavelength, required for optical powering of the sensor head. Furthermore, a commercial photodiode is used in the read-out unit for recovering the received signal from the optical domain and assign it to an electrical interface. The realized read-out unit is shown in Fig. 6.7 (a). The integrated sensor head (see Fig. 6.7 (b)) consists of a planar 4 mm long monopole antenna which is connected via the TIA to a multiple quantum well electro-absorption modulator. The necessary power to drive the TIA and the modulator is provided by the GaAs PVC array that neither adds significant metallic parts nor significantly increases the overall size of the sensor head.

The performance of the developed fiber-coupled E-field sensor system was analyzed with respect to the sensitivity, i.e. the minimum detectable electric field strength, and its dynamic range. These measurements were carried out within the specified frequency range from 10 MHz up to 6 GHz, using a spectrum analyzer with a measurement bandwidth set to 1 Hz. At first, different electric field strengths were applied to the sensor's antenna and the frequency dependent minimum detectable electric field for a SNR = 1 was measured.

As can be seen from the upper diagram in Fig. 6.8 the minimum detectable electric field strength is below the required 100 mV/m level within the full bandwidth from 10 MHz up to 6 GHz. The highest sensitivity with a minimum detectable electric field strength of 16 mV/m was achieved at 0.9 GHz. Furthermore, the dynamic range experimentally was characterized by increasing the electric field strength up to the 1 dB compression point, i.e. until the signal at the read-out unit deviates by 1 dB from the linear behavior. The measured dynamic range is depicted in lower diagram in Fig. 6.8.

As can be seen, a maximum dynamic range varies between 70 - 74 dB for the frequency range of 10 MHz up to 1 GHz. At higher frequencies, the dynamic range slightly decreases down to 58 dB at 6 GHz. Thus, at 6 GHz the sensor allows the measurement of electric fields with field

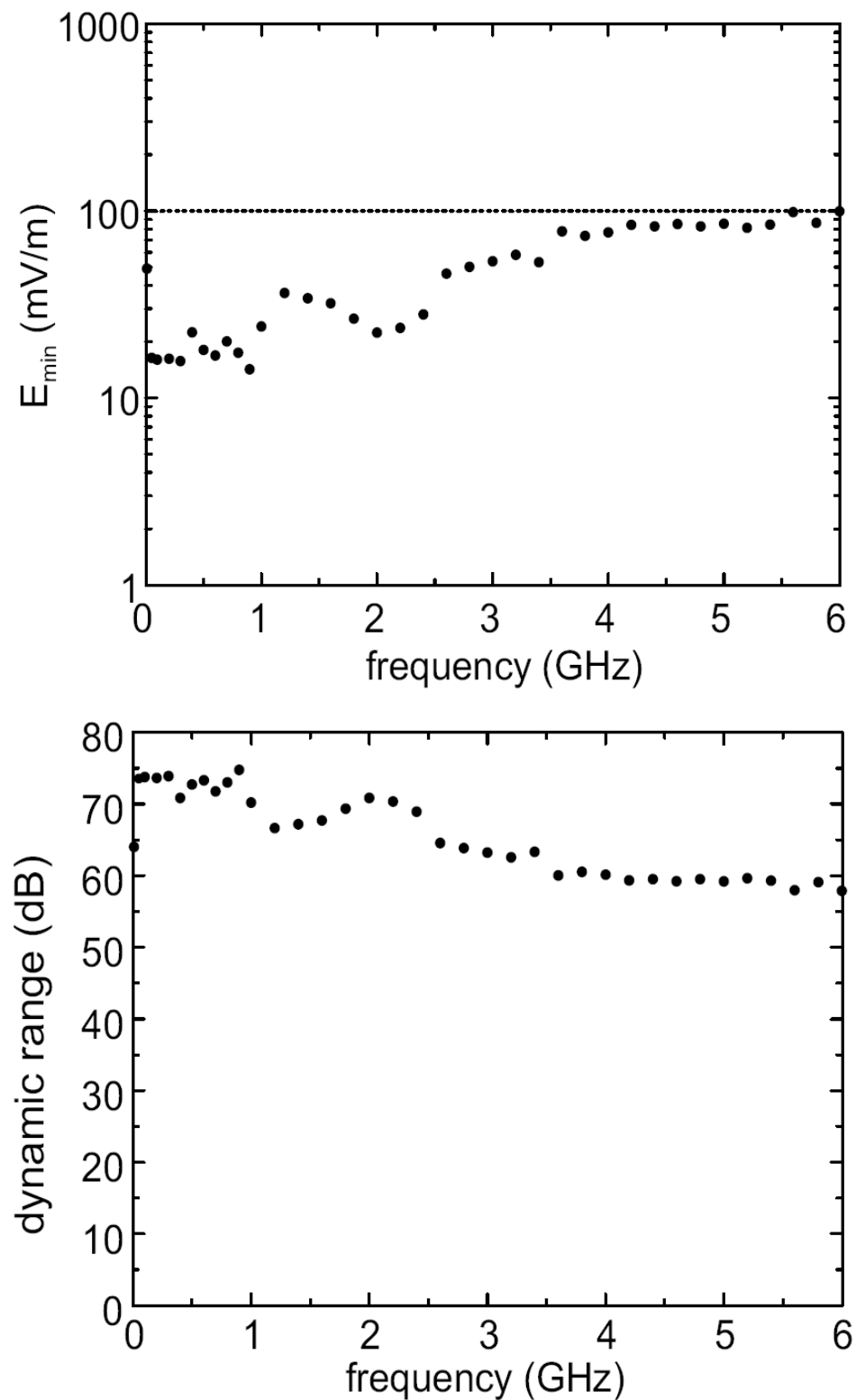
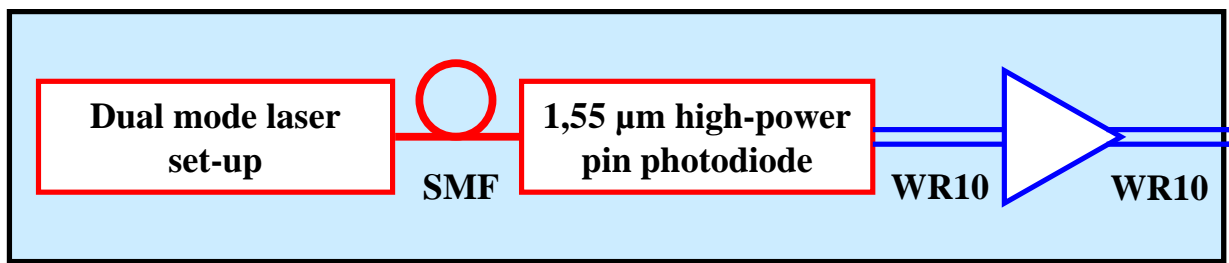


Fig. 6.8 Sensitivity (upper diagram) and dynamic range (lower diagram) of the developed electric-field photonic-based sensor system.

strengths between 100 mV/m up to about 80 V/m.

### 6.2.2 Millimeter-wave (75-110 GHz) photonic synthesizer

A promising concept for the generation of frequency-tunable cw-signals with low phase-noise is the photonic synthesizer concept based upon optical heterodyning. As discussed in chapter 2, the principle of optical heterodyning is based upon the interference of two coherent optical waves with slightly different frequencies  $\omega_1$  and  $\omega_2$ . In section 2.1, it was theoretically shown that this results in a "beat" wave which oscillates at the difference frequency  $\omega_2 - \omega_1$  between the two incident optical waves. Changing the wavelength, respectively the angular frequency, of one of the constituent waves thus results in a change of the difference frequency of the beat signal which is finally detected in a high-frequency photodiode for the generation of cw-signal at the beat frequency. The photonic synthesizer or photonic oscillator concept is a rather new technique for providing frequency-tunable and low-phase noise continuous-wave signals. Compared to purely electrical sources and all-optical sources, such as quantum cascade lasers, a photonic synthesizer exhibits a number of unique features like frequency-tunability, ultra-wideband operation, and the possibility to operate without cryogenic cooling. Because of these advantages, the photonic synthesizer concept can potentially become an alternative signal generation technology to existing all-electronic solutions for a number of applications including instrumentation, communications, and sensing/radar. According to a study initiated by the European Space Agency (ESA), the photonic approach based upon advanced photo-detectors is even considered as one of the most promising candidates for millimeter-wave signal generation [121].



*Fig. 6.9 Schematic diagram of the photonic millimeter-wave synthesizer based upon optical heterodyning.*

Because of its unique features, photonic synthesizers are applicable for broadband wireless communications, radio-astronomy, and millimeter-wave imaging. Since the performance of a photonic synthesizer is strongly related to the invention of high-frequency and high output power

photodetectors, those types of millimeter-wave photonic components are also being studied intensively in order to enhance the available output power levels at millimeter-wave frequencies.

In this section, a frequency-tunable photonic millimeter-wave synthesizer which features a flat frequency response over the entire W-band is presented. A schematic of the developed photonic synthesizer is shown in Fig. 6.9. As can be seen, the photonic synthesizer is based upon optical heterodyning of a two-mode  $1.55\text{ }\mu\text{m}$  laser signal in a high-power pin photodiode which is further connected to a WR10 rectangular waveguide. A two-stage limiting amplifier with an inter-stage isolator and a noise figure of  $4.5\text{ dB}$  was further employed to achieve a flat frequency response. The main purpose of the amplifier was not to amplify the photodetector's output signal, but the amplifier is acting as a limiting amplifier for achieving an extremely flat frequency response over the entire W-band which is required in several applications such as millimeter-wave imaging. The gain of the employed limiting amplifier is shown in Fig. 6.10.

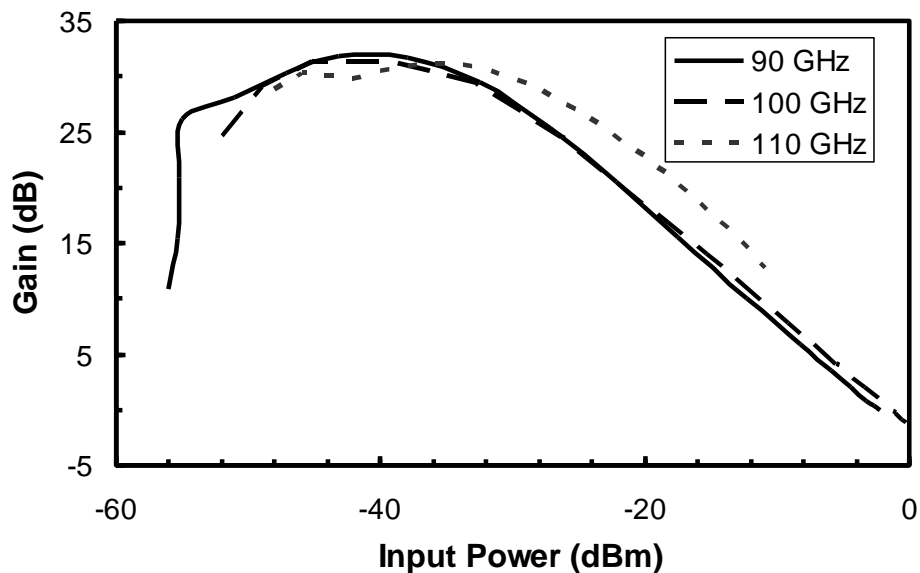


Fig. 6.10 Millimeter-wave gain of the limiting amplifier versus the input power at different frequencies.

As can be seen, the amplifier's gain depends linearly on the millimeter-wave input power within the input power region of interest, i.e. from about  $-35\text{ dBm}$  to  $0\text{ dBm}$ . For input power levels between  $-50\text{ dBm}$  and  $-35\text{ dBm}$ , the amplifier's gain is almost constant.

The key component of the photonic synthesizer is the high-power broadband pin photodiode with a bandwidth of  $f_{3\text{dB}} > 70\text{ GHz}$  [41], which was further coupled to a WR10 waveguide output. At  $1.55\text{ }\mu\text{m}$  wavelength, the waveguide coupled photodiode exhibits a responsivity of about  $0.3\text{ A/W}$ . The PD's photocurrent linearly increases with increasing optical input power until optical saturation due to internal field screening is achieved. As internal field screening

strongly depends on the applied voltage, the optical saturation power increases with applied reverse bias. At a reverse bias of 3V, no saturation was observed up to an optical input power of 40mW [41]. The frequency response of the photodiode was measured using an external W-band mixer and an Agilent electrical spectrum analyzer. The relative frequency response of the photodiode coupled to a WR10 waveguide output is shown in Fig. 6.11.

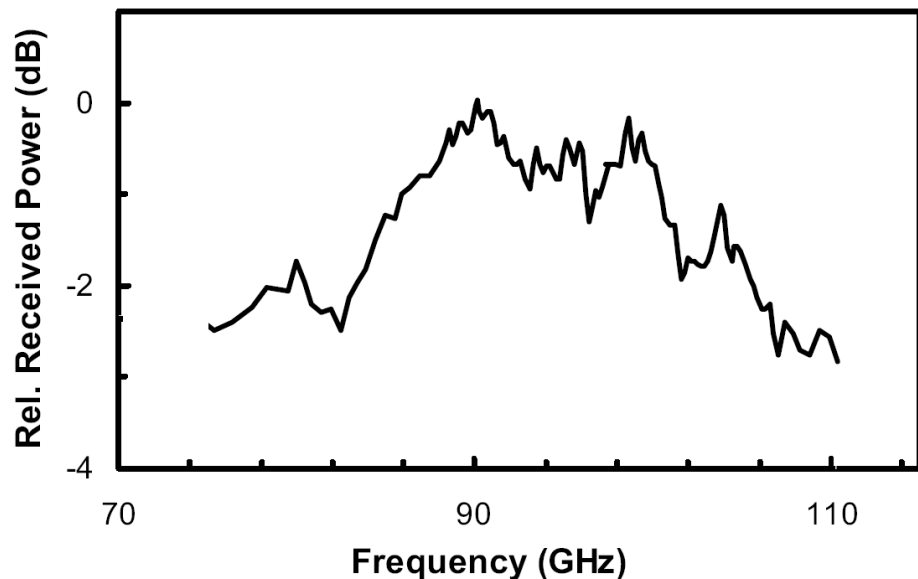


Fig. 6.11 Relative frequency response of the waveguide coupled pin photodiode.

As can be seen from Fig. 6.11, the photodiode exhibits a quite flat frequency response for the entire W-band with a maximum power variation of only 3 dB. It can be further seen that the output power peaks at around 100 GHz due to a partial compensation of photodiode capacitance, leading to a pronounced inductive peaking. At a photocurrent of 10 mA, the photodiode with waveguide output port provides a maximum millimeter-wave power level of -4.88 dBm. This power level would already be sufficient for practical use. For protecting the photodiode, system experiments were only performed at photocurrent levels below 12 mA.

To investigate the frequency response of the photonic synthesizer, the two-mode laser set-up was connected to the photodetector via single mode fiber (SMF) and the photodetector was connected to the amplifier via a WR10 rectangular waveguide. To measure the frequency response of the synthesizer, an external mixer was used to enhance the frequency range of an Agilent spectrum analyzer. Fig. 6.12 shows the measured millimeter-wave output.

As can be seen, the frequency response is extremely flat with a maximum power fluctuation below 3 dB for a wide frequency range from 69 GHz up to 112 GHz. The total frequency-tunability extends from 66 GHz up to 116 GHz. At frequencies lower than 69 GHz, the output power rapidly decreases which is attributed to the lower cut-off frequency of the WR10

waveguide and to the lower gain of the limiting amplifier. At frequencies above 112 GHz, the output power also rapidly drops due to the reduced output power of the photodetector and to the lower gain of the amplifier.

Since the gain of the waveguide amplifier is decreasing for input power levels below -35 dBm, the output power of the photonic synthesizer can still be varied quite linearly by operating the photodetector with a low optical input power level.

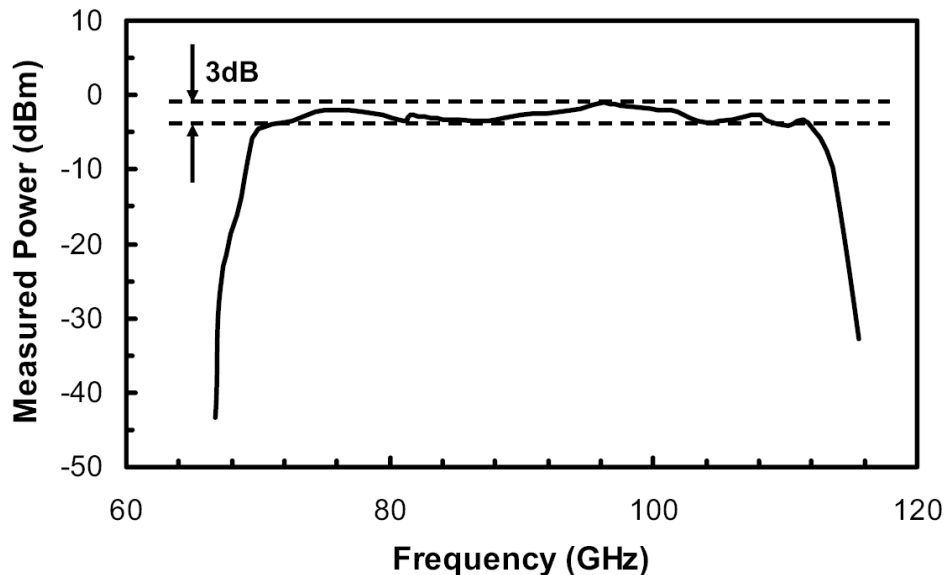
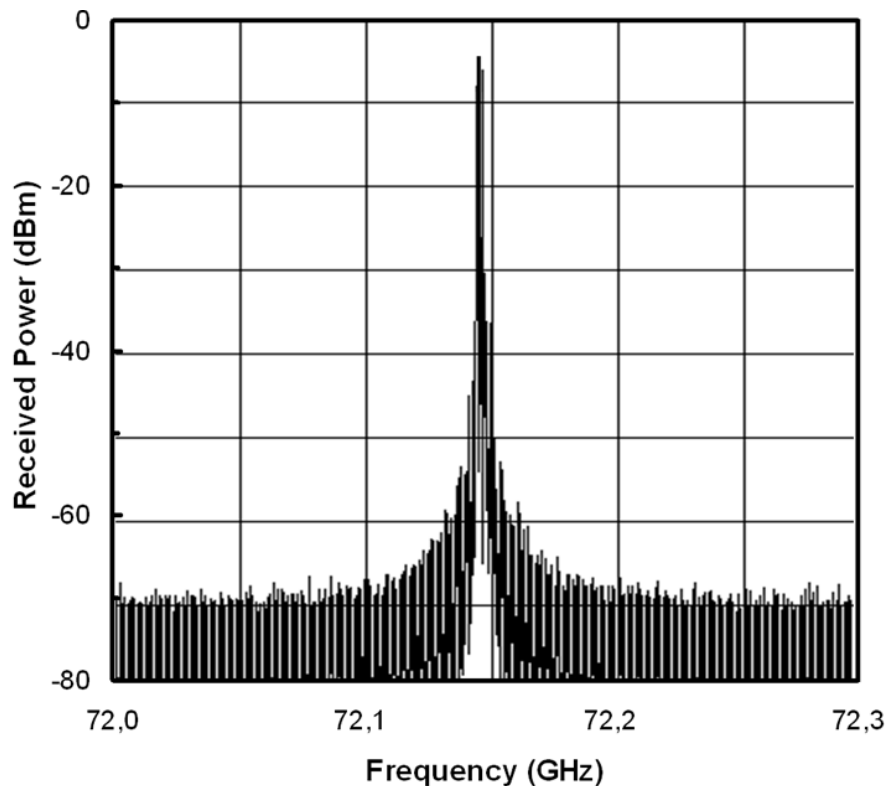


Fig. 6.12 Output power of the photonic millimeter-wave synthesizer versus millimeter-wave frequency. For this experiment, the photodiode was operated at a reverse bias of -2 V and its DC photocurrent was set to 2 mA.

The output power of the photonic synthesizer can be varied linearly (1 dB compression point) from up to about -5 dBm by changing the optical input power level to the PD. The maximum output power level achieved is -0.23 dBm which is limited by internal field screening. It should be noted that the highest output power level is achieved for photocurrents below 12 mA.

Fig. 6.13 shows the typical RF spectrum of the optically generated millimeter-wave signal at about 72 GHz using a spectrum analyzer with an W-band external mixer. As can be seen, the carrier-to-noise ratio exceeds 60 dBc for the measurement bandwidth of a couple of MHz. The phase noise of the optically generated mm-wave signal has further been investigated in more detail by Fedderwitz *et al.* in [42]. Phase noise measurements were carried out using a 50 GHz electrical spectrum analyzer with a computer assisted phase noise capture unit, allowing precise measurement results for frequency offsets in excess of 1 kHz. To measure the phase noise of signals at frequencies in excess of 50 GHz, the measurements were carried out using external harmonic mixers.

For a 100 GHz signal, it was found that the phase noise of the optically generated signal is about 8 dB larger than the reference LO signal applied to the modulator in Fig. 6.9. As an example, at



*Fig. 6.13 RF spectrum of the optically generated millimeter-wave signal at 72.14 GHz.*

an offset frequency of 10 kHz from the carrier the phase noise levels of the LO signal and the optically generated signal are -77.9 dBc/Hz and -69.8 dBc/Hz, respectively. This leads to a phase noise penalty of 2.3 dB, the additional 6 dB are due to the frequency doubling which occurs because the MZM is operated at carrier suppression (see also section 3.2.2). For offset frequencies in excess of 200 kHz, the phase noise of optically generated 100 GHz signal is limited to -93 dBc/Hz. This phase noise level is limited by the accumulated noise power at the PD, including thermal noise, shot noise, and laser-induced relative intensity noise (RIN). It should be noted, however, that the usage of the external mixer is a limiting factor for very low phase noise signals.

The next section will discuss the overall phase noise of optically generated mm-wave signals and different techniques to measure it. On top of that, the next section will also present a new photonic heterodyne technique that allows to measure the residual phase noise coming from the optical sources in a millimeter-wave synthesizer.

### 6.2.3 Phase-noise of the optically generated millimeter-wave signals

This section will focus on the phase noise of optically generated frequency-tunable mm-wave signals. In addition to the overall noise measurement using a direct spectrum technique, also a new approach for measuring the residual phase noise of the optically generated signals using a heterodyne set-up with a photonic reference local oscillator (LO) is presented.

There are many techniques for measuring the phase noise from an oscillator or those added by a device. How precise each of these methods is depends on both, the technique and the characteristics of what is being measured. A rather simple and straight forward technique for measuring the phase noise of an oscillator signal is the direct spectrum technique. In the case of a photonic synthesizer, the optical heterodyne output signal of the photonic local oscillator (PLO) unit is input into a high-frequency photodiode which is further input into an electrical spectrum analyzer (ESA) tuned to the device under tests (DUT) oscillation frequency (see Fig. 6.14). Although this method is quite straight forward as it allows to directly measure the phase noise of the DUT using a legacy spectrum analyzer, it may not be useful under certain circumstances. For example, as the spectral density is measured with existence of the carrier, the direct spectrum technique can be significantly limited by the ESAs dynamic range. In the presence of a high power carrier the minimum noise signal that can be measured at a certain offset frequency is given by the carrier peak power minus the dynamic range of the ESA. Especially for low-noise photonic sources and at high offset frequencies this can be a substantial limitation. In case of a carrier frequency drift, this method may also not be useful for measuring very close-in phase noise (phase noise close to the carrier at low offset frequencies). In addition, most legacy ESA do not differentiate between phase noise (PN) and amplitude noise (AN) but perform a so-called all-noise measurement.

Thus, the direct spectrum technique can only be considered as a quantitative evaluation technique for phase noise measurements if the following conditions are met:

- the ESAs inherent single-sideband (SSB) phase noise at the offset frequency of interest must be substantially lower than the noise of the DUT
- the noise of the DUT at the offset frequency of interest must be higher than the carrier signal power minus the ESAs dynamic range
- the amplitude noise of the DUT must be significantly below its phase noise (typically 10 dB will suffice)

In the following, different techniques for measuring the phase noise and the residual phase noise of a frequency-tunable photonic oscillator which is the DUT are studied.

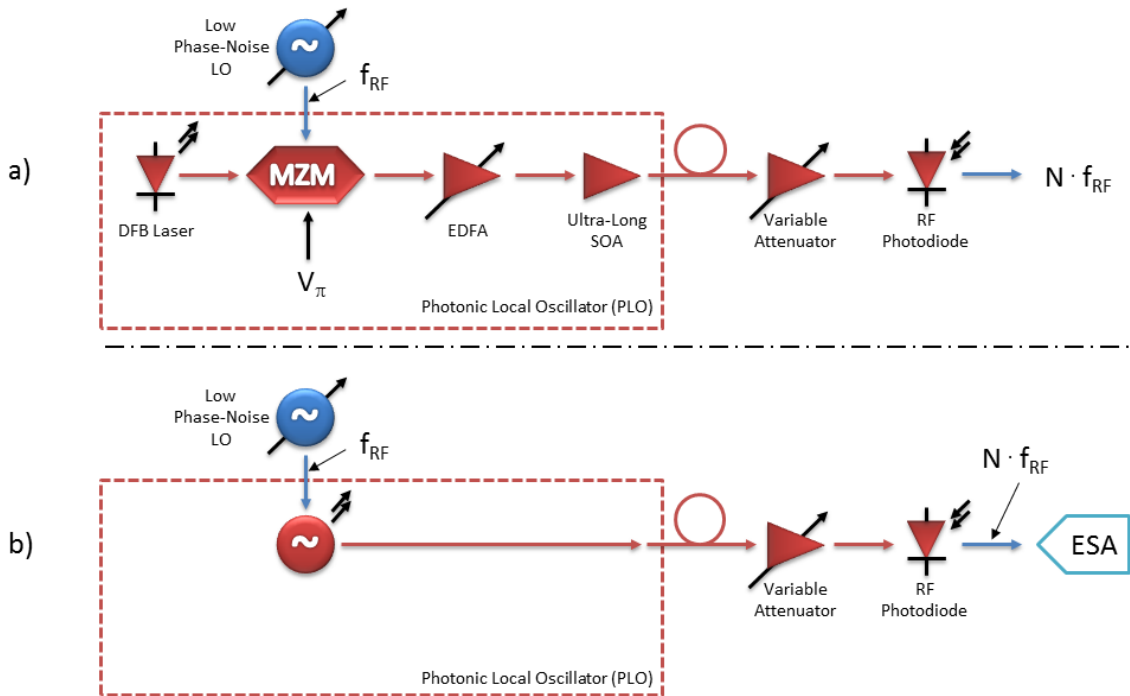


*Fig. 6.14 a) Detailed schematic illustration of the developed frequency-tunable photonic mm-wave synthesizer and b) schematic illustration of direct spectrum phase noise measurement using an electrical spectrum analyzer (ESA).*

The photonic oscillator studied in this section is presented in Fig. 6.14 a. It was developed for the European Space Agency (ESA) within the PHOMIGEN project [255]. Key objective was the development of a low phase noise but nevertheless frequency-tunable photonic source for W-band operation (75-115 GHz). The developed photonic synthesizer consists of the so-called photonic LO (PLO) unit for generating an optical heterodyne dual-frequency signal and a high-frequency photodiode module for o/e-conversion. The PDs 3dB cut-off frequency and DC responsivity are 110 GHz and 0.61 A/W, respectively. The photonic local oscillator consists of a 1550 nm DFB laser source (LD) with a subsequent EDFA and polarization controller (not shown in the figure). A MZM modulator biased at  $V_\pi$  and driven by a low-phase noise LO is used for generating a double side band optical signal with a suppressed carrier (DSB-CS). An EDFA precedes the ultra-long SOA (UL-SOA) in order to obtain the required optical input power necessary for driving the UL-SOA in the non-linear regime. This way, the optical difference frequency is being multiplied due to four-wave mixing in the nonlinear section of the UL-SOA (see also section 2 for FWM in SOA). Detailed investigations of the operation conditions for the MZM and the UL-SOA were carried out for achieving a high optical multiplication factor and a high conversion efficiency [255-258]. The developed photonic LO allows at least twelve times

optical multiplication. However, for the sake of conversion efficiency, the 6th harmonic ( $N=6$ ) was used in the following experiments as it was found experimentally that the conversion efficiency was improved by 5 dB when using  $N=6$  instead of  $N=12$ . For achieving optimum conversion efficiency with  $N=6$ , the output power of the LO was set to +18 dBm and the frequency was tuned between 15.833-19.166 GHz. The input power of the UL-SOA was set to +8 dBm. To protect the PD from damage, the optical input power into the PD was limited to about +7 dBm using a variable optical attenuator.

When aiming at measuring the noise of the optically generated signal in the W-band, another challenge arises. This is due to the fact that ESAs are typically limited in maximum operation frequency to below 50 GHz. Thus it becomes necessary to first down-convert the optically generated mm-wave signal to a microwave frequency for being able to measure its phase noise using the direct spectrum technique. This approach is scheduled in Fig. 6.15.

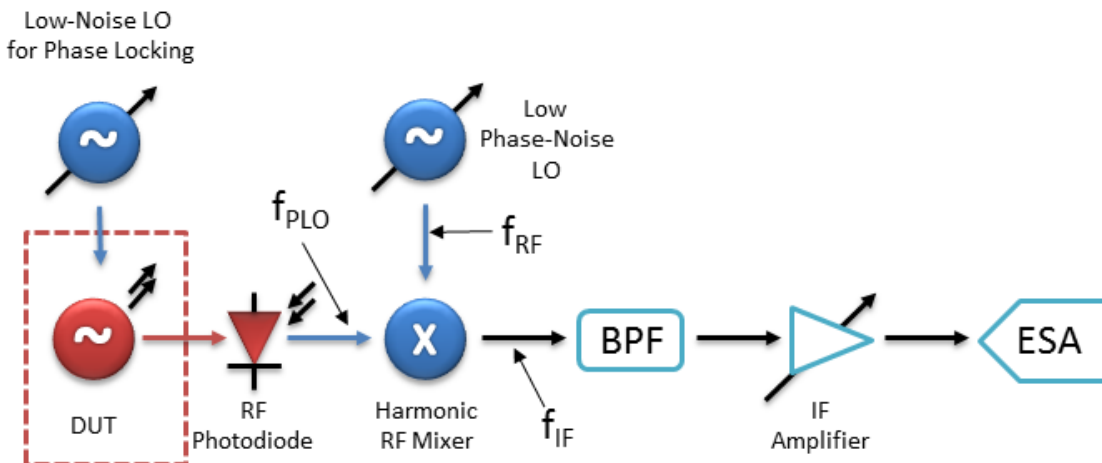


Fig. 6.15 Direct spectrum phase noise measurement using a sub-harmonic mixer driven by a low phase noise electrical LO for down-converting the optically generated mm-wave signal to a microwave frequency.

As can be seen from Fig. 6.15, the photonic LO is locked to a low-frequency electrical reference oscillator and its optical output is input into a high-frequency photodiode. Next, the W-band output signal of the photodiode is down-converted to a microwave frequency using a sub-harmonic mixer (here Agilent 11970W) which is driven by an external local oscillator operating at a specified sub-harmonic.

The problem with respect to phase noise measurements of the optically generated mm-wave signal is that the phase noise of the local oscillator used to down-convert the mm-wave signal to a lower microwave frequency puts another limit on the minimum detectable noise power. This is especially crucial for low phase noise photonic synthesizers. The limitation can also be seen

from the following analysis of the DUT signal and the down-converted intermediate frequency signal:

$$S_{\text{DUT}} = A_{\text{DUT}}(t) \cos(2\pi f_{\text{DUT}} t + \varphi_{\text{DUT}}(t)), \quad (114)$$

$$S_{\text{LO}} = A_{\text{LO}} \cos(2\pi f_{\text{LO}} t + \varphi_{\text{LO}}(t)), \quad (115)$$

$$S_{\text{IF}} \propto A_{\text{DUT}}(t) \cos(2\pi(f_{\text{DUT}} - nf_{\text{LO}})t + \varphi_{\text{DUT}}(t) - n\varphi_{\text{LO}}(t)). \quad (116)$$

Here,  $S_{\text{DUT}}$  denotes the signal under test,  $S_{\text{LO}}$  is the local oscillator signal and  $S_{\text{IF}}$  is the resulting intermediate frequency signal at the output of the sub-harmonic mixer.  $A_{\text{DUT}}$  and  $\varphi_{\text{DUT}}$  represent the amplitude and phase noise of the mm-wave signal,  $\varphi_{\text{LO}}$  denotes the phase noise of the sub-harmonic local oscillator. As can be seen from eq. (116), the phase noise of the intermediate frequency signal contains both, the phase noise of the DUT and the phase noise of the electrical LO used for down-conversion. Thus, the phase noise of the intermediate frequency signal  $L_{\varphi,\text{IF}}$  is given as:

$$L_{\varphi\text{IF}} = L_{\varphi\text{DUT}} + n^2 L_{\varphi\text{LO}}. \quad (117)$$

As can be seen from eq. (117), the phase noise of the intermediate frequency is the sum of the phase noise of the DUT and the phase noise of the sub-harmonic local oscillator multiplied by the sub-harmonic number squared. For example, if one uses the tens sub-harmonic frequency for down-converting the optically generated mm-wave signal in a sub-harmonic mixer, then the intermediate frequency's phase noise includes the phase noise of the original mm-wave signal (to be measured) plus the sub-harmonic LO plus 20 dB. This leads to a significant limitation because if the phase noise of the mm-wave DUT signal is lower than the multiplied phase noise of the electrical LO used for down-conversion, i.e.  $L_{\varphi,\text{DUT}} < n^2 L_{\varphi,\text{LO}}$ , then it cannot be detected with this approach. This limitation becomes especially significant when using the built-in local oscillators of legacy standard ESAs because the phase noise of their integrated LO is usually not very good.

To reduce the above limitation, a special low-phase noise synthesizer (Agilent E8257D with low-phase noise UNX option) was used in the following experiments to down-convert the optically generated signal to an IF frequency of 10 MHz. After band pass filtering and amplification, the signal was recorded using a high-resolution 100 MHz digital oscilloscope

(Agilent DSO6014). The oscilloscope retrieves the phase of the intermediate frequency signal with comprises the phase noise of the DUT as well as the phase noise of the harmonic synthesizer signal used for down-conversion. The sampled intermediate frequency signal ( $S_{IF}$ ) is then further processed in the digital domain using a Fast Fourier Transformation (FFT) to obtain the phase noise as described above. The advantage of the described set-up is that quadrature can be easily achieved within the digital domain; the disadvantage is that there is a large IF signal to be sampled which limits the dynamic range of the measurement. The noise floor of the measurement technique is thus limited by the precision of the AD sampling as well as by the noise of the harmonic synthesizer signal.

Fig. 6.16 shows the measured phase noise of an optically generated 100 GHz mm-wave signal (blue solid line) using the developed PHOMIGEN photonic synthesizer presented in Fig. 6.14. The red line shows the expected phase noise floor set by the driving low-noise synthesizers used to lock the PLO and to down-convert the signal.

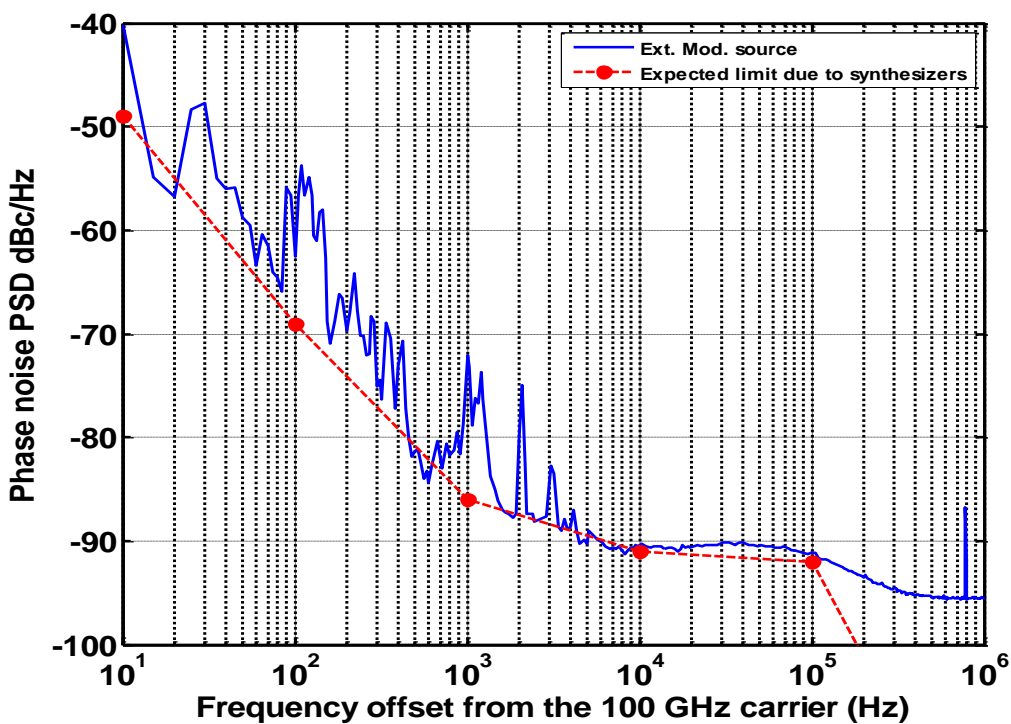


Fig. 6.16 Phase noise of the signal delivered by the photonic external modulation source.

As can be observed from Fig. 6.16, the absolute phase noise of the generated 100 GHz signal is -91 dBc/Hz @ 10 kHz offset from the 100 GHz carrier. Fig. 6.16 also shows the expected phase noise limit due to the electrical LOs and it can be seen, that the measured phase noise is mainly determined by this phase noise coming from the electrical LOs. Especially in the frequency range above 2 kHz the measured absolute noise appears to be limited mainly by the phase noise of both electrical LOs which indicates that the residual phase noise coming from the optical part

of the external modulation source is indeed much lower than the measured value of -91 dBc/Hz @ 10 kHz offset. Below 2 kHz, additional phase noise coming from the optical source was observed and is considered to be due to the used EDFA employed to drive the UL-SOA in the non-linear regime (see also Fig. 6.14).

The above discussion clearly reveals that in order to measure only the residual phase noise coming from the optical source, it is necessary to further reduce the phase noise floor of the measurement set-up. To achieve this, a new photonic heterodyne discriminator set-up is presented.

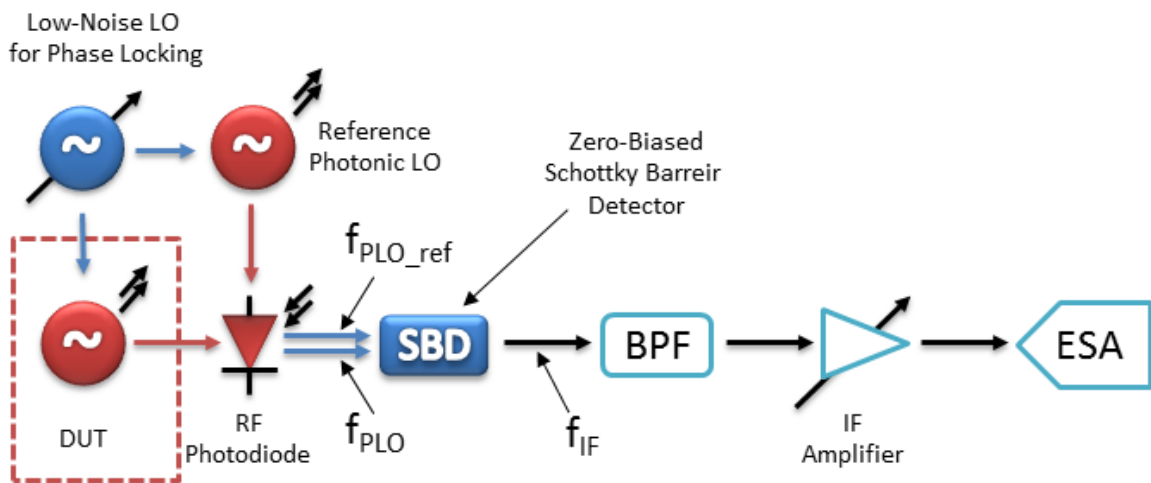


Fig. 6.17 New photonic heterodyne phase noise measurement set-up using a photonic LO to down-convert the optically generated mm-wave signal from the DUT.

As can be seen from Fig. 6.17, in the presented photonic heterodyne noise measurement set-up, the electrical LO for down-conversion is replaced by a photonic LO. The two optically generated 100 GHz range signals are then directly mixed using a W-band Schottky barrier diode (SBD). The intermediate frequency  $f_{\text{IF}}$  between the two photonic LOs was set again to 10 MHz. The phase noise of the intermediate frequency signal  $L_{\varphi,\text{IF}}$  is then given as:

$$L_{\varphi \text{ IF}} = (L_{\varphi \text{ DUT}} + n^2 L_{\varphi \text{ LO-DUT}}) - (L_{\varphi \text{ PLO}} + m^2 L_{\varphi \text{ LO-PLO}}). \quad (118)$$

Here  $L_{\varphi,\text{DUT}}$  and  $L_{\varphi,\text{PLO}}$  represent the phase noise of the DUT and the second photonic LO used to down-convert the mm-wave signal as discussed above.  $L_{\varphi,\text{LO-DUT}}$  and  $L_{\varphi,\text{LO-PLO}}$  represent the phase noise of the electrical LO used to lock the DUT and the photonic LO, respectively. For the reference photonic LO, a 100 GHz range 1.55 μm dual-frequency laser source developed by THALES was used [259].

For being able to detect only the residual phase noise coming from the optical DUT and in order not to be limited by the phase noise of the electrical LOs, both the DUT and the reference photonic LO were locked by the same electrical LO. This way the multiplication factors are equal, i.e.  $n=m$  and of course  $L_{\phi,\text{LO-DUT}} = L_{\phi,\text{LO-PLO}}$ . Because of this, the phase noise of the driving electrical LO is cancelled out (see also eq. (118)) and thus the sampled intermediate frequency signal at 10 MHz only consists of the phase noise of the DUT and the phase noise of the reference photonic LO. Since there is also no electrical LO required to down-convert the signal, the presented heterodyne measurement technique is not any more limited by the phase noise of the electrical LOs.

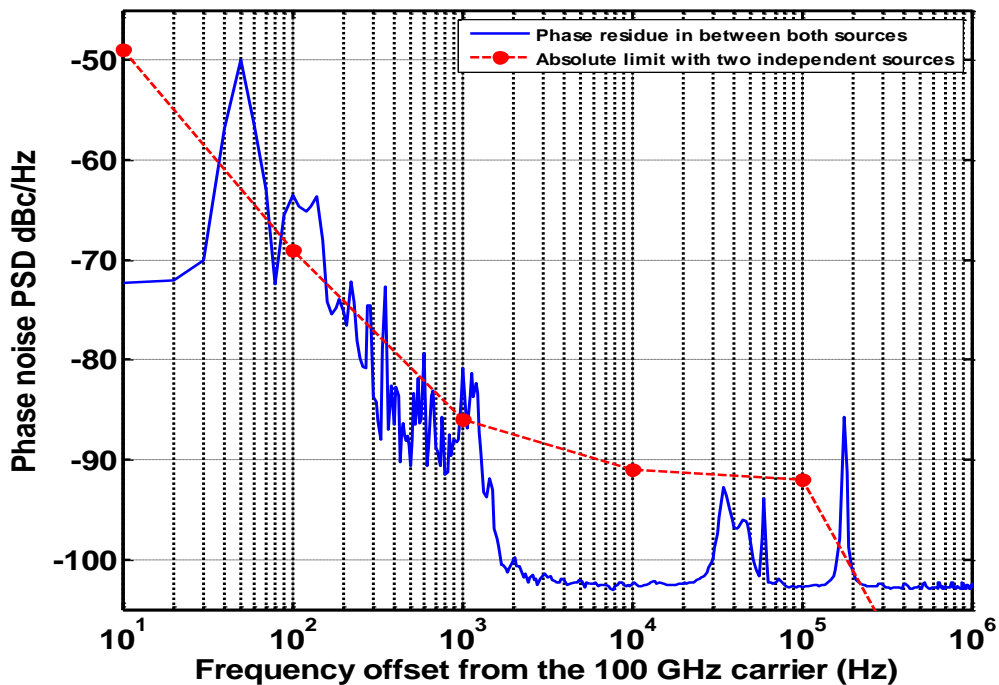


*Fig. 6.18 Residual phase noise in between dual-frequency laser and the photonic synthesizer under test measured with a Schottky diode.*

Fig. 6.18 shows the measured residual phase noise of the two photonic LOs (solid blue line). For comparison, it also shows the phase noise floor of the standard direct spectrum set-up. As expected, the proposed heterodyne set-up indeed allows measuring the residual phase noise of the two photonic LOs at noise levels below the limit of the direct spectrum technique. From the results in Fig. 6.18, it is clearly seen that the residual phase noise of the developed photonic synthesizer is limited by the thermal noise floor to -103 dBc/Hz at offset frequencies above 2 kHz from the 100 GHz carrier. Therefore, it is confirmed that the residual noise form the optical synthesizer under test is below this limit for both sources at 10 kHz. As already observed in Fig. 6.16, the heterodyne set-up also confirms the presence of additional noise at offset frequencies below 2 kHz which is traced back to the EDFA used in the photonic synthesizer. Finally, it

should be noted that the strong noise peak at about 200 kHz offset is due to the dual-wavelength THALES laser and not due to the developed photonic synthesizer. This can be concluded from the absence of this peak in Fig. 6.16.

## 7 Conclusion

Key objective of this habilitation treatise was a theoretical and experimental study of novel and advanced functional microwave photonic components and techniques for applications in high-frequency analog systems; mainly for applications in wireless communications, sensing, and instrumentation. Already in the introduction, the roots of the term “Microwave Photonics” and the history of the corresponding research field were described. Advanced microwave photonic techniques for high-frequency signal generation were studied in the second chapter. Optical signal generation by four wave mixing, cross phase, cross absorption, and cross gain modulation in highly nonlinear optical fibers or in semiconductor optical amplifiers was studied. Also, opto-electric oscillators and RF signal generation by optical intensity modulation and direct detection were investigated. Experimentally, a focus was laid upon optical heterodyning for microwave signal generation. Advanced microwave photonic components and several locking techniques for generating low-phase microwave signals were presented. Particularly, mode-locked lasers for 60 GHz, high-frequency photodiodes for ultra-wideband DC-110 GHz and resonant 100 GHz signal generation were developed and employed for optical heterodyne microwave generation.

The limitations on the fiber transmission length in microwave radio-over-fiber systems due to attenuation and dispersion effects were addressed in chapter 3. For conventional optical double-sideband modulation, it was shown theoretically that in a 60 GHz radio-over-fiber system employing standard single mode fiber, chromatic dispersion will limit the maximum fiber span to about 500 m. This was further confirmed by an experimental frequency-domain investigation. To extend the transmission length in 60 GHz systems, a pre-chirping technique was developed which allows to significantly extent the maximum fiber length in 60 GHz RoF system beyond this dispersion-limit. In addition, it was furthermore shown that much longer transmission spans are possible when using dispersion-tolerant advanced modulation techniques such as double-sideband with suppressed carrier modulation.

The focus of the fourth chapter of this habilitation treatise was on novel and advanced semiconductor-based microwave photonic devices which were developed and fabricated within this work. An analysis was developed that allows studying the high-frequency limitations of e.g. travelling-wave photodiodes such as transit times, microwave losses, and velocity mismatch with respect to the semiconductor layer structure and topology of the devices. Furthermore, ultra-wideband travelling-wave photodiodes with coplanar outputs were developed and successfully employed for optical microwave generation up to 200 GHz. An excellent agreement between the analytical prediction and the experimental achievements was found, indicating that the observed frequency response is mainly dedicated to transit time limitations and microwave losses. In

addition to photodiodes with coplanar outputs, also antenna integrated photodetectors were developed and employed for signal generation up to 1 THz. Those devices were successfully employed in a joint experiment with the Max Planck Institut für Radioastronomie for pumping a radio-astronomical receiver at 460 GHz. For enabling full-duplex systems, novel InP-based electroabsorption transceiver (EAT) were developed and employed in full-duplex microwave radio-over-fiber systems.

The applicability of microwave photonic components and techniques for enabling wireless communications with ultra-high data rates was studied in chapter 5. Traditionally, wireless links, e.g. for mobile backhauling systems, were operated in the microwave domain at carrier frequencies below 40 GHz and typically relied on all-electronic RF solutions. It has been shown that because of the congestion in the conventional microwave bands (most notably in dense and urban areas – example: 38 GHz) and because of regulatory constraints the maximum throughput of microwave radio systems is limited to a maximum of a few 100 Mbit/s. Thus, it was concluded that future wireless access and mobile backhauling systems will have to operate at carrier frequencies above 40 GHz where sufficient bandwidth is available. This will allow wireless systems of much higher capacity to be engineered and deployed, requiring of course new technologies and new concepts. This brings microwave photonics into play. In comparison to all-electronic wireless systems, photonic solutions generally have the edge whenever high aggregate bit rates and/or long transmission distances are involved. In this work, it has been shown that both advantages are deeply rooted in physics: the high optical carrier frequencies allow for high-capacity systems at very small relative bandwidths and optical fiber allows transporting broadband as well as high-frequency signals at very low loss. In chapter 5, novel microwave photonic concepts for ultra-high data-rate wireless links were studied. Experimentally, novel architectures for 60 GHz photonic wireless systems utilizing microwave photonic components and techniques were demonstrated to operate at record transmission speeds of 27 Gb/s; data-rate levels that were previously only known from fiber-optic communications. This opens up new application fields, especially in mobile backhauling, and optical access but also for disaster recovery.

Besides communications, microwave photonics is also of interest for many other applications, particularly in instrumentation, sensing, security, radar, and medical applications. The ability to generate highly stable and spectrally pure millimeter wave signals by optical means, as well as the ultra-wide features and the low-transmission loss are inherent advantages of the technology for various applications. In the last chapter, photonic-based sensor and photonic-based high-frequency sources were presented. Especially, a microwave (300 MHz to 6 GHz) electric-field sensor and a millimeter-wave photonic synthesizer with a wide frequency-tuning range from 75 GHz to 115 GHz and very low phase noise <-103 dB/c/Hz were developed.

## Annexes

### Annex I Abbreviations

3G	third generation
3R	re-amplification, reshaping, and retiming
ACMA	Australian Communications and Media Authority
ADSL	asymmetric digital subscriber loop
AN	amplitude noise
APD	avalanche photodiode
APON	asynchronous-transfer-mode passive optical network
ARIB	Association of Radio Industries and Business
ASE	amplified spontaneous emission
ASK	amplitude-shift keying
AWG	arrayed waveguide Grating
AWGN	additive white Gaussian noise
BER	bit error rate
BNetzA	Bundesnetzagentur
BPON	broadband passive optical network
BS	base station
BSC	base station controller
BTS	base transceiver station
BtB	back-to-back
BW	bandwidth
CATV	cable television
CEPT	Commission for European Post and Telecommunications
CH	carrier-heating
CO	central office
CS	central station
CSR	carrier to sideband ratio
cw	continuous wave
dB	decibel
dBm	the measured power referenced to one milliwatt
DC	direct current
DCF	dispersion compensation fiber
DFN	Deutsches Forschungsnetz
DFB-LD	distributed feedback laser diode
DIPP	dispersion induced power penalty
DPSK	differential phase-shift keying
DSB	double sideband
DSB-SC	double sideband suppressed carrier
DSF	dispersion shifter fiber
DSL	digital subscriber line
DUT	device under test
EA	electrical amplifier
EAM	electro-absorption modulator
EAT	electro-absorption transceiver

ECC	Electronic Communications Committee
ECL	external cavity lasers
EDFA	erbium-doped fiber amplifiers
EIRP	equivalent isotropically radiated power
EM	electromagnetic
EMI	electromagnetic interference
E/O	electro-optic
EPON	Ethernet passive optical network
ESA	electrical spectrum analyzer
ETSI	European Telecommunication Standards Institute
EVS	enhanced vision systems
FBG	fiber Bragg Grating
FCC	Federal Communication Commission
FD	frequency doubler
FDD	frequency division duplex
FEC	forward-error-correction
FFT	fast Fourier transformation
FM	frequency multiplier
FP	Fabry-Perot
FPR	Fabry-Perot resonator
FTTH/P	fiber-to-the-home/premise
FWM	four-wave mixing
Gbit/s	gigabit per second = $10^9$ bits per second
GHz	gigahertz = $10^9$ cycles per second
GPON	gigabit passive optical network
GSM	global standard for mobile communications
HDTV	high-definition television
HNL-DSF	highly nonlinear dispersion-shifted fiber
HPBW	half power beam width
HSPA	high speed packet access
IC-SMT	Industry Canada Spectrum Management and Telecommunications
ICT	information and communications technology
IDU	indoor unit
IEEE	Institute of Electrical and Electronics Engineers
IF	intermediate frequency
IM	intensity modulation
ISP	internet service provider
ITU	International Telecommunications Union
LEOS	Lasers and Electro-Optic Society
LiNbO <sub>3</sub>	Lithium Niobate
LN-MZM	LiNbO <sub>3</sub> Mach-Zehnder modulator
LO	local oscillator
LoS	line of sight
LPF	low-pass filter
LTE	long-term evolution
MATP	maximum transmission point
MESFET	metal semiconductor field effect transistor
MITP	minimum transmission point
MLLD	mode-locked laser diode

---

MPHPT	Ministry of Public Management, Home Affairs, Posts and Telecommunications, Japan
MQW	multi-quantum well
MTE	mobile terminal equipment
MWP	microwave photonics
MZDI	Mach-Zehnder delay interferometer
MZM	Mach-Zehnder modulator
NLoS	non-line of sight
NOLM	nonlinear optical loop mirror
NRZ	non-return to zero
NTT	Nippon Telegraph and Telephone
OBPF	optical band pass filter
OC	optical coupler
OCS	optical carrier suppression
ODU	outdoor unit
O/E	opto-electrical
OEO	opto-electric oscillator
OF	optical filter
OFDM	orthogonal frequency-division multiplexing
OL	optical interleaver
OLT	optical line terminal
ONU	optical network unit
OOK	on-off keying
PC	polarization controller
PIN	positive-intrinsic-negative
PLO	photonic local oscillator
PM	phase modulation
PN	phase noise
PON	passive optical network
PPM	pulse position modulation
PRBS	pseudo-random bit sequence
PS	power splitter
PSK	phase shift keying
PtP	point to point
PVC	photovoltaic cell
QD	quantum dot / quantum dash
QPSK	quadrature phase-shift keying
QAM	quadrature amplitude modulation
RF	radio frequency
ROADM	reconfigurable optical add/drop multiplexer
RoF	radio-over-fiber
RZ	return to zero
SA	saturable absorber
SBD	Schottky barrier diode
SCM	subcarrier multiplexing
SDTV	standard-definition television
SFDR	spurious-free dynamic range
SHB	spectral hole burning
SIS	superconductor-insulator-superconductor

SMF	single mode fiber
SMF-28	single mode fiber (corning)
SNR	signal to noise ratio
SOA	semiconductor optical amplifier
SQW	single-quantum well
SSB	single sideband
TCO	total cost of ownership
TDD	time division duplex
TDM	time-division multiplexing
TIA	transimpedance amplifier
TL	tunable laser
TOF	tunable optical filter
TTD	true time delay
TUD	Technische Universität Dresden
TW	travelling-wave
TWPD	travelling-wave photodetector
UL-SOA	ultra-long semiconductor optical amplifier
UTC	uni-travelling-carrier
WDM	wavelength division multiplexing
Wi-Fi	wireless fidelity
WiMAX	worldwide interoperability for microwave access
WLAN	wireless local area network
WPAN	wireless personal area network
WR	waveguide rectangular
WSS	wavelength selective switch
XAM	cross absorption modulation
XGM	cross gain modulation
XPM	cross phase modulation

**Annex II      Constants**

Boltzmann constant	$k = 1.381 \cdot 10^{-23} \text{ J} \cdot \text{K}^{-1}$
	$k = 8.617 \cdot 10^{-5} \text{ eV} \cdot \text{K}^{-1}$
Characteristic impedance of vacuum	$z_0 = 376.730 \Omega$
Electric constant	$\epsilon_0 = 8.854 \cdot 10^{-12} \text{ As} \cdot \text{m}^{-1}$
Electron charge	$q = 1.602 \cdot 10^{-19} \text{ As}$
Electron mass	$m_e = 9.109 \cdot 10^{-31} \text{ kg}$
Magnetic constant	$\mu = 12.566 \cdot 10^{-7} \text{ H} \cdot \text{m}^{-1}$
Molar gas constant	$R = 8.314 \text{ J} \cdot \text{mol}^{-1} \cdot \text{K}^{-1}$
Planck constant	$h = 6.626 \cdot 10^{-34} \text{ Js}$
	$h = 4.136 \cdot 10^{-15} \text{ eV} \cdot \text{s}$
Speed of light in vacuum	$c_0 = 299792458 \text{ m} \cdot \text{s}^{-1}$

### Annex III Theory for Mach-Zehnder modulator

Assuming an ideal Mach-Zehnder modulator with zero optical insertion loss, an ideal 3dB coupler, and equally long waveguide arms as well as an optical confinement of 100%, the complex electrical field strength of the optical wave in the modulators' output waveguide can be expressed as:

$$\begin{aligned}
 \hat{\underline{E}}_{out} &= \frac{\hat{\underline{E}}_{in}}{2} e^{(j\beta_1 L)} + \frac{\hat{\underline{E}}_{in}}{2} e^{(j\beta_2 L)} \\
 &= \frac{\hat{\underline{E}}_{in}}{2} [\cos(\beta_1 L) + j \sin(\beta_1 L) + \cos(\beta_2 L) + j \sin(\beta_2 L)] \\
 &= \frac{\hat{\underline{E}}_{in}}{2} [\cos(\beta_1 L) + \cos(\beta_2 L) + j(\sin(\beta_1 L) + \sin(\beta_2 L))]
 \end{aligned} \tag{119}$$

By using the following trigonometric relations:

$$\begin{aligned}
 \cos(\alpha) + \cos(\beta) &= 2 \cdot \cos\left(\frac{\alpha + \beta}{2}\right) \cdot \cos\left(\frac{\alpha - \beta}{2}\right) \\
 \sin(\alpha) + \sin(\beta) &= 2 \cdot \sin\left(\frac{\alpha + \beta}{2}\right) \cdot \cos\left(\frac{\alpha - \beta}{2}\right)
 \end{aligned} \tag{120}$$

equation (119) can be re-written as:

$$\begin{aligned}
\hat{\underline{E}}_{out} &= \hat{\underline{E}}_{in} \left[ \cos\left(\frac{\beta_1 + \beta_2}{2}L\right) \cos\left(\frac{\beta_1 - \beta_2}{2}L\right) \right. \\
&\quad \left. + j \sin\left(\frac{\beta_1 + \beta_2}{2}L\right) \cos\left(\frac{\beta_1 - \beta_2}{2}L\right) \right] \\
&= \hat{\underline{E}}_{in} \cdot \cos\left(\frac{\beta_1 - \beta_2}{2}L\right) \left[ \cos\left(\frac{\beta_1 + \beta_2}{2}\right) + j \sin\left(\frac{\beta_1 + \beta_2}{2}\right) \right] \quad (121) \\
&= \hat{\underline{E}}_{in} \cdot \cos\left(\frac{\beta_1 - \beta_2}{2}L\right) e^{j\left(\frac{\beta_1 + \beta_2}{2}\right)L} \\
&= \hat{\underline{E}}_{in} \cdot \cos\left(\frac{\Delta\beta L}{2}\right) e^{j\bar{\beta}L}
\end{aligned}$$

with

$$\begin{aligned}
\Delta\beta &= \beta_2 - \beta_1 = \frac{2\pi}{\lambda_2} - \frac{2\pi}{\lambda_1} = \frac{2\pi \cdot n_2}{\lambda} - \frac{2\pi \cdot n_1}{\lambda} = \frac{2\pi}{\lambda} \cdot \Delta n \quad (122) \\
\bar{\beta} &= \frac{\beta_2 + \beta_1}{2}
\end{aligned}$$

Given that in Lithium Niobate the voltage induced refractive index change is given by:

$$\Delta n = \frac{1}{2} \cdot n_0^3 \cdot r_{ij} \cdot \frac{V}{d} \quad (123)$$

where  $n_0$  is the refractive index without an applied electric field,  $r_{ij}$  is the relevant electrooptic parameter depending e.g. on material, polarization etc.,  $d$  is the distance of the electrodes, and  $V$  is the applied voltage.

Thus eq. (122) can be written as:

$$\Delta\beta \cdot L = \frac{2\pi}{\lambda} \cdot \Delta n \cdot L = \frac{\pi}{\lambda} \cdot n_0^3 \cdot r_{ij} \cdot \frac{V}{d} \cdot L \quad (124)$$

From eq. (124), one can now calculate the voltage  $V_\pi$ , required to achieve a total phase difference between the both arms of  $180^\circ$  where total destructive interference will occur and thus the output intensity – in the considered ideal case – will be zero.

$$\Delta\beta \cdot L = \pi = \frac{\pi}{\lambda} \cdot n_0^3 \cdot r_{ij} \cdot \frac{V_\pi}{d} \cdot L \quad (125)$$

Thus the required voltage  $V_\pi$  required for a  $180^\circ$  phase shift is:

$$V_\pi = \frac{\lambda \cdot d}{n_0^3 \cdot r_{ij} \cdot L} \quad (126)$$

By extending eq. (124) with  $V_\pi/V_\pi$  according to eq. (126), we can write:

$$\Delta\beta \cdot L = \frac{\pi}{\lambda} \cdot n_0^3 \cdot r_{ij} \cdot \frac{V}{d} \cdot L \cdot \frac{n_0^3 \cdot r_{ij} \cdot L}{V_\pi} = \pi \cdot \frac{V}{V_\pi} \quad (127)$$

And therefore eq. (121) becomes:

$$\hat{\underline{E}}_{out} = \hat{\underline{E}}_{in} \cdot \cos\left(\frac{\Delta\beta L}{2}\right) e^{j\bar{\beta}L} = \hat{\underline{E}}_{in} \cdot \cos\left(\frac{\pi}{2} \cdot \frac{V}{V_\pi}\right) e^{j\bar{\beta}L} \quad (128)$$

Assuming now for simplicity linear polarized plane electromagnetic waves, we can calculate the output intensity  $I_{out}$  of from  $\hat{\underline{E}}_{out}$  using Maxwell's equation and the Poynting vector as described in eqs. (1)-(5):

$$I_{out} \sim \frac{1}{2 \cdot z_0} \cdot \left| \vec{\underline{E}}_{out} \right|^2 = \frac{1}{2 \cdot z_0} \cdot \hat{\underline{E}}_{out}^2 \cdot \cos^2\left(\frac{\pi}{2} \cdot \frac{V}{V_\pi}\right). \quad (129)$$

Normalizing eq. (129) with the input intensity yields:

$$\frac{I_{out}}{I_{in}} = \cos^2\left(\frac{\pi}{2} \cdot \frac{V}{V_\pi}\right). \quad (130)$$

For a sinusoidal electrical input voltage  $V$  with angular frequency  $\omega_m$  and amplitude  $v_m$  superimposed on a DC voltage  $V_{DC}$  we get:

$$V = V_{DC} + v_m \sin(\omega_m t) \quad (131)$$

By introducing eq. (131) into eq. (130) and by using the following trigonometric relations:

$$\begin{aligned} \cos^2(\alpha) &= \frac{1}{2}(1 + \cos(2\alpha)) \\ \cos(\alpha + \beta) &= \cos(\alpha)\cos(\beta) - \sin(\alpha)\sin(\beta) \\ \sin(x\sin(\alpha)) &= 2 \cdot \sum_{n=1}^{\infty} J_{2n-1}(x) \cdot \sin((2n-1)\cdot\alpha) \\ \cos(x\cos(\alpha)) &= J_0(x) + 2 \cdot \sum_{n=1}^{\infty} J_{2n}(x) \cdot \sin(2n\alpha) \end{aligned} \quad (132)$$

one yields:

$$\begin{aligned} \frac{I_{out}}{I_{in}} &= \frac{1}{2} + \frac{1}{2} \chi \cdot J_0\left(\pi \frac{v_m}{V_\pi}\right) + \\ &+ \chi \cdot \sum_{n=1}^{\infty} J_{2n}\left(\pi \frac{v_m}{V_\pi}\right) \cos(2n\omega_m t) - \psi \cdot \sum_{n=1}^{\infty} J_{2n-1}\left(\pi \frac{v_m}{V_\pi}\right) \sin((2n-1)\omega_m t) \end{aligned} \quad (133)$$

where  $\chi = \cos(\pi V_{DC}/V_\pi)$ , and  $\psi = \sin(\pi V_{DC}/V_\pi)$ .

**Annex IV     Definition of optical wavelength bands**

Band	Designation	Wavelength range
O-Band	Original band	1260 nm to 1360 nm
E-Band	Extended band	1360 nm to 1460 nm
S-Band	Short band	1460 nm to 1530 nm
C-Band	Conventional band	1530 nm to 1565 nm
L-Band	Long band	1565 nm to 1625 nm
U-Band	Ultra long band	1625 nm to 1675 nm

## Annex V Definitions of microwave, mm-wave and terahertz frequency bands

ITU	IEEE	WR	Designation	Frequency range
SHF			Superhigh frequency ( ITU band number 10)	3 GHz to 30 GHz
S			IEEE: short wave	2 GHz to 4 GHz
	S		WR-284	2.6 GHz to 3.95 GHz
	E		WR-229	3.3 GHz to 4.9 GHz
C			<u>Compromise between S and X</u>	4 GHz to 8.2 GHz
	G		WR-187	3.95 GHz to 5.85 GHz
	F		WR-159	4.9 GHz to 7.05 GHz
	C		WR-137	5.85 GHz to 8.2 GHz
X			X for cross	8 GHz to 12 GHz
	H		WR-112	7.05 GHz to 10 GHz
	X		WR-90	8.2 GHz to 12.4 GHz
K <sub>u</sub>			Kurz-under	12 GHz to 18 GHz
	K <sub>u</sub>		WR-62	12.4 GHz to 18 GHz
K			Kurz (German for short)	18 GHz to 27 GHz
	K		WR-51	15 GHz to 22GHz
	K		WR-42	18 GHz to 26.5 GHz
EHF			Extremely high frequency (ITU band number 11)	30 GHz to 300 GHz
K <sub>a</sub>			Kurz-above	27 GHz to 40 GHz
	K <sub>a</sub>		WR-28	26.5 GHz to 40 GHz
V				40 GHz to 75 GHz
	Q		WR-22	33 GHz to 50 GHz
	U		WR-19	40 GHz to 60 GHz
	V		WR-15	50 GHz to 75 GHz
W			W follows V in the alphabet	75 GHz to 110 GHz
	E		WR-12	60 GHz to 90 GHz
	W		WR-10	75 GHz to 110 GHz
	F		WR-8	90 GHz to 140 GHz
	D		WR-6	110 GHz to 170 GHz
	G		WR-5	140 GHz to 220 GHz
			WR-4	170 GHz to 260 GHz
			WR-3	220 GHz to 325 GHz
THz			Terahertz (ITU band 12)	300 GHz to 3000 GHz
	Y		WR-2	325 GHz to 500 GHz
			WR-1.5	500 GHz to 750 GHz
			WR-1	750 GHz to 1100 GHz

## Annex VI List of Figures

FIG. 2.1 PRINCIPLE OF OPTICAL HETERODYNE SIGNAL GENERATION. TWO COHERENT OPTICAL WAVES WITH SLIGHTLY DIFFERENT FREQUENCIES $\omega_1$ AND $\omega_2$ (TYPICALLY IN THE INFRARED REGION) ARE SUPERIMPOSED. THIS RESULTS IN A "BEAT" WAVE WHOSE AMPLITUDE ENVELOPE VARIES ACCORDING TO THE DIFFERENCE FREQUENCY $\omega_2-\omega_1$ BETWEEN THE TWO INCIDENT OPTICAL WAVES. FINALLY, THE BEAT WAVE IS HETERODYNED IN A PHOTOMIXER.	15
FIG. 2.2 PRINCIPLE SET-UP OF A PHOTONIC LOCAL OSCILLATOR CONSISTING OF A STABILIZED OPTICAL SOURCE GENERATING A PHASE LOCKED OPTICAL HETERODYNE SIGNAL AND A HIGH-FREQUENCY PHOTODETECTOR GENERATING THE ELECTRICAL BEAT SIGNAL IN THE THz FREQUENCY REGIME.	19
FIG. 2.3 PRINCIPLE SET-UP OF A PHOTONIC LOCAL OSCILLATOR CONSISTING OF A STABILIZED OPTICAL SOURCE FOR GENERATING AN OPTICAL COMB SIGNAL FEATURING A CONSTANT DIFFERENCE FREQUENCY $F_c$ BETWEEN THE ADJACENT LIGHT WAVES.	20
FIG. 2.4 FREQUENCY TUNABLE PHOTONIC MM-WAVE GENERATION USING A DUAL-WAVELENGTH LASER SET-UP [40].	21
FIG. 2.5 MEASURED AND SIMULATED NORMALIZED FREQUENCY RESPONSE OF A RESONANT 100 GHz PHOTODIODE DESIGN [44, 45]. MEASUREMENTS WERE CARRIED OUT USING AN OPTICAL HETERODYNE SET-UP. THE INSET SHOWS A PHOTOGRAPH OF THE CHARACTERIZED RESONANT 100 GHz PD WITH THE UTC-TW PD SECTION ON THE LEFT HAND SIDE AND THE RESONANT OPEN STUB WITH IMPEDANCE TRANSFORMER ON THE RIGHT HAND SIDE.	23
FIG. 2.6 OUTPUT POWER OF A CONSTRUCTED PHOTONIC MILLIMETER-WAVE SYNTHESIZER VERSUS MILLIMETER-WAVE FREQUENCY [41].	23
FIG. 2.7 MASK LAYOUTS FOR DUAL FOUR-SECTION DBR LASER WITH ANGLED FACET MODE EXPANDERS (TOP), DUAL FOUR-SECTION DBR LASER WITH DUAL-SOA OUTPUT (MIDDLE) AND DUAL FOUR-SECTION DBR LASER WITH SINGLE SOA OUTPUT [36, 50]. THE DUAL-WAVELENGTH LASERS WERE FABRICATED BY CIP TECHNOLOGIES LTD.	25
FIG. 2.8 DIFFERENCE FREQUENCY OF AN INTEGRATED DUAL-WAVELENGTH DBR LASER DEPENDING ON THE FORWARD CURRENT APPLIED TO REAR GRATING OF THE UPPER DBR LASER. THE FORWARD CURRENT TO THE REAR GRATING OF THE LOWER DBR LASER WAS FIXED TO 6 mA.	26
FIG. 2.9 OPTICAL OUTPUT SPECTRA OF A 710 $\mu\text{m}$ LONG FABRY-PEROT BASED InP MLLD HAVING A 6 LAYER ACTIVE QUANTUM-DASH GAIN MATERIAL.	28
FIG. 2.10 SELF PULSATION ELECTRICAL SPECTRUM OF THE MODE-LOCKED LASER DIODE DRIVEN AT 370 mA.	28
FIG. 2.11 SINGLE SIDE BAND PHASE NOISE OF THE 58.8 GHz TONE GENERATED BY A 710 $\mu\text{m}$ LONG MLLD AT A BIAS CURRENT OF 211 mA.	29
FIG. 2.12 PRINCIPLE OF FREQUENCY SYNTHESIS SCHEME [70].	31

---

FIG. 2.13 CONCEPTUAL DIAGRAM OF OPTICAL INJECTION LOCKING (OIL): FREE RUNNING SLAVE LASER (A), FREE RUNNING SLAVE LASER WITH INJECTED LIGHT FROM A MASTER LASER (B), AND INJECTION LOCKED SLAVE LASER (C).....	32
FIG. 2.14 BLOCK DIAGRAM OF A HETERODYNE OPTICAL PHASE LOCKED LOOP (OPLL).....	34
FIG. 2.15 SCHEMATIC OF THE OPTICAL PHASE LOCK LOOP DEVELOPED WITHIN IPHOBAC [36].....	35
FIG. 2.16 BLOCK DIAGRAM OF AN OIPLL SYSTEM [88]. THE PHASE DETECTOR AND OFFSET FREQUENCY LO ARE NECESSARY IN HETERODYNE OIPLL SYSTEMS BUT ARE NOT REQUIRED IN HOMODYNE OIPLLs WITH A DC OUTPUT SIGNAL OF THE PD.....	37
FIG. 2.17 SCHEMATIC ILLUSTRATION OF A MACH-ZEHNDER MODULATOR BASED UPON $\text{LiNbO}_3$ .....	39
FIG. 2.18 NONLINEAR TRANSFER CHARACTERISTIC OF AN MZM. THE MAXIMUM TRANSMISSION POINT (MATP) MIGHT NOT BE ACHIEVED EXACTLY AT ZERO VOLT APPLIED BIAS DUE TECHNOLOGICAL IMPERFECTIONS, E.G. IN THE CASE OF NOT EQUIALLY LONG WAVEGUIDES. ....	39
FIG. 2.19 OPTICAL HETERODYNE SET-UP FOR TESTING PHOTODIODES UP TO HIGHEST FREQUENCIES [42]. .....	42
FIG. 2.20 CONCEPT OF AN OPTO-ELECTRIC OSCILLATOR (OEO) SET-UP [95]. .....	43
FIG. 2.21 LUMPED ELEMENT MODEL FOR AN UL-SOA CONSISTING OF A LINEAR GAIN SECTION AND A NONLINEAR SECTION EXHIBITING A 3 <sup>RD</sup> ORDER NON-LINEARITY. ....	46
FIG. 2.22 SCHEMATIC ILLUSTRATION OF THE EXPERIMENTAL SET-UP USED OPTICAL MULTIPLICATION OF A MICROWAVE LO FREQUENCY BY USING THE CARRIER-SUPPRESSION IN THE MACH-ZEHNDER MODULATOR AS WELL AS NONLINEAR FWM IN THE SOA. AN ARRAYED WAVEGUIDE GRATING (AWG) IS USED TO FILTER OUT THE DESIRED OPTICAL MODES. ....	48
FIG. 2.23 MEASURED PHASE NOISE OF THE 4 GHz LO SIGNAL, AS WELL AS OF THE QUADRUPLED (N=4) OPTICALLY GENERATED SIGNAL AT 16 GHz AND THE 8-TIMES OPTICALLY MULTIPLIED SIGNAL AT 32 GHz. THE MEASUREMENT NOISE FLOOR (MNF) LEVELS AT 16 GHz AND 32 GHz ARE ALSO SHOWN.....	49
FIG. 2.24 RF CONVERSION EFFICIENCY VS. LO DRIVE POWER FOR DIFFERENT SOAs. ....	50
FIG. 2.25 CONCEPT OF EXPLOITING XPM IN A STRAIGHT HNL-DSF. THE OPTICAL INPUT SIGNAL INTO THE HNL-DSF IS COMPOSED OF A DSB-SC OPTICAL CONTROL SIGNAL AROUND $\omega_c$ AND AN ADDITIONAL CW OPTIC PROBE SIGNAL AT $\omega_{ps}$ . ....	51
FIG. 3.1 SCHEMATIC OF BEER-LAMBERT ABSORPTION OF A LIGHT BEAM AS IT TRAVELS THROUGH A MATERIAL. ....	55
FIG. 3.2 ATTENUATION COEFFICIENT (SOLID LINE) FOR A STANDARD SINGLE MODE GLASS FIBER VERSUS OPTICAL WAVELENGTH. DASHED LINES ARE REPRESENTING INDIVIDUAL LOSS CONTRIBUTIONS SUCH AS RAYLEIGH SCATTERING, OH <sup>-</sup> ABSORPTION AND OTHER EFFECTS. ....	57
FIG. 3.3 CHIRP VALUE (A) AND MODULATION INDEX (B) OF HIGH-SPEED EAM VERSUS REVERSE BIAS [118]. .....	62
FIG. 3.4 EXPERIMENTAL SET-UP OF A 60 GHz FIBER-OPTIC LINK [118]. .....	63
FIG. 3.5 BER VERSUS CHIRP PARAMETER FOR FIXED RECEIVED OPTICAL POWER OF -12 dBm [118]. .....	64
FIG. 3.6 MINIMUM REQUIRED RECEIVED OPTICAL POWER FOR BER = $10^{-10}$ VERSUS FIBER LENGTH.....	65
FIG. 3.7 BER VERSUS RECEIVED OPTICAL POWER AND OPTICAL DSB SPECTRUM. ....	66
FIG. 3.8 DISPERSION LIMITED (3dB PENALTY) SMF TRANSMISSION LENGTH FOR CHIRPED MM-WAVE MODULATED (DSB) OPTICAL SIGNALS AT 1.55 $\mu\text{m}$ WAVELENGTH. ....	68

---

FIG. 3.9 CORRECTED PHOTODETECTED ELECTRICAL POWER AS A FUNCTION OF FIBER LENGTH.....	71
FIG. 4.1 THE ELECTROMAGNETIC SPECTRUM BETWEEN 30 GHz AND 3000 THz. THE TERM THz REGION IS COMMONLY APPLIED TO THE SUBMM-WAVE FREQUENCY RANGE WHICH EXTENDS FROM 300 GHz UP TO ABOUT 3 THz.....	73
FIG. 4.2 SCHEMATIC DIAGRAM OF THE FABRICATED 1.55 $\mu$ M TWPD.....	77
FIG. 4.3 DETAILED CROSS SECTION OF THE FABRICATED TWPD.....	78
FIG. 4.4 QUASI-STATIC EQUIVALENT TRANSMISSION LINE CIRCUIT FOR UNIT LENGTH TWPD.....	84
FIG. 4.5 TLM MODEL DESCRIBING THE DISTRIBUTED CURRENT GENERATION ALONG THE TWPD.....	85
FIG. 4.6 EXPERIMENTALLY (CIRCLES) AND NUMERICALLY (SOLID LINES) DETERMINED CHARACTERISTIC IMPEDANCE OF THE HYBRID COPLANAR/MICROSTRIP TRANSMISSION LINE.....	86
FIG. 4.7 THEORETICALLY DETERMINED CHARACTERISTIC IMPEDANCE AND ELECTRICAL PROPAGATION CONSTANT OF THE HYBRID COPLANAR/MICROSTRIP TRANSMISSION LINE.....	87
FIG. 4.8 BROADBAND K <sub>A</sub> TO G-BAND MM-WAVE GENERATION USING THE TWPD. THE ASSOCIATED FREQUENCY BANDS OF THE APPLIED COPLANAR PROBES AND MIXERS ARE SHOWN.....	88
FIG. 4.9 GENERATED MM-WAVE POWER AT 110 GHz VERSUS THE OPTICAL INPUT POWER.....	89
FIG. 4.10 GENERATED MM-WAVE POWER AT 132 GHz VERSUS THE APPLIED REVERSE BIAS.....	90
FIG. 4.11 GENERATED MM-WAVE POWER AT 132 GHz VERSUS THE POLARIZATION ANGLE.....	90
FIG. 4.12 EXPERIMENTALLY (CIRCLES) AND NUMERICALLY (SOLID LINE) DETERMINED BROADBAND MM-WAVE GENERATION USING THE TWPD.....	91
FIG. 4.13 OPERATION PRINCIPLE (LEFT HAND) AND SCHEMATIC STRUCTURE OF THE DEVELOPED COMPONENT COMPRISED PASSIVE OPTICAL WAVEGUIDE, PHOTOMIXER, LOW-LOSS ANTENNA FEED AND A BROADBAND LPTA-STRUCTURE (RIGHT HAND). ....	92
FIG. 4.14 SCHEMATIC CROSS SECTION (MIDDLE) OF THE DEVELOPED TRAVELLING-WAVE PHOTOMIXER, ENLARGED ACTIVE SECTION (LEFT HAND) AND 3-DIMENSIONAL MODEL (RIGHT HAND). ....	93
FIG. 4.15 SEM-PHOTOGRAPHS OF THE DEVELOPED PHOTONIC TRANSMITTER CHIP. TOP VIEW OF THE FABRICATED ANTENNA-INTEGRATED PHOTOMIXER (LEFT HAND) AND CLOSE-UP VIEW OF THE CENTER OF THE LPTA STRUCTURE WITH MICROSTRIP CIRCUITRY, ACTIVE PHOTOMIXER SECTION AND PASSIVE OPTICAL WAVEGUIDE (RIGHT HAND). ....	94
FIG. 4.16 30-300 GHz CHARACTERIZATION OF THE DEVELOPED PHOTOMIXER USING A SET OF NARROW-BAND SCHOTTKY DIODE POWER DETECTORS.....	95
FIG. 4.17 HIGH-POWER CHIP-LEVEL MEASUREMENTS OF AN LPTA-INTEGRATED PHOTOMIXER AT A DC-BIAS LEVEL OF -2V AND A PHOTOCURRENT UP TO -6 MA AT 33 GHz, 100 GHz, 200 GHz AND 300 GHz.....	96
FIG. 4.18 TOP VIEW OF A PACKAGED ANTENNA-INTEGRATED PHOTOMIXER (LEFT HAND) AND BOTTOM VIEW (RIGHT HAND) SHOWING THE QUASI-OPTICS FOR EFFICIENT RADIATION PATTERN GENERATION. ....	96
FIG. 4.19 SCHEMATIC DRAWING OF THE INTEGRATED 460 GHz PHOTONIC TRANSMITTER.....	97
FIG. 4.20 SEM PICTURE OF WAVEGUIDE PHOTODETECTOR WITH INTEGRATED SLOT ANTENNA AND BIAS-T CIRCUITRY. .....	98
FIG. 4.21 GENERATED MM-WAVE POWER VERSUS BEAT FREQUENCY AND VERSUS OPTICAL INPUT POWER AT A BEAT FREQUENCY OF 110 GHz.....	99

FIG. 4.22 SET-UP FOR 460 GHz SUB-MM WAVE GENERATION AND TRANSMISSION INTO THE SIS-JUNCTION OF AN HETERODYNE ASTRONOMICAL RECEIVER.....	100
FIG. 4.23 DC BIAS CURVES OF THE SIS-JUNCTION AS A FUNCTION OF OPTICAL PUMP POWER. INSET: SUB-MM SIGNAL POWER VERSUS DC-PHOTOCURRENT.....	101
FIG. 4.24 MEASURED THz OUTPUT POWER OF A WR10 INTEGRATED 1.55 $\mu$ M TWPD.....	102
FIG. 4.25 MEASURED FREQUENCY RESPONSE OF WAVEGUIDE (WR8 & WR5) INTEGRATED PHOTONIC TRANSMITTER EMPLOYING 1.55 $\mu$ M TWPD.....	103
FIG. 4.26 MEASURED RECEIVED POWER FROM AN TWPD INTEGRATED WITH A PLANAR BOW-TIE ANTENNA. THE THz POWER HAS BEEN MEASURED USING A GOLAY CELL.....	104
FIG. 4.27 SCHEMATIC SET-UP OF A FULL-DUPLEX TRANSCEIVER FUNCTION USING INDIVIDUAL OPTICAL COMPONENTS (UPPER, A) AND THE DEVELOPED MONOLITHIC INTEGRATED R-EAT COMPONENT (B) WHICH FULFILLS THE SAME FUNCTION.....	105
FIG. 4.28 BAND GAP ENERGIES IN MEV DEPENDING ON THE GALLIUM CONCENTRATION X AND THE ARSENIDE CONCENTRATION Y. INDICATED ARE ALSO RELATIONS FOR LATTICE MATCHED InGaAsP ON InP AS WELL AS FOR -1% TENSILE AND +1% COMPRESSIVE STRAINED BULK InGaAsP ON InP.....	107
FIG. 4.29 OPTICAL CONFINEMENT FACTOR FOR FUNDAMENTAL AND FIRST ORDER TE AND TM MODES AS A FUNCTION OF THE RIB HEIGHT. THE INSET SCHEMATICALLY SHOWS THE CROSS SECTION OF THE DOUBLE HETERO STRUCTURE WAVEGUIDE LAYER.....	108
FIG. 4.30 MAXIMUM POWER VARIATION $\Delta L$ OF THE LIGHT REFLECTED AT THE FRONT FACET AS A FUNCTION OF THE FRONT FACET REFLECTIVITY AND ON-STATE SINGLE-PATH LOSS FOR A BACK FACET REFLECTIVITY OF 95% (LEFT). MEASURED FRONT FACET SPECTRAL REFLECTIVITY AFTER AR COATING, USING A 215 NM THICK SiO $\lambda/4$ LAYER.....	110
FIG. 4.31 SCHEMATIC TOP VIEW OF THE R-EAT SHOWING THE V-GROOVE IN FRONT OF THE ACTIVE R-EAT SECTION SUPPORTING THE FIBER-CHIP COUPLING AND THE BENDED COPLANAR 50 $\Omega$ TRANSMISSION LINES, ENSURING HIGH-FREQUENCY OPERATION (TOP LEFT), CLOSE-UP DRAWING OF THE R-EAT FRONT FACET WITH ANTI-REFLECTION (AR) COATING (TOP RIGHT), SEM PHOTO OF THE T-SHAPED FRONT FACET (BOTTOM LEFT), AND SEM PICTURE OF THE FRONT FACET WITH V-GROOVE (BOTTOM RIGHT). ....	111
FIG. 4.32 FUNDAMENTAL AND THIRD ORDER OUTPUT POWER VERSUS ELECTRICAL INPUT POWER FOR TRANSMIT (LEFT) AND RECEIVE (RIGHT) OPERATION.....	112
FIG. 4.33 BIT ERROR RATE VERSUS RECEIVED OPTICAL POWER FOR A 1 Gb/s ASK SIGNAL USING EITHER THE R-EAT AS RECEIVER OR A COMMERCIAL PD.....	113
FIG. 5.1 AVERAGE INTERNET TRAFFIC AND PEAK INTERNET TRAFFIC AT THE WORLDWIDE LEADING INTERNET EXCHANGE NOTE (DE-CIX) LOCATED IN FRANKFURT AM MAIN [160]. COURTESY FROM DE-CIX. ....	114
FIG. 5.2 DISTRIBUTION OF HANDSETS BY NETWORK GENERATION FOR WESTERN EUROPE [161].....	115
FIG. 5.3 MOBILE DATA USE IN HONG KONG [162]. ....	115
FIG. 5.4 WIRELESS BACKHAUL GLOBAL MIX IN 2010 [166]. ....	116
FIG. 5.5 SCHEMATIC ARCHITECTURE OF A WIRELESS SYSTEM. COURTESY FROM ALCATEL-LUCENT. ....	117

FIG. 5.6 EXAMPLE OF THE AVERAGE HOP LENGTH VARIATION ACROSS EUROPE, NORTH AFRICA AND WESTERN PARTS OF RUSSIA CALCULATED WITH ITU RAIN MODEL IN KM FOR 1 GBIT/S AND 99.999% AVAILABILITY. COURTESY FROM ALCATEL-LUCENT.....	117
FIG. 5.7 REVENUE FROM MOBILE BROADBAND PER GEOGRAPHIC REGION FOR YEARS 2008 TO 2014 [163].....	119
FIG. 5.8 GLOBAL MOBILE BACKHAUL EQUIPMENT MARKET BY MEDIA TYPE FOR 2006-2013. MARKET DATA ON THE RIGHT HAND SIDE GRAPH IS IN MILLION DOLLARS [171]. .....	120
FIG. 5.9 SCHEMATICS OF PHOTONIC TECHNIQUES FOR SIGNAL GENERATION AND TRANSMISSION OF Gb/S WIRELESS SIGNALS. BASEBAND OVER FIBER WITH BASEBAND TO RF UP-CONVERSION IN THE BS (A), INTERMEDIATE FREQUENCY (IF) OVER FIBER WITH IF TO RF UP-CONVERSION IN THE BS (B), AND RF OVER FIBER (RoF) (C). .....	127
FIG. 5.10 SPECTRAL EFFICIENCIES FOR DIFFERENT MODULATION SCHEMES: ON-OFF KEYING (OOK), PHASE SHIFT KEYING (PSK), QUADRATURE AMPLITUDE MODULATION (QAM), AND PULSE POSITION MODULATION (PPM). REQUIRED SNR PER BIT FOR THE VARIOUS MODULATION FORMATS ARE ALL GIVEN FOR A BER = $2 \cdot 10^{-3}$ [197]. THE SOLID LINE REPRESENTS THE MAXIMUM SPECTRAL EFFICIENCY ACCORDING TO THE SHANNON-HARTLEY THEOREM, AS GIVEN IN EQ. (82). .....	131
FIG. 5.11 CONSTELLATION DIAGRAMS FOR DIFFERENT MODULATION FORMATS SHOWING THE NORMALIZED VECTOR COORDINATES FOR EACH SYMBOL POINT AND ITS BIT MAPPING. CONSTELLATION IS SHOWN FOR CONVENTIONAL AMPLITUDE SHIFT KEYING (ASK) WHICH IS USUALLY DENOTED AS ON-OFF KEYING (OOK) (A). ALSO, CONSTELLATIONS OF HIGHER MODULATION FORMATS ARE SHOWN, INCLUDING QUADRATURE PHASE SHIFT KEYING (QPSK) (B), 8-ARY PHASE SHIFT KEYING (8-PSK) (C) AS WELL AS HIGHER ORDER SQUARE QUADRATURE AMPLITUDE MODULATION (QAM). (D-F). .....	132
FIG. 5.12 THROUGHPUT VERSUS RF CHANNEL BANDWIDTH FOR DIFFERENT MODULATION SCHEMES. CALCULATION CONSIDERS AN FEC WITH 6% OVERHEAD AND A TYPICAL BAND ROLL-OFF OF 10%. .....	133
FIG. 5.13 ILLUSTRATION OF THE KEY COMPONENTS FOR A POINT-TO-POINT (PtP) LINE OF SIGHT (LoS) WIRELESS LINK USING RoF TRANSPORT BETWEEN THE INDOOR-UNITS (IDU) AND THE OUTDOOR UNITS (ODU), i.e. THE ANTENNAS.....	134
FIG. 5.14 SCHEMATIC OF A POINT-TO-POINT WIRELESS LINK WITH LINE OF SIGHT (LoS) PROPAGATION PATH.....	135
FIG. 5.15 A POINT-TO-POINT WIRELESS LINK WITH LINE OF SIGHT (LoS) PROPAGATION PATH.....	140
FIG. 5.16 A POINT-TO-POINT WIRELESS LINK WITH LINE OF SIGHT (LoS) PROPAGATION PATH.....	142
FIG. 5.17 SPECIFIC ATTENUATION FROM 1 TO 350 GHZ FOR DRY AIR AT SEA-LEVEL (AIR PRESSURE OF 1013 hPa, TEMPERATURE OF 15°C) AND FOR WATER VAPOR WITH A DENSITY OF 7.5 g/m <sup>3</sup> .....	143
FIG. 5.18 A POINT-TO-POINT WIRELESS LINK WITH LINE OF SIGHT (LoS) PROPAGATION PATH. ....	144
FIG. 5.19 A POINT-TO-POINT WIRELESS LINK WITH LINE OF SIGHT (LoS) PROPAGATION PATH. ....	145
FIG. 5.20 A POINT-TO-POINT WIRELESS LINK WITH LINE OF SIGHT (LoS) PROPAGATION PATH. ....	146
FIG. 5.21 RIN VS. FREQUENCY FOR AN IN-PLANE DIODE WITH THE LASER'S AVERAGE OPTICAL POWER AS A PARAMETER [207]. .....	150
FIG. 5.22 ANTENNA NOISE FIGURE VS. CARRIER FREQUENCY IN THE MICROWAVE AND MILLIMETER-WAVE REGION. NOISE TEMPERATURE IS INDICATED FOR HORIZONTAL ( $\phi = 0^\circ$ ) WIRELESS TRANSMISSION, AS WELL AS FOR AN ELEVATION ANGLE OF 10° [211, 212]. .....	153

FIG. 5.23 SCHEMATIC OF RoF DOWN- AND UPLINK TRANSMISSION USING AN ELECTRO-ABSORPTION TRANSCEIVER (EAT). UPLINK TRANSMISSION IS BASED UPON AN EAT DEVICE AS AN OPTICAL MODULATOR IN A LOOPED-BACK CONFIGURATION (A), DOWNLINK TRANSMISSION IS ACHIEVED EMPLOYING THE SAME EAT AS A PHOTODIODE (B).....	156
FIG. 5.24 RF UP- AND DOWNLINK INSERTION LOSS VERSUS OPTICAL WAVELENGTH AT DIFFERENT REVERSE VOLTAGES APPLIED TO THE EAT.....	156
FIG. 5.25 OPTICAL INPUT SPECTRUM OF THE EAT (A) AND SPECTRA OF THE MM-WAVE MODULATED OPTICAL DOWNLINK (B) AND UPLINK SIGNALS (C).....	158
FIG. 5.26 EXPERIMENTAL SET-UP FOR FULL-DUPLEX ANALOG RF FIBER-OPTIC TRANSMISSION OF A 256 Mb/s PRBS (DOWNLINK) AND 56 Mb/s PRBS (UPLINK) SIGNAL. FREQUENCIES USED FOR UP- AND DOWNLINK SUBCARRIER WERE 3 GHz AND 10 GHz, RESPECTIVELY.....	159
FIG. 5.27 MEASURED BIT ERROR RATES (BER) WITH RESPECT TO RECEIVED OPTICAL POWER FOR UPLINK (A) AND DOWNLINK (B) TRANSMISSION.....	160
FIG. 5.28 SCHEMATIC OF THE CONSTRUCTED 60-GHz RoF LINK CONSISTING OF AN OPTICAL MM-WAVE CARRIER GENERATION (DSB-SC) UNIT AND A SUBSEQUENT BROADBAND DATA MODULATION (OOK).....	161
FIG. 5.29 MEASURED BER AS A FUNCTION OF RECEIVED POWER LEVEL FOR MULTI-GIGABIT BROADBAND WIRELESS DATA TRANSMISSION OVER 2.5 M.....	163
FIG. 5.30 MEASURED BER AS A FUNCTION OF RECEIVED POWER FOR DIFFERENT BIT RATES UP TO 12.5 Gb/s AND WIRELESS DISTANCES UP TO 50 M.....	164
FIG. 5.31 MAXIMUM WIRELESS PATH LENGTHS FOR 50 dBi GAIN ANTENNAS UNDER DIFFERENT WEATHER CONDITIONS. ....	165
FIG. 5.32 SCHEMATIC OF THE COMPACT 60 GHz PHOTONIC WIRELESS LINK CONSISTING OF AN OPTICAL MM-WAVE CARRIER GENERATOR BASED UPON EXTERNAL MODULATION, A SUBSEQUENT BROADBAND OFDM DATA MODULATION, A PHOTONIC WIRELESS TRANSMITTER AND A WIRELESS COHERENT RECEIVER. THE CONFIGURATION FOR WIRELESS AND BACK-TO-BACK EXPERIMENTS IS FURTHER INDICATED IN THE FIGURE. ..	167
FIG. 5.33 RECEIVED SPECTRUM AND CONSTELLATION DIAGRAM OBTAINED AFTER PHOTONIC UP-CONVERSION, 10 M OF FIBER-OPTIC AND 2.5 M OF WIRELESS TRANSMISSION. THE 7 GHz BANDWIDTH OFDM SIGNAL WITH 8-QAM SUBCARRIER MODULATION GIVES A DATA TRANSMISSION RATE OF 20.28 GBIT/s. ....	169
FIG. 5.34 RECEIVED SPECTRUM AND CONSTELLATION DIAGRAM OBTAINED AFTER PHOTONIC UP-CONVERSION, 10 M OF FIBER-OPTIC AND 2.5 M OF WIRELESS TRANSMISSION. THE 7 GHz BANDWIDTH OFDM SIGNAL WITH 16-QAM SUBCARRIER MODULATION GIVES A DATA TRANSMISSION RATE OF 27.04 GBIT/s. ....	169
FIG. 6.1 ORIGINS OF THE 278 SURVEY PARTICIPANTS WORLDWIDE. THE ORIGINS OF 84 PARTICIPANTS ARE UNKNOWN. ....	175
FIG. 6.2 SKETCH OF THE OPTICALLY POWERED INTEGRATED ELECTRO-OPTICAL FIELD SENSOR.....	183
FIG. 6.3 CALCULATED SENSITIVITY LIMIT OF THE SENSOR SYSTEM AS A FUNCTION OF LASER POWER. ....	185
FIG. 6.4 VOLTAGE GAIN OF THE GaAs MESFET TRANZIMPEDANCE AMPLIFIER UNDER OPERATIONAL CONDITIONS (THE SHADED FRAME INDICATES SPECIFICATION).....	186
FIG. 6.5 CROSS-SECTION OF SINGLE PVC (A) AND PHOTOGRAPH OF A REALIZED ARRAY OF 5 PVCs (B). ....	187

FIG. 6.6 CURRENT-VOLTAGE (UPPER FIGURE) AND POWER-VOLTAGE (LOWER FIGURE) OF THE FABRICATED PVC ARRAY CONSISTING OF SIX CELLS IN SERIES.....	188
FIG. 6.7 REALIZED READ-OUT (A) AND SENSOR HEAD (B).....	189
FIG. 6.8 SENSITIVITY (UPPER DIAGRAM) AND DYNAMIC RANGE (LOWER DIAGRAM) OF THE DEVELOPED ELECTRIC- FIELD PHOTONIC-BASED SENSOR SYSTEM.....	191
FIG. 6.9 SCHEMATIC DIAGRAM OF THE PHOTONIC MILLIMETER-WAVE SYNTHESIZER BASED UPON OPTICAL HETERODYNING.....	192
FIG. 6.10 MILLIMETER-WAVE GAIN OF THE LIMITING AMPLIFIER VERSUS THE INPUT POWER AT DIFFERENT FREQUENCIES.....	193
FIG. 6.11 RELATIVE FREQUENCY RESPONSE OF THE WAVEGUIDE COUPLED PIN PHOTODIODE.....	194
FIG. 6.12 OUTPUT POWER OF THE PHOTONIC MILLIMETER-WAVE SYNTHESIZER VERSUS MILLIMETER-WAVE FREQUENCY. FOR THIS EXPERIMENT, THE PHOTODIODE WAS OPERATED AT A REVERSE BIAS OF -2 V AND ITS DC PHOTOCURRENT WAS SET TO 2 mA.....	195
FIG. 6.13 RF SPECTRUM OF THE OPTICALLY GENERATED MILLIMETER-WAVE SIGNAL AT 72.14 GHz.....	196
FIG. 6.14 A) DETAILED SCHEMATIC ILLUSTRATION OF THE DEVELOPED FREQUENCY-TUNABLE PHOTONIC MM-WAVE SYNTHESIZER AND B) SCHEMATIC ILLUSTRATION OF DIRECT SPECTRUM PHASE NOISE MEASUREMENT USING AN ELECTRICAL SPECTRUM ANALYZER (ESA).....	198
FIG. 6.15 DIRECT SPECTRUM PHASE NOISE MEASUREMENT USING A SUB-HARMONIC MIXER DRIVEN BY A LOW PHASE NOISE ELECTRICAL LO FOR DOWN-CONVERTING THE OPTICALLY GENERATED MM-WAVE SIGNAL TO A MICROWAVE FREQUENCY.....	199
FIG. 6.16 PHASE NOISE OF THE SIGNAL DELIVERED BY THE PHOTONIC EXTERNAL MODULATION SOURCE.....	201
FIG. 6.17 NEW PHOTONIC HETERODYNE PHASE NOISE MEASUREMENT SET-UP USING A PHOTONIC LO TO DOWN- CONVERT THE OPTICALLY GENERATED MM-WAVE SIGNAL FROM THE DUT.....	202
FIG. 6.18 RESIDUAL PHASE NOISE IN BETWEEN DUAL-FREQUENCY LASER AND THE PHOTONIC SYNTHESIZER UNDER TEST MEASURED WITH A SCHOTTKY DIODE.....	203

## References

- [1] D. Jäger, "Microwave photonics," in *Optical Information Technology*, Eds. S. D. Smith and R. F. Neale, Springer Verlag, ISBN: 3-540-56563-9, pp. 328-333, 1993.
- [2] D. Jäger and A. Stöhr, "Microwave photonics," in *European Microwave Conference*, pp. 1-4, 2001.
- [3] A. J. Seeds, "Microwave photonics," *IEEE Transactions on Microwave Theory and Techniques*, vol. 50, pp. 877-887, 2002.
- [4] A. J. Seeds and K. J. Williams, "Microwave photonics," *IEEE/OSA Journal of Lightwave Technology*, vol. 24, pp. 4628-4641, 2006.
- [5] J. Capmany and D. Novak, "Microwave photonics combines two worlds," *Nature Photonics*, vol. 1, pp. 319-330, 2007.
- [6] J. Yao, "Microwave photonics," *IEEE/OSA Journal of Lightwave Technology*, vol. 27, pp. 314-335, 2009.
- [7] T. Berceli and P. Herczfeld, "Microwave photonics - A historical perspective," *IEEE Transactions on Microwave Theory and Techniques*, vol. 58, pp. 2992-3000, 2010.
- [8] A. J. Seeds, M. J. Fice, C. P. Liu, L. Ponnampalam, F. Pozzi, C. C. Renaud, E. Rouvalis, and R. J. Steed, "New applications for microwave photonics," in *IEEE Photonics Society Annual Meeting*, Belek-Antalya, Turkey, 2009.
- [9] <http://cordis.europa.eu/fp7/ict/photonics/>.
- [10] J. G. Droysen, "Des Aischylos Werke," Berlin, G. Finke, 1832.
- [11] A. A. Huerdeman and J. Wiley, "The worldwide history of telecommunications," Wiley Online Library, ISBN: 0471205052, 2003.
- [12] T. Standage, "The Victorian internet," Phoenix, ISBN: 0753807033, 1999.
- [13] D. T. Emerson, "The work of Jagadis Chandra Bose: 100 years of millimeter-wave research," *IEEE Transactions on Microwave Theory and Techniques*, vol. 45, pp. 2267-2273, 1997.
- [14] F. G. Conrad and M. F. Schober, "Envisioning the survey interview of the future," Wiley-Blackwell, ISBN: 0471786276, 2008.
- [15] R. Lucky, "Leadership and life in the old bell labs," *IEEE Signal Processing Magazine*, vol. 21, pp. 6-8, 2004.
- [16] D. B. Keck, "Optical fiber spans 30 years," *Lightwave*, vol. 17, pp. 78-82, 2000.
- [17] A. Einstein, "Zur Quantentheorie der Strahlung," *Physikalische Zeitschrift*, vol. 18, pp. 121-128, 1917.
- [18] A. Einstein, "Fundamental ideas and problems of the theory of relativity," *Les Prix Nobel*, pp. 482-490, 1922.
- [19] F. Nebeker, "Charles Townes, the maser, and the relationship between engineering and science," *Engineering Science and Education Journal*, vol. 4, pp. S41-S46, 1995.
- [20] T. H. Maiman, "Stimulated optical radiation in ruby," *Nature*, vol. 187, pp. 493-494, 1960.
- [21] R. Dupuis, "An introduction to the development of the semiconductor laser," *IEEE Journal of Quantum Electronics*, vol. 23, pp. 651-657, 1987.
- [22] H. Krömer, "Nobel lecture: Quasielectric fields and band offsets: Teaching electrons new tricks," *Reviews of Modern Physics*, vol. 73, pp. 783-793, 2001.
- [23] Z. I. Alferov, "Nobel lecture: The double heterostructure concept and its applications in physics, electronics, and technology," *Reviews of Modern Physics*, vol. 73, pp. 767-782, 2001.
- [24] C. K. Kao, "Nobel lecture: Sand from centuries past: Send future voices fast," *Reviews of Modern Physics*, vol. 82, p. 2299, 2010.
- [25] C. K. Kao, "Dielectric-fibre surface waveguides for optical frequencies," *Proceedings of the IEE*, vol. 113, pp. 1151-1158, 1966.
- [26] R. Mears, L. Reekie, I. Jauncey, and D. Payne, "Low-noise Erbium-doped fibre amplifier operating at 1.54 μm," *Electronics Letters*, vol. 23, pp. 1026-1028, 1987.

- [27] S. Poole, D. Payne, R. Mears, M. Fermann, and R. Laming, "Fabrication and characterization of low-loss optical fibers containing Rare-Earth ions," *IEEE/OSA Journal of Lightwave Technology*, vol. 4, pp. 870-876, 1986.
- [28] A. Stöhr, K. Kitayama, R. Heinzelmann, M. Alles, and D. Jäger, "Recent developments in microwave photonics: High-speed devices for millimeter-wave fiber-wireless signal transmission," in *International Conference on Applications of Photonic Technology*, Ottawa, 1998.
- [29] A. Vilcot, B. Cabon, and J. Chazelas, "Microwave photonics: From components to applications and systems," Springer, ISBN: 1402073623, 2003.
- [30] C. H. Lee, "Microwave photonics," vol. 124, CRC, ISBN: 0849339243, 2007.
- [31] S. Iezekiel, "Microwave photonics: Devices and applications," Wiley-IEEE Press, ISBN: 0470848545, 2009.
- [32] T. E. Darcie, A. Stöhr, and P. K. L. Yu, "Guest editorial special issue on microwave photonics," *IEEE/OSA Journal of Lightwave Technology*, vol. 26, pp. 2336-2337, 2008.
- [33] A. Stöhr, "Pushing the boundaries," *IEEE Microwave Magazine*, vol. 10, pp. 106-115, 2009.
- [34] A. Seeds, "Microwave photonic links," in *International Topical Meeting on Microwave Photonics*, Ogunquit, pp. 16-19, 2004.
- [35] IPHOBAC, [www.ist-iphobac.org](http://www.ist-iphobac.org).
- [36] IPHOBAC, "Publishable final IPHOBAC activity report," Duisburg, 2010.
- [37] A. Stöhr, "The European IPHOBAC project: Millimeter-wave photonic components and technologies for communications, radar and instrumentation," in *IEEE Lasers and Electro-Optics Society Annual Meeting*, pp. 16-17, 2008.
- [38] F. van Dijk, B. Charbonnier, S. Constant, A. Enard, S. Fedderwitz, S. Formont, I. F. Lealman, F. Lecoche, F. Lelarge, D. Moodie, L. Ponnampalam, C. Renaud, M. J. Robertson, A. J. Seeds, A. Stöhr, and M. Weiss, "Quantum dash mode-locked lasers for millimeter wave signal generation and transmission," in *IEEE Photonics Society Annual Meeting*, pp. 187-188, 2010.
- [39] F. van Dijk, A. Enard, X. Buet, F. Lelarge, and G.-H. Duan, "Phase noise reduction of a quantum dash mode-locked laser in a millimeter-wave coupled opto-electronic oscillator," *IEEE/OSA Journal of Lightwave Technology*, vol. 26, pp. 2789-2794, 2008.
- [40] A. Stöhr, R. Heinzelmann, C. Kaczmarek, and D. Jäger, "Ultra-broadband Ka to W-band 1.55 μm travelling-wave photomixer," *Electronics Letters*, vol. 36, pp. 970-972, 2000.
- [41] A. Stöhr, M. Weiß, A. Malcoci, A. G. Steffan, D. Trommer, A. Umbach, and D. Jäger, "Wideband photonic millimeter-wave synthesizer using a high-power pin waveguide photodiode," in *European Microwave Conference*, pp. 588-591, 2007.
- [42] S. Fedderwitz, V. Rymanov, M. Weiß, A. Stöhr, D. Jäger, A. G. Steffan, and A. Umbach, "Ultra-broadband and low phase noise photonic millimeter-wave generation," in *International Topical Meeting on Microwave Photonics. Jointly held with the 2008 Asia-Pacific Microwave Photonics Conference, MWP/APMP*, pp. 283-286, 2008.
- [43] M. Weiß, A. Stöhr, A. Malcoci, A. G. Steffan, D. Trommer, A. Umbach, and D. Jäger, "Ultra-wideband photonic millimeter-wave synthesizers with coaxial (DC-110GHz) and rectangular waveguide (69-112GHz) output ports," in *European Conference on Optical Communication*, Berlin, 2007.
- [44] A. Madjar, N. Koka, J. Bloch, P. K. L. Yu, A. Stöhr, and D. Jäger, "A UTC-TW photo detector operating at frequencies exceeding 100 GHz," in *European Microwave Conference*, pp. 377-380, 2008.
- [45] A. Madjar, N. Koka, J. Bloch, P. K. L. Yu, A. Stöhr, and D. Jäger, "A novel analytical model as a design tool for uni-traveling-carrier traveling wave photo detectors approaching 1 THz," *IEEE Transactions on Microwave Theory and Techniques*, vol. 57, pp. 223-230, 2009.
- [46] D. Klümper, "Aufbau und Charakterisierung planar gekopplerter optischer 40 Gb/s Empfänger," Diplomarbeit, Universität Duisburg-Essen, 2003.
- [47] A. Stöhr, C. C. Renaud, D. Moodie, A. G. Steffan, L. Pavlovic, D. Jäger, A. J. Seeds, M. Robertson, A. Umbach, M. Vidmar, M. Weiss, V. Rymanov, S. Fedderwitz, G. Tsianos, and L. Naglic, "Optical millimeter-wave generation using 1.55 μm photodiodes with and without integrated antennas," in *URSI General Assembly*, Chicago, 2008.

- [48] M. Al-Mumin, C. Kim, I. Kim, N. Jaafar, and G. Li, "Injection locked multi-section gain-coupled dual mode DFB laser for terahertz generation," *Optics Communications*, vol. 275, pp. 186-189, 2007.
- [49] IPHOBAC, "First IPHOBAC periodic activity report," Duisburg, 2007.
- [50] IPHOBAC, "Second IPHOBAC periodic activity report," Duisburg, 2008.
- [51] IPHOBAC, "Third IPHOBAC periodic activity report," Duisburg, 2010.
- [52] D. Wake, C. R. Lima, and P. A. Davies, "Optical generation of millimeter-wave signals for fiber-radio systems using a dual-mode DFB semiconductor laser," *IEEE Transactions on Microwave Theory and Techniques*, vol. 43, pp. 2270-2276, 1995.
- [53] J. Le Gouët, L. Morvan, M. Alouini, J. Bourderionnet, D. Dolfi, and J.-P. Huignard, "Dual-frequency single-axis laser using a lead lanthanum zirconate tantalate (PLZT) birefringent etalon for millimeter wave generation: Beyond the standard limit of tunability," *Optics Letters*, vol. 32, pp. 1090-1092, 2007.
- [54] PHOMIGEN, [www.phomigen.eu](http://www.phomigen.eu).
- [55] J. Renaudier, B. Lavigne, F. Lelarge, M. Jourdran, B. Dagens, O. Legouezigou, P. Gallion, and G. H. Duan, "Standard-compliant jitter transfer function of all-optical clock recovery at 40 GHz based on a quantum-dot self-pulsating semiconductor laser," *IEEE Photonics Technology Letters*, vol. 18, pp. 1249-1251, 2006.
- [56] B. A. Khawaja and M. J. Cryan, "Wireless hybrid mode locked lasers for next generation radio-over-fiber systems," *IEEE/OSA Journal of Lightwave Technology*, vol. 28, pp. 2268-2276, 2010.
- [57] A. Stöhr, S. Babié, P. Cannard, B. Charbonnier, F. van Dijk, S. Fedderwitz, D. Moodie, L. Pavlovic, L. Ponnampalam, C. Renaud, D. Rogers, V. Rymanov, A. Seeds, A. Steffan, A. Umbach, and M. Weiß, "Millimeter-wave photonic components for broadband wireless systems," *IEEE Transactions on Microwave Theory and Techniques* vol. 58, pp. 3071-3082, 2010.
- [58] F. Lelarge, B. Dagens, J. Renaudier, R. Brenot, A. Accard, F. van Dijk, D. Make, O. Le Gouezigou, J. G. Provost, and F. Poingt, "Recent advances on InAs/InP quantum dash based semiconductor lasers and optical amplifiers operating at 1.55 m," *IEEE Journal of Selected Topics in Quantum Electronics*, vol. 13, pp. 111-124, 2007.
- [59] A. Stöhr, A. Akroud, R. Buß, B. Charbonnier, F. v. Dijk, A. Enard, S. Fedderwitz, D. Jäger, M. Huchard, F. Lecoche, J. Marti, R. Sambaraju, A. Steffan, A. Umbach, and M. Weiß, "60 GHz radio-over-fiber technologies for broadband wireless services," *Journal of Optical Networking*, 2009.
- [60] F. van Dijk, A. Enard, A. Akroud, G. H. Duan, and F. Lelarge, "Optimization of a 54.8 GHz coupled opto-electronic oscillator through dispersion compensation of a mode-locked semiconductor laser," in *International Topical Meeting on Microwave Photonics. Jointly held with the 2008 Asia-Pacific Microwave Photonics Conference*, pp. 279-282, 2008.
- [61] R. Paschotta and U. Keller, "Passive mode locking with slow saturable absorbers," *Applied Physics B: Lasers and Optics*, vol. 73, pp. 653-662, 2001.
- [62] H. A. Haus, "Mode-locking of lasers," *IEEE Journal of Selected Topics in Quantum Electronics*, vol. 6, pp. 1173-1185, 2002.
- [63] S. Arahira and Y. Ogawa, "40 GHz actively mode-locked distributed Bragg reflector laser diode module with an impedance-matching circuit for efficient RF signal injection," *Japanese Journal of Applied Physics*, vol. 43, pp. 1960-1964, 2004.
- [64] S. Bennett, B. Cai, E. Burr, O. Gough, and A. J. Seeds, "1.8-THz bandwidth, zero-frequency error, tunable optical comb generator for DWDM applications," *IEEE Photonics Technology Letters*, vol. 11, pp. 551-553, 1999.
- [65] M. Endo, "Optical frequency comb generator using a single-sideband suppressed-carrier modulation in an amplified circulating fiber loop," *Laser Physics*, vol. 12, pp. 679-683, 2002.
- [66] P. Jessen and M. Kristensen, "Generation of a frequency comb with a double acousto-optic modulator ring," *Applied Optics*, vol. 31, pp. 4911-4913, 1992.
- [67] T. Kawanishi, T. Sakamoto, S. Shinada, and M. Izutsu, "Optical frequency comb generator using optical fiber loops with single-sideband modulation," *IEICE Electronics Express*, vol. 1, pp. 217-221, 2004.

- [68] F. V. Kowalski, P. D. Hale, and S. J. Shattil, "Broadband continuous-wave laser," *Optics Letters*, vol. 13, pp. 622-624, 1988.
- [69] T. Saitoh, M. Kourogi, and M. Ohtsu, "A waveguide-type optical-frequency comb generator," *IEEE Photonics Technology Letters*, vol. 7, pp. 197-199, 1995.
- [70] O. P. Gough, C. F. C. Silva, and A. J. Seeds, "Exact millimetre wave frequency synthesis by injection locked laser comb line selection," in *International Topical Meeting on Microwave Photonics*, pp. 61-64, 1999.
- [71] T. Udem, J. Reichert, R. Holzwarth, and T. W. Hänsch, "Accurate measurement of large optical frequency differences with a mode-locked laser," *Optics Letters*, vol. 24, pp. 881-883, 1999.
- [72] N. Park and P. F. Wysocki, "24-line multiwavelength operation of erbium-doped fiber-ring laser," *IEEE Photonics Technology Letters*, vol. 8, pp. 1459-1461, 1996.
- [73] I. Morohashi, T. Sakamoto, H. Sotobayashi, T. Kawanishi, and I. Hosako, "Broadband optical comb generation using Mach-Zehnder-modulator-based flat comb generator with feedback loop," in *European Conference on Optical Communication*, Torino, pp. 1-3, 2010.
- [74] M. Kourogi, K. Nakagawa, and M. Ohtsu, "Wide-span optical frequency comb generator for accurate optical frequency difference measurement," *IEEE Journal of Quantum Electronics*, vol. 29, pp. 2693-2701, 1993.
- [75] J. P. Weber, B. Stoltz, H. Sano, M. Dasler, O. Oberg, and J. Waltz, "An integratable polarization-independent tunable filter for WDM systems: The multigrating filter," *IEEE/OSA Journal of Lightwave Technology*, vol. 14, pp. 2719-2735, 1996.
- [76] L. Goldberg, H. Taylor, J. Weller, and D. Bloom, "Microwave signal generation with injection-locked laser diodes," *Electronics Letters*, vol. 19, pp. 491-493, 1983.
- [77] L. Goldberg, A. M. Yurek, H. F. Taylor, and J. F. Weller, "35 GHz microwave signal generation with an injection-locked laser diode," *Electronics Letters*, vol. 21, pp. 814-815, 1985.
- [78] F. Mogensen, H. Olesen, and G. Jacobsen, "FM noise suppression and linewidth reduction in an injection-locked semiconductor laser," *Electronics Letters*, vol. 21, pp. 696-697, 1985.
- [79] E. K. Lau, "High-speed modulation of optical injection-locked semiconductor lasers," *PhD Thesis*, EECS Department, University of California, Berkeley, 2006.
- [80] T. B. Simpson, J. M. Liu, and A. Gavrielides, "Bandwidth enhancement and broadband noise reduction in injection-locked semiconductor lasers," *IEEE Photonics Technology Letters*, vol. 7, pp. 709-711, 1995.
- [81] J. Wang, M. K. Haldar, L. Li, and F. V. C. Mendis, "Enhancement of modulation bandwidth of laser diodes by injection locking," *IEEE Photonics Technology Letters*, vol. 8, pp. 34-36, 1996.
- [82] R. Lang, "Injection locking properties of a semiconductor laser," *IEEE Journal of Quantum Electronics*, vol. 18, pp. 976-983, 1982.
- [83] R. Adler, "A study of locking phenomena in oscillators," *Proceedings of the IRE*, vol. 34, pp. 351-357, 1946.
- [84] E. K. Lau, X. Zhao, H. K. Sung, D. Parekh, C. Chang-Hasnain, and M. C. Wu, "Strong optical injection-locked semiconductor lasers demonstrating >100-GHz resonance frequencies and 80-GHz intrinsic bandwidths," *Optics Express*, vol. 16, pp. 6609-6618, 2008.
- [85] A. Ng'oma, D. Fortusini, D. Parekh, W. Yang, M. Sauer, S. Benjamin, W. Hofmann, M. C. Amann, and C. J. Chang-Hasnain, "Performance of a multi-Gb/s 60 GHz radio over fiber system employing a directly modulated optically injection-locked VCSEL," *IEEE/OSA Journal of Lightwave Technology*, vol. 28, pp. 2436-2444, 2010.
- [86] L. Langley, M. Elkin, C. Edge, M. Wale, U. Gliese, X. Huang, and A. Seeds, "Packaged semiconductor laser optical phase-locked loop (OPLL) for photonic generation, processing and transmission of microwave signals," *IEEE Transactions on Microwave Theory and Techniques*, vol. 47, pp. 1257-1264, 1999.
- [87] C. Walton, A. C. Bordonali, and A. J. Seeds, "High-performance heterodyne optical injection phase-lock loop using wide linewidth semiconductor lasers," *IEEE Photonics Technology Letters*, vol. 10, pp. 427-429, 1998.

- [88] A. C. Bordonalli, C. Walton, and A. J. Seeds, "High-performance phase locking of wide linewidth semiconductor lasers by combined use of optical injection locking and optical phase-lock loop," *IEEE/OSA Journal of Lightwave Technology*, vol. 17, p. 328, 1999.
- [89] L. Kazovsky, "Balanced phase-locked loops for optical homodyne receivers: Performance analysis, design considerations, and laser linewidth requirements," *IEEE/OSA Journal of Lightwave Technology*, vol. 4, pp. 182-195, 1986.
- [90] L. Enloe and J. Rodda, "Laser phase-locked loop," *Proceedings of the IEEE*, vol. 53, pp. 165-166, 1965.
- [91] J. E. Bowers, A. Ramaswamy, L. A. Johansson, J. Klamkin, M. Sysak, D. Zibar, L. Coldren, M. Rodwell, L. Lembo, R. Yoshimitsu, D. Scott, R. Davis, and P. Ly, "Linear coherent receiver based on a broadband and sampling optical phase-locked loop," in *International Topical Meeting on Microwave Photonics*, pp. 225-228, 2007.
- [92] R. T. Ramos and A. J. Seeds, "Delay, linewidth and bandwidth limitations in optical phase-locked loop design," *Electronics Letters*, vol. 26, pp. 389-391, 1990.
- [93] R. T. Ramos, P. Gallion, D. Erasme, A. J. Seeds, and A. Bordonalli, "Optical injection locking and phase-lock loop combined systems," *Optics Letters*, vol. 19, pp. 4-6, 1994.
- [94] G. H. Smith, D. Novak, and Z. Ahmed, "Overcoming chromatic-dispersion effects in fiber-wireless systems incorporating external modulators," *IEEE Transactions on Microwave Theory and Techniques*, vol. 45, pp. 1410-1415, 1997.
- [95] X. S. Yao and L. Maleki, "Converting light into spectrally pure microwave oscillation," *Optics Letters*, vol. 21, pp. 483-485, 1996.
- [96] X. S. Yao and L. Maleki, "Optoelectronic microwave oscillator," *J. Opt. Soc. Am. B*, vol. 13, pp. 1725-1735, 1996.
- [97] X. S. Yao and L. Maleki, "Multiloop optoelectronic oscillator," *IEEE Journal of Quantum Electronics*, vol. 36, pp. 79-84, 2000.
- [98] E. Shumakher, "The optoelectronic oscillator: Review and recent advances," in *IEEE International Conference on Microwaves, Communications, Antennas and Electronics Systems*, pp. 1-5, 2009.
- [99] S. Poinsot, H. Porte, J.-P. Goedgebuer, W. T. Rhodes, and B. Boussert, "Continuous radio-frequency tuning of an optoelectronic oscillator with dispersive feedback," *Optics Letters*, vol. 27, pp. 1300-1302, 2002.
- [100] D. Eliyahu and L. Maleki, "Tunable, ultra-low phase noise YIG based opto-electronic oscillator," in *IEEE MTT-S International Microwave Symposium*, pp. 2185-2187, 2003.
- [101] S. Fedderwitz, A. Stohr, S. Babiel, V. Rymanov, and D. Jäger, "Optoelectronic K-band oscillator with gigahertz tuning range and low phase noise," *IEEE Photonics Technology Letters*, vol. 22, pp. 1497-1499, 2010.
- [102] J. J. O'Reilly, P. M. Lane, R. Heidemann, and R. Hofstetter, "Optical generation of very narrow linewidth millimetre wave signals," *Electronics Letters*, vol. 28, pp. 2309-2311, 1992.
- [103] J. J. O'Reilly and P. M. Lane, "Fibre-supported optical generation and delivery of 60 GHz signals," *Electronics Letters*, vol. 30, pp. 1329-1330, 1994.
- [104] J. Zhang, H. Chen, M. Chen, T. Wang, and S. Xie, "Photonic generation of a millimeter-wave signal based on sextuple-frequency multiplication," *Optics Letters*, vol. 32, pp. 1020-1022, 2007.
- [105] S. Fedderwitz, "Generation of Frequency-Tunable and Low Phase Noise Micro- and Millimeter-Wave Signals using Microwave Photonic Technologies," *PhD Thesis*, Universität Duisburg-Essen, 2013 (to be submitted).
- [106] G. Bramann, H. J. Wünsche, U. Busolt, C. Schmidt, M. Schlak, B. Sartorius, and H. P. Nolting, "Two-wave competition in ultralong semiconductor optical amplifiers," *IEEE Journal of Quantum Electronics*, vol. 41, pp. 1260-1267, 2005.
- [107] P. Runge, "Nonlinear effects in ultralong semiconductor optical amplifiers for optical communications: Physics and applications," *PhD Thesis*, Technische Universität Berlin, 2010.
- [108] C. Bornholdt, J. Slovák, B. Sartorius, M. Schlak, and C. Schmidt, "Optical comb generator using pulse compression in ultra-long semiconductor amplifiers," in *European Conference on Optical Communication*, pp. 173-174, 2005.
- [109] W. Tianliang, C. Minghua, C. Hongwei, Z. Jian, and X. Shizhong, "Millimeter-wave signal generation using two cascaded optical modulators and FWM effect in

- semiconductor optical amplifier," *IEEE Photonics Technology Letters*, vol. 19, pp. 1191-1193, 2007.
- [110] T. Wang, M. Chen, H. Chen, and S. Xie, "Millimetre-wave signal generation using FWM effect in SOA," *Electronics Letters*, vol. 43, pp. 36-38, 2007.
- [111] G. A. Sefer and K. I. Kitayama, "Frequency comb generation by four-wave mixing and the role of fiber dispersion," *IEEE/OSA Journal of Lightwave Technology*, vol. 16, pp. 1596-1605, 1998.
- [112] A. Stöhr, "Entwicklung und Realisierung elektrooptischer Wellenleiter-Schalter für photonische Systeme im Wellenlängenbereich um  $1\mu\text{m}$ ," VDI Verlag, ISBN: 3-18-349010-2, 1997.
- [113] Y. K. Seo, C. S. Choi, and W. Y. Choi, "All-optical signal up-conversion for radio-on-fiber applications using cross-gain modulation in semiconductor optical amplifiers," *IEEE Photonics Technology Letters*, vol. 14, pp. 1448-1450, 2002.
- [114] F. Koyama and K. Iga, "Frequency chirping in external modulators," *IEEE/OSA Journal of Lightwave Technology*, vol. 6, pp. 87-93, 1988.
- [115] F. Devaux, Y. Sorel, and J. F. Kerdiles, "Simple measurement of fiber dispersion and of chirp parameter of intensity modulated light emitter," *IEEE/OSA Journal of Lightwave Technology*, vol. 11, pp. 1937-1940, 1993.
- [116] N. Henmi, T. Saito, M. Yamaguchi, and S. Fujita, "10-Gb/s, 100-km normal fiber transmission experiment employing a modified prechirp technique," 1991.
- [117] N. Mineo, K. Yamada, K. Nakamura, S. Sakai, and T. Ushikubo, "60-GHz band electroabsorption modulator module," in *Optical Fiber Communication Conference*, San Jose, pp. 287-288, 2002.
- [118] A. Stöhr, K. I. Kitayama, and T. Kuri, "Chirp optimized 60 GHz millimeter-wave fiber-optic transmission incorporating EA-modulator," in *European Conference on Optical Communication*, pp. 669-670 vol.1, 1998.
- [119] R. Kurz, S. Guilloteau, and P. Shaver, "The Atacama Large Millimetre Array," *The Messenger*, vol. 107, pp. 7-12, 2002.
- [120] P. H. Siegel, "Terahertz technology," *IEEE Transactions on Microwave Theory and Techniques*, vol. 50, pp. 910-928, 2002.
- [121] B. Leone, V. Krozer, M. Feiginov, H. Roskos, H. Quast, T. Löffler, G. Loata, G. Döhler, P. Kiesel, and M. Eckardt, "Optical Far-IR wave Generation-An ESA review study," in *International Symposium on Space Terahertz Technology*, pp. 328-343, 2003.
- [122] K. Kato, "Ultrawide-band/high-frequency photodetectors," *IEEE Transactions on Microwave Theory and Techniques*, vol. 47, pp. 1265-1281, 1999.
- [123] T. Nagatsuma, H. Ito, and T. Ishibashi, "High power RF photodiodes and their applications," *Laser & Photonics Reviews*, vol. 3, pp. 123-137, 2009.
- [124] E. Brown, "THz generation by photomixing in ultrafast photoconductors," *International Journal of High Speed Electronics and Systems*, vol. 13, pp. 497-546, 2003.
- [125] A. Stöhr, R. Heinzelmann, A. Malcoci, and D. Jäger, "Optical heterodyne millimeter-wave generation using  $1.55\ \mu\text{m}$  traveling-wave photodetectors," *IEEE Transactions on Microwave Theory and Techniques*, vol. 49, pp. 1926-1933, 2001.
- [126] A. Stöhr and D. Jäger, "THz photomixers: An overview," in *Millimeter-Wave and Terahertz Photonics*. vol. 6194, Eds. A. Stöhr and D. Jäger, Proceedings of the SPIE, ISBN: 0-8194-6250-0, p. 61940D, 2006.
- [127] A. Stöhr and D. Jäger, "Optical generation of millimeter-wave signals," in *International Topical Meeting on Micorwave Photonics*, Ed. S. Iezekiel, John Wiley & Sons Ltd., ISBN: 0470848545, 2009.
- [128] M. Alles, U. Auer, F. J. Tegude, and D. Jager, "Distributed velocity-matched  $1.55\ \mu\text{m}$  InP travelling-wave photodetector for generation of high millimeterwave signal power," pp. 1233-1236, 1998.
- [129] T. Chau, N. Kaneda, T. Jung, A. Rollinger, S. Mathai, Y. Qian, T. Itoh, M. Wu, W. Shillue, and J. Payne, "Generation of millimeter waves by photomixing at  $1.55\ \text{m}$  using InGaAs-InAlAs-InP velocity-matched distributed photodetectors," *IEEE Photonics Technology Letters*, vol. 12, pp. 1055-1057, 2000.
- [130] K. S. Giboney, J. Rodwell, and J. E. Bowers, "Traveling-wave photodetector theory," *IEEE Transactions on Microwave Theory and Techniques*, vol. 45, pp. 1310-1319, 1997.

- [131] J. Soohoo, S. K. Yao, J. Miller, R. Shurtz, Y. Taur, and R. Gudmundsen, "A laser-induced traveling-wave device for generating millimeter waves," *IEEE Transactions on Microwave Theory and Techniques*, vol. 29, pp. 1174-1182, 1981.
- [132] V. M. Hietala, G. Vawter, T. Brennan, and B. Hammons, "Traveling-wave photodetectors for high-power, large-bandwidth applications," *IEEE Transactions on Microwave Theory and Techniques*, vol. 43, pp. 2291-2298, 1995.
- [133] Y. L. Huang and C. K. Sun, "Nonlinear saturation behaviors of high-speed pin photodetectors," *IEEE/OSA Journal of Lightwave Technology*, vol. 18, pp. 203-212, 2000.
- [134] D. X. Zhu, S. Dubovitsky, W. H. Steier, J. Burger, D. Tishinin, K. Uppal, and P. D. Dapkus, "Ambipolar diffusion coefficient and carrier lifetime in a compressively strained InGaAsP multiple quantum well device," *Applied Physics Letters*, vol. 71, p. 647, 1997.
- [135] P. Berini, A. Stöhr, K. Wu, and D. Jäger, "Normal mode analysis and characterization of an InGaAs/GaAs MQW field-induced optical waveguide including electrode effects," *IEEE/OSA Journal of Lightwave Technology*, vol. 14, pp. 2422-2435, 1996.
- [136] K. J. Williams, R. D. Esman, and M. Dagenais, "Effects of high space-charge fields on the response of microwave photodetectors," *IEEE Photonics Technology Letters*, vol. 6, pp. 639-641, 1994.
- [137] D. Jäger, "Slow-wave propagation along variable Schottky-contact microstrip line," *IEEE Transactions on Microwave Theory and Techniques*, vol. 24, pp. 566-573, 1976.
- [138] M. Weiß, A. G. Steffan, S. Fedderwitz, G. Tsianos, A. Stöhr, and D. Jäger, "Highly-compact fibre-optic package for 30-300GHz wireless transmitter modules," in *Electronics Systemintegration Technology Conference*, pp. 1111-1114, 2008.
- [139] D. A. Tulchinsky, X. Li, N. Li, S. Demiguel, J. C. Campbell, and K. J. Williams, "High-saturation current wide-bandwidth photodetectors," *IEEE Journal of Selected Topics in Quantum Electronics*, vol. 10, pp. 702-708, 2004.
- [140] K. Williams, "Comparisons between dual-depletion-region and uni-travelling-carrier pin photodetectors," *IEE Proceedings Optoelectronics*, vol. 149, pp. 131-137, 2002.
- [141] A. Malcoci, A. Stöhr, K. Lill, F. Siebe, P. van der Waal, A. Sauerwald, R. Gusten, and D. Jäger, "Optical submillimeter-wave generation employing antenna integrated ultra-fast travelling-wave 1.55 μm photodetectors," in *IEEE MTT-S International Microwave Symposium*, pp. 143-146, 2003.
- [142] A. Stöhr and D. Jäger, "Ultra-wideband travelling-wave photodetectors for THz signal generation," in *IEEE Lasers and Electro-Optics Society Annual Meeting*, pp. 200-201, 2004.
- [143] J. Payne, B. Shillue, and A. Vaccari, "Photonic techniques for use on the atacama large millimeter array," in *International Topical Meeting on Microwave Photonics*, pp. 105-108, 1999.
- [144] T. H. Wood, E. C. Carr, B. L. Kasper, R. A. Linke, C. A. Burrus, and K. L. Walker, "Bidirectional fibre-optical transmission using a multiple-quantum-well (MQW) modulator/detector," *Electronics Letters*, vol. 22, pp. 528-529, 1986.
- [145] R. B. Welstand, S. A. Pappert, C. K. Sun, J. T. Zhu, Y. Z. Liu, and P. K. L. Yu, "Dual-function electroabsorption waveguide modulator/detector for optoelectronic transceiver applications," *IEEE Photonics Technology Letters*, vol. 8, pp. 1540-1542, 1996.
- [146] L. Noel, D. Wake, D. G. Moodie, D. D. Marcenac, L. D. Westbrook, and D. Nesson, "Novel techniques for high-capacity 60-GHz fiber-radio transmission systems," *IEEE Transactions on Microwave Theory and Techniques*, vol. 45, pp. 1416-1423, 1997.
- [147] L. D. Westbrook and D. G. Moodie, "Simultaneous bi-directional analogue fibre-optic transmission using an electroabsorption modulator," *Electronics Letters*, vol. 32, pp. 1806-1807, 1996.
- [148] L. D. Westbrook, L. Noel, and D. G. Moodie, "Full-duplex, 25 km analogue fibre transmission at 120 Mbit/s with simultaneous modulation and detection in an electroabsorption modulator," *Electronics Letters*, vol. 33, pp. 694-695, 1997.
- [149] A. Stöhr, K. Kitayama, and D. Jäger, "Error-free full-duplex optical WDM-FDM transmission using an EA-Transceiver," in *International Topical Meeting on Microwave Photonics*, Princeton, pp. 37-40, 1998.
- [150] CIP Technologies Ltd., [www.ciphotonics.com](http://www.ciphotonics.com).

- [151] A. Stöhr, K. Kitayama, and D. Jäger, "Full-duplex fiber-optic RF subcarrier transmission using a dual-function modulator/photodetector," *IEEE Transactions on Microwave Theory and Techniques*, vol. 47, pp. 1338-1341, 1999.
- [152] A. Stöhr, T. Kuri, K. Kitayama, R. Heinzelmann, and D. Jäger, "Full-duplex 60 GHz fibre optic transmission," *Electronics Letters*, vol. 35, pp. 1653-1655, 1999.
- [153] M. Silver and E. P. O'Reilly, "Optimization of long wavelength InGaAsP strained quantum-well lasers," *IEEE Journal of Quantum Electronics*, vol. 31, pp. 1193-1200, 1995.
- [154] K. Hagedorn, R. Gindera, A. Stöhr, and D. Jäger, "Heterogeneous wireless/wireline optical access networks with the R-EAT as backend component," in *Microwave and Terahertz Photonics*, Eds. A. Stöhr, D. Jäger, and S. Iezekiel, SPIE, pp. 27-33, 2004.
- [155] G. Wingen, "Vertikale Wanderwellenmodulatoren auf Quantenfilmbasis für die optische Informationsverarbeitung," *PhD Thesis*, Universität Duisburg-Essen, 2001.
- [156] T. Alder, R. Heinzelmann, S. Leonhard, A. Stöhr, and D. Jäger, "Fiber-chip-coupling based on in InP V-groove technology," in *IEEE Lasers and Electro-Optics Society Annual Meeting LEOS*, pp. 40-41, 1998.
- [157] T. Alder, R. Heinzelmann, S. Leonhard, A. Stöhr, and D. Jäger, "Faser-Wellenleiter-Kopplung auf der Basis von InP-V-Gruben und faseroptischen Modenfeld-Transformatoren," in *ITG/VDE-Workshop über Photonische Integration und Aufbautechnik*, Berlin, 1999.
- [158] T. Alder, A. Stöhr, R. Heinzelmann, and D. Jäger, "High-efficiency fiber-to-chip coupling using low-loss tapered single-mode fiber," *IEEE Photonics Technology Letters*, vol. 12, pp. 1016-1018, 2000.
- [159] K. Hagedorn, R. Gindera, A. Stöhr, and D. Jäger, "Simultaneous transmission of 2.5 Gb/s base band signal and microwave signals employing a 1.55 μm R-EAT for hybrid wireless/wireline networks," in *European NEFERTITI Workshop*, York, pp. 27-33, 2004.
- [160] DE-CIX, <http://www.de-cix.net/content/network.html>
- [161] T. Husson, "Western European mobile forecast, 2009 to 2014," *Forrester Research*, 2009.
- [162] N. Burley, "Mobile broadband traffic management and QoS prioritisation," *OVUM*, 2009.
- [163] M. Mackenzie and S. Hartley, "Mobile broadband growth forecast, 2008-2014," *OVUM*, 2009.
- [164] N. Cooper, "Top 10 issues in mobile for 2009," *Analysis Mason*, 2009.
- [165] Anonymous, "Europe to see huge growth in mobile broadband services despite recession," *Pyramid Research*, vol. 1, 2009.
- [166] J. Grivolas, "Wireless solutions for cellular backhaul," *OVUM*, 2008.
- [167] Fujitsu, "Understanding mobile wireless backhaul," [http://www.bulldogsolutions.net/Fujitsu/Knowledgebase/microsite/Fujitsu\\_Wireless\\_Bac\\_khaul.pdf](http://www.bulldogsolutions.net/Fujitsu/Knowledgebase/microsite/Fujitsu_Wireless_Bac_khaul.pdf).
- [168] P. Donegan, "Ethernet backhaul quarterly market tracker," *Heavy Reading*, 2009.
- [169] B. Charbonnier, "Private discussions," 2009.
- [170] Infonetics Research Inc., "Biannual worldwide and regional market size and forecasts," 2009.
- [171] M. Walker, "Wireless backhaul: Opportunities for optical and switching/routing vendors," *OVUM*, 2009.
- [172] ETSI, "Fixed radio systems; characteristics and requirements for point-to-point equipment and antennas; Part 4-1: System-dependent requirements for antennas," ETSI EN 302 217-4-1, 2006.
- [173] MPHPT, "Specified low power radio station (12) 59-66 GHz band," in *Regulation for the Enforcement of the Radio Law 6-4-2*, 2000.
- [174] FCC, "Code of federal regulation, title 47 telecommunications, part 15," FCC 47 CFR 15.255, 2008.
- [175] IC-SMT, "Radio standards specification (RSS-210)," Issue 6, Industry Canada Spectrum Management Telecommunications, Canada, 2005.
- [176] ECC, "Use of the 64-66 GHz frequency band for fixed service," ECC Recommendation (05)02, 2009.
- [177] ETSI, "Technical characteristics of multiple gigabit wireless systems in the 60 GHz range," System Reference Document, ETSI TR 102 555, 2007.
- [178] ECC, "Use of the 57-64 GHz frequency band for point-to-point fixed wireless services," ECC Recommendation (09)01, 2009.

- [179] ACMA, "Radiocommunications (low interference potential devices) class licence 2000," Australian Communications and Media Authority, 2009.
- [180] KCC, "Frequency allocation comment on 60 GHz band," Korea Communications Commission, 2006.
- [181] FCC, "Allocations and service rules for the 71-76 GHz, 81-86 GHz, and 92-95 GHz bands," Federal Communications Commission 03-248, 2003.
- [182] FCC, "Allocations and service rules for the 71-76 GHz, 81-86 GHz, and 92-95 GHz bands," Federal Communications Commission 05-45, 2005.
- [183] DGTP, "Consultation on a renewed spectrum policy framework for Canada and continued advancement in spectrum management," DGTP-001-05, 2005.
- [184] ECC, "Radio frequency channel arrangements for fixed service systems operating in the bands 71-76 GHz and 81-86 GHz," ECC Recommendation (05)07, 2009.
- [185] ETSI, "Fixed radio systems; point-to-point equipment; radio equipment and antennas for use in point-to-point millimetre wave applications in the fixed services (mmwFS) frequency bands 71 GHz to 76 GHz and 81 GHz to 86 GHz," ETSI TS 102 524, 2006.
- [186] A. Stöhr and D. Jäger, "Photonic millimeter-wave and terahertz source technologies," in *International Topical Meeting on Microwave Photonics*, pp. 1-4, 2006.
- [187] ACMA, "Allocations and service rules for the 71-76 GHz, 81-86 GHz and 92-95 GHz bands," Australian Communications and Media Authority, ACMA SP 2006-11, 2006.
- [188] ECMA, "High rate 60 GHz PHY, MAC and HDMI PAL," European Computer Manufacturers Association, ECMA-387, 2008.
- [189] BNetzA, "Allgemeinzuteilungen für Punkt-zu-Punkt Richtfunk im Frequenzbereich 59-64 GHz," Bundesnetzagentur, Mitteilungen 217/2008, 2008.
- [190] IEEE802.16, "IEEE standard for local and metropolitan area networks - Part 16: Air interface for broadband wireless access systems" IEEE Std. 802.16-2009, 2009.
- [191] ARIB, "Millimeter-wave video transmission equipment for specified low power radio station," Association of Radio Industries and Businesses, ARIB STD T-69, 2001.
- [192] ARIB, "Millimeter-wave data transmission equipment for specified low power radio stations (ultra high speed wireless LAN system)," Association of Radio Industries and Businesses, ARIB STD T-74, 2001.
- [193] K. Kitayama, A. Stöhr, T. Kuri, R. Heinzelmann, D. Jäger, and Y. Takahashi, "An approach to single optical component antenna base stations for broad-band millimeter-wave fiber-radio access systems," *IEEE Transactions on Microwave Theory and Techniques*, vol. 48, pp. 2588-2595, 2000.
- [194] K. I. Kitayama, T. Kuri, R. Heinzelmann, A. Stöhr, D. Jäger, and Y. Takahashi, "A good prospect for broadband millimeter-wave fiber-radio access system-an approach to single optical component at antenna base station," in *IEEE MTT-S International Microwave Symposium*, pp. 1745-1748, 2000.
- [195] R. V. L. Hartley, "Transmission of information," *Bell System Technical Journal*, vol. 3, p. 535, 1928.
- [196] C. E. Shannon, "Communications in the Presence of Noise," *Proceedings of the IRE*, vol. 37, pp. 10-21, 1949.
- [197] J. Proakis, "Digital communications," New York, ISBN: 978-0072321111, 2001.
- [198] M. Frecassetti, "Wireless transmission - Toward millimeter applications," Alcatel-Lucent, Wireless Transmission business unit, 2008.
- [199] M. Frecassetti, D. Mandich, R. Pellizzoni, and R. Valtolina, "Exploiting 70-90 GHz band for efficient gigabit wireless communications," in *European Conference on Wireless Technology*, pp. 353-356, 2004.
- [200] J. M. Gomez, "Satellite broadcast systems engineering," Artech House, ISBN: 1-58053-313-2, 2002.
- [201] H. T. Friis, "A note on a simple transmission formula," *Proceedings of the IRE*, vol. 34, p. 245, 1946.
- [202] ITU, "Recommendation ITU-R P.676-4" in *Attenuation by Atmospheric Gases*: International Telecommunication Union, 2001.
- [203] R. Crane, "Prediction of attenuation by rain," *IEEE Transactions on Communications*, vol. 28, pp. 1717-1733, 2002.
- [204] T. Maseng and P. Bakken, "A stochastic dynamic model of rain attenuation," *IEEE Transactions on Communications*, vol. 29, pp. 660-669, 2002.

- [205] E. Matricciani, "Physical-mathematical model of the dynamics of rain attenuation based on rain rate time series and a two-layer vertical structure of precipitation," *Radio Science*, vol. 31, pp. 281-295, 1996.
- [206] ITU, "Specific attenuation model for rain for use in prediction methods," in *ITU Recommendation P.838-3*, 2005.
- [207] L. Coldren and S. Corzine, "Diode lasers and photonic integrated circuits," John Wiley New York, ISBN: 0471118753, 1995.
- [208] N. Olsson, "Lightwave systems with optical amplifiers," *IEEE/OSA Journal of Lightwave Technology*, vol. 7, pp. 1071-1082, 2002.
- [209] G. Walker, R. Steele, and N. Walker, "Optical amplifier noise figure in a coherent optical transmission system," *IEEE/OSA Journal of Lightwave Technology*, vol. 8, pp. 1409-1413, 2002.
- [210] R. C. Steele, G. R. Walker, and N. G. Walker, "Sensitivity of optically preamplified receivers with optical filtering," *IEEE Photonics Technology Letters*, vol. 3, pp. 545-547, 1991.
- [211] E. K. Smith, "Centimeter and Millimeter Wave Attenuation and Brightness Temperature due to Atmospheric Oxygen and water vapor," *Radio Science*, vol. 17, pp. 1455-1464, 1982.
- [212] FCC, "Millimeter wave propagation: spectrum management implications," in *Bulletin Number 70*: Federal Communications Commission, 1997.
- [213] A. Stöhr, R. Heinzelmann, and D. Jäger, "Microwave and millimetre-wave fibre optic links: Full-duplex fibre-wireless network architecture employing EA-transceiver," in *MICROCOLL Conference*, Budapest, pp. 41-46, 1999.
- [214] A. Stöhr, R. Heinzelmann, and D. Jäger, "Millimetre-wave bandwidth electroabsorption modulators and transceivers," in *International Topical Meeting on Microwave Photonics*, pp. 125-128, 2000.
- [215] A. Stöhr, R. Heinzelmann, K. Kitayama, and D. Jäger, "EA-transceiver for full-duplex WDM ring networks," in *URSI International Symposium on Signals, Systems, and Electronics ISSSE*, pp. 384-387, 1998.
- [216] A. Stöhr, R. Heinzelmann, K. Kitayama, T. Kuri, and D. Jäger, "Photonics for millimeter-wave broadband wireless," in *Terahertz and Gigahertz Electronics and Photonics II*. vol. 4111, Eds. R. J. Hwu and K. Wu, Proceedings of the SPIE, pp. 1-8, 2000.
- [217] A. Stöhr, R. Heinzelmann, T. Kuri, K. Kitayama, and D. Jäger, "Full-duplex 60 GHz fibre-wireless networks employing EA-transceiver," in *European Microwave Conference, Workshop on Optical Technologies for Microwave Systems*, Munich, pp. 24-33, 1999.
- [218] A. Stöhr, K. Kitayama, and T. Kuri, "Fiber-length extension in an optical 60-GHz transmission system using an EA-modulator with negative chirp," *IEEE Photonics Technology Letters*, vol. 11, pp. 739-741, 1999.
- [219] Y. Lize, L. Christen, S. Nuccio, X. Wu, A. Willner, R. Kashyap, and M. Faucher, "Optical error correction using passive optical logic gates demodulators in differential demodulation," pp. 1-2, 2008.
- [220] M. Weiß, M. Huchard, A. Stöhr, B. Charbonnier, S. Fedderwitz, and D. S. Jäger, "60-GHz Photonic millimeter-wave link for short- to medium-range wireless transmission up to 12.5 Gb/s," *IEEE/OSA Journal of Lightwave Technology*, vol. 26, pp. 2424-2429, 2008.
- [221] R. Prasad, "OFDM for wireless communications systems," Artech House Publishers, ISBN: 1580537960, 2004.
- [222] S. L. Jansen, I. Morita, N. Takeda, and H. Tanaka, "20-Gb/s OFDM transmission over 4,160-km SSMF enabled by RF-pilot tone phase noise compensation," 2007.
- [223] A. J. Lowery, L. B. Du, and J. Armstrong, "Performance of optical OFDM in ultralong-haul WDM lightwave systems," *IEEE/OSA Journal of Lightwave Technology*, vol. 25, pp. 131-138, 2007.
- [224] Z. Jia, "Optical millimeter-wave signal generation, transmission and processing for symmetric super-broadband optical-wireless access networks," *PhD Thesis*, Georgia Institute of Technology, 2008.
- [225] Comotech, <http://www.comotech.com>.
- [226] E-Band Communications Corporation, [www.e-band.com](http://www.e-band.com).

- [227] Loea, <http://www.loeacom.com>.
- [228] Elva-1, <http://www.elva-1.com>.
- [229] Rayawave, <http://www.rayawave.com>.
- [230] Gigabeam, <http://www.gigabeam.com>.
- [231] Proxim Wireless, <http://www.proxim.com>.
- [232] Asyrmatos, <http://www.asyrmatos.com/mmwcd.php>.
- [233] T. Kuri, K. Kitayama, Y. Ogawa, and a. A. Stöhr, "Fiber-optic transmission experiment of 60GHz-band millimeter-wave downlink using an external modulation," *Technical Report of IEICE*, 1998.
- [234] T. Kuri, K. Kitayama, A. Stöhr, and Y. Ogawa, "Fiber-optic millimeter-wave downlink system using 60 GHz-band external modulation," *IEEE/OSA Journal of Lightwave Technology*, vol. 17, pp. 799-806, 1999.
- [235] Y.-K. Seo, J.-H. Seo, and W.-Y. Choi, "60 GHz radio-on-fiber distribution of  $2 \times 622$  Mb/s WDM channels using remote photonic-frequency upconversion," *Microwave and Optical Technology Letters*, vol. 39, pp. 201-203, 2003.
- [236] A. Hirata, T. Kosugi, H. Takahashi, R. Yamaguchi, F. Nakajima, T. Furuta, H. Ito, H. Sugahara, Y. Sato, and T. Nagatsuma, "120 GHz band millimeter-wave photonic wireless link for 10 Gb/s data transmission," *IEEE Transactions on Microwave Theory and Techniques*, vol. 54, pp. 1937-1944, 2006.
- [237] T. Nagatsuma, H.-J. Song, Y. Fujimoto, K. Miyake, A. Hirata, K. Ajito, A. Wakatsuki, T. Furuta, N. Kukutsu, and Y. Kado, "Giga-bit wireless link using 300-400 GHz bands," in *International Topical Meeting on Microwave Photonics Valencia*, 2009.
- [238] H.-J. Song, K. Ajito, A. Hirata, A. Wakatsuki, Y. Muramoto, T. Furuta, N. Kukutsu, T. Nagatsuma, and Y. Kado, "8 Gbit/s wireless data transmission at 250 GHz," *Electronics Letters*, vol. 45, 2009.
- [239] R. W. Ridgway and D. W. Nippa, "Generation and modulation of a 94-GHz signal using electrooptic modulators," *IEEE Photonics Technology Letters*, vol. 20, pp. 653-655, 2008.
- [240] A. Stöhr, A. Akroud, R. Buß, B. Charbonnier, F. van Dijk, A. Enard, S. Fedderwitz, D. Jäger, M. Huchard, F. Lecoche, J. Marti, R. Sambaraju, A. Steffan, A. Umbach, and M. Weiß, "60 GHz radio-over-fiber technologies for broadband wireless services," *J. Opt. Netw.*, vol. 8, pp. 471-487, 2009.
- [241] M. Weiß, "60 GHz photonic millimeter-wave communication systems," *PhD Thesis*, Universität Duisburg-Essen, 2010.
- [242] I. G. Insua, D. Plettemeier, and C. G. Schäffer, "Simple remote heterodyne RoF system for Gbps wireless access," in *International Topical Meeting on Microwave Photonics Valencia*, 2009.
- [243] J. Yu, J. Hu, D. Qian, Z. Jia, G. Chang, and T. Wang, "Transmission of microwave-photonics generated 16Gbit/s super broadband OFDM signals in radio-over-fiber system," pp. 1-3, 2008.
- [244] G. Chang, A. Chowdhury, Z. Jia, H. Chien, M. Huang, J. Yu, and G. Ellinas, "Key technologies of WDM-PON for future converged optical broadband access networks [invited]," *IEEE/OSA Journal of Optical Communications and Networking*, vol. 1, pp. C35-C50, 2009.
- [245] A. Ng'oma, M. Sauer, F. Annunziata, W.-J. Jiang, P.-T. Shih, C.-T. Lin, J. Chen, and S. Chi, "14 Gbps 60 GHz RoF link employing a simple system architecture and OFDM modulation," in *International Topical Meeting on Microwave Photonics Valencia*, 2009.
- [246] A. Stöhr, M. Weiß, V. Polo, R. Sambaraju, J. L. Corral, J. Marti, M. Huchard, B. Charbonnier, I. Siaud, S. Fedderwitz, and D. Jäger, "60 GHz radio-over-fiber techniques for 10 Gb/s broadband wireless transmission," in *Wireless World Research Forum*, Ottawa, 2008.
- [247] G. Chang, A. Chowdhury, H. Chien, and G. Ellinas, "Architectures and technologies for very high throughput in-building wireless services using radio-over-fiber networks," in *IEEE LEOS Summer Topical Meeting*, Newport Beach, pp. 37-38, 2009.
- [248] M. Sauer, A. Ng'oma, and A. Kobyakov, "Fiber-Radio Solutions for In-Building High Speed Wireless Networks," in *SPIE Broadband Access Communication Technologies IV*, vol. 7620, 2010.

- [249] A. Ng'oma, C.-T. Lin, L.-Y. Wang He, W.-J. Jiang, F. Annunziata, J. Chen, P.-T. Shih, J. George, and S. Chi, "31 Gbps RoF System Employing Adaptive Bit-Loading OFDM Modulation at 60 GHz," in *Optical Fiber Communications Conference OFC/NFOEC* Los Angeles, paper OWT7, 2011.
- [250] X. Pang, A. Caballero, L. Dogadaev, V. Arlunno, R. Borkowski, J. S. Pedersen, L. Deng, F. Karinou, F. Roubeau, D. Zibar, X. Yu, and I. Tafur Monroy, "100 Gbit/s hybrid optical fiber-wireless link in the W-band (75-110 GHz)," *Optics Express*, vol. 19, pp. 24944-24949, 2011.
- [251] S. Koenig, J. Antes, D. Lopez-Diaz, I. Kallfass, T. Zwick, C. Koos, W. Freude, and J. Leuthold, "High-Speed Wireless Bridge at 220 GHz Connecting Two Fiber-Optic Links Each Spanning up to 20 km," in *Optical Fiber Communication Conference (OFC/NFOEC 2012)* Los Angeles, p. OM2B.1, 2012.
- [252] CENELEC, "Considerations for evaluation of human exposure to electromagnetic fields (EMFs) from mobile telecommunication equipment (MTE) in the frequency range 30 MHz - 6 GHz," in *ES 95009: European Committee For Electrotechnical Standardization*, 1998.
- [253] A. Stöhr, R. Heinzelmann, T. Langer, C. Rheinfelder, W. Heinrich, T. Alder, D. Kalinowski, M. Schmidt, M. Groß, and D. Jäger, "Novel analog optical RF E-field sensor," in *Photonics and Radio Frequency II*, vol. 3463, Eds. G. J. Zagar, A. P. Goutzoulis, and A. R. Pirich, Proceedings of the SPIE, pp. 158-167, 1998.
- [254] A. Stöhr, R. Heinzelmann, T. Alder, R. Buß, and D. Jäger, "Electroabsorption modulators for broadband fiber electro-optic field sensors," in *Applications of Photonic Technologies* 2 New York, Plenum Press, ISBN: 0-306-45808-X, pp. 871-876, 1997.
- [255] L. Morvan, G. Pillet, A. Stöhr, and A. Garcia, "Demonstrator Building Report," PHOMIGEN technical report TN4, 2012.
- [256] A. Garcia, G. Pillet, L. Manager, L. Morvan, S. Babiel, S. Fedderwitz, and A. Stöhr, "Low Phase Noise and Frequency Tunable 95-115 GHz Photonic LO Based Upon DSB-SC Modulation in an MZM and FWM in an UL-SOA," in *IEEE International Topical Meeting on Microwave Photonics (MWP)* Noordwijk, The Netherlands, 2012.
- [257] A. Garcia, S. Fedderwitz, and A. Stöhr, "Optical Generation of Low-Phase Noise Microwave Signals using Nonlinear MZM and Ultra-Long SOA," in *International Microwave and Optoelectronics Conference (IMOC 2011)*, pp. 255-259, 2011.
- [258] A. Garcia, V. Rymanov, and A. Stöhr, "Low Phase Noise Photonic Millimeter Wave Generation using a Nonlinear MZM and Four Wave Mixing in Ultra Long SOAs," in *Progress in Electromagnetics Research Symposium PIERS 2012*, Moscow, 2012.
- [259] P. Pillet, L. Morvan, L. Ménager, A. Garcia, S. Babiel, and A. Stöhr, "100 GHz phase-locked dual-frequency laser", IEEE International Topical Meeting on Microwave Photonics," in *IEEE International Topical Meeting on Microwave Photonics (MWP)* Noordwijk, The Netherlands, 2012.